

Investigation of large-scale structures in turbulent boundary layer and their detections by wall-based sensors array

Thesis submitted to the University of Nottingham for the degree of Doctor of Philosophy in the Faculty of Engineering

April 2020

By

Noura Rkiouak, M.Sc.

Department of Mechanical, Materials and Manufacturing Engineering

Contents

Chapter 1 Introduction 1

1.1 Nature of the problem 1

1.2 Aims and Objectives 2

1.3 Thesis Outline 4

Chapter 2 Literature review 5

2.1 Turbulent boundary layers – Turbulent wall flows 5

Turbulence statistics 5

Mean Velocity Profiles - Turbulent Boundary Layers 6

Inner layer 7

Buffer layer 8

Logarithmic layer 8

Outer layer 8

Wake region 8

Shear Produces Turbulence 8

2.2 Near-wall region 9

2.2.1 Near-wall control 12

2.3 Large-scale structure 15

2.3.1 Large-scale control 21

2.4 Inner and outer region 23

Chapter 3 Experimental facility, equipment and set-up 29

Part 1: Wind tunnel and HWA descriptions and uncertainties 30

3.1.1 Wind tunnel 30

3.1.2 Thermal Anemometry System 33

Part 2: s-PIV and synchronisation uncertainties 66

3.2.1 Particle Image Velocimetry System 66

3.2.2 PIV and A/D synchronisation 90

3.2.3 Sampling frequency – Reliability of the Labview program 93
3.2.4 Chapter Summary 94
Chapter 4 Method validation 95
4.1 Introduction 95
4.2 Turbulent Boundary Layer Profiles and Characteristics 95
4.2.1 Mean and statistics profiles 96
4.2.2 Turbulent Boundary Layer Characteristics 103
4.3 PIV validation 103
4.3.1 Boundary layer 104
4.3.2 Identification of hairpin structures through hairpin signature in x-y plane 105
4.3.3 Hairpin Detection Method 108
4.3.4 Hairpin vortex packets in x-y plane 110
4.3.5 Large-scale structures using PIV 113
4.4 S-PIV accuracy and validation 118
4.4.1 Brightness of images 119
4.4.2 Particle density/distribution (Particles per interrogation volume) 122
4.4.3 Averaging values in z-direction 124
4.5 Comparison of stereoscopic PIV and Hot-Wire statistics of turbulent boundary layer 127
4.5.1 Introduction 127
4.5.2 S-PIV in comparison with HW 127
4.6 Chapter Summary 135
Chapter 5 Near-wall investigations at different wall-normal positions and Reynolds Number Dependence 138
5.1 Introduction 138

5.2 Near-wall structures in comparison with large-scale structures using hot-wire array and PIV 138
5.2.1 Instantaneous skin-friction mapping at different Reynolds Number Dependence 138
5.3 Skewness and kurtosis measurements with respect to the Reynolds Number Dependence 150
5.4 Cross-correlation measurements with respect to the Reynolds Number Dependence 155
5.4.1 Cross-correlation measurements with respect to the Reynolds Number Dependence in the spanwise direction 155
5.4.2 Cross-correlation measurements with respect to the Reynolds Number Dependence in the streamwise direction 162
5.5 Chapter Summary 168
Chapter 6 On the relation of large-scale structures and skin-friction 170
6.1 Introduction 170
6.2 Effect of large-scale structures on the wall skin-friction fluctuations 170
6.2.1 PIV plane at same level as hot-wire rake 171
6.2.2 S-PIV upstream of hot-wire rake 172
6.3 Chapter Summary 185
Chapter 7 Conclusions and Future Recommendations 186
References 190

Abstract

Only limited DNS and experimental information about the interaction between wall skin-friction fluctuations and large-scale structure is available. The ability to gain insight into this interaction experimentally is substantial. This research study presents results of an experimental investigation to study stereoscopic PIV by highlighting the results obtained with s-PIV in comparison with the one obtained by hot-wire (HW) sensors. It is followed the investigations of Reynolds numbers that are lower than available prior experimental and span the DNS and experimental ranges in the literature. It ends on the experimental investigation, at $Re_\tau = 568$, of the effects of large-scale structures on wall shear-stress fluctuations. Both, flow visualisation and hot-wire anemometry are used simultaneously to investigate their correlation. The idea is to use the signals from a rake of twenty hot-wire sensors placed at the wall, to reconstruct the instantaneous profile of the skin-friction fluctuation. By projecting this signal in time and using Taylor's hypothesis a view of the mapping of the instantaneous skin-friction is obtained in the *x*-*z* plane. By using stereoscopic PIV, a map of the large scale-structure in the log-region is captured and analysed to identify the large-scale structures in the log-outer regions. Data are taken simultaneously between hot-wire sensors and s-PIV, to obtain information from a map of fluctuating skin-friction signal at the wall together with the large-structure in the log-region. It is shown that large-scale structures exist in the log layer and that they certainly contribute to structures at the wall. Moreover, it is revealed that large-scale structures exist even in the skin-friction fluctuations, which are essentially associated with the large-scale structures in the log layer. Indeed, similarities between the patterns from instantaneous skin-friction map at the wall and the velocity map in the buffer and logarithmic regions are found.

Acknowledgements

Most notably I would like to acknowledge the guidance and encouragement of my supervisor Professor Kwing-So Choi. I thank him for having faith in me and for our intriguing conversations. Professor Kwing-So Choi has provided tremendous support over the last four years and I feel privileged to have been able to work with him.

I would also like to extend my warm thanks to my internal assessor Doctor Donald Giddings for his useful advices. His support and encouraging words allowed me to make it to the end with success.

Thanks must also go to my colleagues at Fluid Group, who prepared important input or acted as peer reviewers, providing comments and suggestions for improving this sector work suggestions over the years. I would like to give special acknowledgement to Doctor Jung-Hoon Kim, who provided much assistance in experiment set-up and valuable discussion. Thanks are further attributed to L4 and Tower Building technicians, for their technical support.

I have to express my deep gratitude to Airbus group innovation, who provided me funding to accomplish this work.

Last but not the least, I would like to show my greatest appreciation to my family especially my Mum, my Dad, my sister Laylla, my brother Yassin, and my dear husband Mohamed for their patience and unconditional support over these years. A special thanks to my spiritual teacher Sidi Abdelouahid Ibn Ajiba, to my best friends Majd, and Inchirah and to my friends Gurbet, and Shahsia for their support.

List of Figures

Figure 1: Time series signal 5
Figure 2: Mean velocity profile of a smooth-flat-plate turbulent boundary layer plotted in log-linear coordinates with law-of-the-wall normalisations 7
Figure 3: Turbulence intensity profile at different free-stream velocities 9
Figure 4: Conceptual model for self-sustaining mechanism (Choi, 1989) 12
Figure 5: Horseshoe structure from Theodorsen (Theodorsen, 1952) 15
Figure 6: Hairpins in high Reynolds number (Head and Bandyopadhyay, 1981) 16
Figure 7: Effect of Reynolds number from Robinson (1991) based on Head and Bandyopadhyay (1981) 16
Figure 8: Parts of a hairpin vortex within the TBL by Robinson (1991) 17
Figure 9: Relationship between ejection/sweep and hairpin vortices in the outer region from Robinson (1991) 17
Figure 10: (a) Conceptual model with induced motion depicting Q2 and Q4 activity. (b) Signature of a hairpin vortex (Adrian et al., 2000a) 18
Figure 11: Very large-scale motions from Kim and Adrian (1999) 19
Figure 12: Energy spectra of the streamwise velocity fluctuations for a turbulent boundary layer at Re_τ = 7300. The dashed lines denote locations of inner and outer spectral peaks (Hutchins and Marusic, 2007b) 20
Figure 13: Instantaneous flow fields from Re_τ = 934 channel simulations. Filtered data (Hutchins and Marusic, 2007a) 21
Figure 14: (Left side) Diagram to show direct intervention of hairpin vortices. (Right side) Ensemble-averaged streamwise velocity (a) without control and (b) with control (Kang et al., 2008) 23
Figure 15: Contours of the filtered *T1* and top view of the low-speed regions in the VLSMs for Re_τ = 640. (a) filtered *T1*; (b) top view of the low-speed regions in the outer layer (Abe et al., 2004) 25
Figure 16: Time series of skin-friction fluctuations from hot film and velocity fluctuations from hot-film probe 6 at z^+ = 0 and hot-wire probe 2 at z^+ = 11 (Hucthins et al. 2011) 27

Figure 17: Skin-friction fluctuations signals from the spanwise array: (a) unfiltered raw data; (b) filter of size 0.5δ x 0.16δ (streamwise and spanwise) applied (Hutchins et al. 2011) 27
Figure 18: Streamwise velocity fluctuations at $y+$ = 13.5. (Agostini and Leschziner, 2014b) 28
Figure 19: Front view schematic of test section of the wind-tunnel 30
Figure 20: Trip device 30
Figure 21: Schematic of test section of the wind-tunnel. 1 Wall probes, 2 Moving traverse table and 3 Upper wall test surface 32
Figure 22: Corners of the wind-tunnel 33
Figure 23: Hot-wire principle 34
Figure 24: Miniature wire-probe, 55P15 and probe support (Dantec Measurement Technology) 35
Figure 25: Miniature wire-probe, 55P16 (Dantec Measurement Technology) 36
Figure 26: (Top) Flow master calibration curves and (Bottom) curve fitting error 37
Figure 27: Hot-wire calibration curve (top) whole range and (bottom) at low velocities 39
Figure 28: Error between measured data points and those predicted by different calibration method 40
Figure 29: Relationship of the velocity versus voltage profiles 41
Figure 30: Calibration curve at 17.5^0C 42
Figure 31: Calibration curve at 21.1^0C 42
Figure 32: Calibration curve at 23^0C 42
Figure 33: FFT analysis of signal from hot-wire sensor 44
Figure 34: Effect of the heat transfer on Dantec 55P16 hot-wire probe measurements 45
Figure 35: Home-built KI-NI997 CTA board 47
Figure 36: home-built CTA enclosure 47
Figure 37: The square wave test response of hot-wire probe operated by a CTA (after (Bruun, 1995b)) 48
Figure 38: Mean velocity profile 51
Figure 39: Turbulence intensity profile 51

Figure 40: Skewness 51
Figure 41: Kurtosis 51
Figure 42: Power spectral density (PSD) Dantec commercial unit and multi-channel unit 52
Figure 43: Schematic diagram of the wall hot-wire method 54
Figure 44: 20 channels hot-wire system placed on the upper wall of the wind tunnel 54
Figure 45: Dimensions of the 20 cavities on the upper wall of the wind tunnel 55
Figure 46: Diagram of hot-wire anemometry set-up to investigate the turbulent boundary layer. 56
Figure 47: Schematic of the hole/cavity drilled in the upper wall of the wind tunnel through the 12 mm Perspex. 56
Figure 48: Set-up of a scale to set the sensors at a known distance of 0.5mm from the wall 57
Figure 49: Positions of the sensors from the wall at 0.5 mm 58
Figure 50: Position of the sensors from the wall 58
Figure 51: Positions of the sensors to the wall at 0.12 mm 59
Figure 52: Mean streamwise velocity profile for data placed under the holes in comparison of the data not placed under the holes 60
Figure 53: Turbulence intensity profiles for data placed under the holes in comparison of the data not placed under the holes 61
Figure 54: Energy spectra from the hot-wire sensors for various locations .. 61
Figure 55: Energy spectra from the hot-wire sensors with and without particles 62
Figure 56: Example of application of median filtering 64
Figure 57: PIV overview (Johnson et al., 2006) 67
Figure 58: Seeding Injector 68
Figure 59: Seeding injector dimensions 69
Figure 60: Overlap of the interrogation area 69
Figure 61: Analysing with DantecStudio using PIV 70
Figure 62: Large multi-level target with a two-level grid of dots (Dantec Reference Manual) 71

Figure 63: Back and front view configuration adapted from Dantec (Reference Manual). 72
Figure 64: Arrangement between cameras/laser in relation to the wind tunnel section. 73
Figure 65: Sketch of the structurally enhanced frame work (Will Bowling). 75
Figure 66: schematic of s-PIV set up with cameras put on side (plan view). 77
Figure 67: Optimal camera configuration for an optimal determination of the s-PIV calibration coefficients with cameras put on the side. 77
Figure 68: Right and left calibration grid images obtained by each camera using double sided (multi-level) calibration target. 77
Figure 69: Rotation of camera placed on Scheimpflug mount with 105 mm lens. 78
Figure 70: Top corner filled (left side) and side corner filled (right side) 78
Figure 71: Schematic of experimental arrangement demonstrating the position of the cameras and laser 79
Figure 72: Optimal camera configuration for an optimal determination of the s-PIV calibration coefficients with cameras put on the top. 79
Figure 73: calibration images from back (right) and front (left) cameras. 80
Figure 74: Near wall field of view obstructed due to hot-wire holes 81
Figure 75: upper wall Perspex 81
Figure 76: Flow visualisation with seeding put on top of the wind tunnel (local seeding). 84
Figure 77: Flow visualisation with seeding put on back of the wind tunnel. 85
Figure 78: Stand for calibration target at holes level. 86
Figure 79: Imaging model for each camera. The average reprojection errors of the marked locations were estimated to be 0.244 and 0.247 pixels for the left and right camera, respectively. 88
Figure 80: 3D PIV vector map obtained after stereo PIV processing. The scale below the vector map illustrates the magnitude and direction of the out-of-plane velocity component. 90
Figure 81: Timing diagram of synchronization between the camera and the laser (Dynamic Studio Manual). 92

Figure 82: Connection diagram for s-PIV measurements (Modified from DynamicStudio Manual) 92
Figure 83: Synchronization test 93
Figure 84: Signal from Signal Generator set at 100 Hz, 2Vpp sampled at 1000 Hz for 10 seconds 94
Figure 85: Mean velocity profile, $u+$ vs. $y+$ at a free-stream velocity of 2.2 m/s at x=3.2 m. 97
Figure 86: Turbulence intensity profile at 2.2 m/s. 97
Figure 87: Profile of 3rd and 4th moment at x = 3.2 m from the inlet of the test section. The x-axis represents the nominal y (y_n) and the y-axis represents skewness and kurtosis factors Reт = 423. 98
Figure 88: Mean velocity profile at U_∞=3.2 m/s, Re_τ=587 with different possibilities of y^+=0 to find the wall position. 99
Figure 89: Turbulence intensity profiles at 3.2 m/s in comparison with others. 99
Figure 90: Profile of 3rd and 4th moment at x = 3.2 m from the inlet of the test section. The x-axis represents the nominal y^+ (y^+_n) and the y-axis represents skewness and kurtosis factors for Reт = 568. 100
Figure 91: Mean velocity profile at U_∞ = 7.4 m/s, Re_τ = 1310 with different possibilities of y = 0 to find the wall position. 101
Figure 92: Turbulence intensity profiles at 7.4 m/s in comparison with others. 102
Figure 93: Profile of mean, 2nd, 3rd and 4th moment of the velocity at x = 3.2 m for U_∞ = 7.4 and Re_τ = 1310. 102
Figure 94: Mean streamwise velocity profile 104
Figure 95: Single hairpin vortex signature in the streamwise-wall-normal plane from fluctuating velocities 107
Figure 96: Example of vortex identification and extraction in an instantaneous, two dimensional PIV velocity field 109
Figure 97: Packet of hairpin vortex with signature in the streamwise-wall-normal plane from fluctuating velocities 112
Figure 98: Hairpin structure identification in x-y plane from iso-contour 113
Figure 99: Visualisation of vortices. Green iso-surface: $|\lambda_{ci}|_{iso} = 0.18|\lambda_{ci}|_{max}$ at x^+ = 1000 to 3500. 115

Figure 100: Visualisation of vortices. Green iso-surface: $|\lambda_{ci}|_{iso} = 0.18|\lambda_{ci}|_{max}$ at $x^+ = 3000$ to 5000 116
Figure 101: Visualisation of vortices. Green iso-surface: $|\lambda_{ci}|_{iso} = 0.18|\lambda_{ci}|_{max}$ at $x^+ = 5000$ to 7500 117
Figure 102: Visualisation of vortices. Green iso-surface: $|\lambda_{ci}|_{iso} = 0.18|\lambda_{ci}|_{max}$ at $x^+ = 2.5$ to $2.85*10^4$ 118
Figure 103: Statistics Profiles in linear abscissa. 120
Figure 104: Statistics Profiles in logarithmic abscissa. 120
Figure 105: Particle density distribution, IA size 64x64pixels, image 1000 a) frame 1 and b) frame 2 123
Figure 106: Mean Streamwise (left) and fluctuating (right) velocity maps ... 125
Figure 107: Mean Streamwise velocity map after post-processing, rotation of 3°. 125
Figure 108: Statistics Profiles in linear abscissa. 126
Figure 109: Statistics Profiles in logarithmic abscissa. 126
Figure 110: Mean velocity profile and turbulence statistics linear abscissa. 129
Figure 111: Mean velocity profile and turbulence statistics logarithmic abscissa. 130
Figure 112: Statistics Profiles using different IA sizes in logarithmic abscissa. 133
Figure 113: Statistics Profiles using different IA sizes in linear abscissa. ... 134
Figure 114: Errors estimated between values from different IA sizes and HW 134
Figure 115: Streamwise- Spanwise instantaneous velocity fluctuation maps at 4 *y*+ positions and 3 Reynolds numbers without filter. 142
Figure 116: Streamwise- Spanwise instantaneous velocity fluctuation maps at 4 *y*+ positions and 3 Reynolds numbers without filter with the spanwise resolution (same spacing between each sensor for all the Reynolds numbers). 143
Figure 117: Streamwise- Spanwise instantaneous voltage fluctuation maps at different Reynolds Number and at *y*+ = 1. a) No filter. b) 93, 88 and 96 w.u. x 2δ filter size. c) 93, 88 and 96 w.u. x 20δ filter size 146
Figure 118: Streamwise- Spanwise instantaneous voltage fluctuation maps at different Reynolds Number and at y+ = 3. 147

Figure 119: Streamwise- Spanwise instantaneous voltage fluctuation maps at different Reynolds Number and at y+ = 0. 148
Figure 120: Skewness and Kurtosis with authors listed in Table 6 (right: y^+ < 1.4). 152
Figure 121: Skewness and Kurtosis at different y+ and Re_τ for 20 sensors. 154
Figure 122: Two-point spanwise correlation coefficients of velocity fluctuations at different Reynolds Numbers and y-locations. 157
Figure 123: Spanwise two-point correlation coefficient at y+ = 11 from Abe et al. (1972)..... 158
Figure 124: Two-point correlations in the spanwise direction at different y^+ locations from the wall. 161
Figure 125: Two-point streamwise correlation coefficients at different Reynolds Number 164
Figure 126: Two-point correlations in the streamwise direction at different locations from the wall. 164
Figure 127: Two-point streamwise correlation coefficients of velocity fluctuations at Re_τ = 640 from Abe et al (2001) 164
Figure 128: Two-point streamwise correlation coefficients at different Reynolds Number 165
Figure 129: Two-point streamwise correlations Re_τ = 180 from Kim et al. (1987) 165
Figure 130: Streamwise correlations of the streamwise velocity fluctuation Ruu at (●) Re_τ = 1120 (Note their z-direction is our y-direction) from Hucthins et al. (2007a) 165
Figure 131: Length scale over boundary layer thickness at Re_τ = 423, 568 and 1410..... 167
Figure 132: Fluctuating friction signals from the spanwise array and velocity signals from PIV at hole level. Interpolated data..... 171
Figure 133: Fluctuating friction signals from the spanwise array and velocity signals from PIV, filter size: 137 x 408 wall unit in the spanwise and the streamwise directions, respectively at hole level. Filtered data..... 172
Figure 134: Skin-friction maps by hot-wires vs. velocity maps by PIV, Original data..... 175

Figure 135: Skin-friction maps by hot-wires vs. velocity maps by PIV, interpolated data 176
Figure 136: Fluctuating friction signals from the spanwise array and velocity signals from PIV, filter size: 137 x 408 wall unit in the spanwise (z) and the streamwise (x) directions, respectively. 177
Figure 137: Time series of velocity fluctuations at y+ = 27, 53, 80 and 106 wall unit and skin-friction fluctuations (20 000 wall unit). The data was obtained simultaneously. 178
Figure 138: Cross-correlation of skin-friction fluctuation and velocity fluctuations at y+ = 27, 80, 106 and 133 in the streamwise direction at z+ = 400. 181
Figure 139: Correlation coefficient Ruu between skin-friction and 3 wall normal positions along z+ 184

List of Tables

Table 1: The four quadrants contributing to the Reynolds stress, adapted from Wallace et al. (1972). 11
Table 2: Turbulence Intensity of Wind Tunnel 31
Table 3: Constants for King's law curve fit 38
Table 4: Error in the estimated velocity at different temperature 43
Table 5: The cut-off frequency of the twenty sensors 48
Table 6: Turbulent boundary layer parameters commercial unit versus multi-channel unit 52
Table 7: Position of each sensors from the wall 59
Table 8: Characteristics of turbulence for data under holes vs no holes 60
Table 9: Size of median filter, cells versus wall unit, for different free-stream velocities 64
Table 10: Fundamental quantities for the measurements using the current set up 87
Table 11: Turbulent Boundary Layer Characteristics 103
Table 12: Characteristics of the turbulent boundary layer measured with 2D PIV 104
Table 13: Near-wall structures frequency of streamwise and spanwise length at Re_τ = 568 114
Table 14: Quantities for the measurements in this section 119
Table 15: Number of particles for several images out of 5000 images (I) for IA of 64x64 pixel. 124
- Table 16: Quantities for the measurements in this section 127
Table 17: Formulae 128
Table 18: IA sizes in pixels, mm and wall unit 132
Table 19: Summary of interrogation areas sizes 132
Table 20: Modification of spacing between sensors at different Reynolds numbers 143
Table 21: Near-wall structures frequency of streamwise and spanwise length at different Reynolds numbers 145
Table 22: Figure Legend 145

Table 23: Skewness and Kurtosis at various Reynolds number and y^+ positions for 20 sensors 151
Table 24: Measured moments of the streamwise velocity fluctuations. 153
Table 25: Minimum correlations coefficient peak at different Reynolds numbers 155
Table 26: Spanwise spacing between sensors at different Reynolds numbers 156
Table 27: Length scale over boundary layer thickness at Re_τ = 423, 568 and 1410. 167
Table 28: Means and standard deviation of the normalised velocity fluctuations 172
Table 29: Correlation coefficient between signal of skin-friction vs. y+=27,106, and 133 181
Table 30: Correlation coefficient between signal at y+=27 vs. y+=106 and y+=133 181
Table 31: Correlation coefficient Ruu between skin-friction and 3 wall normal positions along z+ 184

Nomenclature

A	Calibration constant
a	Hot-wire heating ratio (R_w/R_a)
B	Calibration constant
C	Calibration constant
d	Diameter
dt	Time between the two consecutive laser pulses
E	Voltage
Ea	Acquired voltage during calibration
Es	Energy per sample
Ew	Voltage of the hot-wire sensor
e'	Root mean square of the instantaneous voltage
F	Calibration constant
Fc	Cut-off frequency
H	Shape factor, δ^*/θ
I	Turbulence intensity
l^+	Viscous length scale
K	Kurtosis factor
k	Length
n	Calibration constant
P	Pressure
P_{mean}	Power of mean signal
P_{noise}	Power of noise signal
Q	Q criteria
R	Resistance
Ra	Resistance of wire at ambient temperature, Ta
Rc	Cable resistance
Rl	Lead resistance
$Rx(\tau)$	Autocorrelation function
Re	Reynolds number
Rw	Resistance of heated wire at temperature, Tw
$Re\theta$	Momentum thickness Reynolds number ($U\infty\theta/\nu$)

Re_τ	Friction velocity Reynolds number ($u_\tau \delta/\nu$)
R_0	Cold resistance
R_{uu}	Autocorrelation coefficient function
S	Skewness factor
t	Time
T	Temperature
T^+	Period
Ta	Ambient temperature
T_0	Temperature obtained during the calibration
T_w	Wire temperature
τ_{wall}	Wall stress
U	Mean streamwise velocity
$U\infty$	Free-stream velocity
U_c	Convection velocity
U_e	Estimated velocity through curve fitting
U_m	Velocity measured with the Flow-Master
u_{rms}	Standard deviation of velocity fluctuations
u	Streamwise velocity component
u^*	Friction velocity
u_{local}	Local velocity in the wall-normal direction
u'	Streamwise fluctuation
v	Wall-normal instantaneous velocity
ν	Kinematic viscosity
ν/u^*	Viscous length
V_{mean}	Voltage of mean signal
V_{noise}	Voltage of noise signal
w	Spanwise velocity
x	Streamwise coordinate
y	Wall-normal coordinate
y_n	Nominal wall-normal coordinate
z	Spanwise coordinate
z_r	Total spanwise spacing of the rake of sensors
z_s	Spanwise spacing between each sensor

κ	Constant von Karman
λ_{ci}	Local velocity gradient tensor
λ_2	Swirling strength
Δ	Change in a quantity, Velocity gradient tensor for vortex identification
δ	Boundary layer thickness
δ^*	Displacement thickness
θ	Momentum thickness
μ	Dynamic viscosity
v	Kinematic viscosity (μ/ρ)
ρ	Density
σ	Standard deviation
τ	Shear stress; time delay
τw	Mean wall shear stress (skin-friction)
ω	Vorticity
∇u	Velocity gradient tensor

Abbreviations

AC	Alternating current
ADC	Analogue-to-Digital Converter
A/D	Analogue-to-Digital Converter
AP	Adaptive PIV
BL	Boundary Layer
BNC	Bayonet Neill–Concelman
CTA	Constant Temperature Anemometer
dB	Decibel
DC	Direct current
DEHS	Di(2-Ethylhexyl) Sebacate
DNS	Direct Numerical Simulation
DO	Digital output
ds (subscript)	DynamicStudio
FOV	Field of view
hf6	Hot-film 6
hw2	Hot-wire 2
HS	Hairpin Signatures
HV	Hairpin Vortex
HVS	Hairpin Vortex Signature
IA	Interrogation Area
IEA	International Energy Agency
ICAO	International Civil Aviation Organization
IMF	Image Modeling Fit
LEBUs	Large-Eddy-Break-Up
LSMs	Large-Scale Motions
LDA	Laser Doppler Anemometer
m (subscript)	Matlab
PCHIP	Piecewise Cubic Hermite Interpolating Polynomial
PIV	Particle Image Velocimetry
Rms	Root-Mean-Square
SNR	Signal to noise ratio

s-PIV	Stereoscopic PIV
TBL	Turbulent Boundary Layer
VLSMs	Very Large Scale Motions
Q1	Quadrant 1
Q2	Quadrant 2
Q3	Quadrant 3
Q4	Quadrant 4
3D	Tree-dimensional
2D	Two-dimensional
2D3C	Two dimensions - Three components

Chapter 1 Introduction

1.1 Nature of the problem

The turbulent energy loss is one of the major challenges encountered by aircraft designers. It is the aerodynamic force that opposes an aircraft's motion through the air that is generated by every part of the external surface of the aircraft (Nicolai and Carichmer, 2010). Aircraft are carefully designed to minimise drag, but because they are large and fly at high speeds, it is still a major factor. The drag produced by the shape of the aircraft can be kept to a minimum by streamlining, but much of the remaining drag is a result of skin friction. Indeed, half of the energy spent in transporting fluids and aircraft through air is dissipated by turbulence in the immediate closeness of walls caused by turbulent skin-friction. Drag is mainly a result of three components including wave drag, form drag and skin-friction drag. Wave drag is related to the formation of surface waves or shock waves, form drag results from the difference in pressure between the wake of an object and the upstream and finally skin-friction drag is a consequence of the action of fluid shear at the interface between a fluid and solid.

In this way, a decrease in skin-friction drag translates into a reduction in fuel consumption. Given that fuel consumption is likely to rise dramatically in the next decade or two the interest in the matter is growing. It is predicted that fuel consumption in aviation will rise by a factor of 2 by 2050 (IEA, 2009). In 2010, aviation accounted for about 2% of the total global CO_2 emissions and around 12% of the CO_2 emissions from all transportation sources (ICAO, 2010). The European Union is taking action to reduce aviation emissions in Europe and working with the international community to develop measures with global reach (European Commissions, 2001).

This generates interest amongst researchers to investigate the structures within the turbulent boundary layer that are responsible for increased skin-friction. Developments in our understanding of the boundary-layer structure sheds further light on the complex flow dynamics and also offers basic input to

flow control strategies leading to a reduction of large vehicle drag and hence, by implication, emission levels.

While there has been achievements with these techniques, in the laboratory at least, there are many problems such as the effectiveness of skin-friction reduction by near-wall control as the Reynolds number increases (Iwamoto et al., 2002). Moreover, a high number of sensors would be needed to implant the existing strategies on aircraft. The structures of the outer layer also need to be manipulated in order to try and possibly achieve the drag reduction more effectively at high Reynolds numbers.

Large-scale controls such as large-eddy break-up devices (LEBU) (HEFNER et al., 1979, CORKE et al., 1979) have shown promising results for reducing skin-friction drag; reductions of around 40% have been reported. However, the net drag reduction using such devices has not been a success yet. In this thesis, attention is turned to those large-scale structures that exist in and beyond the logarithmic region. By such methods, we seek to further our understanding of turbulent boundary layers, aiming specifically to learn more about the interaction between large scale structure and instantaneous wall shear stress experimentally.

1.2 Aims and Objectives

Research into high-Reynolds-number turbulent boundary layers in recent years has brought about a renewed interest in the larger-scale structures which emerge in the outer region due to increased Reynolds number (Metzger and Klewicki, 2001, Hutchins and Marusic, 2007a).

The influence of the large scales on the near-wall is becoming ever clearer, in apparent contradiction to Townsend's inactive motion ideas (Townsend, 1961). According to Townsend, the large-scale motions are a passive part of turbulence meaning that they do not contribute to the shear stress and are considered as inactive motions on the wall region. They are not responsible for the turbulence intensity. Yet, it is revealed that footprint of large-scale structures exist in the wall shear-stress fluctuations at high Reynolds number, which are essentially associated with the large-scale structures in the outer

layer. Through analysis of instantaneous DNS data at $Re_\tau \approx 640$, Abe et al. (2004) were able to conclude that very large structures exist in the outer layer, and that these structures are instantaneously visible in the surface shear-stress fluctuations. Iwamoto et al. (2005) also show instantaneous snapshots of very large scale structures interacting with the near-wall streamwise velocity field at $Re_\tau = 2320$. Finally, very large structures have been observed with lengths as large as 20δ in the streamwise direction and significantly contribute to the total turbulent stress. It is observed that such features in the flow leave a statistical footprint in the instantaneous skin-friction (Hutchins et al., 2011).

However, only limited DNS data gives information about the interaction between wall skin-friction fluctuations and large-scale structure. The ability to gain insight into this interaction experimentally has been substantial. Our aim is to investigate, with hot-wire and stereoscopic PIV techniques, the interactions of the wall skin-friction fluctuations to the large-scale structures.

The principle of the experiment is to use the signals from a rake of twenty hot-wire sensors placed within the viscous sublayer to reconstruct the instantaneous profile of the skin-friction fluctuation. By projecting this signal in time and using Taylor's hypothesis a view of the mapping of the instantaneous skin-friction is obtained in the x-z plane. Simultaneously stereoscopic PIV is used to capture a map of the large scale-structure in the log-region.

In essence, the motivation as part of the project is to investigate the interrelationship between the large-scale structure present in the turbulent boundary layer and the instantaneous skin-friction signal at the wall. For the first time a 2D instantaneous experimental measurement of spanwise HWA related to the s-PIV is done to be compared with the DNS findings, done at $Re_\tau = 640$, about the correlation of wall shear stress with further from wall structures.

1.3 Thesis Outline

Chapter 2 provides a review of the literature with a brief summary of turbulent boundary layer theory in the first section. It continues on a discussion of coherent structures in the boundary layer which are important in drag producing effect. The chapter then moves on to a review of the interactions between inner and outer regions. Then, some of the techniques to reduce drag of a turbulent boundary layer will be discussed, with emphasis on large-scale control techniques.

In Chapter 3, the experimental facility and equipment used in the investigation is discussed. It also describes details of techniques to investigate the near-wall region. In addition, the experimental set-up is included in this section. It documents instrumentation and calibration procedures used throughout the experiments. The details of hot-wire sensors array and s-PIV are outlined.

Chapter 4 describes a series of experiments that were performed to validate the method used in the wind tunnel using two type of equipment; hot-wire sensor and PIV. It also presents results of an experimental investigation to study stereoscopic PIV. The section highlights the results obtained with s-PIV in comparison with the one obtained by hot-wire (HW) sensors.

The focus of chapter 5 is on a study to visualise and identify large-scale structures in the turbulent boundary layer. It is followed by near-wall statistics and structures in turbulent boundary layer at different wall-normal positions and Reynolds numbers

Chapter 6 continues on the study of the relation of large-scale structures and skin-friction. Both, flow visualisation and hot-wire anemometry are used simultaneously to investigate their correlation.

Finally, conclusions and Future Recommendations are made in Chapter 7.

Chapter 2 Literature review

2.1 Turbulent boundary layers – Turbulent wall flows

Let us consider turbulent fluid flows at solid boundaries. At such boundaries, the condition that the fluid velocity is zero applies at every instant in time. The fact that the fluctuations drop to zero at the wall has the particular implication that the Reynolds stress, $-\rho\overline{uv} = 0$, vanish. The only stress exerted directly on the wall is the viscous one. Away from the wall, instead, turbulence generates the Reynolds stress that is typically larger compared to the viscous stress.

Turbulence statistics

For turbulent flow, the velocity record includes both a mean and a turbulent component. We decompose the flow as follows.

$$u(t) = \bar{u} + u'(t)$$
$$v(t) = \bar{v} + v'(t) \quad (1)$$

This is commonly called a Reynolds' decomposition.

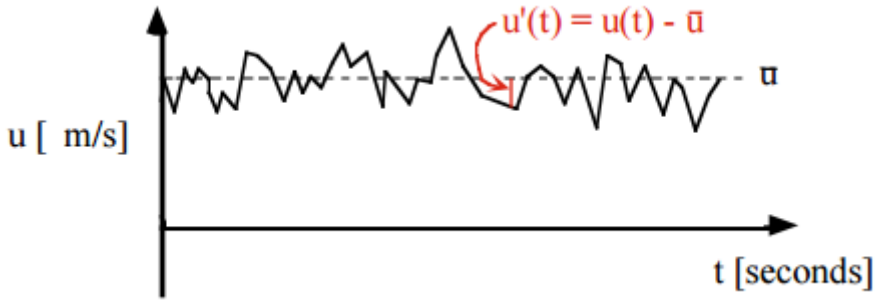


Figure 1: Time series signal

The traditional technique for decomposing turbulent velocity fields is Reynolds decomposition by subtracting the long-time-averaged velocity field from the instantaneous velocity field.

Turbulent eddies create fluctuations in velocity. Because the turbulent motions associated with the eddies are approximately random, we can characterize them using statistical concepts, such as;

Mean velocity

$$U = \bar{u}(t) \tag{2}$$

Turbulence

$$u' = \sqrt{\overline{u'^2}} = u_{rms} \tag{3}$$

The subscript 'rms' stands for root-mean-square. The definition of u_{rms} given in (2) should be recognised as the standard deviation of the set of "random" velocity fluctuations, *u'*. A larger u_{rms} indicates a higher level turbulence.

Turbulence Intensity

The turbulence intensity, I, is defined as the ratio of the root-mean-square of the velocity fluctuations, *u'*, to the free stream velocity, U_∞.

$$I = \frac{u\prime}{U_\infty} \tag{4}$$

Mean Velocity Profiles - Turbulent Boundary Layers

The boundary layer is a very thin layer in the immediate neighbourhood of a solid wall. In that thin layer, the velocity of the fluid increases from zero at the wall to its full value which corresponds to external frictionless flow. At the wall, this is called the "no-slip" condition whereby the fluid velocity matches the boundary velocity. This arises because of viscosity, μ, which is a fluid's resistance to flowing, i.e. fluid friction. The higher its viscosity, the more a fluid shows resistance to flowing. The layers of fluid above the surface are moving so there must be shearing taking place between the layers. The result is that the fluid velocity at the boundary (y = 0) is zero. At some distance above the boundary the velocity reaches a maximum value, U_∞, called the free-stream velocity. Between the wall and the free stream the velocity varies over the vertical coordinate. The spatial variation of velocity is called shear. The wall shear stress is defined as follows:

$$\tau_w = \mu \left(\frac{\partial u}{\partial y}\right)_{y\,=\,0} \tag{5}$$

where μ the dynamic viscosity, u the flow velocity parallel to the wall and y the distance to the wall. The thickness of the boundary layer, δ, is typically defined as the distance above the wall at which the velocity u parallel to the plate

reaches 99 percent of the external velocity U, $u = 0.99\,U_\infty$. Figure 2 depicts a typical mean velocity profile, $u(y)$, above a solid boundary. The horizontal axis (y^+) denotes the distance above the boundary. Different regions or layers are defined on y basis.

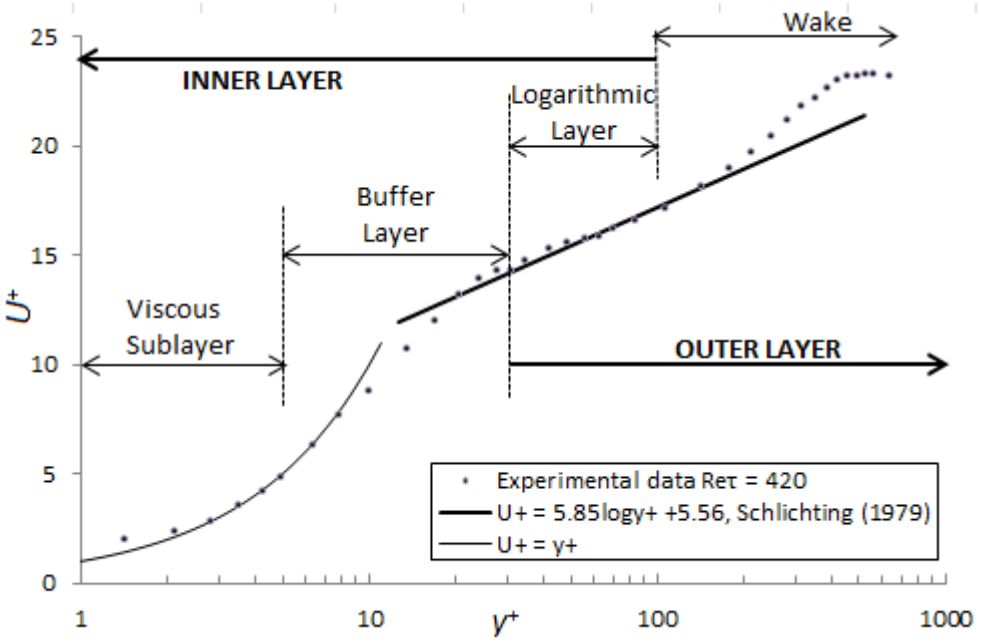


Figure 2: Mean velocity profile of a smooth-flat-plate turbulent boundary layer plotted in log-linear coordinates with law-of-the-wall normalisations

Inner layer

Viscous sublayer

The region closest to the wall in which the viscous shear stress is dominant is called the viscous sublayer. In this region close to the wall, $y^+ < 5$, where friction is important, the variation of the velocity, U^+ is linear with the distance from the wall, y^+ and is given by:

$$U^+ = y^+ \tag{6}$$

The law of the wall implies that in this region the distributions of mean velocity and intensity should be governed by the viscous length scale l^+ ($l^+ = \nu/u^*$, where ν is the kinematic viscosity, $u^* = \sqrt{\tau/\rho}$, where τ is the mean wall-shear stress, and ρ is the density of the fluid).

The + refers to the normalisation by wall variables, y^+ is the wall coordinate: the distance y to the wall, made dimensionless with the friction velocity u^* and

kinematic viscosity *v*, and U^+ is the dimensionless velocity: the velocity *u* parallel to the wall as a function of *y* divided by the friction velocity. The dimensionless coordinates and velocity are given as $y^+ = yu^*/\nu$, $z^+ = zu^*/\nu$, $x^+ = xu^*/\nu$, $U^+ = U/u^*$.

Buffer layer

The buffer layer is the transition region between the viscous sublayer and the log layer where the viscous stress and turbulent stresses are of the same order. It is approximately between 5 and 30 wall units, neither law holds.

Logarithmic layer

The region where the turbulent shear stress is many times greater than the viscous stress where the log-law holds and given by

$$U^+ = \frac{1}{\kappa} ln\, y^+ + B \tag{7}$$

where *κ* (von Karman constant = 0.41) and *B (* = 5.0*)*, are constants.

Outer layer

Wake region

The flow can be considered as inviscid/frictionless in this region, i.e. the viscous effect is very weak.

Shear Produces Turbulence

Turbulence is a flow regime generated by shear. The shear in the boundary layer decreases while moving away from the wall and as a result the turbulence intensity also decreases. Very close to the wall, however, the turbulence intensity is diminished, reaching zero at the wall ($y^+ = 0$). This is because the no-slip condition applies to the turbulent fluctuations as well as to the mean velocity. The turbulence strength increases with the free stream velocity, *u'* scales on U_∞ as seen in Figure 3.

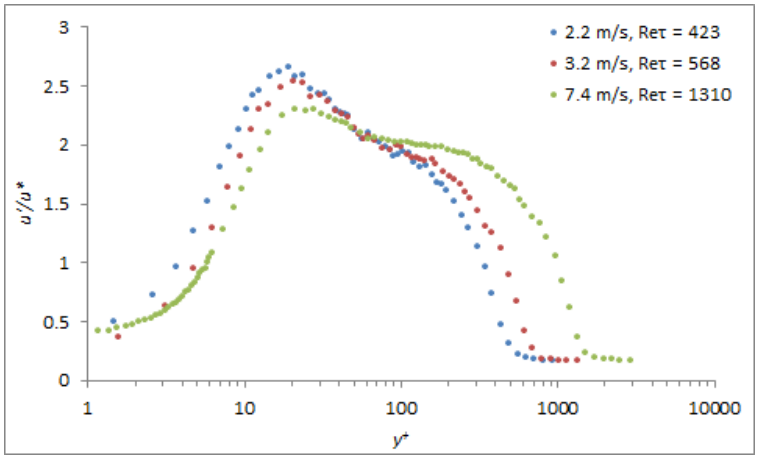


Figure 3: Turbulence intensity profile at different free-stream velocities

Friction velocity, u^*, represents the shear strength and it characterises the shear at the boundary. The definition of u^* is based on the wall stress, τ_{wall}, i.e. the friction velocity characterises the turbulence strength.

2.2 Near-wall region

One of the first groups who discovered the existence of near-wall structure was Kline et al. (1967). In their experiment where hydrogen bubbles technique was used for flow visualisation as well as hot-wire measurements, they visualised the structure of the turbulent boundary layer and showed that the viscous and buffer layer have a clearly defined structure of alternating low and high speed regions of streamwise streaks. Those streaks waver and oscillate within the viscous sublayer – the region next to the wall extending to $y^+ \approx 7$. Although these low-speed streaks occur randomly in the flow, they were seen to have an average spanwise spacing, $z^+ \approx 100$ and their streamwise length up to $x^+ \approx 1000$.

This observation led Kline et al. (1967) to conclude that those structures which take place in the near-wall lift up away from the wall and begin to oscillate to finally break up into a chaotic motion. The lifting of low-speed streak fluid was termed as ejection. Ejections are events accompanying the negative u-component velocity and positive v-component velocity in the region beyond $y^+ = 12$. Few years before, Klebanoff (1954) claimed that the majority of turbulence energy production occurred in the near-wall region.

Corino and Brodkey (1969) confirmed the findings of Kline et al. (1967) by performing high-speed visualisations of the flow. They went further in their research and viewed turbulent flow motions called sweep events. Sweeps are turbulence events associated with negative u-component velocity (streamwise velocity component) and negative v-component velocity (wall-normal velocity component) below $y^+ = 12$. Sweeps are defined by Corino and Bradkey (1969) as large scale motions of accelerated flow towards the wall. These phenomena produce velocity fluctuations near the wall and play significant roles in maintaining turbulence in the boundary layer. Whereas ejections were introduced by Kline et al. (1967) as motions of low speed streaks being oscillated and moved outwards away from the wall. They estimated that the ejections at $y^+ = 12$ contributed for around 70% of the total Reynolds stress within the boundary layer and assumed that the sweeps made up the rest.

Subsequent flow visualisation studies were done by Kim et al. (1971) where they studied the near-wall region by investigating structures based in the turbulent boundary layer (TBL) using hot-wire and hydrogen bubbles technique. They observed the streaky structure as found by Kline et al. (1967) and also found similar results to Corino and Brodkey (1969) and described the entire near-wall production cycle, termed as bursting process. The low-speed streaks move upwards away from the wall, oscillate and break-up. Bursting is defined as a violent outward eruptions of near-wall fluid (Kline et al., 1967, Robinson, 1991). Their experiments (Kim et al., 1971) showed that essentially all of the turbulence production occurred at $y^+ < 100$ during this bursting process. Sweeps and ejections represent the two most important motions.

Wallace et al. (1972) investigated a turbulent boundary layer using cross hot-wires to measure flow structure in the near-wall region. The sweep events are responsible for the generation of turbulence wall-shear stress and they take place close to the wall surface below $y^+ = 12$ (Wallace et al., 1972). The investigation of the u and v components of velocity (u, v are the streamwise and normal velocity fluctuations) led them to find that there are 4 events depending on four possible combinations of velocities. Their analysis of the signals showed that almost all of the Reynolds stress, $-\rho\overline{uv}$ results from ejection, Quadrant 2 (Q2) and sweep, Quadrant 4 (Q4) events shown in Table

1. Q2 is represented by $-u$ and $+v$ (second quadrant event), while Q4 is by $+u$ and $-v$ (fourth quadrant event). Quadrant 1 (Q1) and Quadrant 3 (Q3) events are called respectively, outward and inward interactions. They give negative contributions to the total Reynolds stress, resulting in, a reflection of high velocity sweeps away from the wall and in a deviation of low velocity regions back to the wall, respectively for Q1 ($u > 0$, $v > 0$) and Q3 ($u < 0$, $v < 0$) . (Wallace et al. 1972)

Table 1: The four quadrants contributing to the Reynolds stress, adapted from Wallace et al. (1972).

Quadrant	Type of motion	u	v	$-uv$
1	Interaction (outward)	+	+	-
2	Ejection	-	+	+
3	Interaction (inward)	-	-	-
4	Sweep	+	-	+

Willmarth and Lu (1972) Lu and Willmarth (1973) extended the quadrant analysis and carried out measurements to quantify the contribution of turbulent flow motions to the total Reynolds stress. The quadrant analysis technique based on instantaneous products $u\,v$ is used to obtain averages, in ejection and sweep quadrants, associated with coherent structures contributing significantly to Reynolds stress in a turbulent boundary layer. Willmarth and Lu (1972), concluded that the largest contribution to the Reynolds stress is attributed to the ejections (77%), and the second largest of 55% is attributed to the sweeps near the wall ($y^+ < 12$). This has been anticipated by Corino and Brodkey (1969) in their earlier paper and was in agreement with their studies.

Several models have since been proposed for the exact interaction between the streaks and the sweep and ejection event in the turbulence generation process. Choi (1989) proposed a mechanism for the self-sustaining of turbulence. This mechanism contains 3 stages as seen in Figure 4 where flow is from right to left. During stage 1, a spanwise vortex filament is deformed by

a bursting event that occurs upstream. In stage 2, the deformed vortex filament moves downstream where it develops into a hairpin loop moving away from the wall. Finally in stage 3, the hairpin loop develops due to self-induction and forms a hairpin vortex that moves away from the wall at an angle of around 45^0. The legs of the hairpins remain in the wall region forming a pair of counter-rotating streamwise vortices which induce a low speed fluid. Zhou et al. (1999) suggested a very similar mechanism.

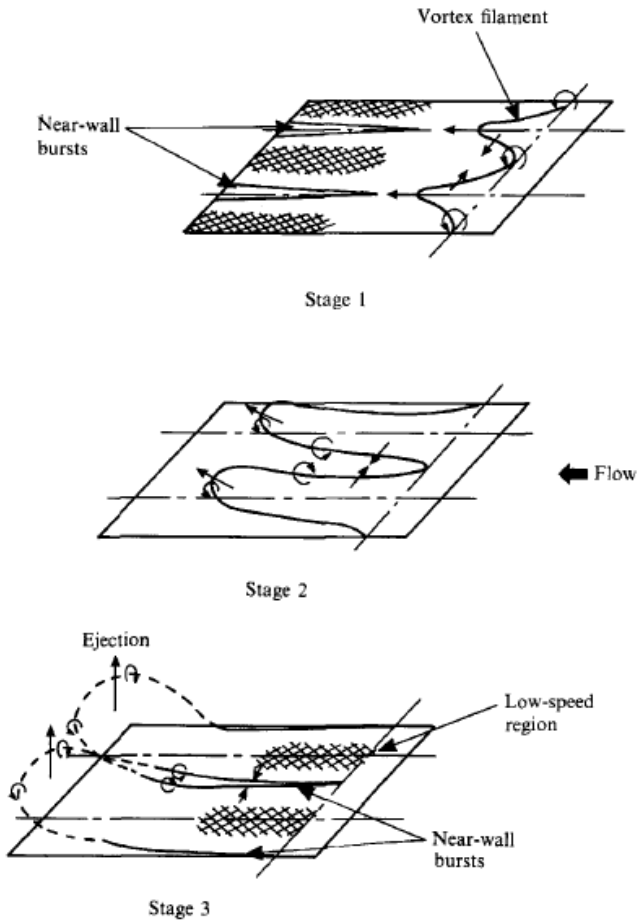


Figure 4: Conceptual model for self-sustaining mechanism (Choi, 1989)

2.2.1 Near-wall control

Through better understanding of the turbulent boundary layer, many studies have been performed in order to determine efficient and feasible control mechanisms. Many researchers have attempted to design devices that interfere with the turbulent boundary layer structures, with the aim of modifying the structures to reduce skin-friction. A brief review of some successful skin-friction drag reduction strategies is given in this section.

One of the successful strategies achieving skin-friction drag was discovered over thirty years ago and known as ‘riblets’. The aim is to use longitudinal grooves on the wall to reduce turbulent skin friction drag. Walsh (1980), Walsh et al. (1982), Bechert et al. (1985) and Bechert et al. (1986) performed a study on the flow over a riblet surface where they showed a reduction of turbulent skin friction. Numerous studies have since been carried out to achieve a better reduction by modifying the size, shape and spacing of the riblets. A good review is given by Walsh (1990). Choi (1989) analysed the velocities over riblets from experimental results and found that the skin-friction fluctuation intensity decreased by half. He suggested that the riblets had an effect on the burst process by reducing the strength and duration of the streaks leading to a reduction in the drag. This passive control mechanism has led to up to 10 % reductions in the drag.

Another technique, owing its existence to the dolphin modelled from dolphin’ skin (Kramer, 1957) is the use of compliant coatings to obtain reduction in drag force. Kramer (1957, 1960) used a combination of materials developed to be similar in properties and mimic dolphin skin. His experiments of comparing bodies coated with and without these materials showed reductions in drag. He suggested that the compliant coatings cause a delay in the transition from laminar to turbulent leading to a drag reduction. Some researchers (Benjamin, 1964) have shifted their focus to the possibility of obtaining drag reduction in the turbulent boundary layer. They argued that the compliant coating technique lead to a drag reduction, by affecting the turbulence generating processes. The maximum drag reduction of 10% was obtained using the compliant coating technique. Choi et al. (1997) studied turbulent drag reduction using compliant surfaces. They performed experiments in a water tunnel and attained a drag reduction of 7%.

By spanwise wall oscillation, a number of proposed drag-reduction strategies are based on the manipulation of the coherent near-wall events. In fact, Jung et al. (1992) showed that a 40% skin friction drag reduction was observed after applying a spanwise oscillation at the wall (period of $T^+ = 100$). By spanwise wall oscillation, the near-wall burst activity is weakened, leading to a reduction in skin-friction (Jung et al., 1992). Choi et al. (1998) also investigated turbulent

boundary layer control by means of spanwise wall oscillation from an experimental study at slightly higher oscillation frequency. They performed their experiments in a wind tunnel and suggested that the drag reduction is due to the creation of spanwise vorticity over the oscillating wall. Those vorticities decrease the mean velocity gradient close to the wall and lead to a reduction in skin-friction. They showed a reduction in turbulent skin-friction drag of up to 45%. In a later study, Choi (2002) explained that the skin-friction drag reduction was due to the sweep events being manipulated by the wall oscillation leading to a reduction of their strength and duration. The near-wall control leads to suppression and significant weakening or considerable elimination of the streaks by spanwise travelling wave (Karniadakis and Choi, 2003).

The techniques outlined above are non-selective control. The opposition control (Choi et al., 1994) is a method to achieve turbulence control and drag reduction by producing a feed-back actuation to the flow when detecting spatial and temporal signatures of events. Real-time opposition control of near-wall turbulence has been carried out in experiments by selectively cancelling the downwash of high-speed fluid during the sweep events. The wall ward movement of high speed region during the sweep events was blocked by the wall normal jet which suggests that the skin friction drag of the TBL can be reduced by opposition control of wall turbulence. There is a difference of 10% by using selective control, supressing only the strong turbulence events, in comparison with non-selective control, 15% vs. 25% (Rebbeck and Choi, 2006).

The focus on near wall is also often justified by the fact that the peak turbulence energy production occurs within the viscous buffer layer, at a wall-normal distance y^+ of approximately 12. Nevertheless, drag reduction performance may reduce while the Reynolds number increases for general near-wall control strategies (Iwamoto et al., 2002). A reason can be that by doing control, the entire near wall is changed and as the Reynolds number increase, this may be affecting the large-scale structure which affect the near-wall structure and then have an impact on the wall performance skin-friction. Furthermore, the implementation of the strategy/technology on the aircraft has to be considered. These near-wall controls are technically complex to achieve in a real-time

situation due to the small scale of actuators and fast response times required. With the actual controls, million sensors will be needed because one actuator will act only for several mm and considering the size of an aircraft, those near-wall strategies may not be convenient.

2.3 Large-scale structure

Theodorsen (1952) was the first to propose that the turbulent boundary layer comprises structures shown to be horseshoe or ring shaped in appearance (as depicted in Figure 5), that originated at the wall and covered a range of scales and are responsible for the transfer of momentum within the boundary layer. He was the first to propose these horseshoe vortices to be the primary element of all turbulent shear flows, but their importance and even their presence have long been recognised (Cantwell, 1981).

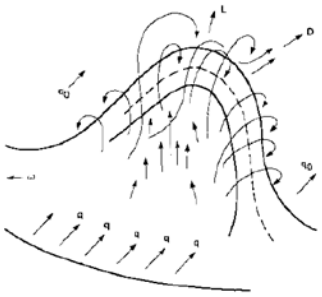


Figure 5: Horseshoe structure from Theodorsen (Theodorsen, 1952)

After the discovery of Theodorsen (1952), it took many years for the scientists such as Head and Bandyopadhyay (1981) to arouse interest in large-scale, outer layer structures of TBL. They provided strong experimental evidence for their omnipresent nature. They were one of the first to observe these horseshoe structures also known as hairpin structures and confirmed that nearly the entire boundary layer consisted of hairpin vortices. They performed smoke flow visualisation in the TBL with a laser sheet inclined to the wall and observed that hairpin structures were inclined, on average, at an angle of 45^0 to the wall extending from the wall with a length appearing to be limited only by the thickness of the boundary layer δ.

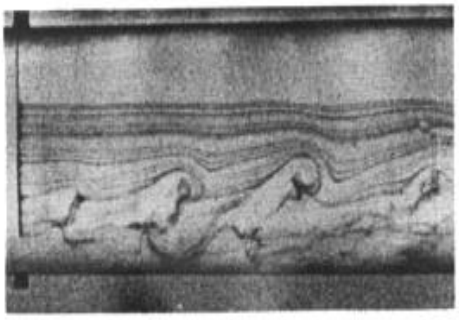


Figure 6: Hairpins in high Reynolds number (Head and Bandyopadhyay, 1981)

They concluded that the hairpin vortices are the major components of a turbulent boundary layer at all Reynolds numbers. Their shapes depend on Reynolds number progressing from loops through horseshoe to elongated hairpin type structure with Reynolds number increasing as shown in Figure 7.

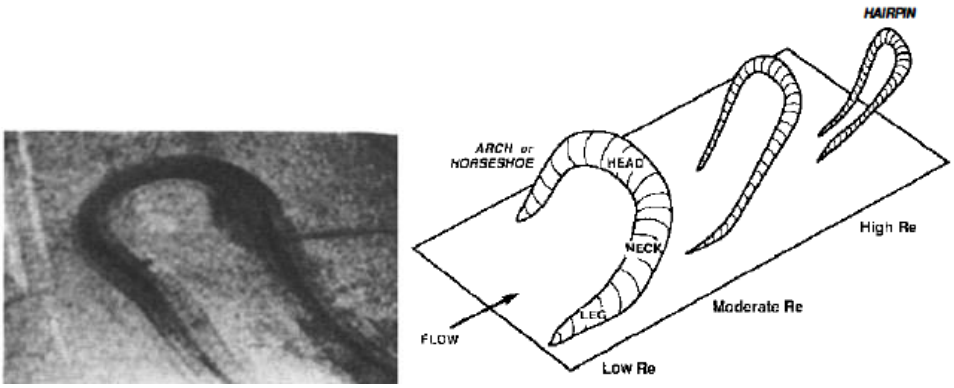


Figure 7: Effect of Reynolds number from Robinson (1991) based on Head and Bandyopadhyay (1981)

Figure 8 shows the idealised hairpin structure which is split up into three parts; the legs in the buffer region, the neck in the log region and the head in the wake region (Wallace, 1985, Robinson, 1991) and is inclined at roughly 45^0 to the wall (Robinson, 1991). Robinson (1991) highlighted that these are not necessarily symmetrical structures and seem to be more common as asymmetric structures, as depicted in Figure 8, which are shaped like canes. This was also recognised by Moin and Kim (1985).

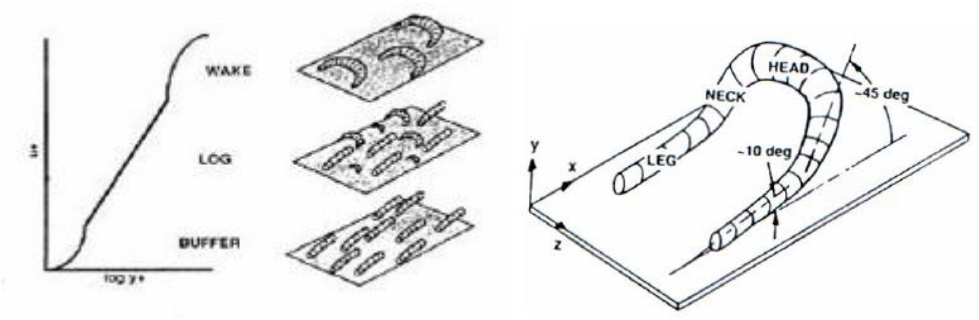


Figure 8: Parts of a hairpin vortex within the TBL by Robinson (1991)

Kim, Kline and Reynolds (1971) observed a rotational motion near the wall which they interpreted as streamwise vortices. Robinson suggested a theory; streamwise vortices are link to the counter-rotating legs near the wall of the hairpin vortices in the TBL. Illustrations from Robinson (1991) of some of the vertical structures and their relationship with near-wall events are shown in Figure 9.

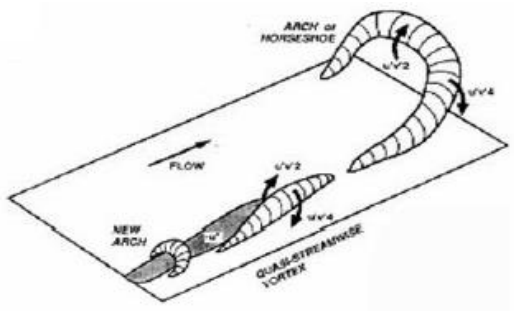


Figure 9: Relationship between ejection/sweep and hairpin vortices in the outer region from Robinson (1991)

Vortical `tornadoes' form astride near-wall regions of low-velocity fluid and grow outward with heads inclined downstream at 45^0, and with spanwise dimensions proportional to the distance from the wall (Theodorsen, 1952). The structures in the turbulent boundary layer are inclined at $40\text{-}50^0$ or at least they are more abundant at this angle (Robinson, 1991).

The last decade of wall-turbulence research has seen great progress in the understanding of the large-scale structure of the flow. This was propelled by the investigation of Kim and Adrian (1999) who proposed a model of hairpin packets to explain the well-known dominance of very-low-frequency energy in the logarithmic region of high-Reynolds-number wall turbulence. Hairpin structures are part of coherent structure, which take place in TBL. Adrian et al. (2000a) observed that those structures were the most observable flow pattern

in a turbulent boundary layer and occurred from $y^+ = 50$. The vortices appear as counter-rotating pairs, with an average spanwise separation of $z^+ \approx 50$ (Rigas et al., 2016, Blackwelder and Eckelmann, 1979) and a spanwise streak-spacing of $z^+ \approx 100$ (Kim et al., 1971).

Arranged together, hairpins form larger scale structures. It seems that packets of hairpins exist in the TBL and that hairpins are not coming singly but together (Zhou et al., 1999, Adrian et al., 2000a). Adrian et al (2000a) claimed that at least one hairpin packet appeared in 85% of all the PIV data that was taken. They also showed that these packets often occur with more than 10 individual hairpins.

The hairpin appearance and characteristics are presented in Figure 10. The vortex head has a Q2 (second quadrant) event located beneath it and at around 45^0 to the wall. Q2 and Q4 (fourth quadrant) vectors represent the ejection and sweep event respectively. It is also suggested that the passage of each individual hairpin in a packet produces its own Q2 event. In this model, the legs of the hairpin vortex are the quasi-streamwise vortices near the wall that are lifting the near wall fluid. In a velocity vector field, there is a velocity vector where the vortex is seen with an inclined region of Q2/Q4 vectors beneath it, it is considered as a hairpin vortex signature (Adrian et al., 2000a). It seems that the ejection event and vorticity are associated with the passage of a hairpin (Adrian et al., 2000a).

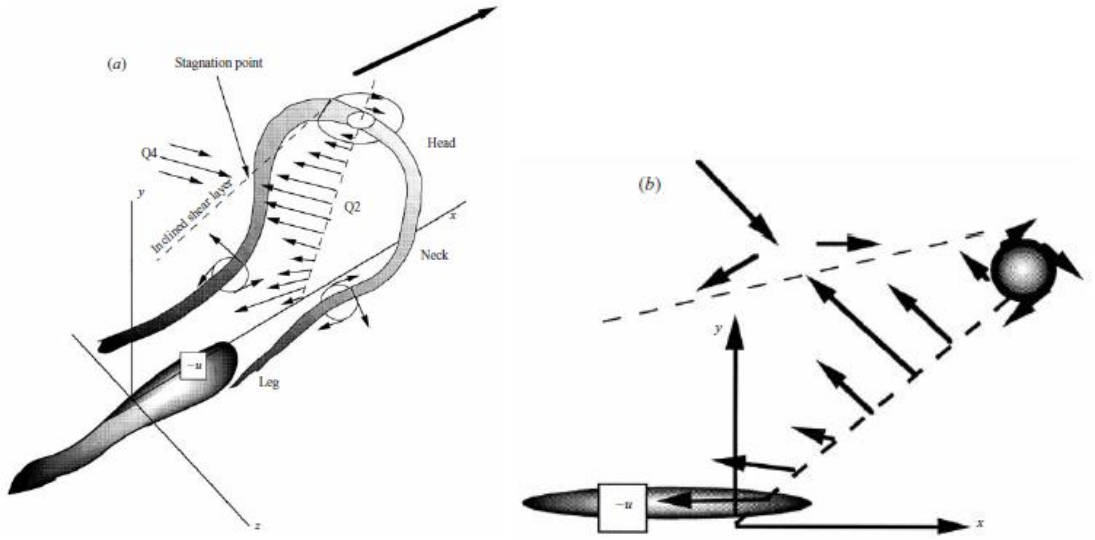


Figure 10: (a) Conceptual model with induced motion depicting Q2 and Q4 activity. (b) Signature of a hairpin vortex (Adrian et al., 2000a)

It is only very recently that Adrian (2000a, 2007), Hutchins (2003), Wu and Moin (2009), Dixit and Ramesh (2010), Rahgozar and Maciel (2011) and others confirmed the obvious and densely populated presence of the large-scale structures in boundary layers.

The large-scale structures, often referred to as the large-scale motions (LSMs), have been observed by Adrian et al. (2000b). These features seem to have a streamwise scale of approximately 2δ (Guala et al., 2006) and are common and essential to the flow dynamics (Adrian et al., 2000a).

Moreover, Kim and Adrian (1999) found the existence of the so-called very large scale motions (VLSMs) shown in Figure 11, which are much longer than the LSMs. They are believed to be created by the vortex packets formed when multiple hairpin structures travel at the same convective velocity (Kim and Adrian, 1999, Zhou et al., 1999, Henry, 2002).These long streamwise scales of the order of boundary layer thickness and larger have been observed experimentally in pipes by Kim and Adrian (1999), Del Alamo et al. (2004), Hutchins and Marusic (2007a), Balakumar and Adrian (2007), and others. These very long meandering structures (VLSMs) consisting of narrow regions of low-momentum streamwise fluid appear in the logarithmic and outer region. These large-scale events have a typical spanwise width of 0.3 - 0.5δ, and persist over very long distances, up to 15δ in the streamwise direction (Hutchins and Marusic, 2007a). They have been interpreted either as long 'trains' of aligned hairpin eddies (Adrian, 2007) or as global modes (Del Alamo and Jimenez, 2006). The LSMs and VLSMs are sometimes not distinguished by the authors and are called large scale structures.

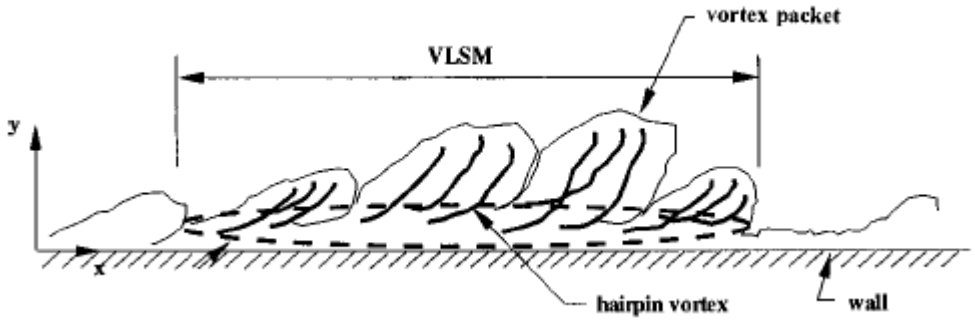


Figure 11: Very large-scale motions from Kim and Adrian (1999)

Studies of the large-scale structures have shown that they dominate in the log-region and are characterised by alternating regions of low and high momentum

(Ganapathisubramani et al., 2003, Del Alamo and Jimenez, 2003, Tomkins and Adrian, 2003, Ganapathisubramani et al., 2005, Hambleton et al., 2006).

Spectral analysis of VLSMs and LSM indicates that they make a significant contribution to the turbulent kinetic energy (Guala et al., 2006, Balakumar and Adrian, 2007). The discovery of an outer "secondary peak" in turbulence energy at high Reynolds numbers has boosted interest in near-wall turbulence. The study of Hutchins and Marusic (2007a, 2007b) clearly shows two distinct (inner and outer) energy peaks as seen in Figure 12. It seems that the inner peak at $y^+ = 15$ is evident at low and high Reynolds number, but the outer peak is barely distinguishable at the lower Reynolds number and start to appear for Re_τ approximately greater than 4000 (Hutchins and Marusic, 2007b, McKeon and Morrison, 2007).

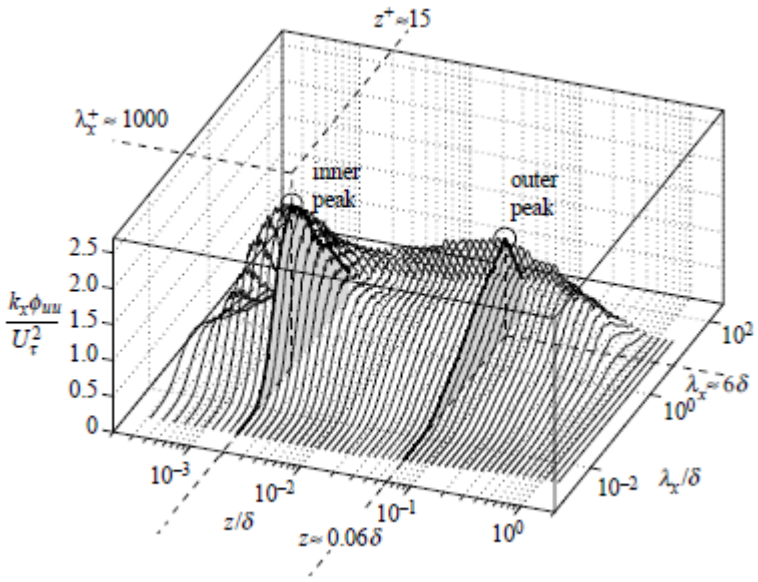


Figure 12: Energy spectra of the streamwise velocity fluctuations for a turbulent boundary layer at Re_τ = 7300. The dashed lines denote locations of inner and outer spectral peaks (Hutchins and Marusic, 2007b)

Importantly, it has been shown that these large-scale structures significantly influence the near-wall region as explained in the previous section. Abe et al. (2004) and Hutchins and Marusic (2007a) have shown that the large-scale fluctuations of the log-layer are superimposed onto the near-wall small scales, hence imposing a 'footprint' at the wall shown in Figure 13.

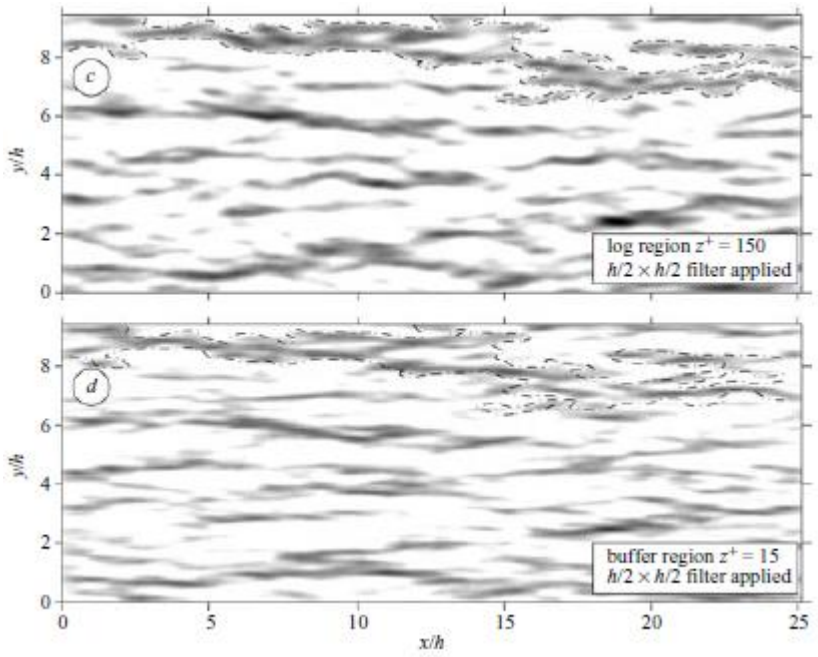


Figure 13: Instantaneous flow fields from Re_τ = 934 channel simulations. Filtered data (Hutchins and Marusic, 2007a)

Furthermore, it has been observed that the large-scale features that inhabit the log-region appear to modulate the amplitude of smaller motions near the wall (Hutchins and Marusic, 2007b). A clear modulation effect has been recently supported by the study of Mathis et al. (2009a) who quantified the degree of amplitude modulation.

It should be noted that both effects, superposition and modulation, have been found to increase as the Reynolds number increases (Hutchins and Marusic, 2007a, Mathis et al., 2009a). This is due to an increase in large-scale activity with Reynolds number (Hutchins and Marusic, 2007a, Hutchins and Marusic, 2007b, Marusic et al., 2010a).

2.3.1 Large-scale control

Research on drag reduction has led to the development of “large-eddy-break-up devices” or LEBUs. LEBUs are thin splitter plates about a boundary layer thickness in length, which are positioned at a height between 0.4δ and 0.8δ above the wall in the outer region of the boundary layer (Bandyopadhyay, 1986, Savill, 1988, HEFNER et al., 1979, CORKE et al., 1979). They are used to manipulate the large-scale structures to reduce the skin-friction. Such devices have been shown to lead to local skin-friction reductions of between

15% and 40%, with some reduction in skin-friction persisting over a downstream distance of 100δ - 150δ. This is accomplished by a corresponding decrease in turbulence intensity, and turbulent Reynolds stress (Westphal 1986, Bonnet et al. 1987, Coustols et al. 1987). However, the net drag reduction using such devices has not been a success yet. The possibility of some net drag reduction is, however seen to exist with shorter devices such as blades.

Another technique known as Vertical Blades (Hutchins and Choi, 2002a) has given prospective results for further investigations on large-scale control. They carried out experiments by placing an array of thin vertical plates in the turbulent boundary layer. A reduction of 30% was found in the local skin-friction further downstream from the position of the plates suggesting that the hairpin vortices were manipulated.

This has led one of authors to investigate further into the subject. Hairpin vortices were generated in a laminar boundary layer in a water channel by periodically pulsing wall-normal jets into the flow through a small hole at the test plate. The synthetic hairpin is created by passing the jet through a hole at a test plate. The control jets were issued directly at the head of hairpins from a 0.25 mm diameter nozzle placed outside of the boundary layer thickness in order to control hairpin vortices. Flow visualisation showed that control jets have destroyed the neck of hairpin vortex (HV) by disconnecting the link between the head and the legs of HV (Kang and Choi, 2005) leading to a skin-friction reduction.

Finally, this motivated the authors (Kang et al., 2008) to carry out the same study but in turbulent boundary layer in a wind tunnel expecting that it will have the same results and lead to a decrease in the drag. The control was done by counteracting the upwash of low-speed flow motion of hairpin vortices (HV) with jets issued from a nozzle placed outside the boundary layer. The control jets were produced by a loudspeaker through a 9 mm diameter nozzle placed outside the BL. Firstly, HV were detected using a hot-wire, and then the detection was followed by an opposition control of HV. Such direct intervention of large-scale, outer-layer structures unlike wall-based turbulence control techniques whose time and length scales reduce with an increase in the

Reynolds number. The scales of the large-scale proposed control are those of the outer layer, making this control technique highly practical. Figure 14 is the result from a direct intervention of hairpin structures in a turbulent boundary layer, demonstrating that this is a promising technique for turbulence control.

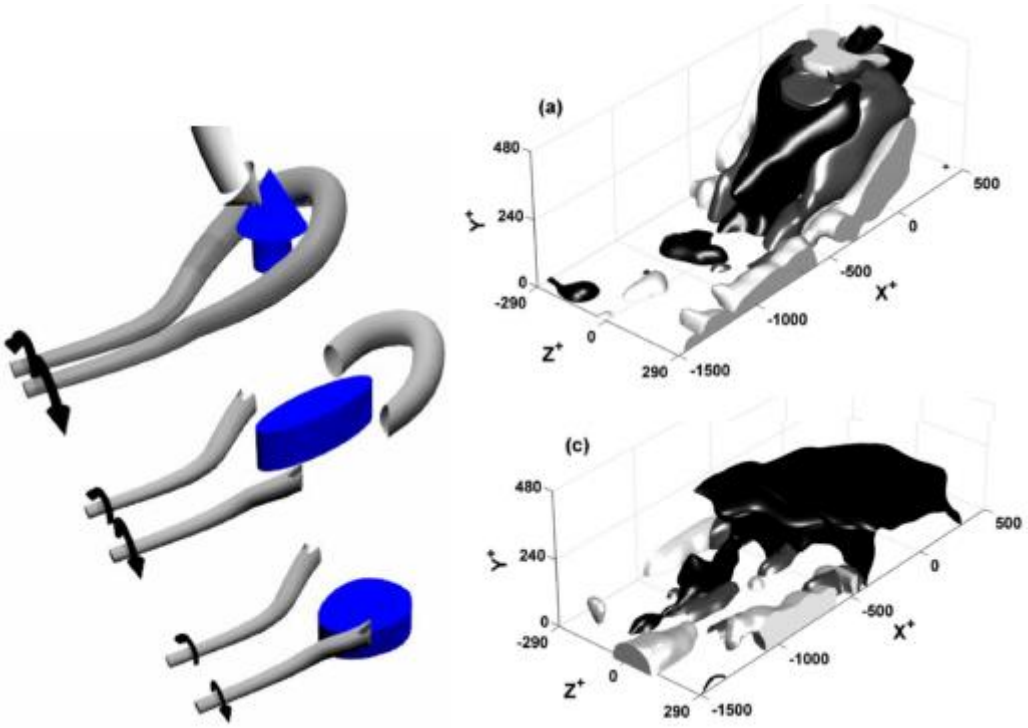


Figure 14: (Left side) Diagram to show direct intervention of hairpin vortices. (Right side) Ensemble-averaged streamwise velocity (a) without control and (b) with control (Kang et al., 2008)

2.4 Inner and outer region

Classically, the near-wall inner region, which scales with friction velocity u^* and the viscous length ν/u^*, is assumed to be independent of the outer region defined as the region $y/\delta > 0.15$ (Panton, 2001), which scales with U_∞ and the boundary layer thickness δ. It is essential to emphasize on the meaning and definition of the Reynolds numbers based on the friction velocity, $Re_\lambda = \frac{\delta u*}{\nu}$. It is the ratio of the boundary layer thickness to the wall unit size. It gives the scale of the large-scale structures expressed in terms of δ in comparison with small structures expressed in viscous length ν/u^*.

The debate is still open as to how the inner region interacts with the outer region and vice versa. There is however clear evidence of indirect interactions

that occur through the growth of vortical structures from the wall to the outer regions. The effect of the outer boundary layer on the inner turbulent production process is not well understood, although it is largely accepted that the outer flow influences the inner region with the passage of large eddies structures (Panton, 2001).

Kline et al (1967) claimed that the low-speed streaks ended with the expulsion of low-speed fluid into the outer region of the boundary layer. They presumed that it could dominate the energy transfer processes between the inner and outer regions. Later, Willmarth and Lu (1972) claimed that near wall streamwise vortices may evolve to a larger scale, producing the intermittent bulges in the outer edge of the boundary layer and thus providing an outward interaction mechanism between the inner and outer regions. It seems that energy resides in the largest eddies and cannot be dissipated until it is transferred to the smaller ones, in which viscosity acts.

Blackwelder and Kaplan (1976) showed that fluids ejected from the near-wall region (burst and ejections) may become bulges in the outer layer. Also, the experiment of Gad-el-Hak and Bandyopadhyay (1994) showed that the turbulent boundary layer consists of bulges of fluid. These bulges of fluid interact with the free-stream, entraining fluid into the turbulent boundary layer (sweep). Those bulges are on the order of the turbulent boundary layer thickness. These studies suggested that burst and ejections may be part of structures that span the whole boundary layer region.

Brown and Thomas (1977) in their experimental results showed that the large structure accounts for very large contributions to the Reynolds stress and suggested the importance of the large scales in generating small-scale disturbances near the wall.

Very long meandering structures of low-momentum streamwise fluid have been observed experimentally by Kim and Adrian (1999), Del Alamo et al. (2004), Hutchins and Marusic (2007a) and others in the logarithmic and outer region. It is believed that these structures certainly do contribute to inner layer structures at high Reynolds number. The importance of the contribution from the outer layer to the inner layer has been indicated by several experimental

studies at high Reynolds numbers. These studies revealed that large-scale motions in the outer layer affect the near-wall region and that this effect increases with increasing Reynolds number. Indeed, Chauhan, Marusic and Hutchins (2011) found that the influence of the low frequency components, i.e., large-scale structures with lengths as large as 20δ in the streamwise direction, on the turbulence statistics (such as energy of u and v fluctuations) increases with increasing Reynolds number. In other words, they have a significant contribution to the total turbulent stress. Furthermore, more recently there has been an increased recognition that near the wall the small-scale near-wall streaks that govern the skin friction are significantly affected by the large-scale structures that populate the outer layer (Hutchins et al., 2011).

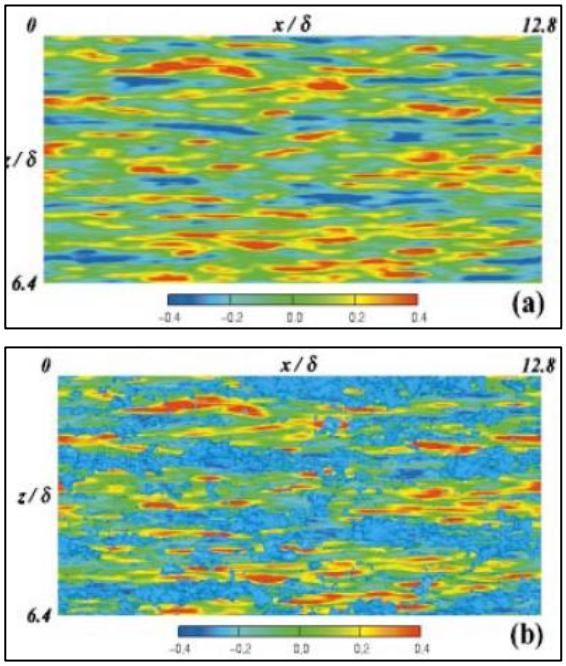


Figure 15: Contours of the filtered *T1* and top view of the low-speed regions in the VLSMs for *Reτ* = 640. (a) filtered *T1*; (b) top view of the low-speed regions in the outer layer (Abe et al., 2004).

Abe et al. (2004) investigated very large-scale structures and their effects on the wall shear-stress fluctuations by DNS data in turbulent channel flow. They showed from the instantaneous flow field (Figure 15) that the very large-scale structures appear in the outer layer and leave footprints at the wall for high Reynolds number. They inspected the interaction between the inner and outer layers and came to the conclusion that the positive and negative (respectively several streaks of positive and negative τ_1 packed together. τ_1 represents

streamwise wall skin-friction,) dominant regions present in the contours of the instantaneous wall skin-friction fluctuations correspond, respectively, to the high- and low-speed regions in the very large-scale motions in the outer layer. Their results indicated that the very large-scale structures leave footprints in the instantaneous wall shear-stress fluctuations for Re_τ = 640 are essentially phenomena associated with the very large-scale motions existing in the outer layer of the flow.

DNS studies have also revealed the footprint of the outer-scaled structures within the inner scaled region (Abe et al., 2004, Hoyas and Jimenez, 2006, Hutchins and Marusic, 2007a, Hutchins and Marusic, 2007b). It seems that those large organised motions superimpose their signature on the near wall-region. Moreover Hutchins and Marusic (2007b) and Mathis et al. (2009a) showed that LSMs modulate the near-wall processes. Schlatter et al. (2009) also showed evidence of modulation of the near-wall cycle motions further from the wall in their DNS data. They suggested that the hairpin packets attached to the wall modulate the near-wall cycle. These results show that motions in the logarithmic and outer layer may have a strong influence on the behaviour of the near-wall turbulence.

Lately, Morrisson et al. (2007) and Morrisson (2007) from DNS observed that large eddies in the inner layer contribute to the energy production and that this large-scale contribution in the inner layer increases as the Reynolds number increases. Later, Hutchins et al. (2009) and Marusic et al. (2010a) have studied the inner-outer interaction by decomposing the scale of the streamwise turbulence intensity profile into small- and large -scale contributions. They found that the small-scale contribution is constant with Reynolds number whereas the large-scale contribution increases with increasing Reynolds number.

Many of the above mentioned studies were consistent with the viewpoint that some superposition (or “footprint”) of the large-scale motions is experienced right to the wall. Hutchins and Marusic (2007b) went further and proposed that this interaction also involved a modulation of the large scales on the small scale, and this effect was quantified by Mathis et al. (2009b). Hutchins et al. (2011) who observed that features in the outer layer such as large-scale

structure (signal from hot-wire probe 2 placed at y+ = 11 in the buffer region) in the flow leave a footprint in the instantaneous skin-friction (signal from hot-film probe 6 placed at the wall) as seen in Figure 16 and Figure 17.

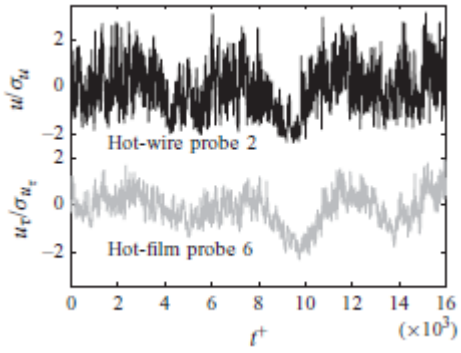


Figure 16: Time series of skin-friction fluctuations from hot film and velocity fluctuations from hot-film probe 6 at $z^+ = 0$ and hot-wire probe 2 at $z^+ = 11$ (Hucthins et al. 2011)

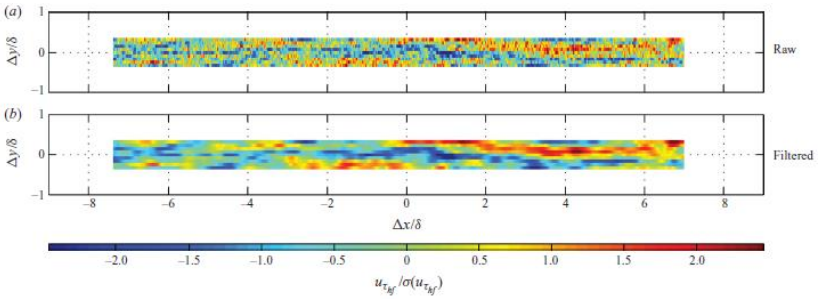


Figure 17: Skin-friction fluctuations signals from the spanwise array: (a) unfiltered raw data; (b) filter of size 0.5δ x 0.16δ (streamwise and spanwise) applied (Hutchins et al. 2011)

Agostini and Leschziner (2014a) used Direct Numerical Simulation (DNS) data for channel flow at Re_τ = 1025 to analyse the interaction between large outer scales in the log-law region and the small-scale, streaky, streamwise-velocity fluctuations in the near-wall layer. With an $x - z$ snapshot at y^+ = 13.5 as seen in Figure 18, they showed contours of streamwise-velocity fluctuations with a clear view of both the small-scale streaks and of the footprints of large-scale outer structures.

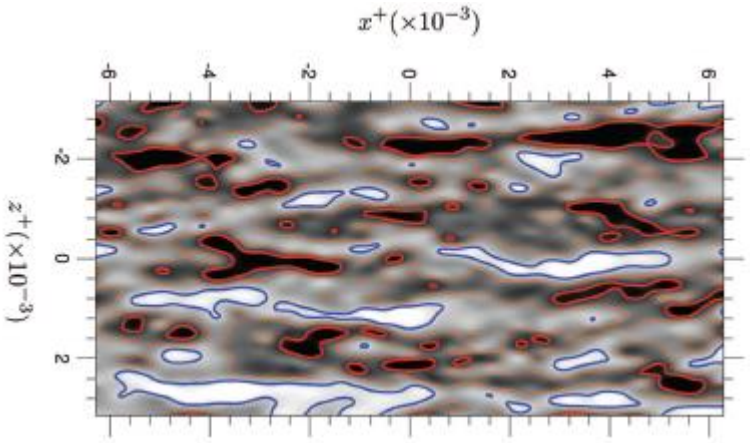


Figure 18: Streamwise velocity fluctuations at *y*+ = 13.5. (Agostini and Leschziner, 2014b)

Chapter 3 Experimental facility, equipment and set-up

This Chapter explains the facility and equipment used in this experimental study and shows all the basic techniques for data acquisition and processing. It is divided into two parts: tunnel and HWA description and uncertainties, and s-PIV and synchronisation uncertainties. The Chapter, however, does not contain information about very specific data processing and analysing techniques which will be shown in detail later.

Part 1: Wind tunnel and HWA descriptions and uncertainties

3.1.1 Wind tunnel

The experiments have been conducted in a laboratory using an open return low-speed wind tunnel, which was also used by Nick Hutchins (2003) and Yong-Duck Kang (2009). The wind tunnel, driven by a 3.7 kW motor and fan, consist of a settling chamber containing honeycomb and nine screens to enhance flow uniformity, followed by a contraction with an area ratio of 9.6:1. The size of the test section area (Figure 19) is 500 mm x 300 mm smooth-wall which is 4000 mm in length from the inlet of the test section to the end of the wind-tunnel and an increasing cross-sectional area width from 400 mm at the start of the test section to 450 mm at the exit to maintain a zero pressure gradient. The maximum free-stream speed measured in the wind-tunnel, using a Dantec 54T29 reference velocity probe, is about 10 m/s.

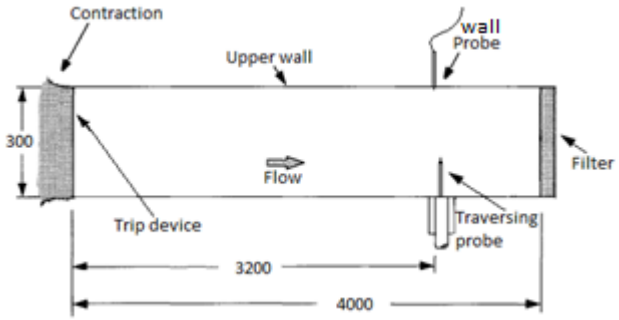


Figure 19: Front view schematic of test section of the wind-tunnel

A trip was placed at the inlet of the test section to make the boundary layer fully turbulent over a flat test surface. The trip device consisted of a zigzag rubber strip of 3 mm high rectangular quadrilateral of 5 mm long mounted on a 1 mm thick sheet, 64 mm wide.



Figure 20: Trip device

With the trip device, the turbulent flow is determined with:

- the Reynolds number, based on the height of the trip and the free-stream velocity of the boundary layer, equal to 1227 for our experiments in comparison with value ≥ 900 to be effective according to Schlichting (1979).
- the mean velocity profile with a logarithmic scale used on the abscissa of to identify any portion of the velocity profile that displays a logarithmic velocity growth that would determine a turbulent boundary layer, resulting in a straight line on the logarithmic plot as seen in our velocity profile (Figure 38).
- the value of the shape factor H, between 1.35 and 1.36, indicating a turbulent mean velocity profile.

⇨ The turbulent nature of the boundary layer in our wind tunnel, is deduced from the value of the Reynolds number, the mean velocity profile following the log-law and the value of the H factors.

Turbulence intensity (Eq. 8) was measured using a hot-wire sensor positioned at the centre of the wind tunnel at three different free-stream velocities and are given in Table 2. It is equivalent to the ratio of the standard deviation of velocity fluctuation to the mean velocity (in percentage).

$$\textbf{Turbulence intensity}\ (\%) = \frac{\sqrt{\overline{u'^2}}}{U_\infty} \cdot \mathbf{100} = \frac{u_{rms}}{U_\infty} \cdot \mathbf{100} \qquad (8)$$

Table 2: Turbulence Intensity of Wind Tunnel

Velocity (m/s)	Turbulence intensity (%)
2.2	0.50
3.2	0.75
7.4	0.69

The turbulence level values were acquired using the multi-channel anemometer system (Chapter 4, page 84) and the calibration was made against a Dantec 54T29 reference velocity probe (velocity reference transducer, pre-calibrated: range 0.2 -30 m/s). The value obtained with Dantec anemometer system was 0.22% at 3.2 m/s against 0.36% with the multi-channel anemometer system at 3 m/s with a calibration done with pitot-tube.

A schematic of the working section of the wind tunnel is included in Figure 21, showing the 20 sensors placed on the upper wall of the wind tunnel where the experiments are performed, the moving traverse table and the filled corners (in blue).

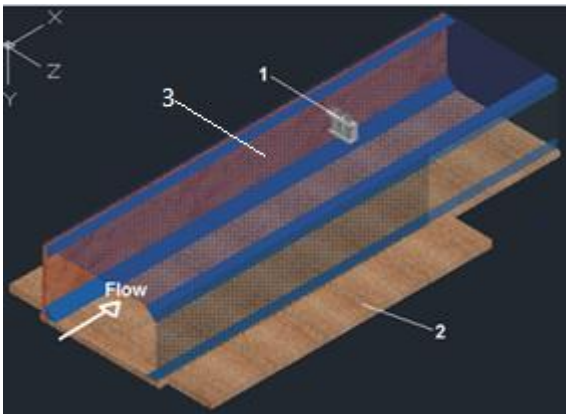


Figure 21: Schematic of test section of the wind-tunnel. 1 Wall probes, 2 Moving traverse table and 3 Upper wall test surface

Corners of the test section were filled to prevent the formation of secondary flows as seen in Figure 21 as blue lines and Figure 22.

The automatic traverse mechanism was used to position the traversing probe at grid points in three axis; *x*, *y* and *z*, which was controlled by a stepper-motor controller with an IEEE-488 interface. Programs to move the (55P15/55P16) hot-wire probe using the 3-component traverse were written using Quick Basic. The hot-wire probe position was adjusted in *x* and *z*, in such a way that the hot wire sensor can approach the wall without breaking the probe.

The traverse step for the hot-wire measurement was 25 μm within 1.5 mm from the wall, which increased to 50 μm from y = 1.5 up to y = 3 mm, and then increased to 100 μm from 3 to 5mm and finally to 200 μm from 5mm upwards. The steps were very small (25 μm) close to the wall in order to increase the measurement accuracy in the near-wall region by obtaining more data near the wall. A total of 127 steps was acquired for the profiles.

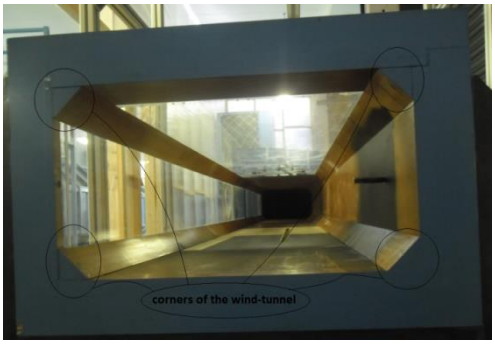


Figure 22: Corners of the wind-tunnel

3.1.2 Thermal Anemometry System

3.1.2.1 Principles

The primary measuring technique for the experimental investigations used for turbulent boundary layer, to obtain the time history of the fluid velocity at a point in a flowing fluid, was thermal anemometry. Thermal anemometry is a widely used method and a good history of this technique can be found in a paper by Freymuth (1968). The initial work on thermal anemometry goes back to the nineteenth century, but the main period for research and development started in 1946 and is still continuing.

The fundamental concept of thermal hot-wire anemometry is based on the convective heat transfer from a heated wire placed in a fluid flow. It consists mainly of a metallic wire sensor which is fixed to the ends of prongs (Figure 23), then placed in the flow for measurements.

The wire is electrically heated (Joule effect) and simultaneously cooled by the convective heat transfer induced by the lower temperature flow. The main feature that allows the hot wire to be used as a measurement device is that its electrical resistance depends on its temperature. Therefore, by direct or indirect measurements of the wire resistance variations, one can infer the heat transfer taking place and then obtain the flow information.

The system is made of a thin wire mounted to two supports and exposed to a velocity U. When a current is passed through the wire, heat is generated. In equilibrium, this must be balanced by heat loss (primarily convective) to the surroundings.

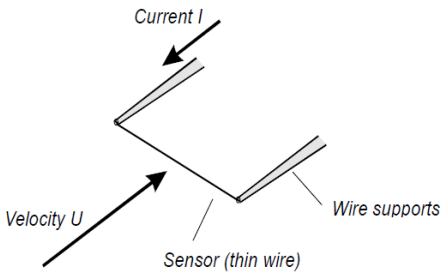


Figure 23: Hot-wire principle

If the velocity changes, the convective heat transfer coefficient, as well as the wire temperature will change and eventually reach a new equilibrium. In other words, the hot-wire anemometer, in which fluid flowing past a thin heated wire carries heat away at a rate, proportional to the fluid velocity.

The heat transfer from the wire is mainly dominated by forced convection and, to minimise the effect of the conductive end losses of heat to the prongs, the wire should be as long as possible, i.e. *k/d (wire configurations)* ≥ 200 (Blackwelder and Haritonidis, 1983), the thermal conductivity of the wire should be low and the wire should have a high temperature coefficient of resistance. However, at very low flow velocities, the natural convection from the hot-wire probe becomes significant but in most hot-wire applications the radiation heat transfer from the wire is very small and can be neglected.

Thermal anemometry is a common method used to measure instantaneous fluid velocity at a single point in space. The advantages of this system over other flow measuring principles are: ease-of use; the output is an analogue voltage which means that no information is lost; very high temporal resolution is attainable. And finally the constant temperature anemometer (CTA) is more affordable than laser Doppler anemometer (LDA) or particle image velocimetry (PIV) systems. The drawbacks related to hot-wire sensors are the wall effect, the temperature drift and their calibrations. This will be discussed in more details in Chapter 4.

3.1.2.2 55P15 and 55P16 Probe

A 55P15 hot-wire probe was used to measure the u-component velocity at a fixed location in the boundary layer. Probe support is achieved via a Dantec 55H22, a 235 mm long, right-angled support. The type is a 55P15 miniature

boundary layer probe provided by Dantec, 5 µm diameter, 1.25 mm long platinum plated tungsten wire sensors and shown in Figure 24.

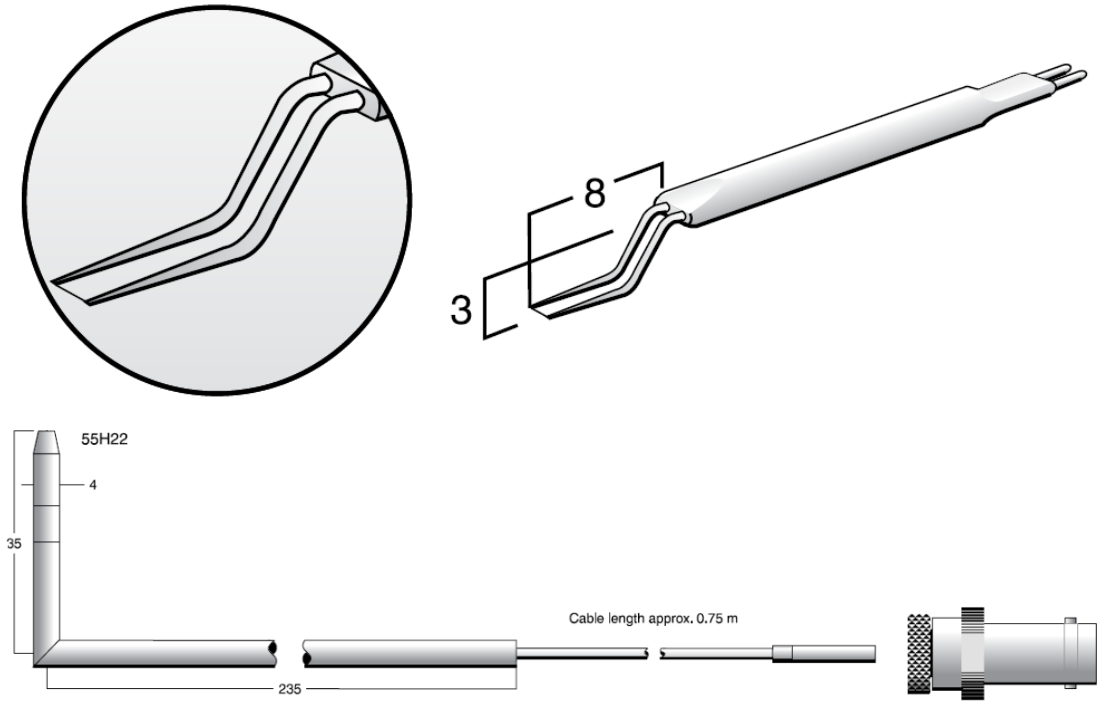


Figure 24: Miniature wire-probe, 55P15 and probe support (Dantec Measurement Technology)

A cable equipped miniature 55P16 wire probe built into one with its straight support and 1 m cable with BNC connector has also been used in the experiments. It is equipped with a sleeve that fully protects the wire when not in use. This miniature wire probes have a 5 µm diameter and 1.25 mm long platinum plated tungsten wire sensor. The wires are welded directly to the prongs and the entire wire length acts as a sensor. The prongs length is 0.5 mm, keeping length to diameter ratio of 200. Thus, the criterion that $l/d > 200$ in order for the effects of heat loss to the prongs to be negligible was satisfied. Figure 25 shows the probe dimensions of the single-sensor miniature wire probes.

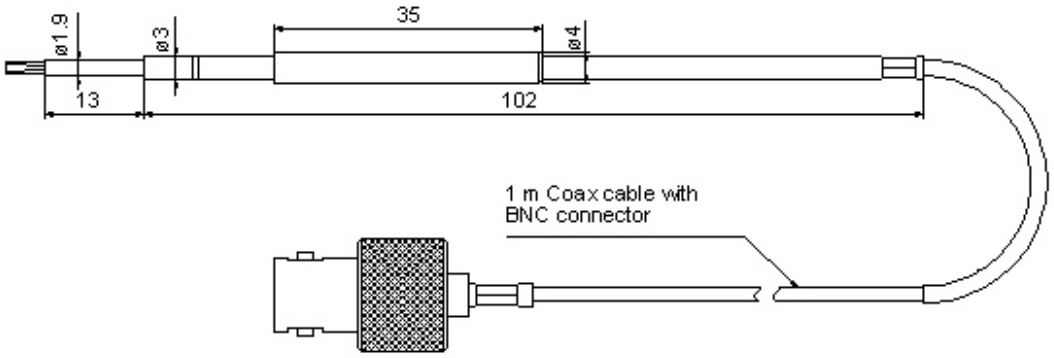


Figure 25: Miniature wire-probe, 55P16 (Dantec Measurement Technology)

Hot-wire probe is set at an overheat ratio of 1.8, being the typical value for a tungsten probe in air (Bruun, 1995b). This ratio, a, is defined as:

$$a = \frac{R_w - R_0}{R_0} \tag{9}$$

where R_w is the resistance of the wire in operation and R_0 is the cold resistance of the wire at ambient conditions. Here the subscript 0 means resistance at ambient conditions.

3.1.2.3 Calibration, temperature compensation and wall effect

The calibration of the hot-wire sensor as well as temperature correction due to the temperature drift and the wall effect are given in this section. This section also highlights the linear relationship between the velocity and the voltage within a certain region of y-position.

The direct output, raw data, contains measurement uncertainties. Consequently, close attention must be paid to both the process of choosing an appropriate method of curve fitting and also the aim to minimise any experimental errors if a good accuracy is to be obtained.

Calibration

The main purpose of any hot-wire calibration is to determine as accurately as possible, the relationship between the Constant Temperature Anemometer (CTA) output voltage (E) and the velocity (U).

In our study, the hot-wire probe was calibrated for velocity in situ against a Dantec 54T29 velocity reference transducer for 30 seconds at 24 different free-stream velocities ranging from 0.2 to 8 m/s and was sampled at a frequency of

1 kHz. The Dantec 54T29 velocity reference transducer was pre-calibrated by the manufacturer, having an accuracy of $\pm$ 0.02 m/s in the velocity range 0.2 to 30 m/s.

The velocity reference transducer is accurate at $\pm$ 2% (0.02 m/s) for the measured range from 0.2 to 30 m/s given by Dantec. Although, in our experiments, the curve fitting accuracy for the velocity reference transducer ranges from 0.1 to 4.1%, as shown in Figure 26.

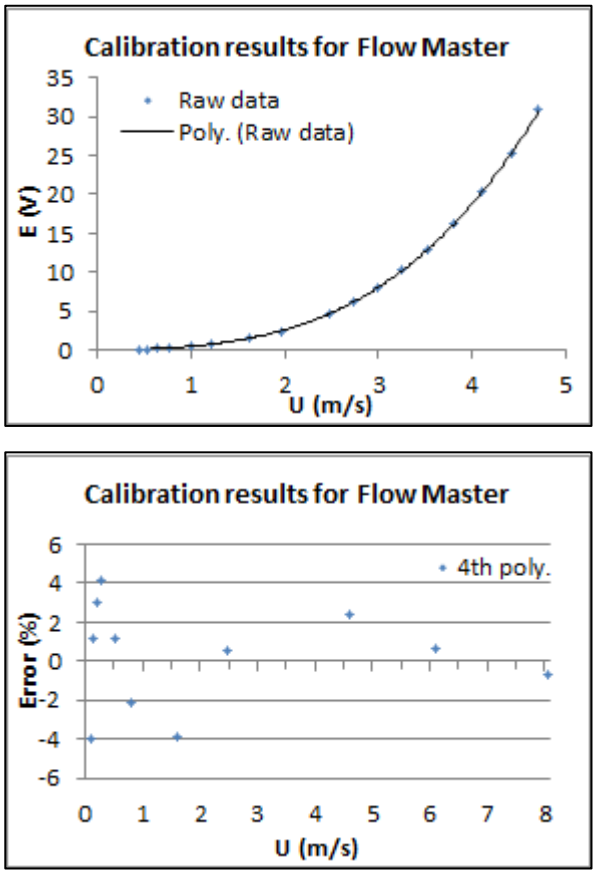


Figure 26: (Top) Flow master calibration curves and (Bottom) curve fitting error

The readings from the hot-wire probe and the velocity reference transducer were taken simultaneously. They were placed 100 mm apart in the spanwise direction and at the same streamwise and wall normal positions. Calibration of hot-wire probe was performed in the centre of the test section of the tunnel located in the free-stream where there is a low turbulence intensity. At y = 150 mm from the upper wall such that they are outside of any boundary layer and 260 mm from the wall in the spanwise direction to avoid secondary flows.

A number of investigators (Bruun, 1995b) have developed different equations to fit the calibration curves. In this study, the methods are investigated to improve the accuracy of probe calibration.

Power law

Following the original hot-wire investigation by King (1914), the relationship $E = F(U)$ is often assumed to be of the form

$$E^2 = A + BU^n, \tag{10}$$

where *E* is the output voltage from the hot-wire, *U* is the true velocity of the flow and *A*, *B* and n are constants. King's law suggested that *n* = 0.5. Although, Bruun (1995) suggested that $n_{optimum}$ varies and should ranges from 0.4 to 0.45. The constant n, with the best calibration fit, i.e. the smallest curve fit error, at 2.2 m/s, 3.2 and 7.4 m/s, was equal to 0.40, 0.50 and 0.50, respectively.

From the calibration curve, the calibration constants *A*, *B* and *n* were obtained and shown in Table 3.

Table 3: Constants for King's law curve fit

	2.2 m/s	3.2 m/s	7.4 m/s
T (^{0}C)	21.3	24.2	25.8
A	3.0057	3.5841	3.5756
B	1.8757	1.296	1.3026
n	0.4	0.5	0.5

Then Equation 10 provides a relationship between *U* and *A*, *B* and *E*. That is, if *A*, *B* and *E* are known, *U* can be evaluated from Equation 10. By inverting Equation 10, the velocity can be obtained; as follows;

$$U = \left(\frac{E^2 - A}{B}\right)^2 \tag{11}$$

It was possible to convert the voltage value and *E* into the corresponding velocity value, *U* by using Equation 11.

Polynomial fit

The polynomial fit can be obtained using computing packages such as Matlab which contains polynomial curve fitting routines based on a least-squares fitting method.

The voltage from the probe and the velocity from the velocity reference transducer are plotted and fitted with a 3rd and 4th order polynomial such as $U = AE^4 + BE^3 + CE^2 + DE + F$. Figure 27 shows the voltages measured against velocity from Dantec velocity reference transducer, the calibrated source, with each curve fitting method applied to the data.

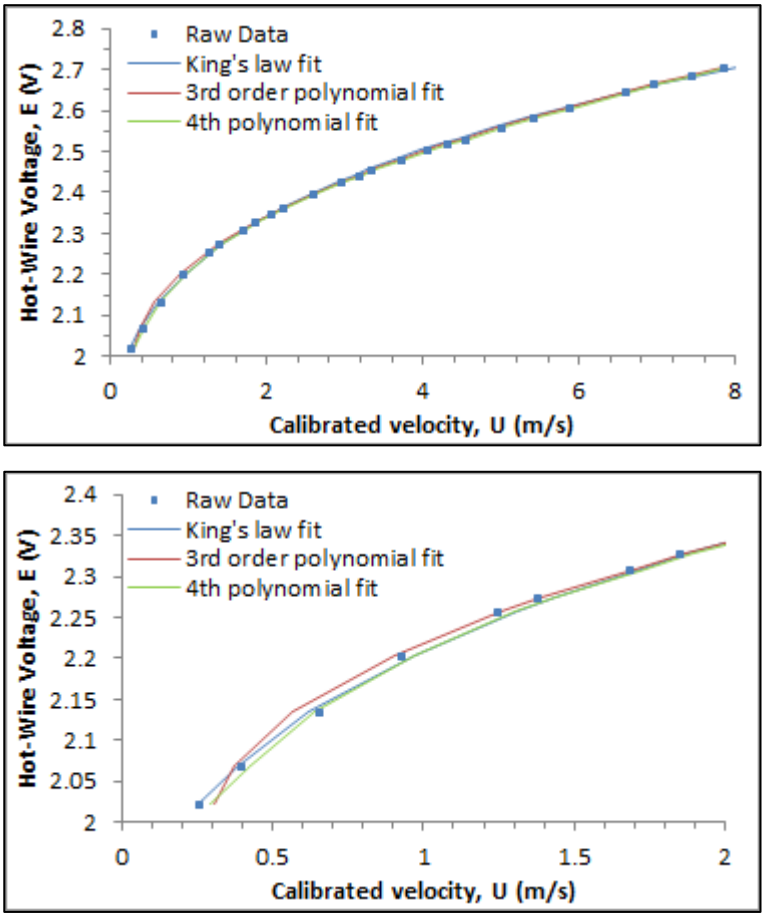


Figure 27: Hot-wire calibration curve (top) whole range and (bottom) at low velocities

Curve fitting error

To test the accuracy of the calibration method, the initial measurements were carried out in a known flow situation. Then, by comparing the results obtained from the selected method with known velocity reference values, we acquired an indication of the accuracy of the curve fit to the data.

Figure 28 shows the percentage of error between raw and estimated data for the methods used. The error is defined as the difference in percentage between the measured and the estimated velocity,

$$Percentage\ of\ error = \left(\frac{U_m - U_e}{U_e}\right) \times 100, \quad (12)$$

where U_m is the velocity measured with the velocity reference transducer and U_e is the estimated velocity through curve fitting.

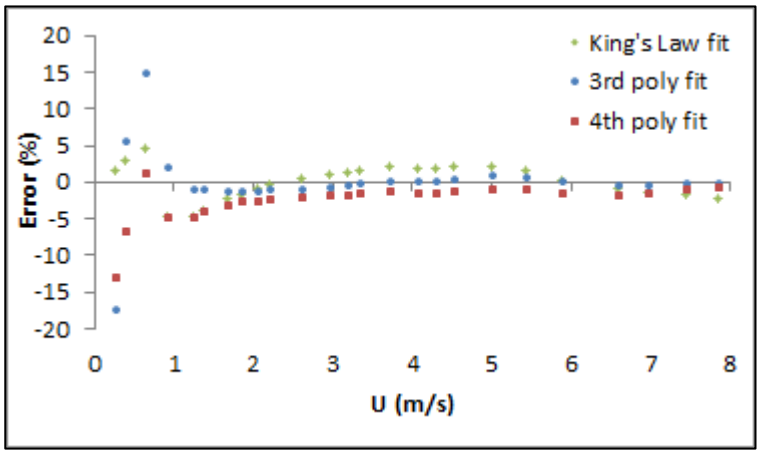


Figure 28: Error between measured data points and those predicted by different calibration method

The King's law equation has a good fit, leading to a 2% of error for velocity ≥ 1 m/s. However, at low velocities U < 1 m/s, King's law fit produces a fit leading to an error of 5%. As for the third order polynomial fit, the curve fitting error for $U \geq 1$ m/s is 1% and for $U < 1$ m/s is 17%. Both fitting methods were compared and the King's law gave a better fitting at low velocity, U < 1 m/s but the third order polynomial was a better fit at velocity > 1 m/s.

King's law and polynomial curve fitting methods are accurate to the error due to scatter of experimental data (within 4%) for $U \geq 1$ m/s. Nevertheless, King's law curve fit was chosen for the calibration as it was the best fit compared to the polynomial fits with a better accuracy for the whole velocity range, 0.2 to 8 m/s as seen in Figure 28.

Linear relationship between the velocity and voltage of the HW

This section highlights the relationship between the velocity and voltage of the data obtained with the HW. The information obtained with HW is the voltage, the velocity is deduced through a calibration curve. Their profiles are investigated to show a linear relationship within our range of interest, in the viscous sublayer. It is seen, in Figure 29, that within the viscous sublayer the voltage and velocity profile are linear.

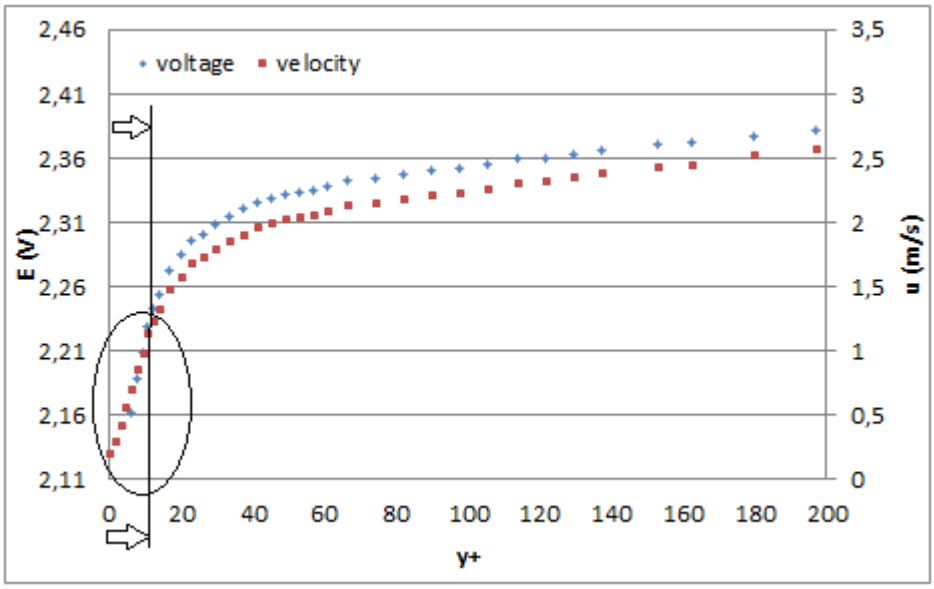


Figure 29: Relationship of the velocity versus voltage profiles

In Chapter 5, the calibrations of the hot-wire sensors were not carried out and the results are given in voltage instead of velocity. As, the instantaneous velocity and skin-friction are functions of voltage and within a certain range of y^+ (for $y^+ \leq 10$) are linear to it.

Temperature compensation

The calibration curve is valid only for the range of velocity and the temperature at which it was obtained. Hot-wire readings suffer from errors due to drift of ambient temperature. The hot-wire probe's output voltage is related to the heat transfer from the probe to the surrounding fluid, where the overheat ratio varies with ambient temperature fluctuation. Two calibrations were performed, one at a temperature of 21.3^0C and the other at 26^0C. The temperature compensation was used for the experiment done at 3.2 (24.2 ^{0}C) and 7.4 m/s (25.8 ^{0}C) where a drift of 1.8 and 0.2 ^{0}C, respectively was found.

The temperature in the working section is monitored using a temperature sensor mounted in the freestream and downstream of the test section in order to omit an error due to temperature differences. If the ambient temperature changes during the measurements, a correction can be applied to the data using the following expression given by Bruun (Bruun, 1995a):

$$E_{corr} = E_a \left(\frac{T_w - T_0}{T_w - T_a}\right)^{0.5} \quad (13)$$

where T_w is the wire temperature, T_0 is the temperature obtained during the calibration, T_a is the ambient temperature, and E_a is the acquired voltage during calibration.

Figure 2, 3 and 4 show a set of calibrations performed for different temperatures and table 1 the error in the estimated velocity.

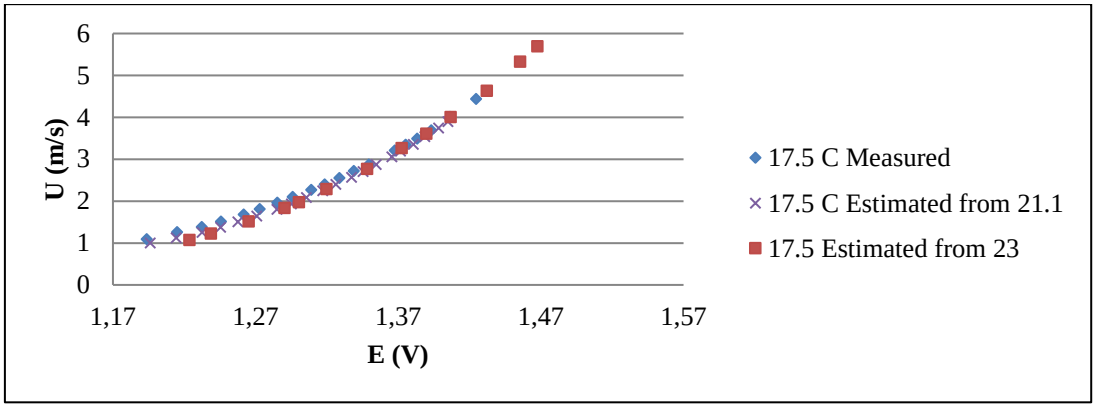


Figure 30: Calibration curve at 17.5^{0}C

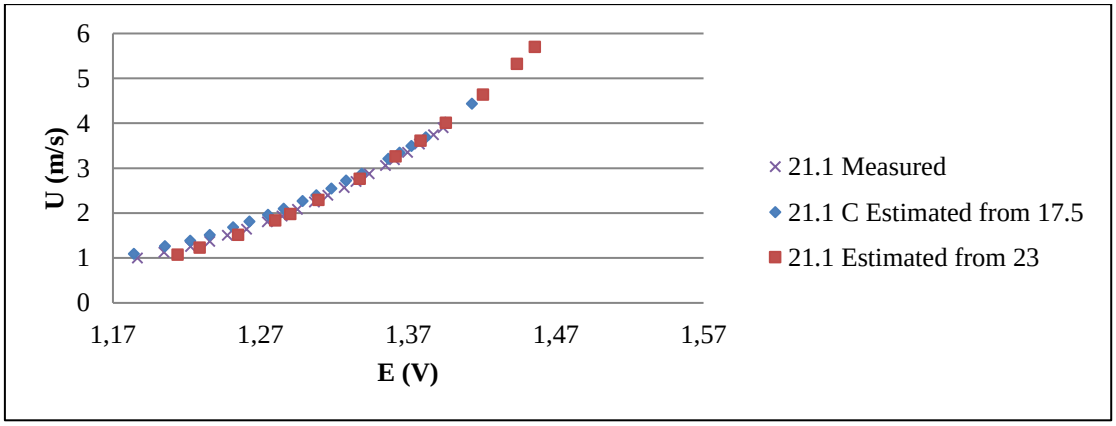


Figure 31: Calibration curve at 21.1^{0}C

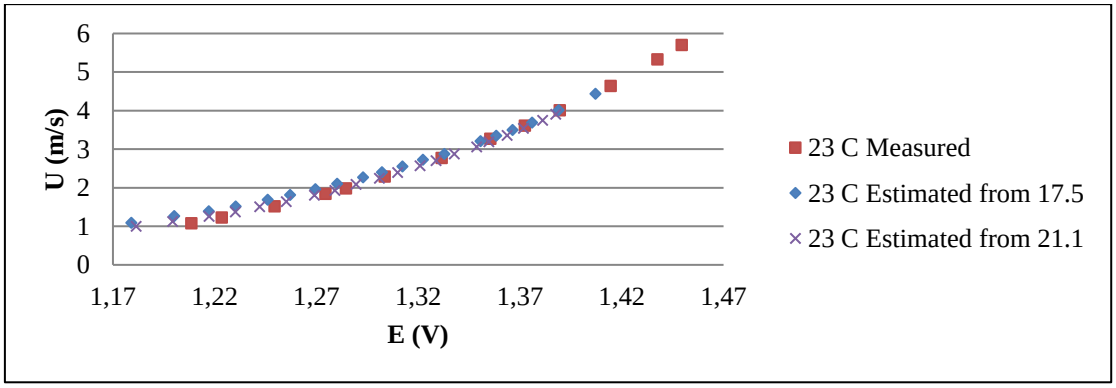


Figure 32: Calibration curve at 23^{0}C

Table 4: Error in the estimated velocity at different temperature

	17.5 C	**21.1 C**	**23 C**
	Error (%)		
17.5 ^{0}C	/	0.8	1.23
21.1 ^{0}C	0.81	/	0.43
23 ^{0}C	1.25	0.43	/

It can be seen from Figure 30, Figure 31 and Figure 32 that when the temperature drifts by less than 5^{0}C the error is lower than 1% which is acceptable but when the drift is above 5^{0}C the error becomes higher and might be a problem. In that case, Hultmark and Smits (Smits, 2010) suggest an alternative correction but in our experiments, the drift was below 5^{0}C.

Noise level

A signal-to-noise ratio compares a level of signal power versus a level of noise power and is most often expressed as a measurement of decibels (dB). Higher numbers generally mean a better specification, since there is more useful information (the signal) than there is unwanted data (the noise).

When measured as the ratio of two energy or power quantities, the SNR is defined on a decibel scale according to the following formula:

$$SNR_{db} = 10 \cdot log_{10} \frac{P_{mean}}{P_{noise}} \quad (14)$$

The highest point (value of mean signal) was 9.788 10^4 and the second highest point (value of the noise) was 3.402 from Figure 33. From equation 14, it can be deducted that:

$$SNR = P_{mean} / P_{noise} = 9.788\ 10^4 / 3.402 = 28\ 771$$

$$\Rightarrow\ P_{noise} = P_{mean} / 28\ 771 \Rightarrow P \propto V^2$$

$$\Rightarrow\ V_{mean} / V_{noise} = 170 \Rightarrow V_{noise} = 0.59\%\ V_{mean}$$

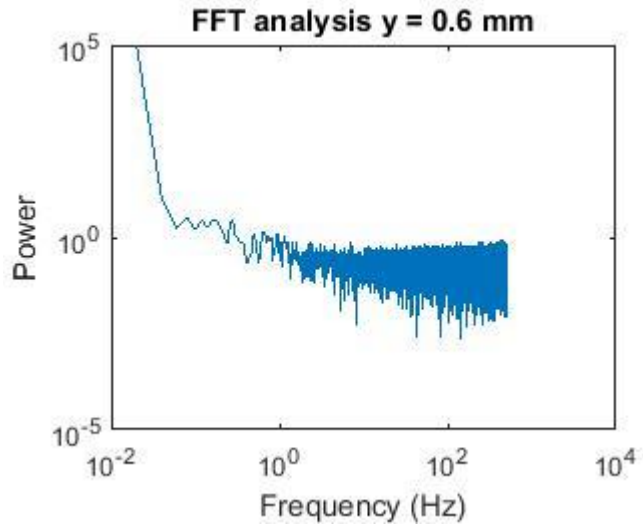


Figure 33: FFT analysis of signal from hot-wire sensor

The noise level is found to be 0.6 % of the mean signal.

Wall effect - Heat Transfer

It is common practice to calibrate hot-wires in a free-stream of constant and known velocity. However, the hot-wire has one major setback: a hot-wire calibrated under free-stream conditions fails to predict the true velocity in the near-wall region of a known flow field (Bruun, 1995b). This can be attributed to the disparity in heat transfer characteristics of the hot-wire sensor in the vicinity of the wall where additional heat is lost directly to the wall. In that way, when hot-wire is utilised for near-wall measurements, additional heat losses occur due to the presence of the wall, resulting in erroneous velocity readings. The wall effect results from the increased heat loss from the probe as it approaches the wall and is a function of both the flow speed and the wall material (Wills, 1962). The effect associated with the heat conduction to the wall takes place for $y < 0.5$ mm ($y^+ < 3$) (Alfredsson et al., 1988, Hutchins and Choi, 2002).

Walls which have thermal conductivities much higher than the fluid affect, to a great extent, the heat loss from the hot wire by changing the temperature distribution around the wire in the wall region. The wall conducts heat from the fluid which is heated by the wire and this heat loss rapidly increases on approaching the wall. Most of the studies agree well within the near wall region that the hot wire sensor cannot be used without a need for wall corrections.

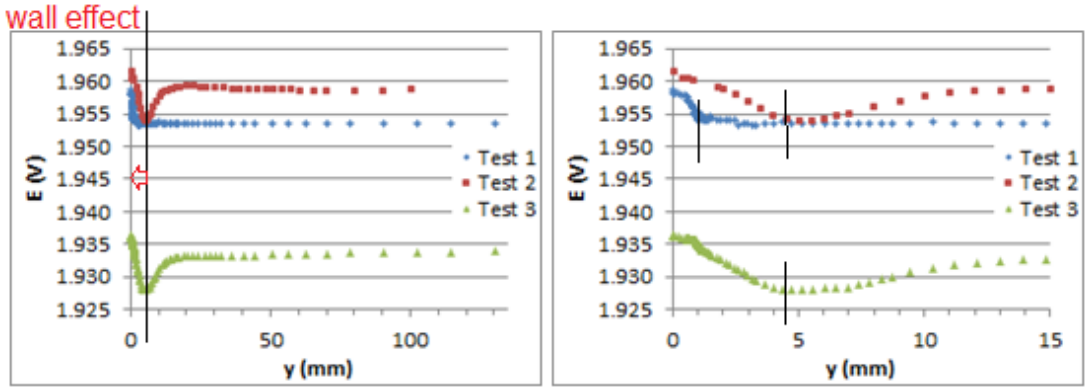


Figure 34: Effect of the heat transfer on Dantec 55P16 hot-wire probe measurements

The tests were made in still air. The first test was conducted at a room temperature of 24.9^{0}C. It showed a trend where there is a decrease of the voltage value of 0.3% from within the hole (page 56) to y = 0.98 mm followed by a region of stabilisation. In this test, the wall position was unknown hence other tests were carried out.

For the second test, it was conducted at a room temperature of 22.2 ^{0}C. The final position of the sensor was at a distance between 98.5 and 98.75 mm from the wall after the measurements were taken. This position was estimated by placing a ruler in the vicinity of the sensor. Knowing that the traversing was programmed from y = 0 mm within the wall until 99.975 mm. It meant that the sensor was within the hole at a depth of 1.045 mm, y_0 = -1.045 mm. As illustrated in

Figure 34, the values of the voltage decrease down to 4.975 mm. A decrease of 0.4% is followed by an increase of 0.3% before stabilising. Thus, it seems that there was an effect on the sensor up to a distance of 3.75 mm from the wall.

A third and final test was carried out at a room temperature of 26.5^{0}C to confirm these data. The sensor was within the hole at a depth of 3.5 mm, y_0 = -3.5 mm. It can be seen that the value of the voltage decreases by 0.4% from position y = 0 to 4.735 mm. It is then followed by an increase of 0.2% before stabilising. There is an effect on the sensor up to distance of 1.635 mm from the wall.

It can be said that there was an effect on the sensor in the vicinity of the wall. But the wall effect tends to increase the measured velocity in the vicinity of the

wall. And in our experiments, in two tests out of three, a decrease of the voltage value was followed by an increase while approaching the wall. The increase trend while approaching the wall is due to the conduction effect as for the decrease of the voltage value, this is explained by the presence of the hole, where the hot-wire sensors are put.

Also, for the three tests conducted, there is a variation, between the maximum and minimum voltage value, of $0.35^{\pm 0.05}\%$. The noise level measured and discussed in section 3.2.3.3 (page 41) is of 0.59% of the mean signal, so the variation of the voltage signal (0.35%) is within this noise level.

Furthermore, the variation in voltage is of 0.006-0.008 V which corresponds in terms of velocity to 0.03-0.04 m/s. Due to the technical limitation of the 55P16 hot-wire sensor given by Dantec, the minimum velocity the probe can measure is 0.2 m/s. It may be used at lower velocities, down to 0.02 m/s as the velocity limit is defined by the onset of natural convection. In other words, the velocity limit is reached when the natural convection overrules the forced convection.

In conclusion, four parameters affect the results of hot-wire:

- the wall effect for $y^+ < 3$
- the noise level; it is of 0.59% of the mean signal
- the technical shortcoming of 55P15 hot-wire sensor; minimum velocity the probe can measure is 0.2 m/s
- the calibration error; 5%

These errors are significantly reduced as the flow speed increases.

3.1.2.4 Constant temperature anemometer board

For velocity measurements, Dantec 56C01 Constant Temperature Anemometer (CTA) was used with Dantec 56C17 bridge units and with Dantec 56N20 signal conditioners.

The twenty CTA boards (Figure 35) that are used for flow measurements are home-built KI-NI997 CTA (Takagi., 1990, Itakura). To operate them, the first step was to mount them in an enclosure with sixty BNC connectors, twenty for the DC component, twenty for the AC component and twenty for the sensors. The CTA unit had to be accessible from the top and the front for the set-up

procedure of the CTA board. Furthermore, the enclosure had to be shielded to isolate the electrical devices from the 'outside world'. The choice of the enclosure was a major challenge as the sizes of the boards were not standard and in the end the chosen enclosure (Figure 36) was modified to fit the twenty boards.



Figure 35: Home-built KI-NI997 CTA board

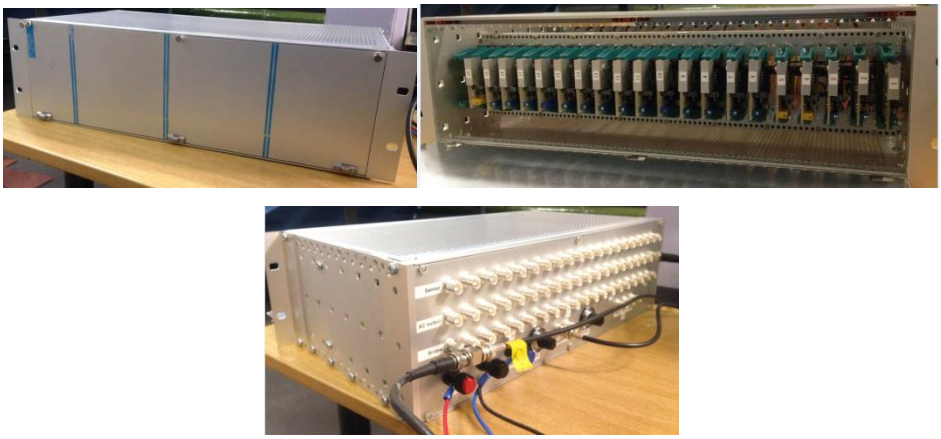


Figure 36: home-built CTA enclosure

Multi-channel anemometry optimisation

The anemometer unit was optimised for each hot-wire probe used in the experiments. The frequency response of a constant temperature anemometer depends on several factors such as the thermal properties of the sensor and the fluid, the overheat ratio, the temperature coefficient of the sensor, the fluid velocity, the gain of the amplifier, the resistance of the bridge, and the bandwidth of the amplifier. The constant temperature anemometer (CTA) bridge responds up to 20 kHz (Itakura) with adequate adjustments.

The method used to test and adjust the hot-wire response is to introduce an electronic disturbance signal into the system such as square-wave and to measure and observe the response of the anemometer’s output signal on an oscilloscope and an analogue-to-digital converter (ADC).

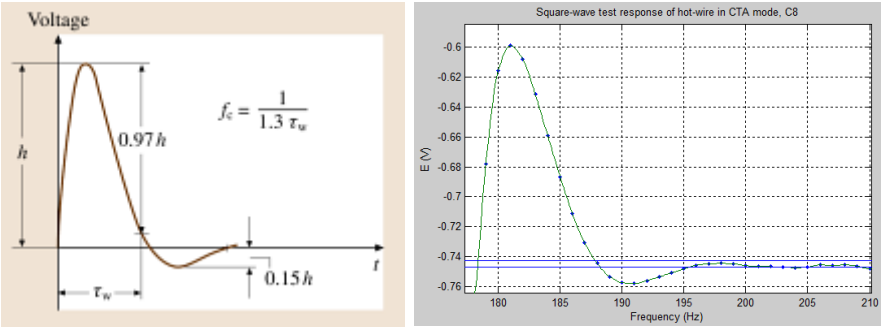


Figure 37: The square wave test response of hot-wire probe operated by a CTA (after (Bruun, 1995b))

Response time is measured as the time (the x-axis represents the frequency and has been converted in time for our data before calculating the cut-off frequency), *τ*, from the beginning of the upward pulse to a point on the way down equal to 3% of the total pulse height as described by Freymuth (1977b). The cut-off frequency, *fc*, can be evaluated from the square wave test (Freymuth, 1977a) as follows:

$$fc = \frac{1}{1.3\tau} \tag{15}$$

A signal generator was used to feed a 200 Hz square-wave with 1 volt peak to peak amplitude into the circuit. The response of the square wave was observed on an oscilloscope and ADC connected to the output of the anemometer.

Table 5: The cut-off frequency of the twenty sensors

	f_w (Hz)	τ_w (µsec)	Sampling rate (Hz)	f_c (kHz)
C1	5.8	116	50000	6.6
C2	8.8	175	50000	4.4
C3	9.4	188	50000	4.1
C4	9.5	189	50000	4.1
C5	9.0	181	50000	4.3
C6	9.4	189	50000	4.1
C7	8.8	175	50000	4.4
C8	9.5	190	50000	4.0
C9	8.7	175	50000	4.4
C10	7.6	152	50000	5.0
C11	8.1	162	50000	4.7
C12	8.1	162	50000	4.7
C13	8.2	164	50000	4.7
C14	8.1	161	50000	4.8
C15	8.1	161	50000	4.8
C16	5.0	100	50000	7.7

C18	4.9	98	50000	7.8
C19	4.8	96	50000	8.0
C20	4.6	92	50000	8.4

The electronics were then adjusted by rotating a variable resistor pot for balance adjustment slowly in either way so as to approach to a waveform shown in Figure 37. The adjustment is carried out with the sensor exposed to a flow similar to the average speed used for experiments but with low turbulence since the response depends on the flow velocity.

Figure 37 shows the CTA system's responses to a square wave test pulse when using the anemometer for such damping conditions. The signal was recorded over a period of 1 second at a sample rate of 50 kHz. This waveform was obtained with a sensor of R = 3.55 Ω and an overheat of 1.8, in a flow speed $U \approx 3$ m/s. The typical response curve was obtained and gave a cut-off frequency, *fc*, ranging from 4 to 8.4 kHz (Table 5) for our twenty sensors which were sufficient for our experiments.

Multi-channel anemometry reliability

In order to compare the performance and check the reliability of the multi-channel anemometer with a commercial Dantec (model 56C01) unit the following test was carried out.

The experiments were performed on the upper side of the wind-tunnel where a transparent wall made of 12 mm thick Perspex is used along the working section up to 2 m long to allow optical access. Measurements were typically taken 3.2 m downstream of the inlet of the test section. The experiments were carried out at 3.2 m/s where the boundary layer had a thickness, δ, of about 67 mm. This correspond to Reynolds numbers, based on the friction velocity (estimation method of the friction velocity is explained in Chapter 4), Re_τ = 568 with $Re_\tau = \frac{\delta u*}{\nu}$.

Measurements were made on a turbulent flow with a 55P15 sensor placed in a traversing system in the wind tunnel. The sensor was firstly connected to a Dantec commercial anemometer unit and then connected to the tested circuit, multi-channel unit. The flow measured was a completely developed turbulent flow with smooth walls and a mean velocity of 3.2 m/s.

The experimental conditions and basic flow parameters are tabulated in Table 6.

Figure 38 shows a typical mean velocity profile. In addition, all turbulence statistics of the streamwise velocity fluctuation show standard profiles for a typical fully developed turbulent boundary layer, including the turbulence intensity profile shown in Figure 29. As shown in Table 6, there are only minimal discrepancies between the profiles of both anemometers which can be explained by either the error in positioning of the sensor at the wall and the estimation of u^* or by the uncertainty in the hot-wire sensor calibration. To overcome this error, more data needs to be taken near the wall and then be fitted in the linear region before finding the real y position at the wall as explained by Hutchins and Choi (2002b).

Skewness and kurtosis factors, defined respectively as follows;

$$S_u = \frac{\overline{u^3(t)}}{\sigma^3} \tag{16}$$

$$K_u = \frac{\overline{u^{4(t)}}}{\sigma^4} \tag{17}$$

where u is the streamwise velocity fluctuation and σ is the standard deviation. Skewness and kurtosis is a measure of the asymmetry and flatness contained in the fluctuating velocity signal, respectively.

The skewness (Figure 30), kurtosis (Figure 31) and power spectrum (Figure 32) curves show a good agreement between the Dantec and multi-channel constant temperature anemometer (CTA) systems.

The discrepancies can also be explained by the estimated value of u^* which can be over or under-estimated. The friction velocity, u^*, was determined by fitting the experimental data from the logarithmic region to the equation $u^+ = 5.85 \log y^+ + 5.56$ (Schlichting, 1979), the so-called Clauser chart method. This was confirmed using the linear region of the boundary layer to check $U^+ = y^+$ in this region.

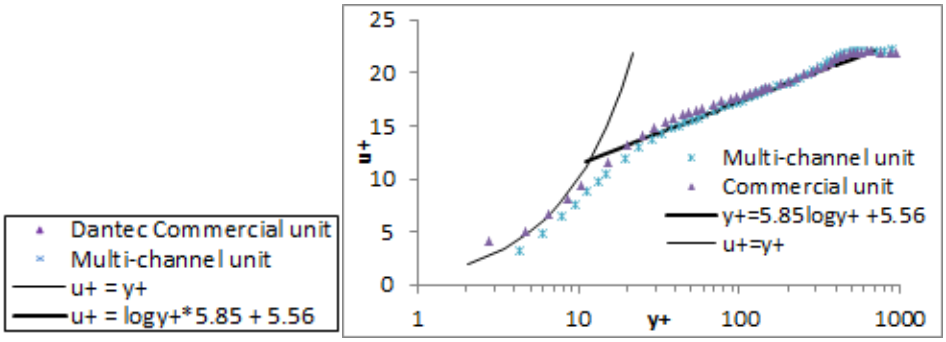


Figure 38: Mean velocity profile

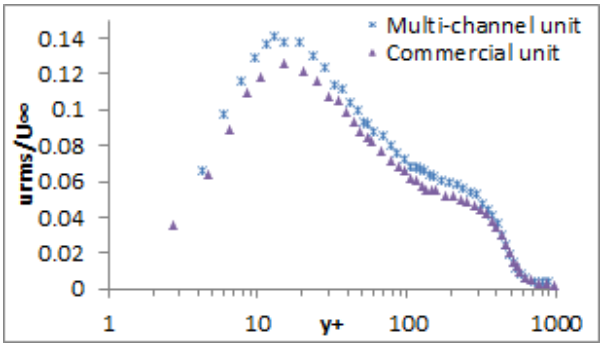


Figure 39: Turbulence intensity profile

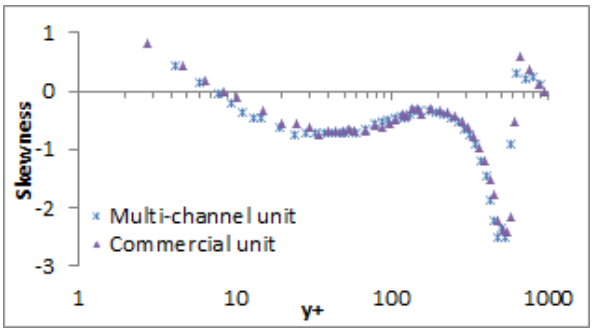


Figure 40: Skewness

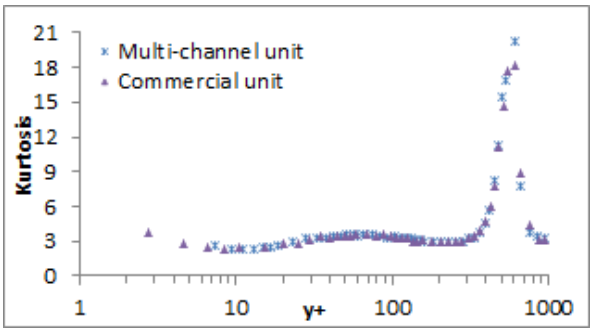


Figure 41: Kurtosis

Table 6: Turbulent boundary layer parameters commercial unit versus multi-channel unit

	Dantec Commercial unit	Multi-channel unit	Difference (%)
U_∞ (m/s)	3.1	3.0	3.3
δ (m)	0.051	0.051	0.0
u^* (m/s)	0.142	0.135	5.2
δ^*(m)	0.0072	0.0086	-16.3
ϑ (m)	0.0053	0.0064	-17.2
H	1.35	1.36	-0.7
I (%)	0.23	0.31	25.8

The calibration curves error impact for 2% of those differences.

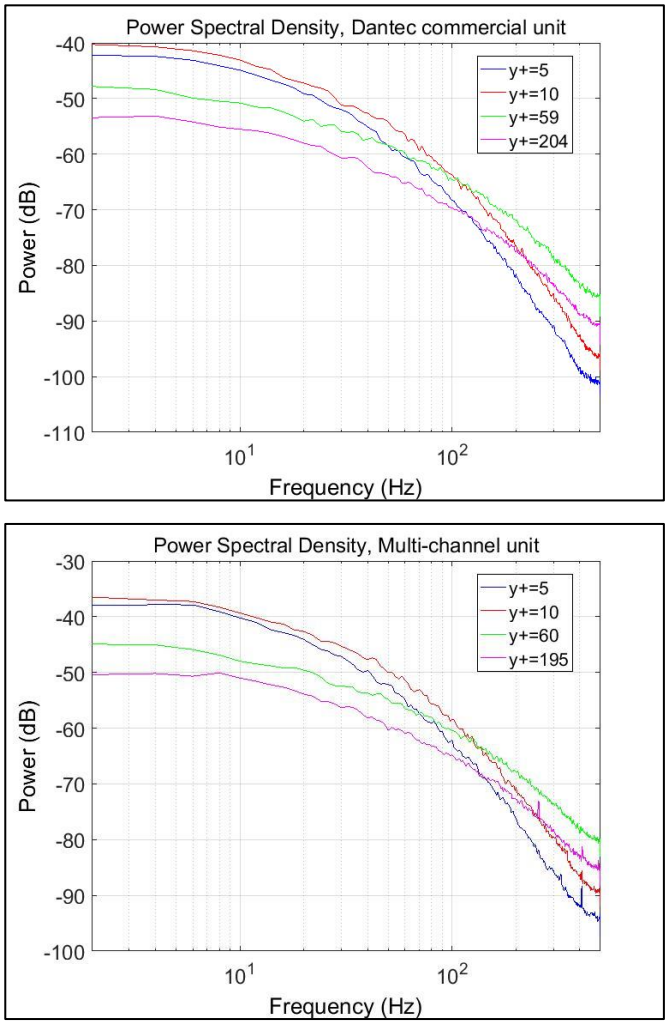


Figure 42: Power spectral density (PSD) Dantec commercial unit and multi-channel unit

Figure 42 shows one-dimensional power spectral density of velocity fluctuations at different wall-normal positons for the two units, namely the multi-

channel and the commercial. The first signal has a power ranging from -40 to -110 dB corresponding to a drop of 70 dB from the maximum to minimal speak. The second power signal ranges from -30 to -100 dB, which is also 70 dB drop. The spectra for the two signals show the same drop-offs. The shapes of the spectra at different wall-normal position for the two signals seem similar as they give a similar distribution over the different frequencies. The length (500Hz) and the width (70 dB) at the same y^+ position for both signals are the same. The energy of the velocity fluctuation is the same through the range of frequencies for both signals.

3.1.2.5 Hot-wire sensor array

Most techniques such as the flush-mounted hot-film suffer from heat losses to the substrate. Instead of using flush-mounted hot-films, Alfredsson et al. (1988) used a hot-wire on the wall, that is elevated only a few μm from the wall to reduce the heat flux to the wall. This technique has been further developed by Fernholz et al. (1996) and a large effort has been put into the design and construction of miniaturised wall-hot-wire sensors for this type of experiment. For our experiments, the choice was given to hot-wire sensors instead of hot-films which are better fit to use in water and oil, but not in air (Fernholz et al., 1996).

A spanwise rake of twenty Dantec 55P16 single sensor hot-wire probes was mounted at the upper wall of the wind tunnel with the aim to investigate the distribution of the instantaneous skin-friction signals in the viscous sublayer. The wall hot-wire probe technique similar to Fernholz (1996) was used in this study to measure the instantaneous skin-friction. The principle of this technique is to mount the probe at a fixed distance h above the wall as seen in Figure 43. It is important that the sensor wires of the probes lie within the viscous sublayer for the estimation of the instantaneous skin-friction as in the near-wall region, the velocity increases linearly with the wall distance, $u^+ = y^+$. In that way, a relationship can be obtained between the velocity and the wall shear stress as long as the maximum distance h from the wall is within the viscous sublayer, $y^+ < 5$.

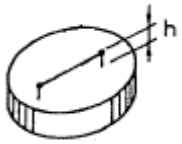


Figure 43: Schematic diagram of the wall hot-wire method

The array was used to compute the space-time wall shear-stress fluctuations. A holder was designed to put the twenty sensors straight in the upper wall of the wind tunnel to be able to measure the shear stress within the viscous sublayer. A friction fit angle shape material, aluminium, was chosen to maintain the sensors fixed and to prevent any bending for the sensors to be straight as seen in Figure 44.

Hot-wire sensors were used to avoid the high heat transfer to the surroundings when using hot-films. A number of twenty sensors were used to have an array length based on Agostini and Leschziner study (2014a) where large-scale structure width ranges from 100 to 800 wall unit at Re_{λ} = 1025.

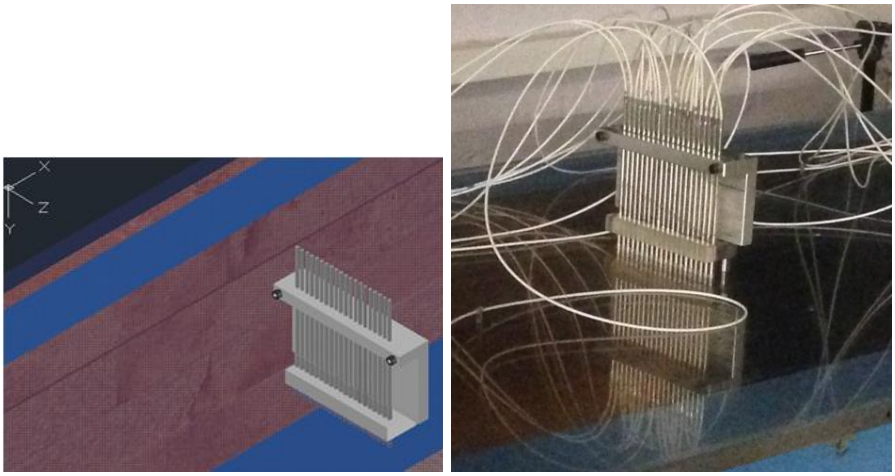


Figure 44: 20 channels hot-wire system placed on the upper wall of the wind tunnel

The hot-wire rake consists of twenty Dantec 55P16 single sensor hot-wire probes with a spanwise spacing of 5 mm (0.07δ, $z^+ = 44$) (as seen in Figure 45), such that the entire rake measures a spanwise domain just greater than one boundary layer thickness, ~ 1.4 δ ($z^+ = 588$). This spacing was used to avoid loss of information on the events at the wall as the streaks seem to have a spanwise order of 100 wall unit (approximately 10 mm). Our aim was to have the sensors as close as possible to each other. However, due to the diameter of the hot-wire being 4 mm, 5 mm of spacing between each sensor was the minimum reachable measure.

The sensor 55P16 was given a preference due to its straight shape and cable-equipped probe. These characteristics were useful as our aim was to put twenty sensors in the upper wall of the wind tunnel through cavities that have been drilled in such a way that the sensors will not affect the flow in comparison with the 55P15.

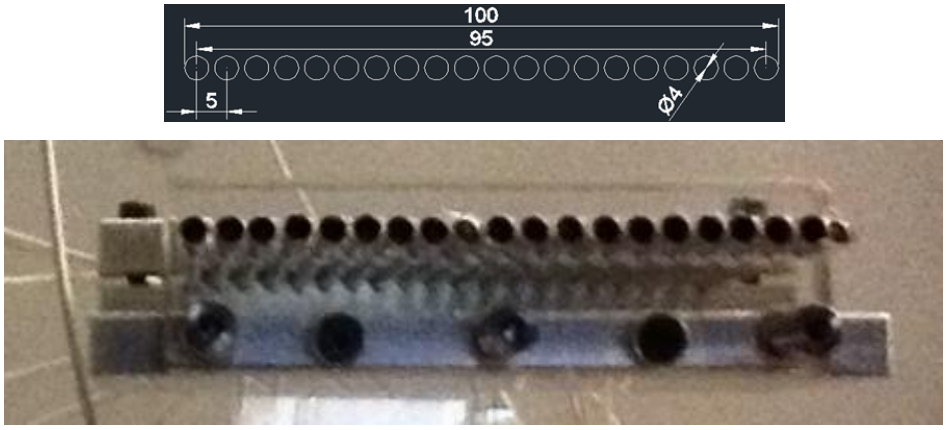


Figure 45: Dimensions of the 20 cavities on the upper wall of the wind tunnel

3.1.2.6 Measurement set-up

The sensors are operated by a twenty channels constant temperature anemometer. The signals from the sensors were sampled using a data acquisition software and digitised through a twenty channels analogue to digital converter (ADC) with the National Instruments CompactRIO-9022 and 9215 systems. The NI 9022 system is a Real-Time Controller, connected to a computer through an Ethernet Cable used for communication and processing for the control of the NI 9215 ADC 5 modules of 4 analogue input channels, ±10 V measurement range with a 16-bit resolution. The controller is programmed using LabVIEW, National Instruments' software platform.

In all cases, prior to sampling, the AC coupled outputs from the anemometer were first offset by the DC coupled voltage and then the signals were amplified by a factor of 10.

The sampling frequency was set at a value equal to twice the maximum frequency of our signal taking into consideration Nyquist criterion. Figure 42 shows the power spectral density of our signal where it can be seen that the maximum frequency equals to 500 Hz. The data to be used in the analysis

were sampled at a frequency of 1 kHz for a period of 50 seconds given a temporal sampling length per data set of 50 000 points.

The instrumentation was made of the hot-wire probes connected to a CTA. The output signal was transferred by a BNC cable to a National Instruments Data acquisition system to a PC and collected by a program in LABVIEW (Figure 46).

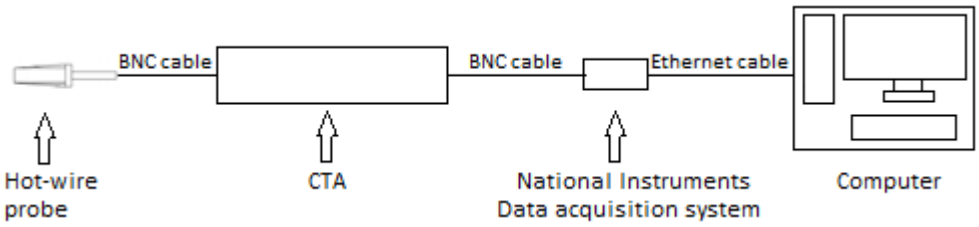


Figure 46: Diagram of hot-wire anemometry set-up to investigate the turbulent boundary layer.

3.1.1.1 Measurement conditions

Experimental arrangement

The hot-wire sensors were positioned 3200 mm downstream from the test section inlet at the measuring upper wall surface of the wind tunnel through 20 holes/cavities with a diameter of 4 mm and 1 mm spacing between each cavity. The cavities were drilled in the upper wall of the wind tunnel through the 12 mm Perspex to allow hot-wire sensors to measure behind the test surface, as can be seen in Figure 47.

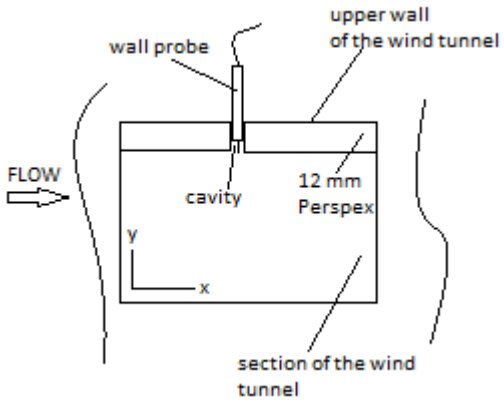


Figure 47: Schematic of the hole/cavity drilled in the upper wall of the wind tunnel through the 12 mm Perspex.

The sensors were positioned manually with the help of plates of known thickness (a thickness of $0.45^{+-0.01}$ mm and 0.15 mm measured with a micrometre), a camera and a tripod. The plates were used to set the sensors at a known position from the wall. They were placed on the upper wall of the wind tunnel behind the rake of sensors. The camera was used to have an enlarged view of the sensors and the plate, and to be able to place the sensors one by one at the same level than the plate. A tripod was used to avoid vibrations and maintain stability. The camera was coupled with a ruler focus on the wire and the wall in order to determine the distance between them. Such method is shown in Figure 48, where the distance is measured in regards to a precision plate.

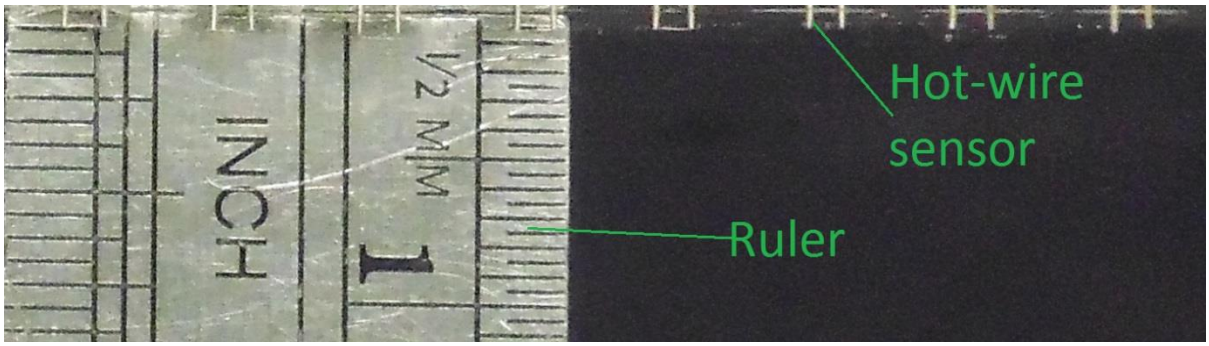


Figure 48: Set-up of a scale to set the sensors at a known distance of 0.5mm from the wall

Different positions were investigated to compare the data within the viscous sublayer and see if there was any observable change.

- The first set position of the sensors from the wall was 0.52 mm with a standard deviation of 0.08. This initial position y = 0.52 mm was estimated by using a ruler put vertically behind the set of sensors as a calibration tool. This technique was supplemented by photographs taken with digital camera, DSC-H200 Sony camera, 8-megapixel lens with 2.4 aperture, with a 26 times optical zoom lenses. The metre rule had a resolution of 0.5 mm, corresponding to the smallest vision on the scale. With this technique, the first measurement location was in the range $0.38 < y < 0.73$ mm with a mean value of 0.52 mm. Note that in Figure 48, a gap can be seen between the top of the ruler and the picture, this is due to the fact that ruler (resolution 0.5 mm) is positioned behind the sensors. The ruler was not used to

measure the sensors height but rather as a calibration tool to get the corresponding mm in pixels; 44 mm ≡ 1700 pixels.

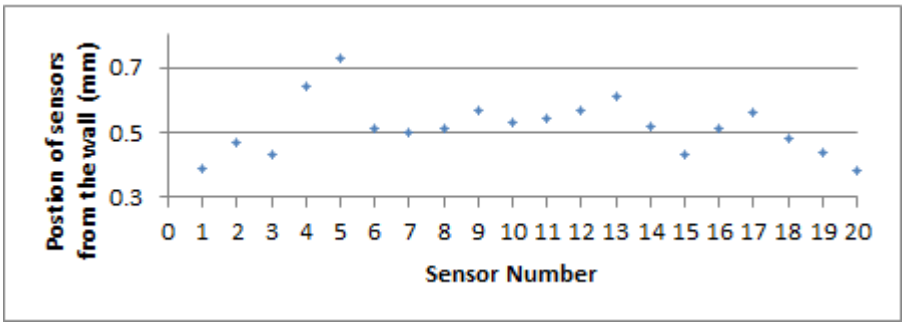


Figure 49: Positions of the sensors from the wall at 0.5 mm

- The second position of the sensors from the wall was 0.15 mm. The set position of the sensors from the wall was found to be 0.12 mm (y^+ = 1.6) with a standard deviation of 0.04. This position was estimated by using a ruler put vertically next to the set of sensors as a calibration tool (1700 pixels corresponds to 44 mm). With this technique, the measurement location was in the range 0.06 < y < 0.21 mm (0.75 < y^+ < 2.7) with a mean value of 0.12 mm (y^+ = 1.6).

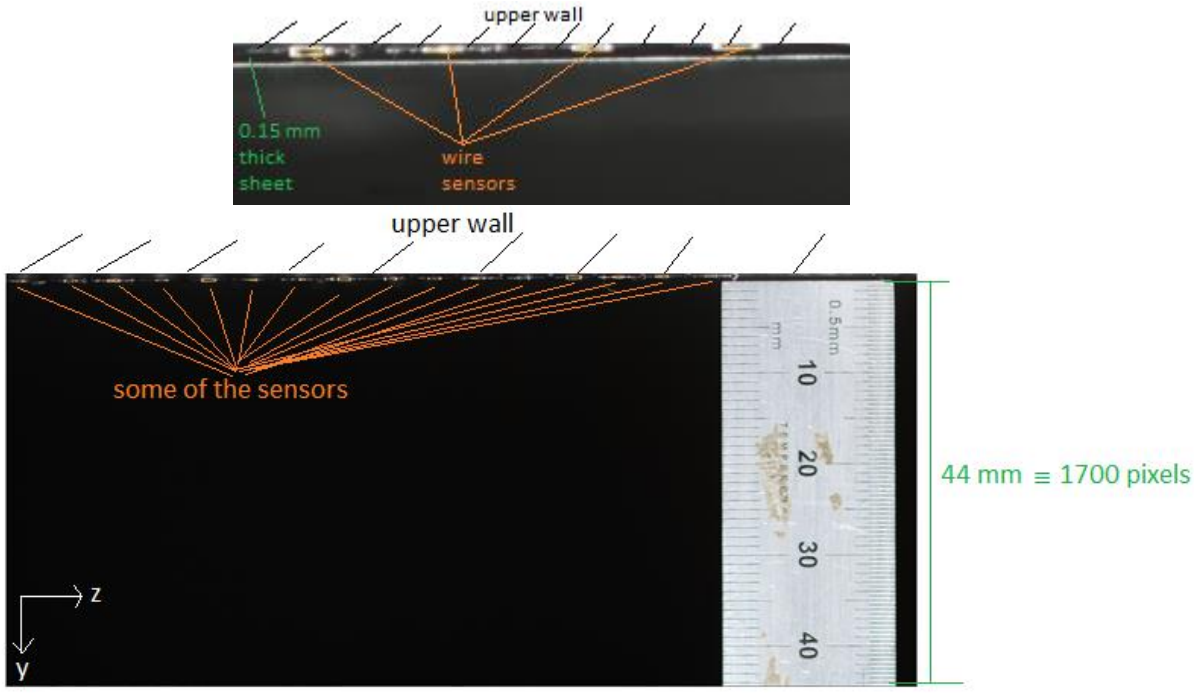


Figure 50: Position of the sensors from the wall

Table 7 shows the position of the sensors to the wall by measuring the left, middle and right side of the wire of the sensors. The wire length was measured

using the calibration method with a value of 1.45 mm, in comparison of the value given by the manufacturer of 1.25 mm.

Table 7: Position of each sensors from the wall

		S1	S2	S3	S4	S5	S6	S7	S8	S9	
pixels	left	-3	-3	-3	-9	-7	-3	-5	-7	-7	
	middle	-2	-5	-5	-8	-8	-4	-4	-7	-7	
	right	-6	-5	-4	-7	-9	-5	-4	-5	-6	
	mean	3.5	4.0	3.8	7.7	8.0	3.7	4.2	6.0	6.3	
	st. dev.	1.8	0.9	1.0	0.8	1.0	0.8	0.3	0.9	0.3	
mm	mean	0.09	0.10	0.10	0.20	0.21	0.09	0.11	0.16	0.16	
		S10	**S11**	**S12**	**S13**	**S14**	**S15**	**S16**	**S17**	**S18**	**S20**
pixels	left	-3	-4	-7	-3	-4	-4	-3	-5	-4	-5
	middle	-3	-2	-6	-3	-4	-4	-3	-6	-2	-5
	right	-3	/	-5	-4	-5	/	-3	-6	/	-6
	mean	3.0	2.5	5.8	3.2	4.2	3.8	3.0	5.5	2.5	5.0
	st. dev.	0.0	1.4	0.8	0.3	0.3	0.4	0.0	0.5	1.4	0.5
mm	mean	0.08	0.06	0.15	0.08	0.11	0.10	0.08	0.14	0.06	0.13

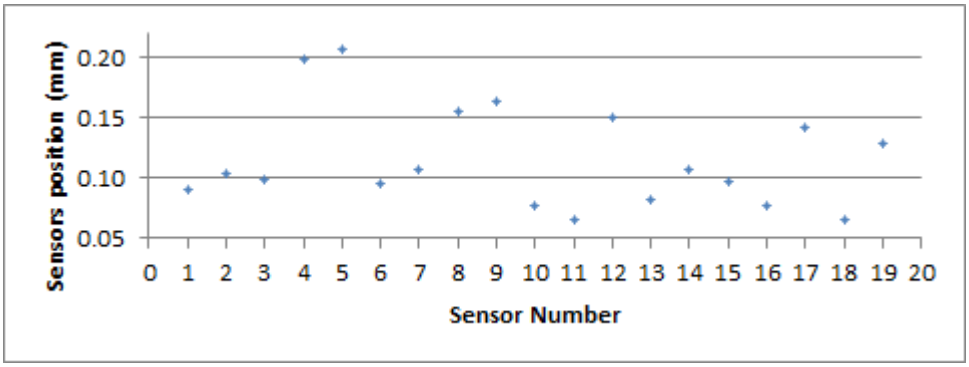


Figure 51: Positions of the sensors to the wall at 0.12 mm

- Finally, two trials were carried out to put the sensors at the wall, $y = 0$. The first trial was done using the Sony camera mentioned earlier. As for the second trial, the previous camera did not give a good quality picture that would enable us to set the sensors at the wall since the pictures were blurred and the wires could not be seen properly. Instead, a Canon EOS 450D Digital SLR Camera 12.2 Megapixel with a Canon EF-S 60mm Macro lens that had a focal length of 60 mm was used to capture clearer pictures and see the wires. The sensors were placed at a position from the wall below $y = 0.17$ mm for the first trial while for the second trial they were at a position smaller than the first trial. However, the exact positions of the

sensors in the second trial are unknown as the technique used had an accuracy of 0.17 mm.

Holes effects on hot-wires

A study of the energy spectra from the hot-wire sensors for various locations was carried out.

Table 8: Characteristics of turbulence for data under holes vs no holes

	U_∞ (m/s)	u^* (m/s)	Re_τ
No holes	3.0	0.135	513
Under holes	3.2	0.132	568

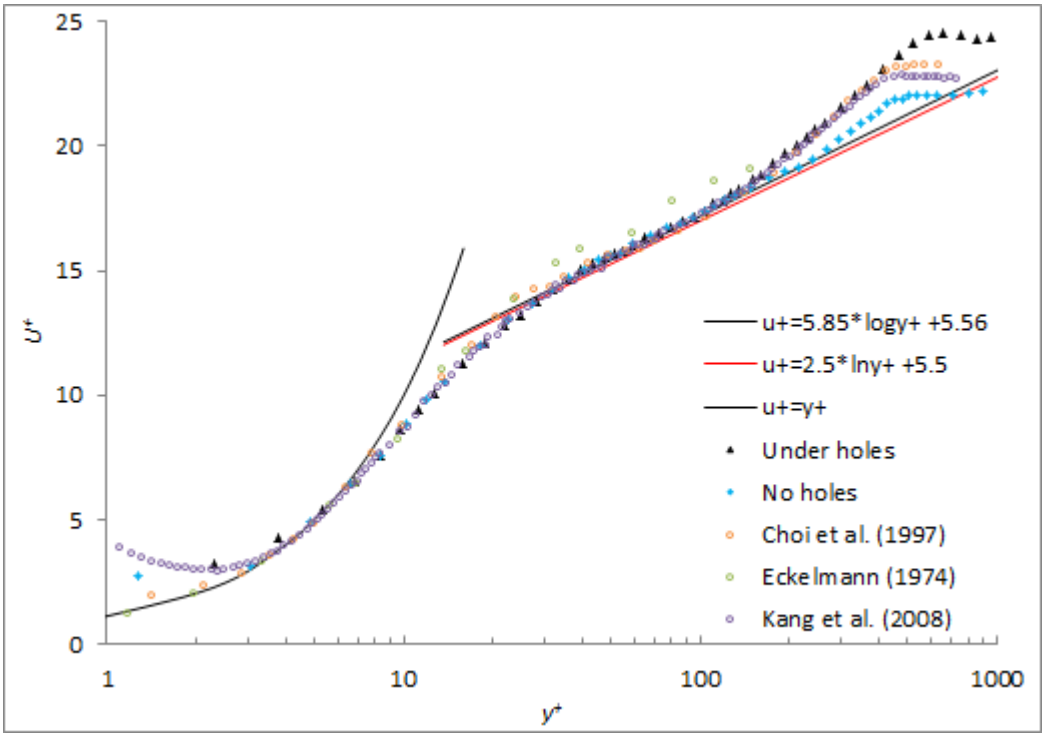


Figure 52: Mean streamwise velocity profile for data placed under the holes in comparison of the data not placed under the holes

The mean streamwise velocity does not seem to be affected by the hole as it is in good agreement with the results of Kang et al. (2008) as seen in Figure 52.

As for the turbulence intensity, from Figure 53, it seems that its value is underestimated for y+ < 50 and overestimated for y+> 80 due to the hole effect. The trends of the profiles are identical. The over/underestimation is not seen

as crucial for our studies as the interest is given to the topology of the structures.

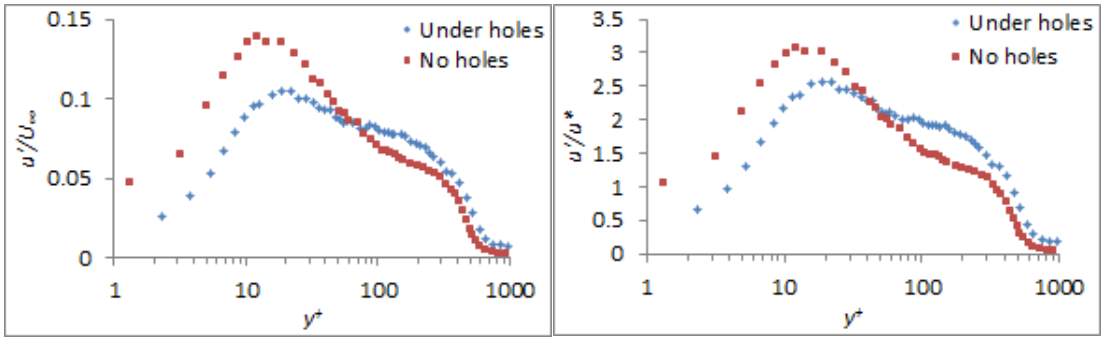


Figure 53: Turbulence intensity profiles for data placed under the holes in comparison of the data not placed under the holes

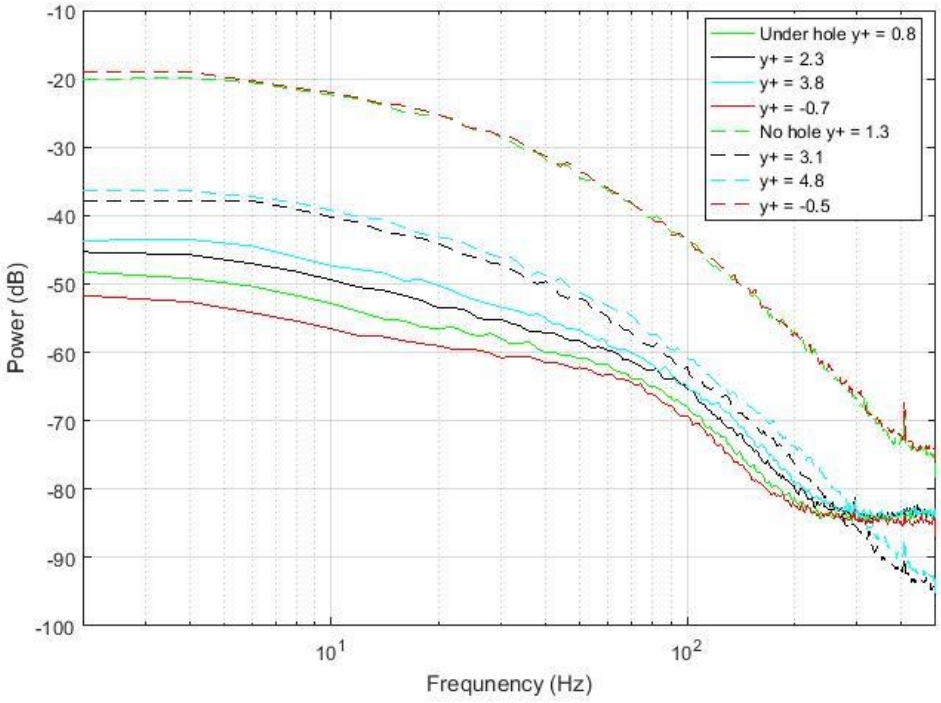


Figure 54: Energy spectra from the hot-wire sensors for various locations

Finally, we can see from Figure 54 that the hole has a small effect in our measurement. Indeed the amplitude of the power seems to decrease for data under the hole in comparison with data not positioned under the hole. A value of 35-40 dB is found for the data under the holes and 50-60 dB for the data away from the holes. It means that the fluctuations in the amplitude for data under the holes are smaller than those away from the holes. However this effect is negligible in this study, the study was focused on large scale structures and small frequencies. Furthermore, a filtering process, to eliminate high

frequencies was performed on the skin-friction data, as this study was interested on large-scale structures only.

Particles effect on hot-wires

An analysis of the particles (for the seeding of PIV) effect on the hot-wire sensors was carried out. It reveals no overall change in hot-wire energy spectra at low frequency.

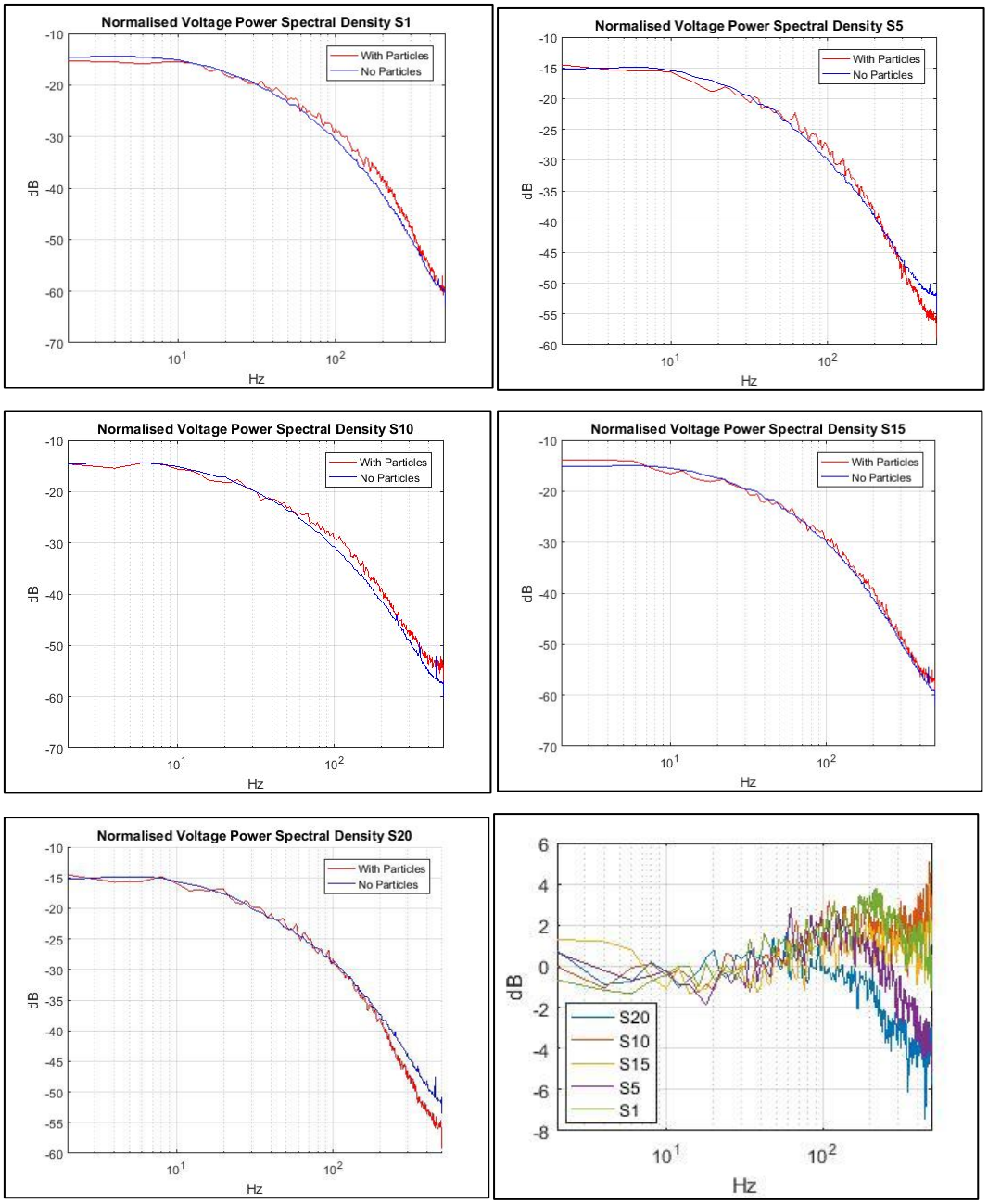


Figure 55: Energy spectra from the hot-wire sensors with and without particles

Possible interference between the hot wires

This is effectively just a mean shift which is subtracted for all subsequent analyses where only the fluctuating part of the hot-wire signal is used and hence does not influence results. Therefore it is concluded that, for the purposes of this study, there is no discernible interference between the hot wires.

Median Filter

Different filters were applied to the fluctuating velocity maps to damp out frequencies coming from structures smaller than 100 viscous length scales. Taylor's hypothesis with $U_c = 13u^*$ was applied first and then followed by the filtering procedure. Figure 117 to Figure 119 show the fluctuating voltage map without and with filter with different filter size applied. The filtering technique enables to identify large-scale patterns from the map. To inspect the very large-scale pattern (long low speed region) of fluctuation voltage in more details, a filtering procedure is applied to the instantaneous field.

The median filtering technique is a non-linear two-dimensional image filtering based on the spatial analysis. The median filtering is a high frequency suppression method which is expected to keep the edges well maintained while doing image smoothing.

The basic premise behind median filtering is to analyse pixel neighbourhoods in the image, sort their intensities, and then choose the middle intensity as the result over a sliding window of fixed size (Huang et al., 1979). It considers each pixel in the image in turn and looks at its nearby neighbours to decide whether or not it is representative of its surroundings. It then replaces the pixel value under evaluation with the *median* of neighbouring pixel values. The median is calculated by first sorting all the pixel values from the surrounding neighbourhood into numerical order and then replacing the pixel being considered with the middle pixel value.

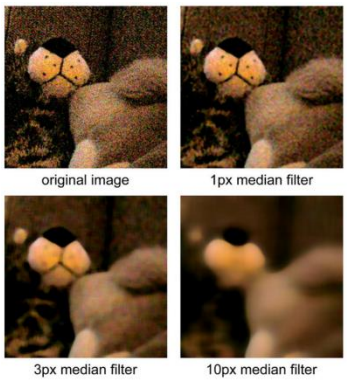


Figure 56: Example of application of median filtering

The size of the filter in cells unit changes depending on the Reynolds number due to the change in skin-friction velocity, u^*. One of the filter size used at 2.2 m/s, Re_τ = 423, is a 9×30 (streamwise x spanwsise) cells neighbourhood. It means that for each pixel of the output image, we would take a 10x30 neighbourhood around the respective pixel in the original image, and assign the median colour value in this neighbourhood to the pixel of output image.

Table 9: Size of median filter, cells versus wall unit, for different free-stream velocities

Re_τ	423		568		1310	
U_∞ (ms^{-1})	2.2		3.2		7.4	
	x	z	x	z	x	z
cells	50000	180	50000	180	50000	180
wall unit	370727.76	588.94	751661.1	838.61	3532776	1818.05
	cells [x^+ x z^+]	wall unit [x^+ x z^+]	cells	wall unit	cells	wall unit
3rd filter size	1130 x 30	8380 x 98	781 x 21	11741 x 98	407 x 10	28783 x 101
2nd filter size	113 x 30	838 x 98	78 x 21	1174 x 98	41 x 10	2878 x 101
1st filter size	9 x 30	67 x 98	19 x 21	286 x 98	10 x 10	720 x 101

At Re_τ = 418, 50000 cells correspond to 370727.76 wall units in x^+ direction and 180 cells corresponds to 588.94 wall units in z^+ direction as shown in Table 9 with other values for higher Reynolds numbers.

The median filtering operation was performed on several cell arrays ranging from 10x10 cells to 1130x30 cells as tabulated in Table 9. For each Re_τ, three filter sizes were applied in the streamwise direction and one filter size in the

spanwise direction. The results will be analysed and explained later. For Re_τ = 423, the total cell size of the fluctuating voltage map is 50000x180 cells, which in terms of wall units, is equal to 370727.76x588.95. Therefore, by proportion, the neighbourhood cell size which is equal to 9x30, whereas, in terms of wall units, is equal to 67x98 along *x*- and *z*-direction, respectively. This means that, all the spatial fluctuations smaller than the size just mentioned are removed during the median filtering stage.

The low-speed fluctuations have a spanwise width of the order 0.3 - 0.5δ (Hutchins and Marusic, 2007a). At Re_τ = 423, this corresponds to 125 - 209 wall units. Considering that criterion, the chosen filter size in the spanwise direction of 98 wall units is considered a proper input value, meaning that all the images are smoothed in a way that all the values less than or equal at 98 wall unit are removed after the filtering operation. For the streamwise direction, the large and very large-scale structures have according to some investigators a streamwise extent from 2-3δ up to more than 20δ (Adrian et al., 2000a, Hutchins and Marusic, 2007a). In our studies, attention was given to structures within this range, thus filter size of 0.5, 2 and 20δ were applied in the streamwise direction.

Part 2: s-PIV and synchronisation uncertainties

3.2.1 Particle Image Velocimetry System

For the visualisation and investigation of the structure in TBL flow, particle image velocimetry (PIV) system from Dantec dynamics was used to extract information about the flow utilizing visualization technique.

It is a technique capable of providing a qualitative description of the flow field but also to extract quantitative information about the instantaneous flow velocity field. With PIV, two pictures of the flow field are captured within a very short time and then points in the flow field are traced from the first picture to the second. Its displacement is recorded via a high-speed camera and divided by the time separation giving a velocity. PIV allows to instantaneously record images of large parts of flow field enabling the detection of large and small scale spatial structures in the flow but also to extract the velocity information out of these images. The major advantage of PIV is the ability to quickly measure the instantaneous flow velocity field within a very short time and over a relatively large area in a non-intrusive manner.

Figure 57 shows a typical PIV setup composed of several sub-systems: a high power light, a camera, a computer and a seeding generator. A high power light source for illumination is required in order that the light scattered by tiny tracer particles will expose the image. The test section is illuminated by an intense plane of light, laser. A dual head pulsed 100 mJ Nd:YAG laser operating at 532 nm. The light scattered by the tracer particles is recorded via a CMOS-based high-speed camera, Phantom v611, with a resolution of 1280 x 800 pixels. A maximum speed of 6242 frames-per-second at full resolution can be achieved. The output of the camera is stored in real time in the memory of a computer directly. Reviews on PIV technique can be found in many research articles (Raffel et al., 1998), Prasad (2000).

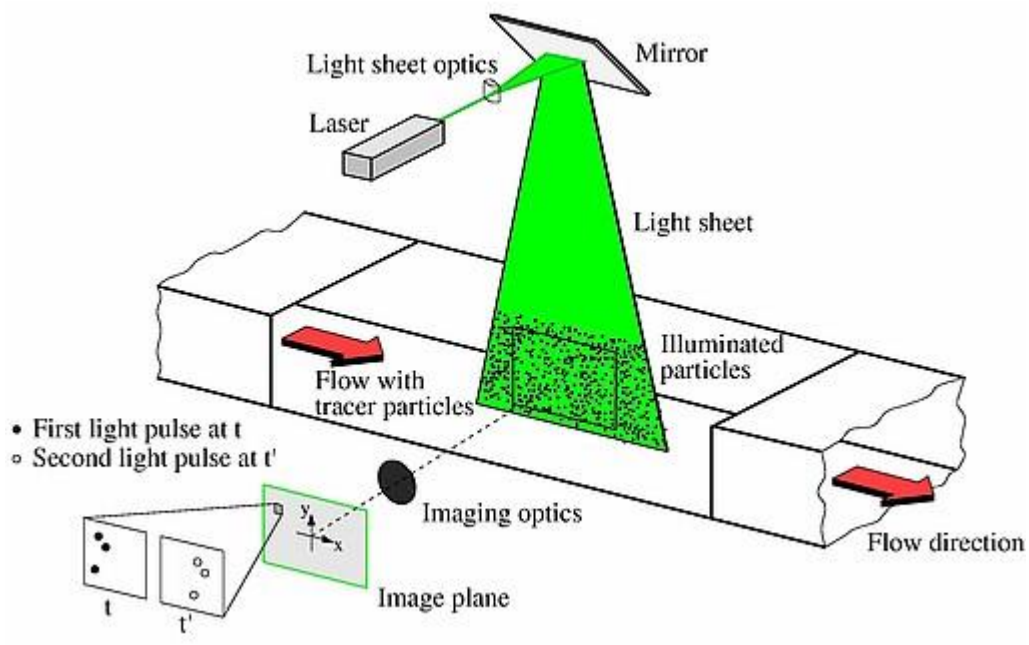


Figure 57: PIV overview (Johnson et al., 2006)

3.2.1.1 Seeding Mechanism for 2D PIV

Particles are needed within the flow, to be distinguished by the high speed camera. The flow velocity is measured indirectly by means of the measurement of the velocity of tracer particles added to the flow. So PIV actually measures the displacement of seeding particles and not the flow itself but it is assumed that the tracer particles move with local flow velocity. For this reason, particles must be chosen very carefully. A seeding particle that is too heavy will not be carried by the flow and will be slow to react in changes in velocity. To faithfully follow the motion of the fluid elements particles have to be small enough but also large enough to scatter light energy sufficient to be seen by the camera and form bright images. In the ideal case, the chosen seeding particle should have the same density as the fluid (Raffel et al., 1998). In this study olive oil (2-10 µm) was used as the tracer particle for 2D PIV experiments conducted. For Stereoscopic PIV (s-PIV) measurements, the flow was seeded with 1 µm Di(2-Ethylhexyl) Sebacate (DEHS) particles with a density of 0.91 g/cm^3 (density of air = 0.001225 g/cm^3).

The distribution of tracer particles in the flow has to be homogeneous for high quality PIV to obtain optimal evaluation. Plus, the injection has to be done without altering the flow. A new seeding injector was fabricated to entrain the

tracer uniformly into the boundary layer of the flow without causing any disruption to the flow. The particles were injected into the boundary layer through an injection slot by pressurizing its holding container slightly above the tunnel pressure with compressed air. The dimensions of the injection slot were 5 mm in height, 240 mm in span, 1 mm in the particles flow direction, and it was inclined at 30^0 to the flat plate (Figure 58 and Figure 59). A small chamber of 300 mm by 70 mm by 17 mm, located above the injection slot, was used to equilibrate pressure and provide uniform jet across the span of the injection slot. The seeding device was located in the upper wall.

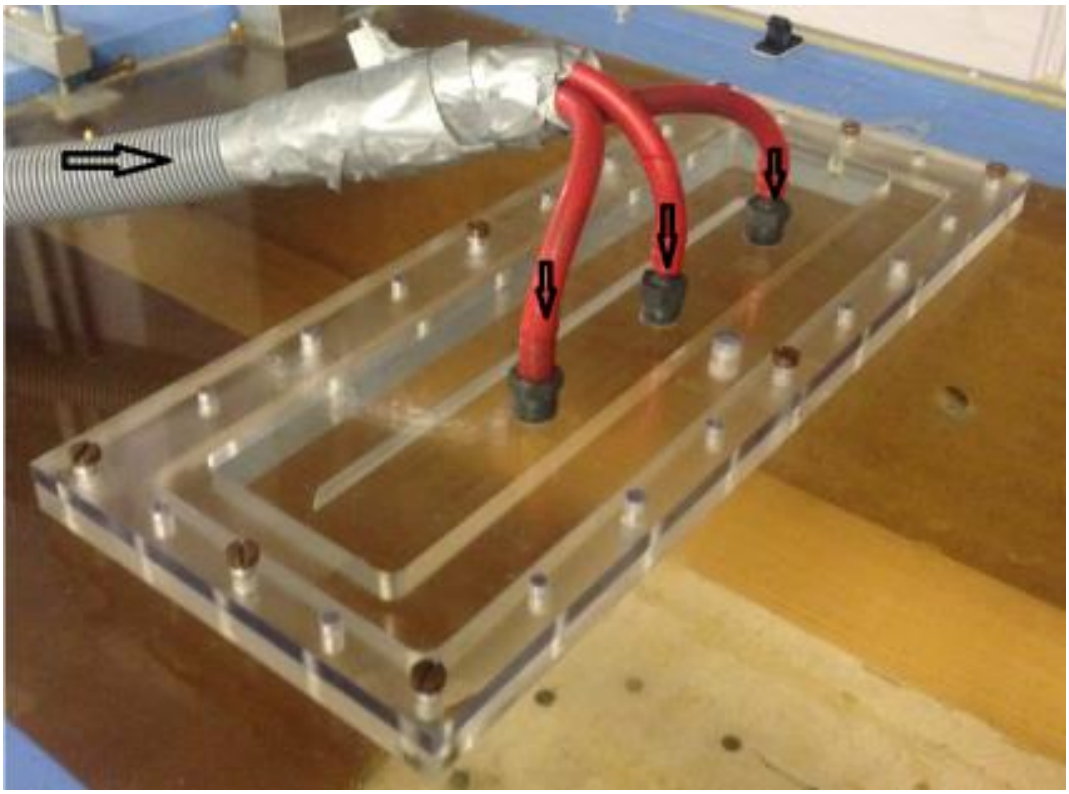


Figure 58: Seeding Injector

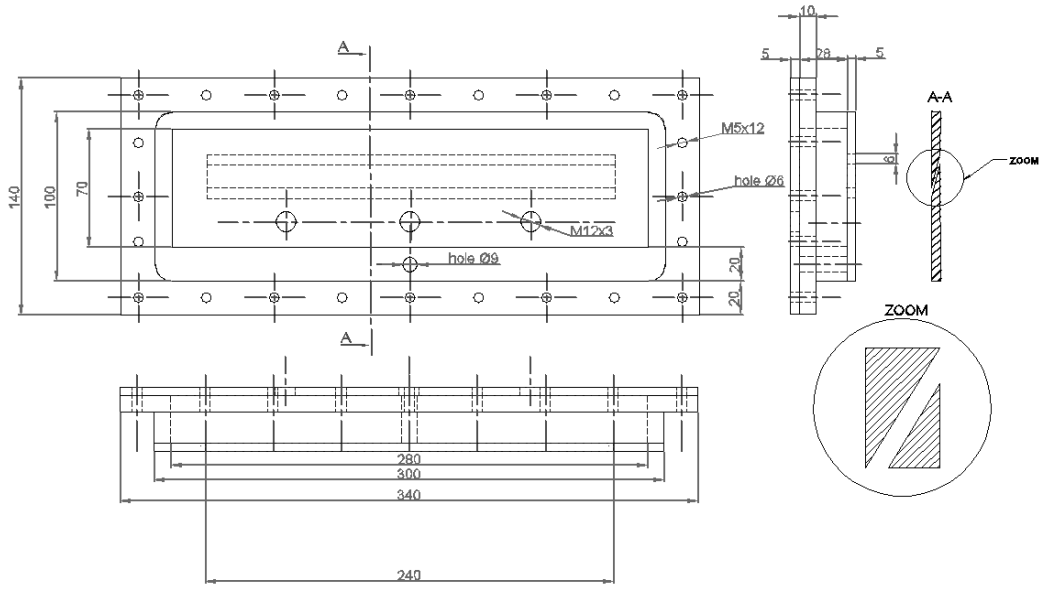


Figure 59: Seeding injector dimensions

3.2.1.2 Capturing of PIV Images

Once a sequence of two image frames is recorded, the images are broken up into smaller subsections called interrogation areas (IA). The size of the IA was chosen so that 10 to 25 particle images are seen in each interrogation area and the particle displacements within the area do not exceed ¼ of the area (Raffel et al., 1998) as there are of some importance in obtaining a good signal peak in the cross-correlation. To reduce this error, the IA can be overlapped which means that there is a new IA every ½ of the area as seen in Figure 60.

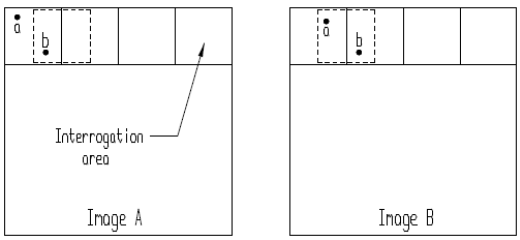


Figure 60: Overlap of the interrogation area

Once the two parameters were determined, the interrogation areas from each image frame at *t* and *t+Δt*, are cross-correlated with each other, pixel by pixel. The correlation produces a signal peak, identifying the common particle displacement. An accurate measure of the displacement - and thus also the velocity - is achieved with sub-pixel interpolation. A velocity vector map over the whole target area is obtained by repeating the cross-correlation for each

interrogation area over the two image frames captured by the camera and shown in Figure 61.

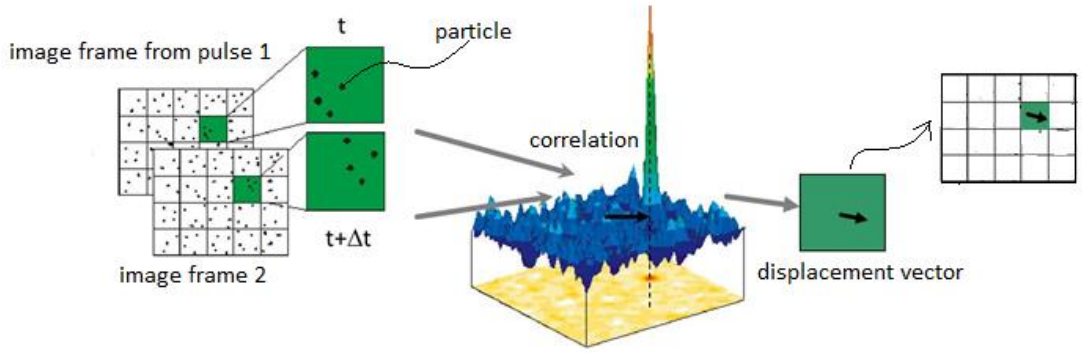


Figure 61: Analysing with DantecStudio using PIV

The repetition rate for PIV measurement was fixed between 300 and 1000 Hz. The mean velocity was subtracted from the averaged velocity to have just the fluctuation part.

The laser and the digital cameras are controlled by a computer using Dynamic Studio software.

3.2.1.3 Stereoscopic PIV Theory

A brief summary of 3 dimensions (3D) stereoscopic PIV (s-PIV) principle is given in this section.

The s-PIV system is identical to the 2 dimensions (2D) PIV system with an additional high-speed camera. This method is used for measuring three velocity components in the planar 2 dimension 3 components (2D3C) region illuminated by a laser light sheet. The third component of velocity measured is the velocity component passing through the laser light sheet.

By placing two cameras so that they observe the plane at different angles, they capture particle displacement images that contain the influence of the third velocity component. Two-velocity component vector maps from each camera are obtained. After image calibration, this third velocity component can be evaluated in addition of the two in-plane velocity components.

In our experiments, the cameras stand on different sides of the light sheet and therefore are placed in the forward scattering direction of the laser light. The

laser sheet was placed in the *z-y* plane, thus the third component of velocity was the *U*-component of velocity.

Multi-level calibration target

In this method, accurate calibration is essential to obtain good results in measurements of the velocity components. For our experiments, a double-sided multi-level calibration target with two level grids of markers (white dots on a black background) was used to calibrate the cameras (Figure 62). The markers are spaced 20 mm apart along x and y directions on both sides of the target. This target is required for image acquisition setups, where cameras are on opposite sides of the lightsheet. Half the markers are in the same level as the zero marker, the other half are in a 2nd level, closer to or farther from the cameras.

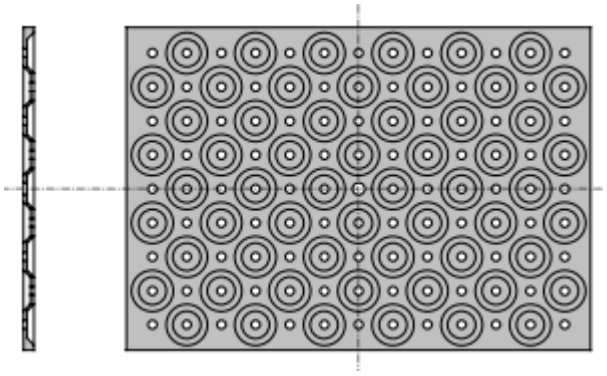


Figure 62: Large multi-level target with a two-level grid of dots (Dantec Reference Manual)

Backlighting is used since the white dots of the large (270×190 mm) multi-level target are made in translucent material. With light turned off, backlighting gives good contrast for the calibration of stereoscopic PIV.

By definition the larger dot is the origin of the coordinate system (0, 0, Z) and the common fix point for the two cameras (Dantec, Reference Manual). Therefore both cameras must be able to see the large dot surrounded by four smaller ones.

The calibration target had two orifices of 3 mm on its side. This was to allow accurate alignment of the calibration target and the laser light inside the wind tunnel. The double side of the target enabled the stereoscopic calibration of the PIV system with a single image, removing the need of traversing the calibration target in the *z* - direction.

(x, y), z co-ordinate system

The *x*- and y- coordinates are identified on the recorded images by the software as for the *z*-coordinates, it needs to be determined. The sign of the *z*-coordinate value needs also to be determined.

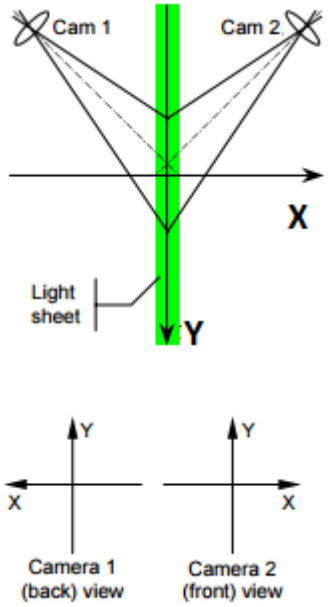


Figure 63: Back and front view configuration adapted from Dantec (Reference Manual).

The cameras are located in the spanwise direction (*z*) at the same distance from the light sheet for the configuration of our experimental setup for s-PIV (Figure 63 and Figure 64). As the two cameras are on opposite sides, both cameras have same signs for the z-coordinates, for the back view, $z = +1$ and for the front view, $z = +3$ were entered. The position $z = 0$ is the position of the

light sheet, i.e. the measurement plane. It represents the position of the calibration target relative to the lightsheet.

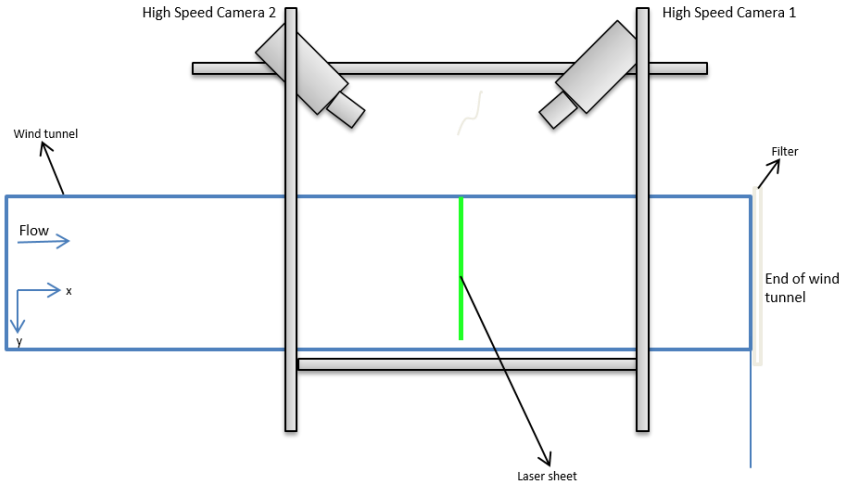


Figure 64: Arrangement between cameras/laser in relation to the wind tunnel section.

The type of calibration target used in our experiments was the large multi-level, 270x190 mm. This corresponds to 2nd level -4 in Dynamic Studio for back and front cameras.

Scheimpflug mounts

The angle between the camera body and camera lens needs to be adjusted in order to focus correctly on the 3D calibration target. To do this, the so-called Scheimpflug condition must be fulfilled. This is achieved by mounting the cameras on Scheimpflug mounts. Scheimpflüg adapters were used with each camera to ensure that each PIV image was in focus.

The two cameras are placed at angles of -45° and 45° with respect of the light sheet to obtain the most accurate out-of-plane displacement (Prasad, 2000). The optical configuration in order to obtain uniform focusing satisfies the Scheimpflug condition (Prasad, 2000).

3.2.1.4 Sources of error

In our experiments, importance was given to the following parameters to measure the velocity as accurately as possible:

- It is important that the images captured have a black background in order to provide enough contrast so that the illuminated seeding particles can be distinguished. An adequate level of contrast is needed between the dark background and the bright particles
- The time delay between illumination pulses must be long enough to be able to determine the displacement between the images of the tracer particles and short enough to avoid particles with an out-of-plane velocity component leaving the light sheet between subsequent illuminations.
- The particle displacements between the first and second frame should not exceed 8 pixels (¼ of the interrogation window size) to reduce the number of pairing losses (loss of particle images within the interrogation window from the first frame to the second frame) for the correlation. As a result, the time between the two consecutive laser pulses (*dt*) has to be adjusted accordingly. However, reducing *dt* below the equivalent of 8-pixel displacements will reduce the velocity dynamic range because the lower end resolution limit is on the order of 0.1 pixel displacement.
- Similar to the 8-pixel displacement within the imaging plane, the highest velocity particles should not traverse more than ¼ of the light sheet thickness, again to reduce the number of pairing losses. Since the time delay between the two laser pulses is used to ensure the best correlations within the light sheet plane, the thickness of the sheet is a variable in this context.

To quantify the experimental error of the PIV measurements, the free-stream velocity measured with s-PIV was compared with the velocity reference transducer. The free-stream velocity, as measured using s-PIV is 4.7 m/s in comparison with 4.6 m/s obtained with the velocity reference transducer, this gives some estimate of the error. The velocity is under-estimated by 0.1 m/s, 4.7 m/s for s-PIV against 4.6 m/s for the velocity reference transducer. This uncertainty of 2% is within the 3-5% error level of PIV measurements (Corino, 1969). Note that the u-component is the least accurate component as it is the component that is perpendicular to the light sheet. As such it goes through the thin sheet, it is difficult to have sufficient mean particle movements within the

laser sheet plane, whilst minimising the particles lost that are travelling through the light sheet in a stereoscopic PIV set-up.

Despite these sources of inaccuracy, the discrepancies are particularly noticeable near the wall but as the interest of this project is on the large-scale structures, this is not viewed as a major problem.

3.2.1.1 S-PIV experimental arrangements

Mounting method

A method of mounting two cameras was established appropriately for stereoscopic PIV measurements. A stand was designed, it was made of aluminium bars to support the cameras and Scheimpflug mounts at the required distance and angle from the 3D calibration target. The stabilisation of the frame was improved by using small L profiles (cut to have the appropriate dimensions and drilled), 40 by 60 mm, to connect the aluminium profiles, and it enabled the bars to be perpendicular and parallel between them. Furthermore, the bars were attached to the traverse system using clamps to make the frame rigid. Figure 65 shows the sketch of the structurally enhanced frame work.

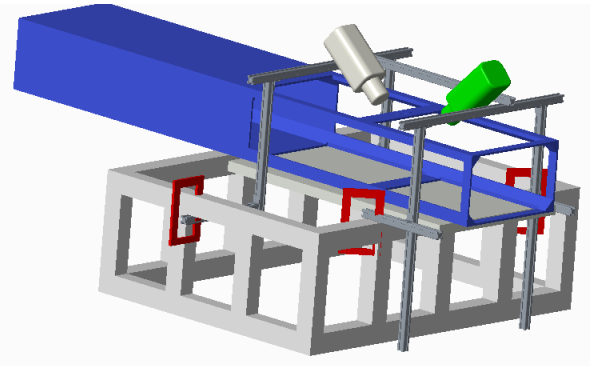


Figure 65: Sketch of the structurally enhanced frame work (Will Bowling).

A spirit level was used to check the parallelism and perpendicularity of the aluminium bars. It is a device designed to indicate whether a surface is horizontal or vertical by the centering of a bubble in a tube filled with ether. The spirit level was positioned on the surface of each bar, in the centre. The bars were levelled until the bubble sat between the two marks (that is, once the bubble inside the spirit tube was centered between the lines on the tube).

Camera position

Before starting the experiments, a decision was made on which setup to use for stereoscopic PIV. Two configurations of s-PIV were investigated to aid the decision on which configuration would be best to use for our experiments.

The cameras could not be put in the end of the wind tunnel as the only available optical walls were the upper wall and one of the side walls. Instead they were positioned either on the side or top of the wind tunnel.

The side and top positions of the cameras were tested by carrying out a s-PIV measurement using a 50 mm lens.

The first section describes the configuration with cameras put on the side wall of the wind tunnel. It is then followed by a section which describes the configuration with cameras put on the top wall of the wind tunnel.

Camera on side wall of the wind tunnel

The cameras were positioned on the aluminium bar using the 50 mm lens at -290 mm and 265 mm in a streamwise direction for camera 1 and 2, respectively and and 300 mm in a spanwise direction from the 3D calibration target as seen in Figure 66. The Scheimpflug angle for camera 1 is set at 7.3^0 and for camera 2 at 8^0.

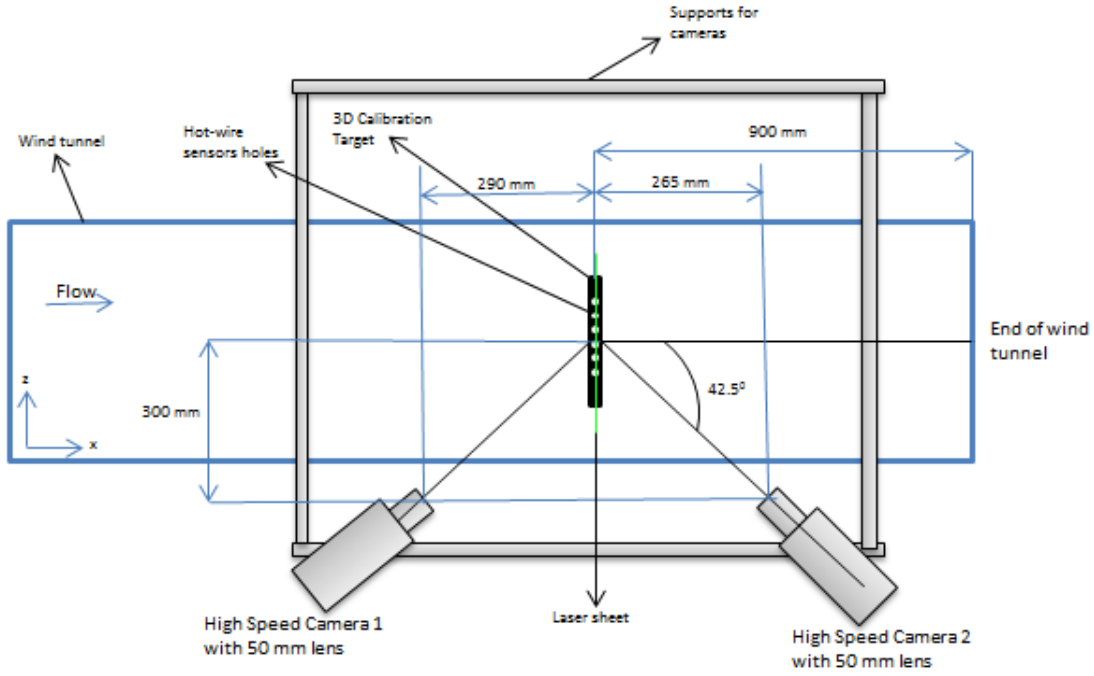


Figure 66: schematic of s-PIV set up with cameras put on side (plan view).



Figure 67: Optimal camera configuration for an optimal determination of the s-PIV calibration coefficients with cameras put on the side.

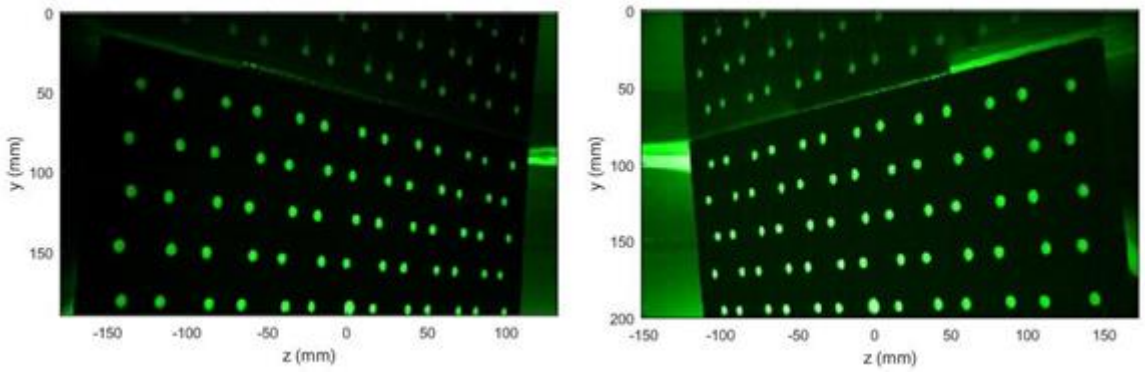


Figure 68: Right and left calibration grid images obtained by each camera using double sided (multi-level) calibration target.

Difficulties

- Near wall region restricted by corner fillet

One of the difficulties met for s-PIV with the camera on the side wall was the field of view in the near wall region being obstructed by the corner fillet. The camera field of view is restricted in the near-wall region, from the wall (0 mm) to about 30 mm which corresponds in walls unit to about 300 due to the filled corner of the wind tunnel. To be able to have a field of view in the near wall an angle of about 5 degree is needed. Using the Scheimpflug mount for s-PIV setup, it will rotate the camera in 2 directions as seen in Figure 69, it cannot be done as it might affect the vector values.

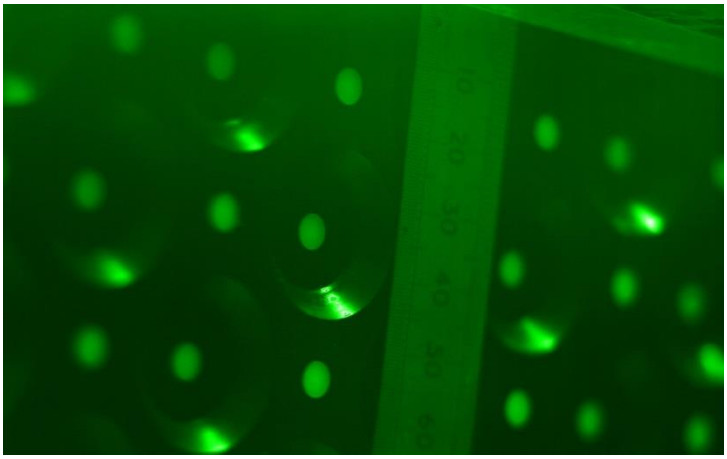


Figure 69: Rotation of camera placed on Scheimpflug mount with 105 mm lens.

Another possibility was to remove the filled corner but it was glued and screwed to the upper and side wall of the wind-tunnel made of Perspex as seen in Figure 70. In addition, removing the filled corner could affect the characteristics of the flow.



Figure 70: Top corner filled (left side) and side corner filled (right side)

Camera on top wall of the wind tunnel

The angle between the two cameras is set to 90 degree giving a viewing angle of 45 degree for each camera. The Scheimpflug condition is adjusted with an angle of 6 and 7 degree for camera 1 (back) and 2 (front), respectively.

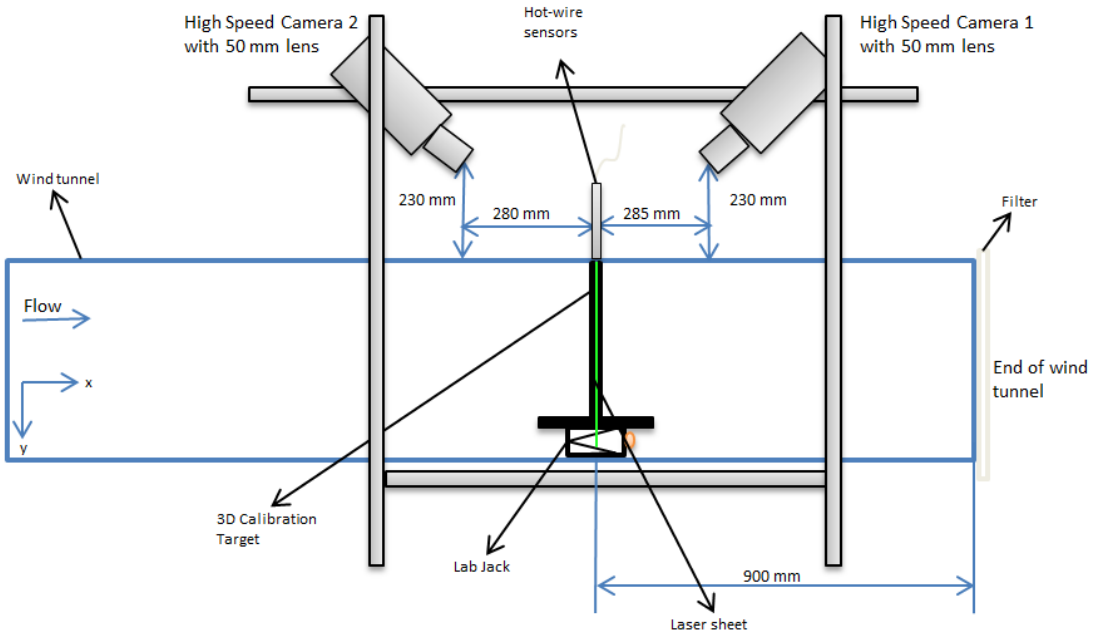


Figure 71: Schematic of experimental arrangement demonstrating the position of the cameras and laser

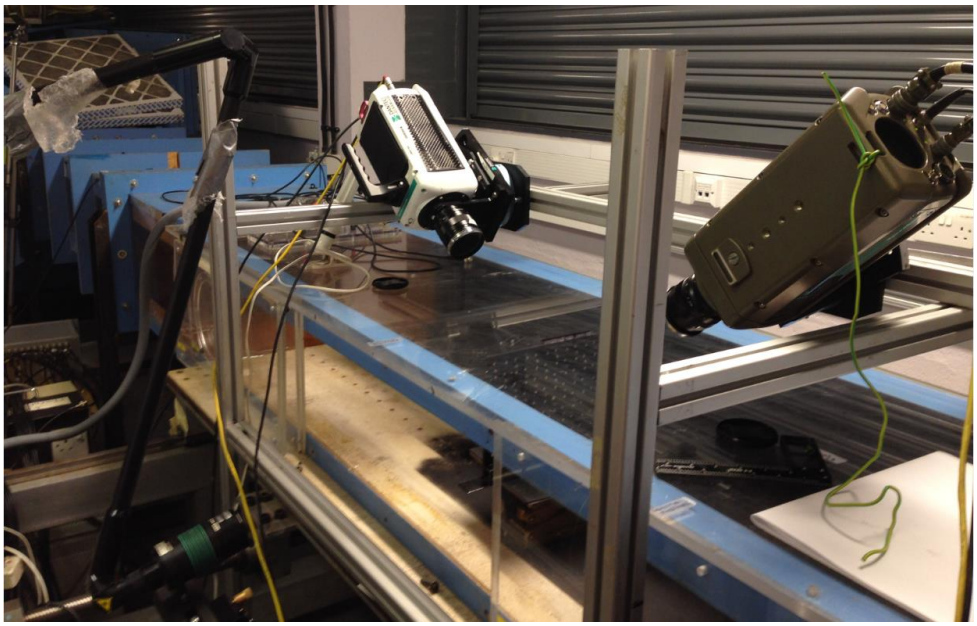


Figure 72: Optimal camera configuration for an optimal determination of the s-PIV calibration coefficients with cameras put on the top.

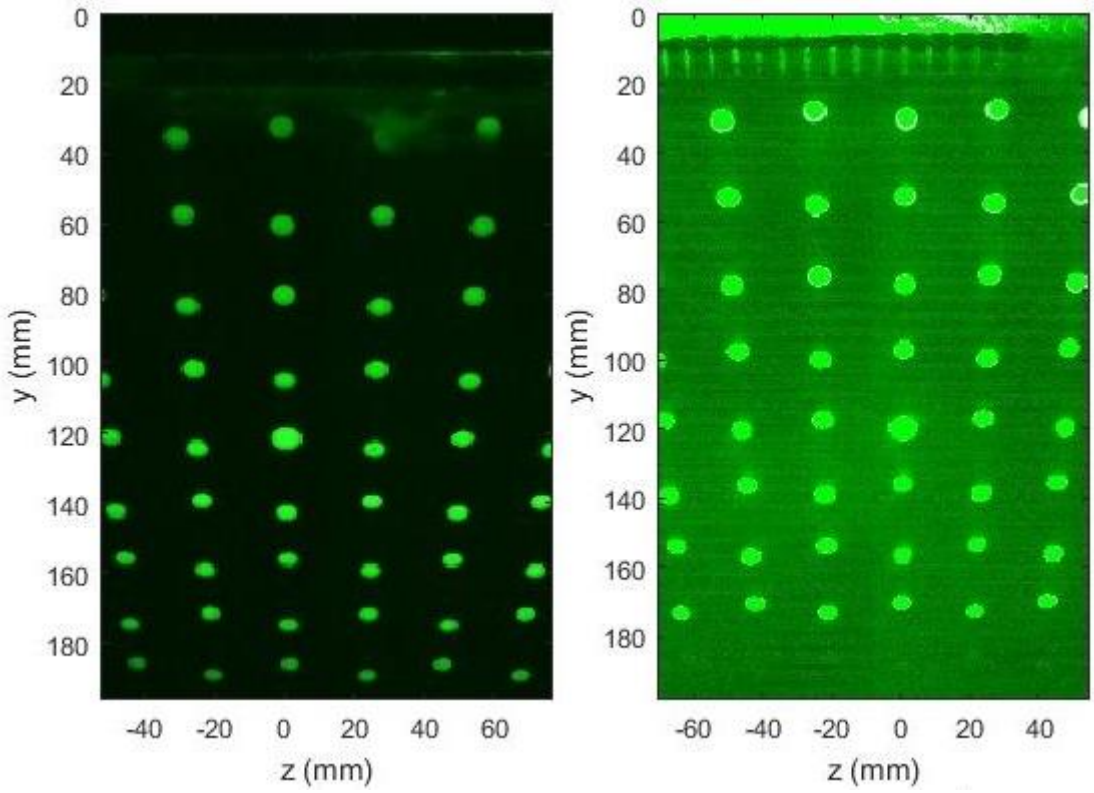


Figure 73: calibration images from back (right) and front (left) cameras.

Difficulties

- Aspect ratio unsuitable for field of view of interest

Using the camera on the top wall with the 50 mm lens, the field of view is y = 200 mm and z = 140 mm in comparison with our field of view of interest which is 80 x 100 mm in y and z direction respectively. This decreased our resolution as a higher field of view was used in comparison with the one we were interested in.

- Near wall field of view obstructed due to hot-wire holes

Due to the hot-wire sensor holes on the upper wall, the camera view was obstructed by about 6 mm which corresponds in wall units to about 60. There was little that can be done to overcome this difficulty.

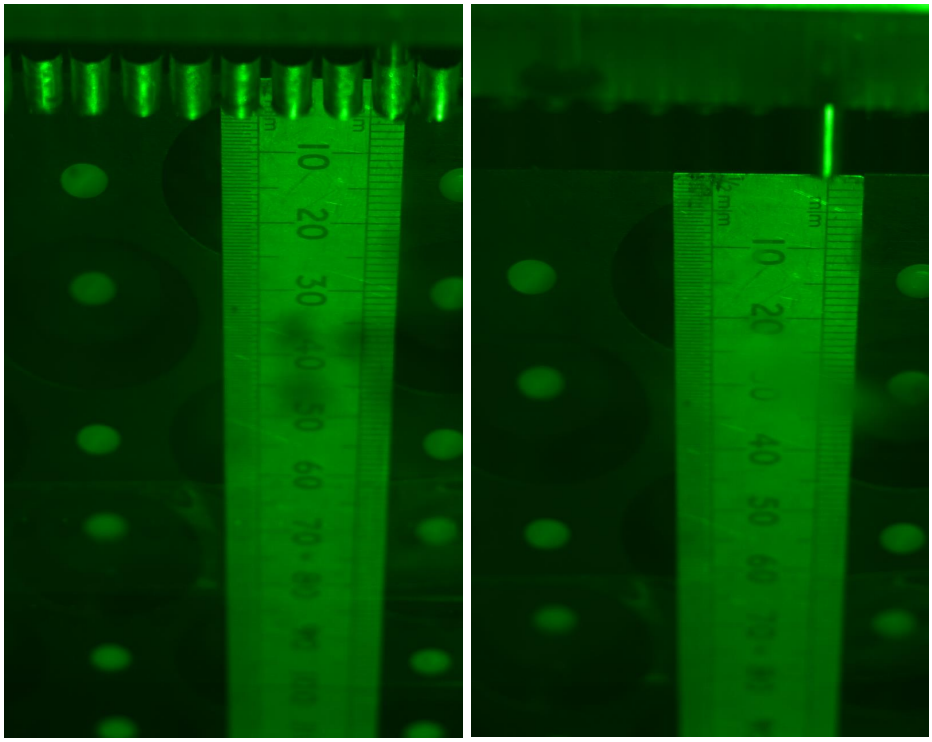


Figure 74: Near wall field of view obstructed due to hot-wire holes

- Perspex on top wall

The upper wall Perspex was polished to get rid of the scratches hence improve the quality of the data.

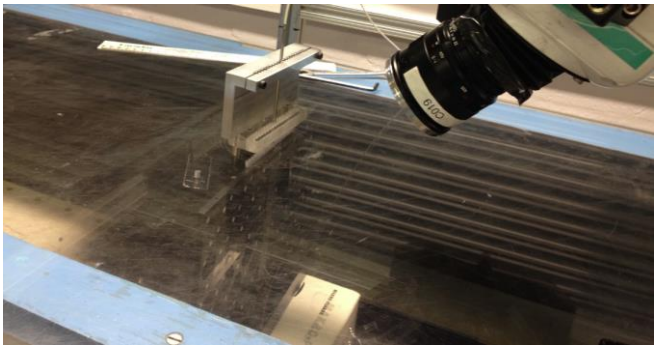


Figure 75: upper wall Perspex

Conclusion

Both configurations gave successful results for our experiments with velocity vector values and velocity profiles for the streamwise velocity component. The results were coherent, realistic and comparable to the value of the free-stream velocity measured with the velocity reference transducer.

As for the camera on the top configuration, about 5 mm (60 w.u.) of the near wall region, this was obstructed by the 12 mm thick holes. To overcome this

obstruction, the calibration target could be put further upstream of the holes, at about 59 cm from the holes so the camera could not get in the way of the sensors (150 mm high). This could have been an option but when analysing the data, it indicates it may be difficult to link both signals as it requires that the structure should persist for at least 0.59 m (~ 7δ) and according to the literature, the length of the large scale structure extends in the streamwise direction from 2δ to 20δ. Instead, two configurations with the cameras on the top were achieved; at the holes and upstream from the holes. Moreover, the fact that 5 mm from the near wall region are lost, should not affect our investigation as the interest in this study is given to large-scale structures.

In both cases, we were losing resolution as the field of view taken by the camera was two times higher in y-direction than the field of view of interest. This is due to the necessity of having to have the larger dot in our field of view for the calibration of the cameras. The larger dot surrounded by the 4 smaller dots (in the 3D calibration target, Figure 62) corresponds to the origin of the coordinate system and common points for both cameras and has to be in the field of view for the calibration of the cameras. This leaded to a larger field of view than the one of interest, 125 mm and 160 mm in the wall normal direction for the side and top configuration, respectively.

Selection of lens

The available lenses are 50 and 105 mm. The lenses were tested and examined by putting one camera at 45 degree to verify which of the lenses was more suitable.

The field of view should be 100 mm x 75 mm in *z* and *y* coordinates, respectively. Those dimensions were set as the hot-wire sensors rake dimension is 100 mm in spanwise direction and the boundary layer thickness is ranging from 65 to 75 mm at 2.2 and 7.4 m/s in wall-normal direction.

50 mm lens

A 50 mm lens was used on the top and side position of the cameras and it was shown that when using the 50 mm lens, the field of view was larger than the one we need; 160 and 280 mm in *y* and *z* direction, respectively. The cameras

could not be put closer to the calibration target on the side view due to limitation caused by the dimension of the wind tunnel. As for the top view, the *y* distance was longer in comparison with the *z* distance because the camera is rotated by 90 degrees. The dimensions of the field of view were about 180 and 130 mm in *y* and *z* direction, respectively.

105 mm lens

The field of view of the 105 mm lens with the top configuration was *y* = 153.1 mm and *z* = 95.7 mm. The field of view for the y direction was higher than the one needed 80 mm, almost double. This could affect the resolution of the camera as only half of this field of view in the *y* direction is used.

The field of view with the 105 mm lens for the side configuration, 80 mm x 160 mm in *y* and *z* directions, respectively, was close to the field of view of interest in our experiments.

In conclusion, the chosen configuration for our experiments was to put the cameras on the top wall, using the 50 mm lens. This being said, choosing a lens of longer focal length would reduce the apparent effect of any out-of-plane motions of particles in the field, but would increase the difficulty of achieving a sharp focus and make the process more susceptible to vibrations. Furthermore, since the spatial resolution is directly dependent on interrogation area width and the resolution of cameras are constant (1280x 800 pixels), the image dimensions should be decreased as much as possible to improve the spatial resolution. Based on this, the choice for our experiment was given to the cameras on the top configuration with 50 mm lens.

Appropriateness of seeding

Seeding particles should be introduced into the flow in sufficient and stable concentrations, with a spatially uniform distribution. A choice must be made between global and local seeding.

For the local seeding, the seeding was inserted to the flow from the upper wall of the wind-tunnel at about 1 m upstream of the hot-wire locations. For the global seeding, the seeding was injected from a chamber just before the fan. Both options were examined and compared.

Local Seeding

If only a restricted portion of the flow field is of interest, it may be acceptable to seed the observation area and so attain a higher concentration. It must, however, still be the objective of local seeding to seed this part of the flow uniformly. Moreover, flow disturbance must be avoided by mounting the seeding probe sufficiently far upstream of the zone of measurement or better by introducing the seeding in a settling chamber.

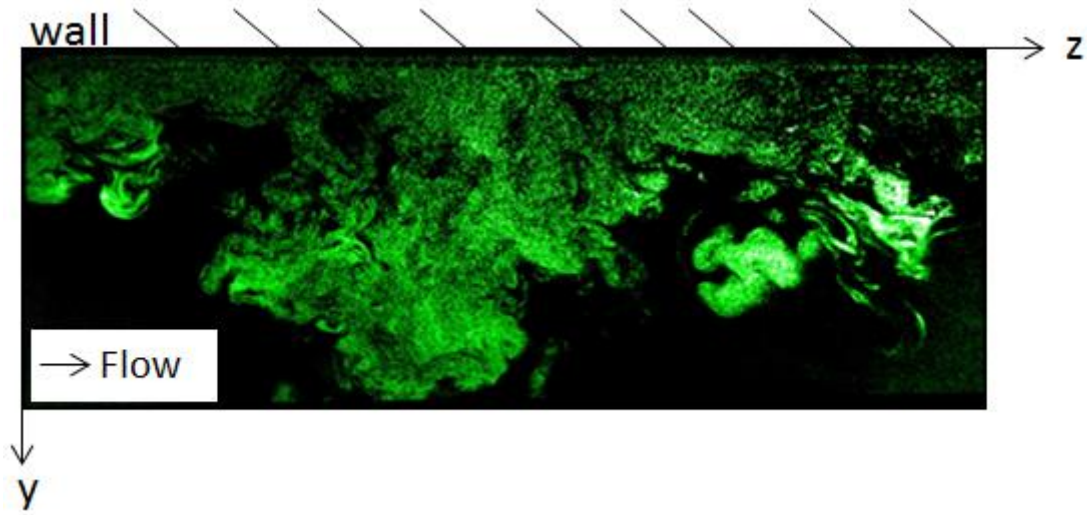


Figure 76: Flow visualisation with seeding put on top of the wind tunnel (local seeding).

It can be seen that by putting the seeding on the top (local seeding), the seeding is denser but not uniform. A uniformity of seeding on entire *y-z* plane at the flow speed at which the future experiments will be done was demonstrated.

Nevertheless, the non-homogeneous condition of the particles affects the flow as the free-stream velocity obtained with this configuration is not in agreement with the velocity reference transducer value, 4.6 m/s measured. In this case, at a distance of about 75 mm from the wall, the velocity measured with PIV is around 3.7 m/s as seen in Figure 76.

Global Seeding

Global seeding, with the particles introduced into the flow well upstream of the region of measurement, it is preferable to ensure that seeding occurs everywhere in this region, so that velocities over the whole flow field of a PIV

experiment are represented as a means of obtaining a spatially homogeneous, though necessarily rather low seeding concentration, seeding the entire flow.

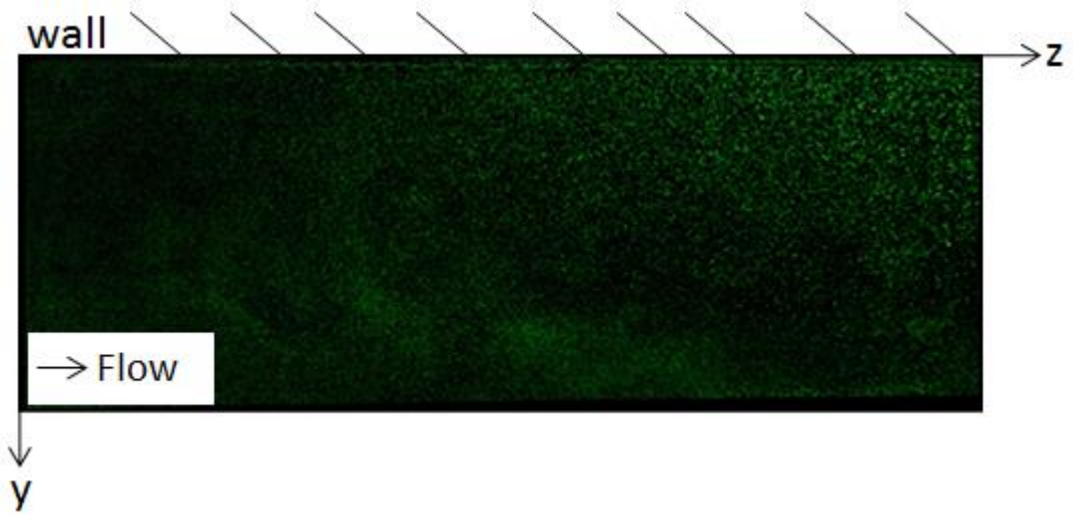


Figure 77: Flow visualisation with seeding put on back of the wind tunnel.

In this case, it can be seen that the particles were homogeneous throughout the field of view, there was a better uniformity but a lack of particle density.

At a distance of about 75 mm from the wall, the velocity measured with PIV was around 4.7 m/s which corresponds to the free-stream velocity measured with the Flow master being 4.6 m/s.

Conclusion

From Figure 76 and Figure 77, it seems that putting the seeding in the chamber gave a better seeding uniformity than putting it on the upper wall. Although it seems that the particles are denser when the seeding is placed on the upper wall in comparison with placing it in the chamber.

Finally when comparing the vector field, the uniformity in that case overcame the density as the flow is affected by the non-uniformity and gives erroneous vectors. In our experiments, the choice is given to the seeding put in the chamber just before the fan (global seeding).

Calibration

Calibration target position

The 3D calibration target had to be placed in the area of measurement where the data would be taken. In these experiments, the measurement area was set from the upper wall to the boundary layer thickness in the wall-normal direction. The target has a height of 190 mm and the wind tunnel height is about 300 mm. A lab jack was used as a stand for the calibration target. The lab jack height can be adjusted accordingly as seen in Figure 78.

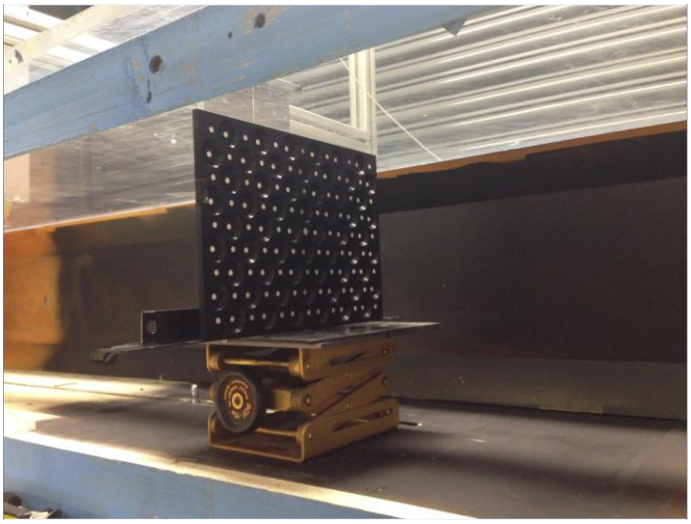


Figure 78: Stand for calibration target at holes level.

For the streamwise direction, two configurations were used. The first one was at the same position of the twenty holes where the hot-wire sensors were placed. The second configuration was 600 mm upstream of the hot-wire sensors hence the view of the near-wall region would not be affected by the holes with 12 mm thickness.

S-PIV calibration

Measurements in the *z-y* plane were conducted using stereoscopic PIV. The stereoscopic PIV system was used with two cameras. Each camera (1280x800 pixels) was used with a 50 mm Sigma f/2.0 lens. For the measurements, image pairs were taken at a frame rate of 1000 Hz with the time delay between frames being typically 200 µs.

Table 10: Fundamental quantities for the measurements using the current set up.

FOV	320 mm x 175 mm (*y, z*)
IA size	16 pixel x 32 pixel (*y, z*)
IA overlap	50%
Spatial resolution	4 x 4.6 pixel/mm (*y, z*)
Time between pulses	200 µs

The data taken with this system was processed using Dynamic Studio software. In total, 5000 image pairs were recorded and analysed, which corresponds to 5 s of data.

A 3D calibration target was put in the measurement area. Since the dots are seen by the cameras simultaneously, using the big dot as a reference, the cameras were adjusted in the streamwise and wall-normal directions in order to have the desired field of view. The field of view (FOV) was 320x175 mm, consequently the spatial resolution is about 4 px/mm (0.25 mm/px) in the wall-normal direction and 4.6 px/mm (0.22 mm/px) in the spanwise direction. This gave a spatial resolution of 2 mm x 3.5 mm in y and z direction, respectively (26 x 46 wall unit).

The cameras were positioned on the aluminium bar using the 50 mm lens at 285 mm and 280 mm from the 3D calibration target in the streamwise direction for camera 1 and 2, respectively and 230 mm in the spanwise direction.

A schematic of the experimental arrangement demonstrating the position of the cameras and laser can be found in Figure 71.

Calibrations of cameras

The angle between the two cameras is set to 90 degrees giving a viewing angle of 45 degrees for each camera. The Scheimpflug condition is adjusted with an angle of 5.5 and 8 degrees for camera 1 (back) and 2 (front), respectively.

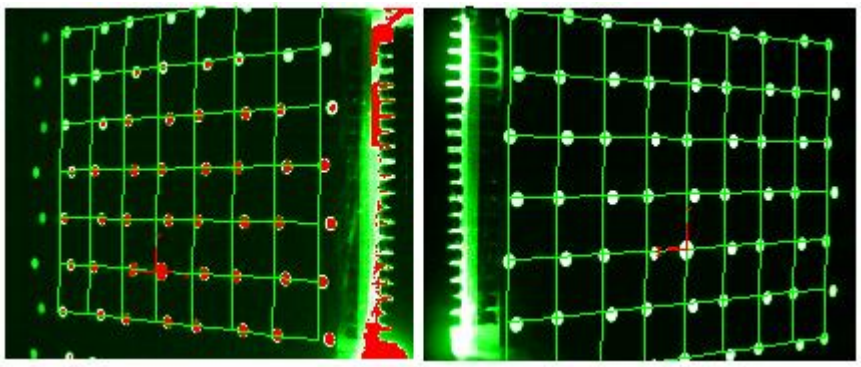


Figure 79: Imaging model for each camera. The average reprojection errors of the marked locations were estimated to be 0.244 and 0.247 pixels for the left and right camera, respectively.

All imaging model fits require images of a calibration target, which are analyzed to determine the imaging model parameters. They have a number of parameters and determining the value of these parameters in a specific image acquisition setup is referred to as "Imaging Model Fit (IMF)". These parameters are fitted to give the best possible match between corresponding coordinates in object space and image plane. The Imaging model fit method consists of two separate tasks. The first task is to identify the pixel coordinates of known points in object space. The second task is to estimate or fit the model that will transform the 3D object points to 2D image points. The first task is achieved by placing a calibration target with identifiable target markers. Dynamic Studio software automatically detects these markers in the image, but the position of the target markers (in object space) need to be known. The second task of fitting the imaging model is carried out using a modified least square method.

The calibration result was overlaid on top of a calibration image. Hereby a grid is displayed on the calibration image to show marker positions predicted by the imaging model fit and it can be verified that it matches the actual markers in the image (Figure 79).

The quality of the calculated imaging model fit is evaluated with the average reprojection error. This number describes the average pixel distance from every marker found to the predicted image location. Figure 79 shows the calibration images of camera 1 and 2 with an average reprojection error of 0.24 and 0.25 pixels for the left and right camera, respectively. The accuracy of the calibration increases as the value of the average reprojection error decreases, and normally accepted value lie below 0.5.

The calibration is successful if the following three points are fulfilled:

- The draw centre IMF marker (the red dot by default) must overlap the zero marker (larger dot). This is due to the fact that by definition the larger dot is the origin of the coordinate system (0, 0, Z) and the common fix point for the two cameras (Dantec Reference Manual). Therefore both cameras must be able to see the large dot surrounded by four smaller ones.
- The IMF grid must intersect at all the other marker positions.
- The average reprojection error lies below 0.5.

In this data set, the three points are fulfilled and the calibration is successful.

The PIV velocity vectors were computed on a 32 x 32 pixel interrogation area with a 50% overlap using the adaptive PIV technique, generating 2968 vectors per image pair. It illustrates how the resultant 3D PIV vector map are laid out after applying the stereo vector processing method. The flow field is displayed using traditional vector plots in 2D, and the scalar quantity of the out-of-plane velocity component is displayed with a scalar map and contours.

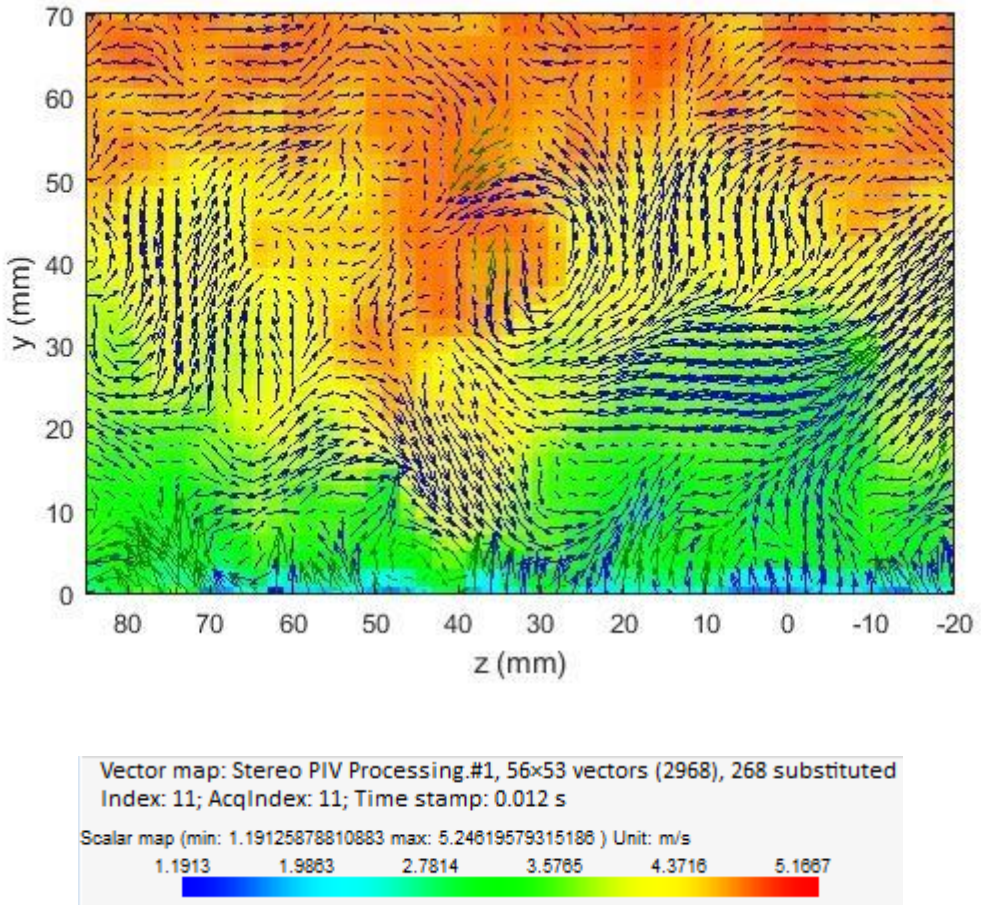


Figure 80: 3D PIV vector map obtained after stereo PIV processing. The scale below the vector map illustrates the magnitude and direction of the out-of-plane velocity component.

Figure 80 shows a 3D vector map representing the in-plane velocities *U* and *V*, while the out-of-plane velocity *W* is shown as a color-coded contour plot underneath the in-plane vectors (left image). From the out-of-plane velocity which represents the streamwise velocity component in our experiments, it can be seen that the velocity vectors value obtained are coherent and comparable with the free-stream velocity measured with the velocity reference transducer of 4.6 m/s.

3.2.2 PIV and A/D synchronisation

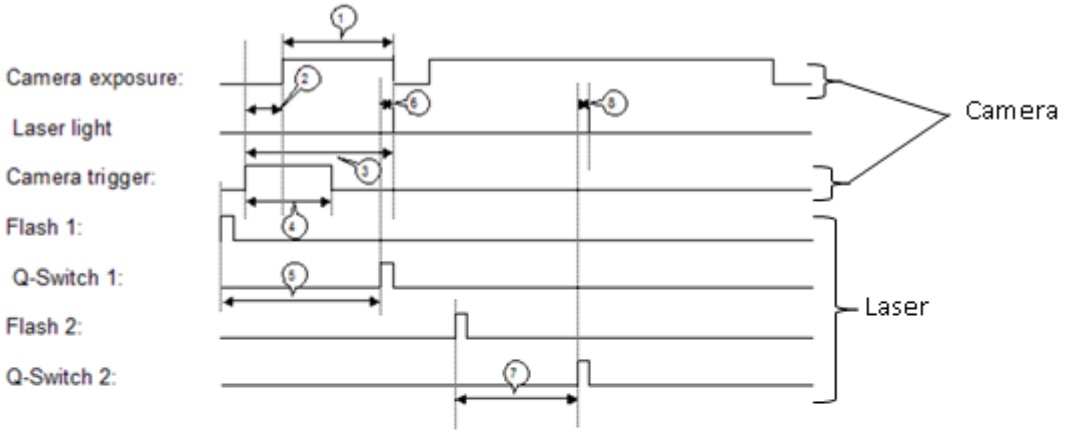
The practical requirements of the synchronization concern the correlation in the time domain of the operations of PIV and hot-wire sensors. It is important to ensure that structures detected by the PIV system are correlated to the corresponding structures detected by hot-wire sensors at the same point in

time. In order to ensure this, the PIV system must start at the same time that the hot-wire sensors data acquisition system starts, so that no delay is observed between the two. This can be achieved by time-synchronizing both measurements.

The ability for a data acquisition system to start other systems with a digital control signal is usually described as a Start Trigger Output. In our case, the specification of the control signal is 7V digital pulses. The synchronization of the analogue output and digital output tasks is done in such a way that a digital pulse is outputted exactly when the analogue signal goes above a certain level, 7V. The digital output signal is then sent to the timer box of PIV to synchronize operations between PIV and hot-wire sensors.

The digital output is integrated within the CompactRio system along with the 20 analogue input. The digital output is controlled through Labview program written by one of our researcher. Labview program is written in such a way that the DO is high (active) when ADC starts sampling.

Figure 81 and Figure 82 show the timing and connection diagrams that illustrate the synchronization between the cameras and the laser. The laser firing and the image capturing are synchronized by the control unit equipped in the Dantec system.



1. Camera exposure timer
2. Delay to open (most often in the range from 1 to 10 microseconds)
3. Camera trigger pulse start time relative to T0
4. Camera trigger pulse width (most often in the range from 1 to 10 microseconds)
5. Flash 1 to Q-Switch 1 delay (most often in the range from 100 to 200 microseconds)
6. Activation delay Q-Switch 1 (most often in the range from 100 to 200 nanoseconds)
7. Flash 2 to Q-Switch 2 delay (most often in the range from 100 to 200 microseconds)
8. Activation delay Q-Switch 2 (most often in the range from 100 to 200 nanoseconds)

Figure 81: Timing diagram of synchronization between the camera and the laser (Dynamic Studio Manual).

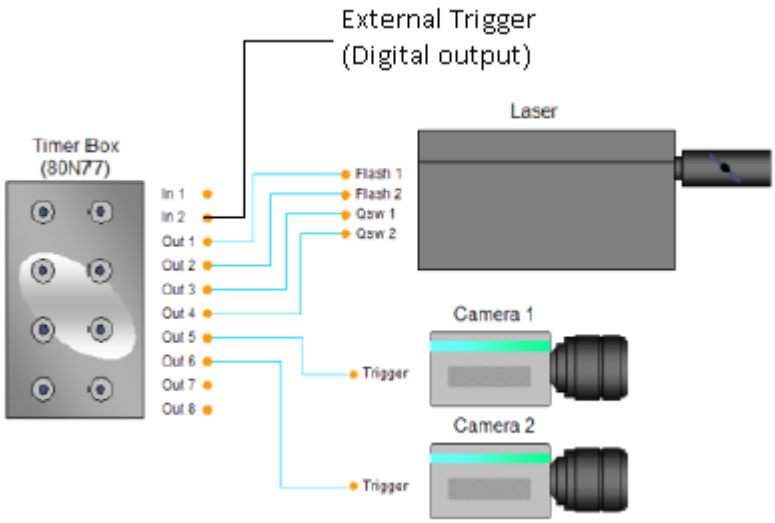


Figure 82: Connection diagram for s-PIV measurements (Modified from DynamicStudio Manual)

The connection for the synchronisation test of the PIV with the data acquisition system is explained:

- A signal generator is connected to the ADC using BNC cable,
- The digital output is connected to the timer box of PIV system and to the ADC using BNC cable

- The camera 1 trigger is connected to the ADC using a T-junction BNC cable

The digital output signal is used to send a pulse to the PIV system through the timer box which is triggered to start recording the images. The signals (Digital output and Trigger Camera 1) are sent to the ADC with the sinusoidal wave from the signal generator. A test is carried out to confirm successful synchronisation between ADC and PIV as shown in Figure 83.

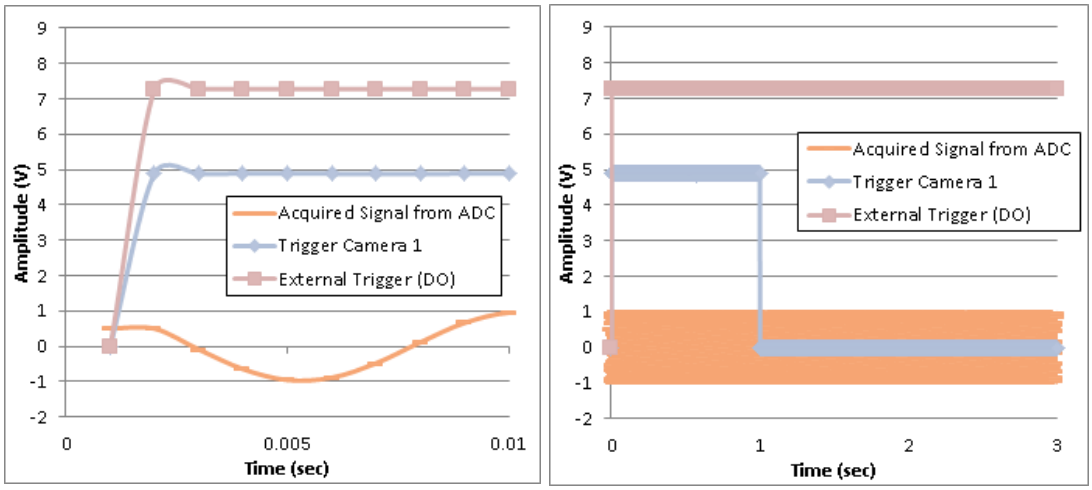


Figure 83: Synchronization test

To summarise, when the sampling of data acquisition starts, the digital output becomes active (from 0 to 7 V) as shown in Figure 83. The signal of DO is then used to trigger the PIV system hence starting recording images as shown in Figure 82 and Figure 83.

3.2.3 Sampling frequency – Reliability of the Labview program

A Labview program, of our group, sample the data from the twenty ADC. The reliability of the program was verified by sampling data from a signal generator where a sinusoidal wave of a known frequency was input to the ADC.

It can be seen in Figure 84 that for a 0.1 second sampling time, there are 10 sinusoidal waves which confirms that data were sampled at 1000 Hz for a signal generator frequency set at 100 Hz.

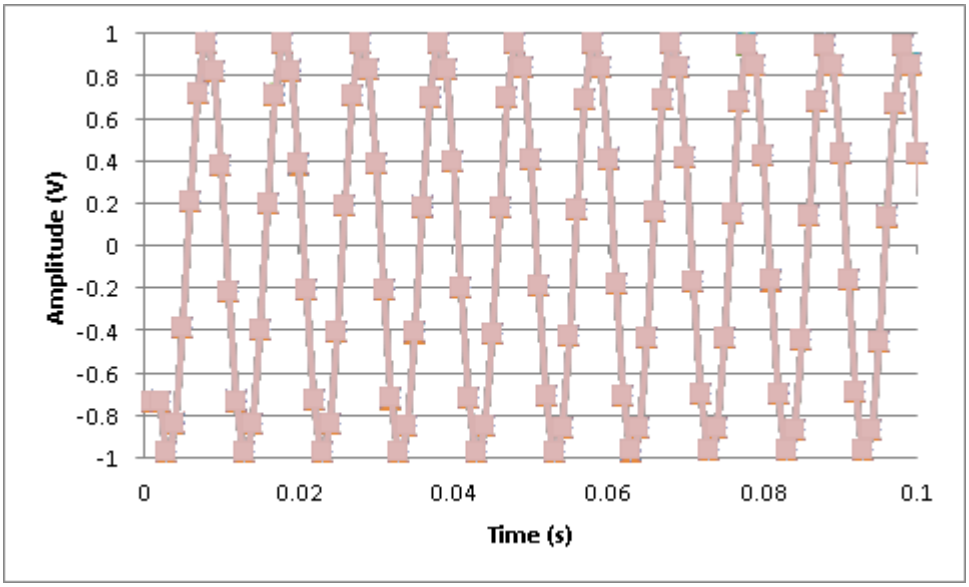


Figure 84: Signal from Signal Generator set at 100 Hz, 2Vpp sampled at 1000 Hz for 10 seconds

It is seen in Figure 84 that for a sampling frequency set at 1000 Hz and sampled for 10 seconds, 10 000 sample points are acquired. This output information also confirms that the frequency was set at 1000 Hz.

3.2.4 Chapter Summary

This chapter reviewed in details the experimental set-up used for our experiments. It first presented the wind-tunnel where all our experiment were conducted. It is then followed by a description of the hot-wire system calibrated with the power law. Errors are due to temperature compensation (1.25%), noise level (0.6%) and wall effect (at y^+ <3). The CTA board is optimised to obtain data from an array of 20 sensors put in holes drilled in the upper wall of the wind tunnel. The array of sensors were put in 4 y-positions; 0.5 mm (standard deviation = 0.08), 0.12 mm (standard deviation 0.04), ~ 0 mm (≤ 0.17 mm) and, 0 mm (< 0.17 mm). This chapters continues with a description of PIV theory and experimental arrangements. For s-PIV, the camera were put on top of wind tunnel with a 50 mm lens and global seeding is performed. It ends with an explanation of the synchronisation between s-PIV and HW systems using a digital output.

Chapter 4 Method validation

Chapter 4 validate the method employed in the experimental facility being used.

4.1 Introduction

The objective of the study described in this section was to have a full velocity profile as a reference to the measurements. As well as to obtain the turbulence statistics near and at the wall without possible wall effect as the hot-wire probe was placed underneath a 4mm-diameter hole as detailed in Chapter 3 (Figure 47).

The mean velocity as well as the turbulence intensity profiles were plotted and compared to those of Choi et al. (2009) and Kang et al. (2008). The values of skewness and kurtosis in the vicinity of the hole were to be compared with those of Laufer (1954), Alfredsson et al. (1988) and Moser et al. (1999). The traverse starting position y_0 in the vicinity of the hole leads to a vertical shift of the velocity profile that is compensated for by the post-processing. The best profile fit was then chosen and a shift was applied to the nominal y.

4.2 Turbulent Boundary Layer Profiles and Characteristics

The 55P15 hot-wire probe was put on a traverse system to obtain a full velocity profile along the wall-normal direction, y-axis, at three free-stream velocities; 2.2, 3.2 and 7.4 m/s. The measurements were typically taken at x = 3.2 m downstream of the trip device where the boundary layer was fully developed with a turbulence intensity (u'/U_∞) of approximately 0.7% measured in the centre of the wind tunnel using velocity reference transducer for the calibration and multi-channel CTA unit. The hot-wire sensor is calibrated in situ against a Dantec 54T29 velocity reference transducer at free stream velocities ranging from 0.7 to 7.8 m/s. The value found for the turbulence intensity with Pitot tube for the calibration and multi-channel CTA unit was 0.3%. The turbulence intensity seems in good agreement with Kang and Choi's (2008) result of 0.3% at 2.42 m/s and x = 2.37 m. For the velocity profile, 127 y-locations (from 1 to

127, location 1 referred to the first point in the hole from the velocity profile followed by 126 locations) were taken and each of these locations was sampled for a period of 50 seconds at a frequency of 1 kHz from within the hole (Figure 47) to a wall-normal position, y, of 150 mm away from the upper wall. A trial and error is applied by plotting the velocity profiles with several values for y_0 (wall position).

4.2.1 Mean and statistics profiles

4.2.1.1 Mean and statistics profiles at 2.2 m/s, $Re_T = 423$

Data have been computed, tabled and plotted to examine the value of the Skewness, Kurtosis, rms velocity and velocity near the wall.

As said earlier, King's law calibration curve was used for presenting the velocity profiles. The mean velocity profile is graphed on Figure 85, using logarithmic axes. The logarithmic portion of the profile appears linear on the logarithmic axis. By fitting the logarithmic portion of the profile, we can estimate the friction velocity, u^* (p.53). The red line is the log-linear fit to the velocity profile. Note that u* was estimated using Clauser method (explained in p. 53). The profile were plotted by varying y_n and u^* values until the satisfactory mean velocity profiles were obtained. If u^* is reduced, the values of the mean velocity are increasing and the profile is shifted upward. When u^* value is increased, the opposite trend happens.

The points near the wall ($y^+ < 4$) affected by the wall effect do not follow the laminar sub-layer profile $u^+ = y^+$. It is also due to the lack of calibration accuracy at low velocity (< 0.2 m/s). Indeed, the curve fit error for $0.68 < U < 1$ m/s was found to be up to 5% representing the difference in velocity measured from the velocity reference transducer and the estimation from the King's law curve fit (see calibration section p. 35). The calibration is done within the velocity range of 0.68 – 8 m/s (which corresponds to $u+ = 7.23$ to 85), the values below 0.68 m/s were extrapolated from the curve fit. Therefore, the mean velocity profile at low velocities is accurate at 5% for velocity ≥ 0.68 m/s. The focus is then given to two regions of the mean velocity profile to be compared with our data, at around $y^+ = 10$, in the buffer region and log region.

By referring to the mean velocity profile plot, the probable wall position is situated between y_n = 1.11 mm and y_n = 1.41 mm (pt 71) as the profiles follow the logarithmic tendency.

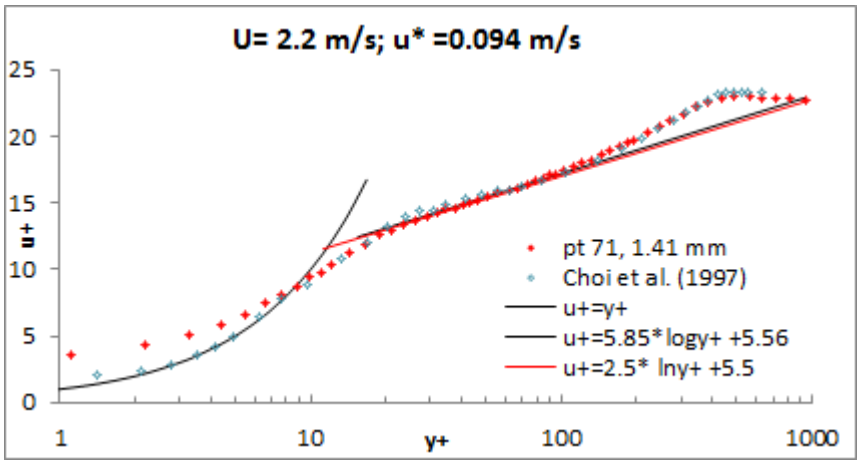


Figure 85: Mean velocity profile, *u*+ vs. *y*+ at a free-stream velocity of 2.2 m/s at x=3.2 m.

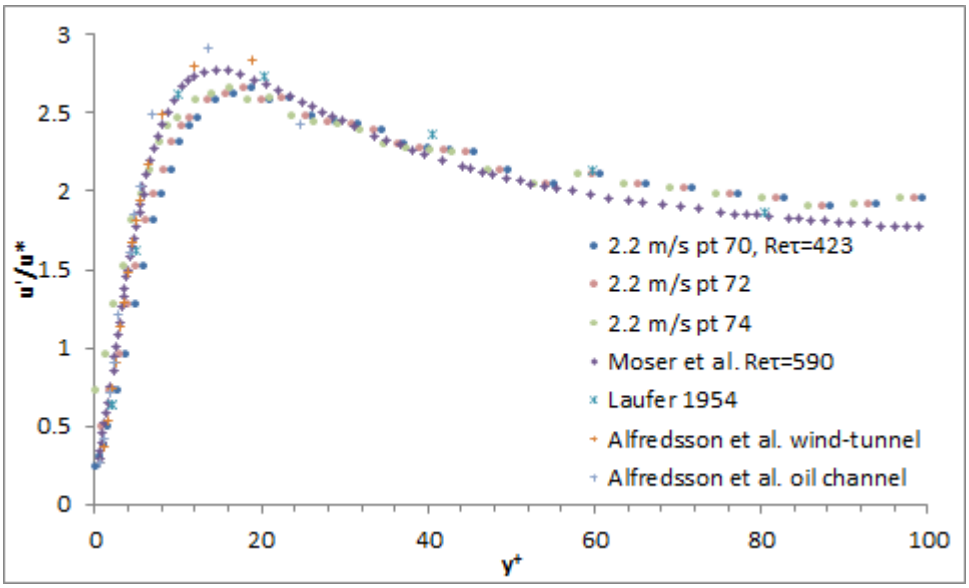


Figure 86: Turbulence intensity profile at 2.2 m/s.

The graph in Figure 87 represents the skewness and kurtosis at the same free-stream velocity of 2.2 m/s (Re_λ = 423) versus the wall distance wall units.

Two points to take into account for the skewness and kurtosis:

- Their values at the wall are constants (Alfredsson et al. 1988) independently of the free-stream velocity, and Reynolds numbers.
- Their quantities are at their maximum closest to the wall while decreasing with an increase in *y* (further away from the wall).

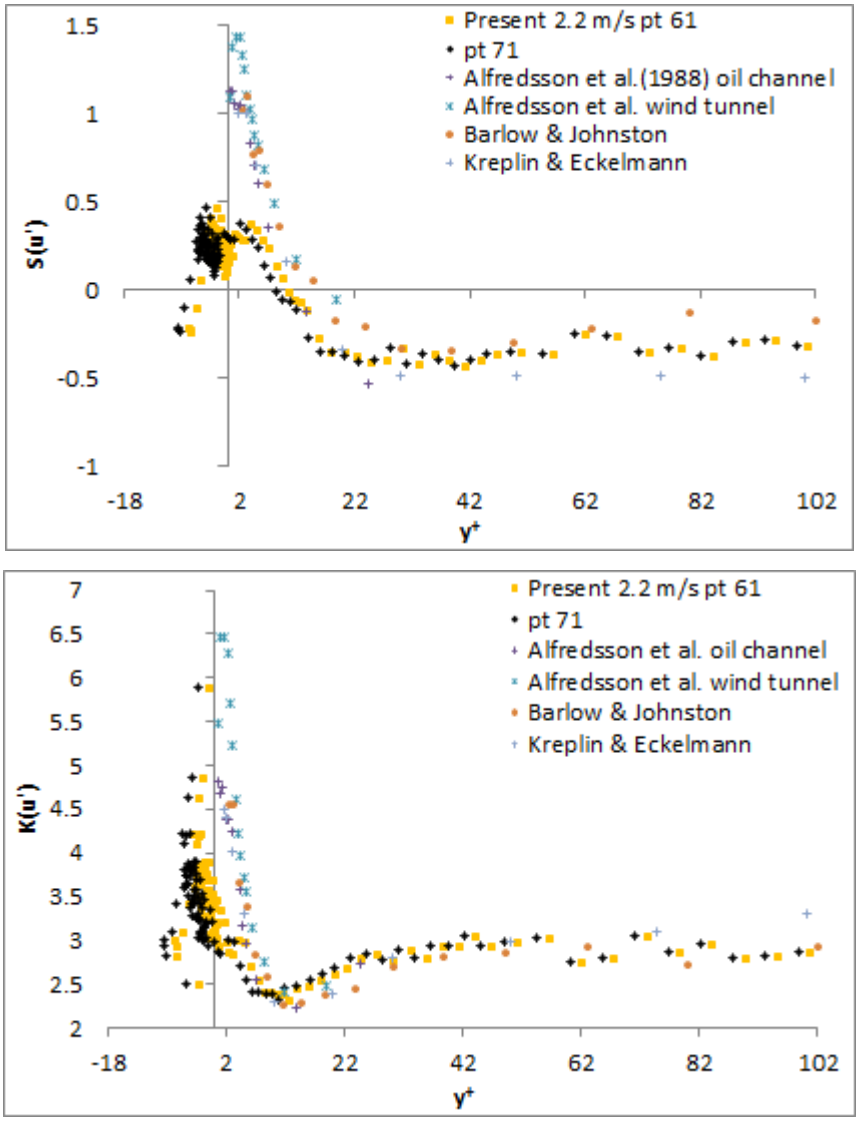


Figure 87: Profile of 3rd and 4th moment at *x* = 3.2 m from the inlet of the test section. The x-axis represents the nominal y (y_n) and the y-axis represents skewness and kurtosis factors Reτ = 423.

S and *K* values are reducing as y^+ is increasing from the nominal *y* = 1.4 mm where a peak value is observed for both factors. At this nominal position (y_n = 1.4 mm) estimated to be the equivalent wall position, the skewness and kurtosis values were 0.32 and 3.3, respectively. Those values seem to differ with the literature (Alfredsson et al. 1988) where it is suggested that the skewness and kurtosis should be 1 and 4.8 respectively, 75% and 26% of difference, respectively. This is due to the hole effect explained in page 58.

At Re_λ = 423, it is found that u^* = 0.094 m/s and the probable wall position is at y_n = 1.4 mm (point 71).

The mean velocity profile seems to be in good agreement from the profiles of Choi (2009) and Kang (2008) , who performed their experiments in the same wind-tunnel.

4.2.1.2 Mean and statistics profiles at 3.2 m/s, Re_τ = 568

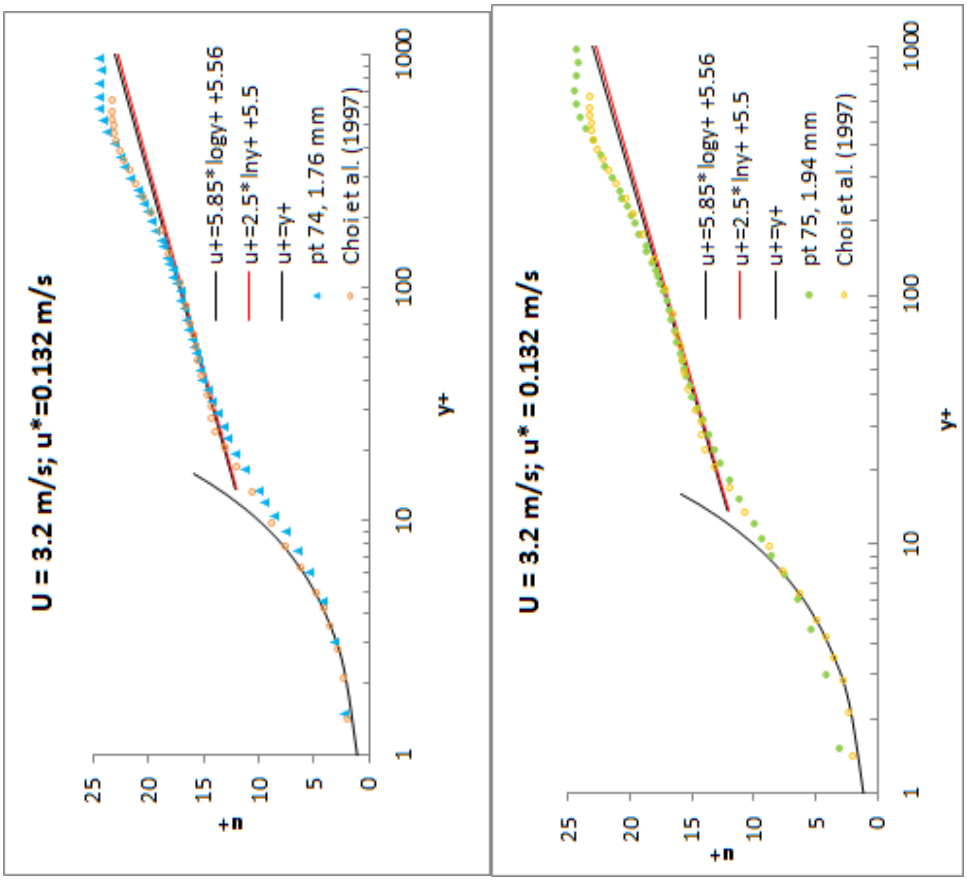


Figure 88: Mean velocity profile at U_∞=3.2 m/s, Re_τ=587 with different possibilities of y^+=0 to find the wall position.

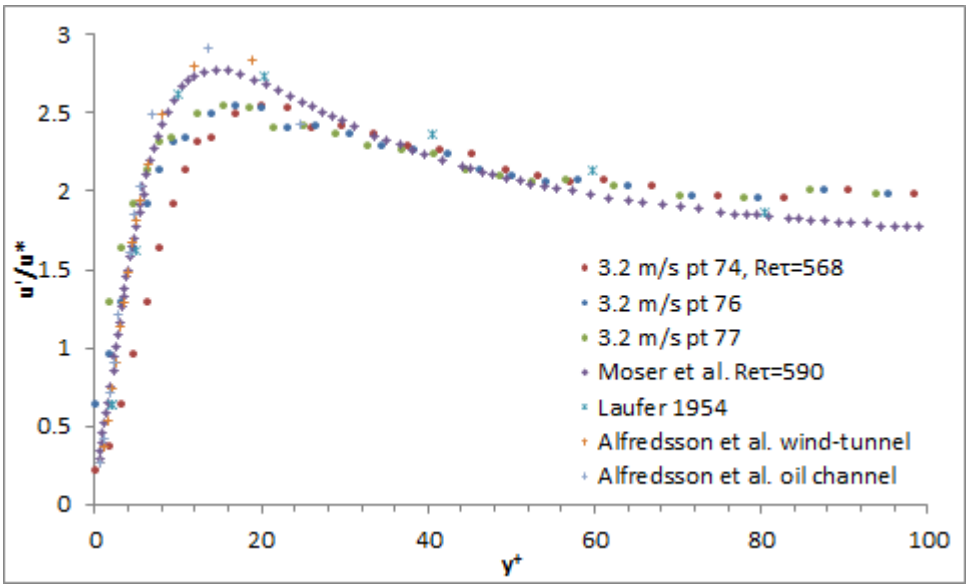


Figure 89: Turbulence intensity profiles at 3.2 m/s in comparison with others.

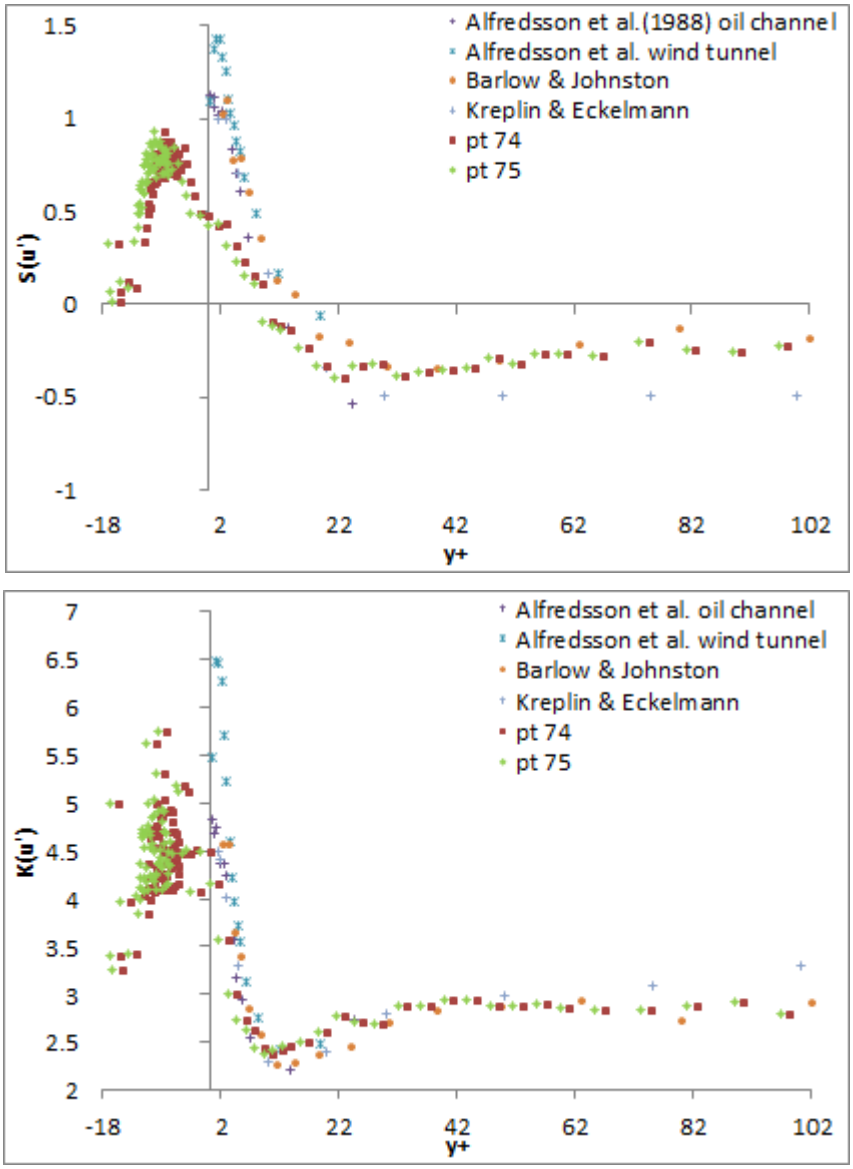


Figure 90: Profile of 3rd and 4th moment at *x* = 3.2 m from the inlet of the test section. The x-axis represents the nominal y^+ (y^+_n) and the y-axis represents skewness and kurtosis factors for Re_τ = 568.

From Clauser fit, u^* is found to be equal to 0.132 m/s. From Figure 88, it can be said that the velocity profile that best fit Choi's (2009) and Kang's (2008) profiles is when $1.76 < y_n < 1.94$ mm (points 74 and 75). At this y_n position, the skewness value seems to fall around 0.48 and the kurtosis around 4.5. It seems that the values for S and K are in better agreement with Alfredsson et al. (1988) in comparison with the values at Re_τ = 423. A value of 0.48 against 1 for skewness and 4.5 against 5 for kurtosis is found between our experimental S and K factors and those of Alfredsson et al. (1988).

4.2.1.3 Mean and statistics profiles at 7.4 m/s, Re_τ = 1310

We can see a small linear region from *y*=0.9 to 1.6 mm.

In terms of mean velocity profile, point 35 (0.85 mm) seems to be a good match for the probable wall position. As at this position, the mean velocity profile is in good agreement with Kang's (2008) profile.

A trial and error is applied by plotting the velocity profile with several values for y_0 (wall position) ranging from 0.85 to 0.93 mm (point 35 to 43).

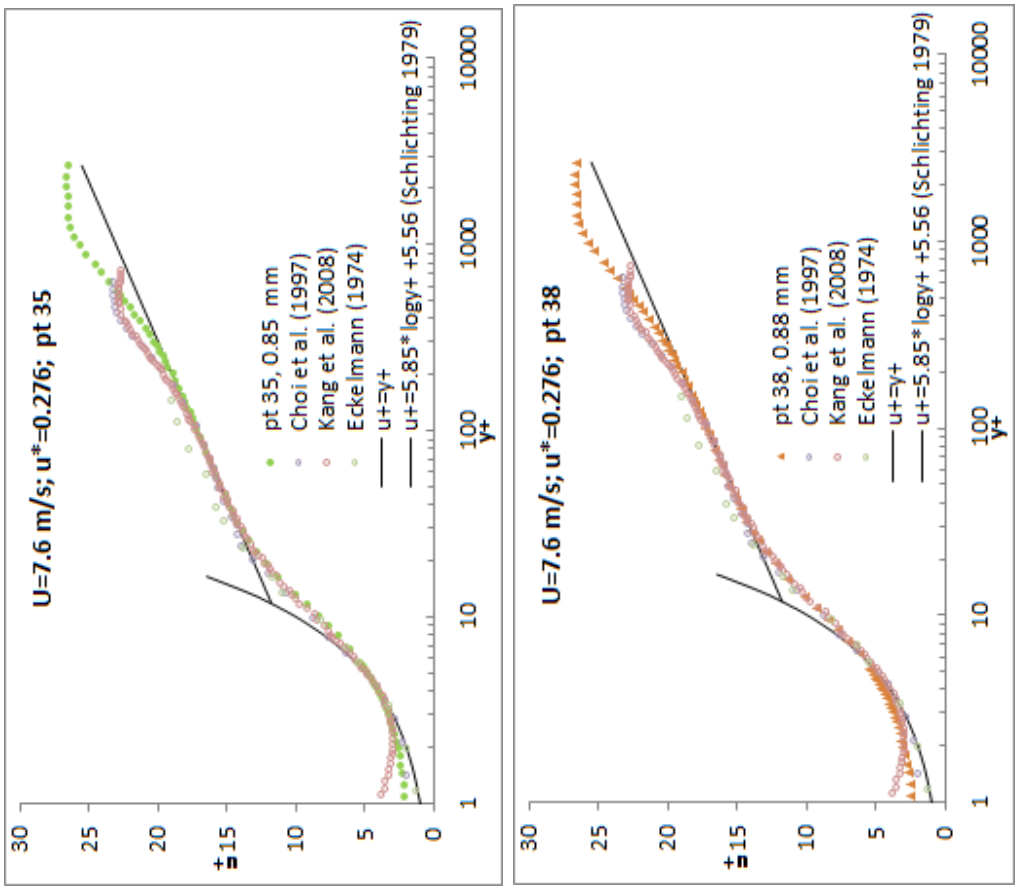


Figure 91: Mean velocity profile at U_∞ = 7.4 m/s, Re_τ = 1310 with different possibilities of *y* = 0 to find the wall position.

u^* is found to be 0.276 m/s at 7.4 m/s. It seems that point 35, y_n = 0.85 mm, is a good compromise for the probable wall position as the mean velocity profile seems to be in very good agreement with Kang's (2008) profile.

Kurtosis stabilisation region extends from 0.84 to 1.05 mm and skewness from 0.63 to 0.99 mm. Values for skewness and kurtosis found at that free-stream velocity of 7.4 m/s seem in good agreement with Alfredsson et al. (1988).

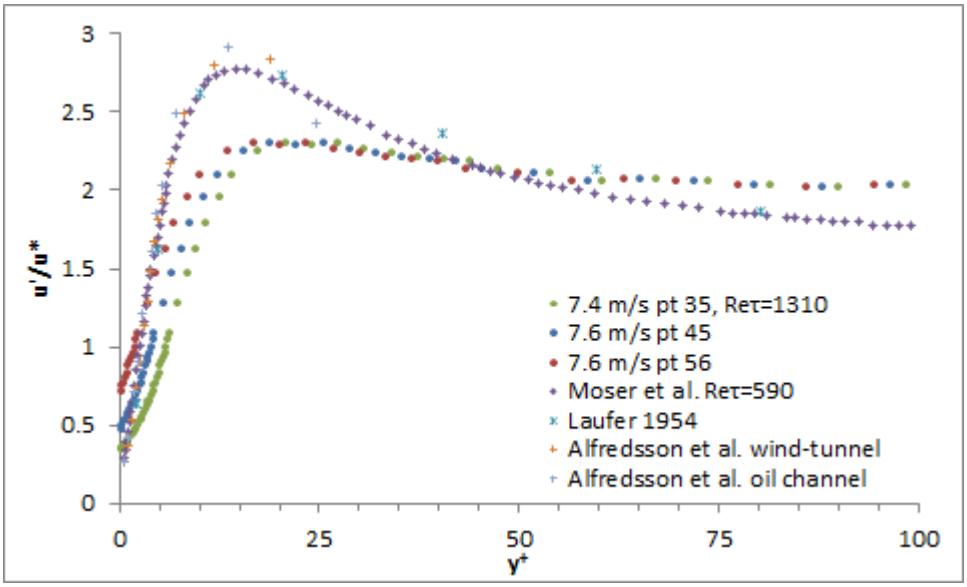
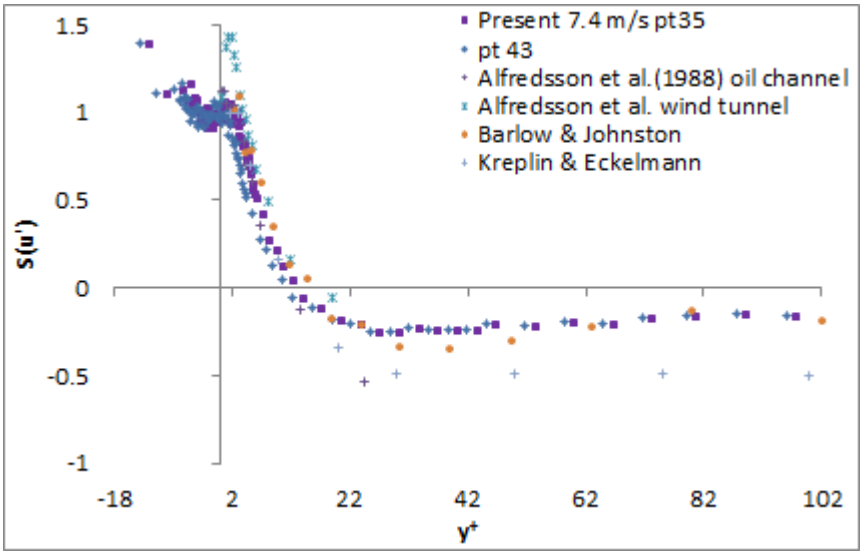


Figure 92: Turbulence intensity profiles at 7.4 m/s in comparison with others.



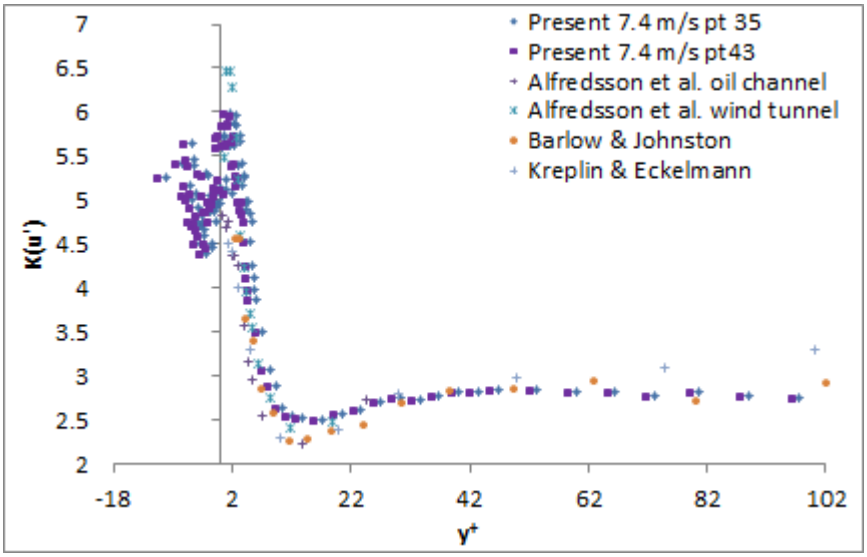


Figure 93: Profile of mean, 2nd, 3rd and 4th moment of the velocity at x = 3.2 m for U_∞ = 7.4 and Re_τ = 1310.

4.2.2 Turbulent Boundary Layer Characteristics

At three free stream velocities of 2.2, 3.2 and 7.4 m/s, the boundary layer thickness, δ at the measuring station increases from 67 mm for 2.1 m/s to 75 mm for 7.4 m/s. The friction velocity, u^*, is estimated from experimental data using Eq. (6), i.e. by the application of a Clauser (1954) chart fit with log-law constants κ (the von Karman constant) = 0.41 and B = 5.0, perhaps the most often cited values for a smooth wall, zero pressure gradient boundary layer although other values are often used as well (Coles, 1969).

With the friction velocity, u^* = 0.094 to 0.276 m/s, the friction Reynolds number, defined as $Re_\tau = u^* \delta / \nu$, where u* is the friction velocity, δ is the boundary layer thickness and ν is the kinematic viscosity of air, ranges from 423 to 1310 (Table 11).

Table 11: Turbulent Boundary Layer Characteristics

U_∞	I	Re_τ	δ	u^*	y^+	y^+
(m/s)	(%)	(/)	(m)	(m/s)	(/)	(/)
2.2	0.76	423	0.067	0.094	0.93	3.1
3.2	0.74	568	0.067	0.131	1.33	4.4
7.4	0.68	1310	0.075	0.276	2.87	9.6

A velocity reduction leads to a decrease of the boundary layer thickening, as shown in Table 11.

4.3 PIV validation

The principal objective of this work is to explore the structure of the outer region using PIV to obtain images of the velocity field. PIV data are less ideal for statistical analysis because it is laborious to obtain and analyse the large number of photographs needed for good statistical stability of the averages. The present PIV technique typically limits the number of practically obtainable photographs.

4.3.1 Boundary layer

The inner-variable scales were determined by estimating the friction velocity (u^*) using the Clauser chart method (Clauser 1956).

Figure 94 shows the mean streamwise velocity profile estimated by ensemble averaging the instantaneous velocity vector fields over 2000 instantaneous photographic realizations as well as the data obtained with hot-wire at 3.2 m/s, Re_τ = 568. The friction velocity, u* from 2D PIV was estimated and found to be 0.155 m/s. For HW experiments, the friction velocity is measured at Re_τ = 423, 568 and 1310. A rough estimation was obtained from the results obtained at Re_τ = 568 and 1310. The estimation of the friction velocity at Re_τ = 695 from HW was equal to 0.178 m/s. There is a difference of 13% between the friction velocity of 2D PIV and HW.

Table 12: Characteristics of the turbulent boundary layer measured with 2D PIV

U_∞ (m/s)	δ (mm)	u^* (m/s)	Re_τ
4.6	66.5	0.155	695

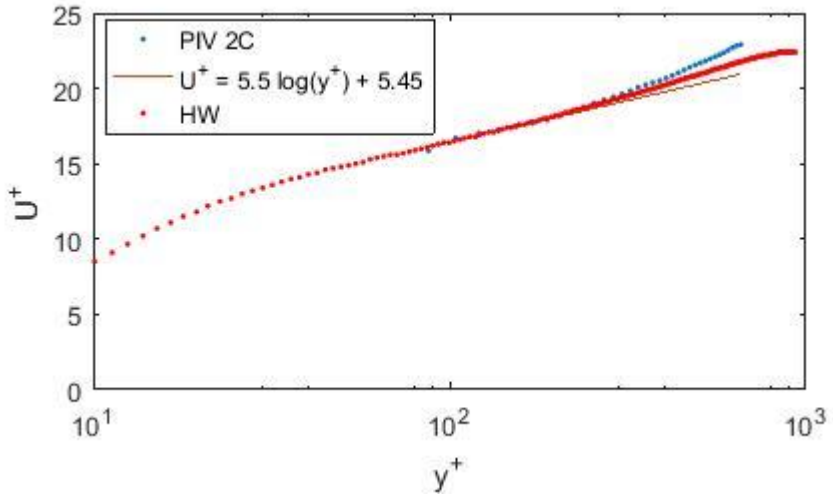


Figure 94: Mean streamwise velocity profile

Figure 94 demonstrates that only the upper end of the log region has been captured by the present results. This is due to the main interest being large-scale structures in the outer region of the boundary layer, which requires a large field of view, and thus sacrifices high resolution near the wall. The mean velocity profiles show the expected logarithmic behaviour for $30y* < y < 0.25\delta$.

4.3.2 Identification of hairpin structures through hairpin signature in x-y plane

The measurement heights extend from about y^+ = 100 to the boundary layer thickness. The instantaneous velocity fields are obtained using PIV in streamwise/wall-normal *x-y* plane. There is significant evidence that in the logarithmic region and beyond, the turbulent boundary layer contains many hairpin-shaped vortices (with one or two legs). The term hairpin vortex, is here taken to represent horseshoe, cane, hairpin, or omega-shaped vortices. A cross-section of three dimensional structures can be viewed via planar PIV data if the laser sheet cuts the mid-plane of the structures. A technique similar to that of Adrian et al. (2000) is used to identify the presence of hairpins and hairpin packets in the present study.

It is necessary to determine how three dimensional coherent structures can be recognized from two dimensional experimental results acquired via PIV measurements. In planar PIV, identification of these vortices typically requires identification of hairpin vortex signatures: in the case of *x-y* plane data, the 2D (2 dimensions) velocity vector pattern created when the measurement volume slices between vortex legs. The signature of the instantaneous velocity field induced by a hairpin vortex which crosses a streamwise/wall-normal plane is also shown in Figure 95 using our PIV data. So the instantaneous velocity pattern in a streamwise/wall-normal cross-section of the hairpin, and in a frame moving with the hairpin, contains the following features:

1. A spanwise vortex core rotating in the same direction as the mean velocity circulation (in direction of flow field) and considered to represent the head of the hairpin. Note that vorticity is not convenient for identification of vortices as it cannot distinguish between pure shearing motion and the swirling motion of a vortex;

2. A region of second-quadrant ejections: $u < 0$, $v > 0$ which is located below and upstream of the vortex head. This ejection event is caused by vortex induction from the legs and the head of the hairpin.

3. A fourth-quadrant region ($u > 0$, $v < 0$) is habitually found to face the second-quadrant event from upstream, as can be seen in Figure 95.

The sharp frontier between the Q2 and Q4 events consists of a stagnation point that resembles a stationary point and an inclined shear layer.

Figure 95 shows as an example numerous vortex cores, which are interpreted to be the heads of hairpin vortices as they contain the 3 features described. Those features are put and shown in Figure 95. The hairpin properties which have been found experimentally in the present work are qualitatively comparable with those found in the works of Adrian (2000) and others (Zhou et al., 1999). Many of these 3D structures, which are randomly located in the boundary layer, cross the laser sheet of the PIV system which was set in a streamwise/wall-normal *x-y* orientation. These structures leave signatures in the measured instantaneous velocity fields. It is important to mention that based on this planar information, we cannot distinguish between symmetric or asymmetric hairpin vortices, nor can we distinguish between omega shape vortices, cane shape vortices, horseshoe vortices and hairpins. So in this study, a hairpin vortex can be symmetric or asymmetric and narrow or wide.

Investigation of the instantaneous velocity fields show that the boundary layer is densely populated with velocity signatures associated with hairpin vortices. In 36% of all examined PIV data, vortex head have hairpin signature. A primary conclusion drawn from the present experimental observations is that hairpin vortex signatures occur very frequently in and beyond the logarithmic region of the turbulent boundary layer.

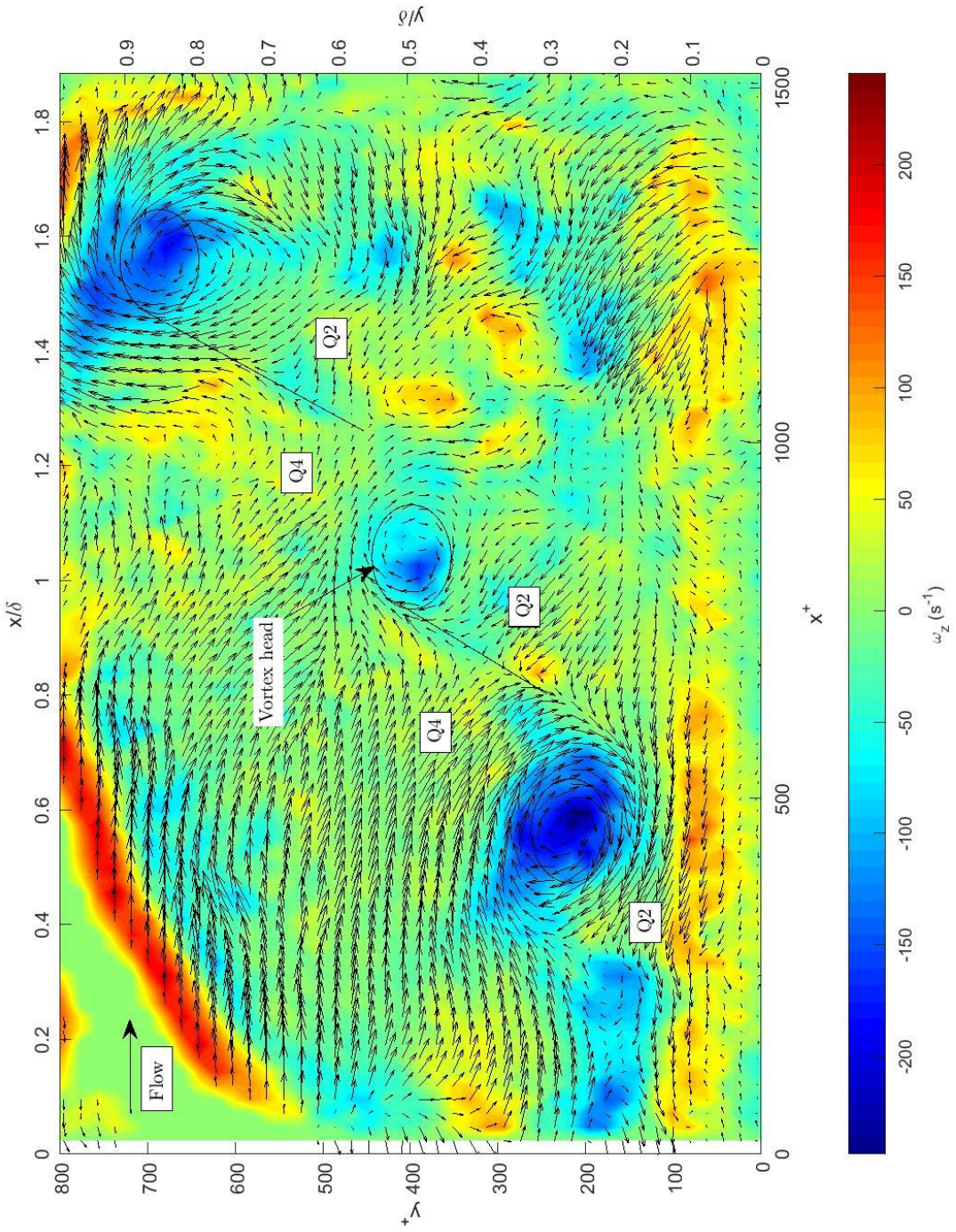


Figure 95: Single hairpin vortex signature in the streamwise-wall-normal plane from fluctuating velocities

4.3.3 Hairpin Detection Method

Various tools and algorithms have been developed and proposed by many investigators for the identification of vortices. It is worth defining the term vortex by referring to Kline et al. (1994): “A vortex exists when instantaneous streamlines mapped onto a plane should to the core exhibit a roughly circular or spiral pattern, when viewed in a reference frame moving with the centre of the vortex core”. As for vorticity, ω, it is defined as the curl of the velocity vector:

$$\omega \equiv \nabla \cdot u \tag{18}$$

The traditional technique to identify vortices employs the iso-surface of vorticity magnitude (Kim et al., 1987). Local methods were developed recently where according to a criterion based on the point values, each point can be classified as inside or outside a vortex. The most widely used local methods for vortex identification are based on the kinematics implied by the velocity gradient tensor, ∇u. Depending on the method, the local criteria is based on the variable:

- λ_2 (Jeong and Hussain, 1995),
- Δ (Karniadakis, 2003), they used the regions of complex eigenvalues of the velocity gradient tensor for vortex identification
- Q (Choi et al., 1997),
- λ_{ci} (Zhou et al., 1999), they followed the work of Perry et al. (1990) in their general classification of the three-dimensional velocity field around a critical point. Zhou and co-workers have used the iso-surfaces of the imaginary part of the complex eigenvalue of the local velocity gradient tensor (λ_{ci}) to visualize vortices in a turbulent channel flow.

These methods automatically eliminates regions having vorticity but no local spiralling motion, such as shear layers, while it is the most important challenge in the traditional technique that employs the iso-surface of vorticity magnitude.

Figure 96 shows an example of vortex identification using an instantaneous velocity field in the z-y plane detected via the mentioned techniques. It can be seen that the $\lambda 2$, Q, λci field are contaminated with noise associated with

differentiation of the PIV velocity data. It contains many regions of concentrated vorticity. Some of the weaker fluctuations may be noise in the vorticity measurements, so we will concentrate on the strongest regions only.

It is worth mentioning that what are truly measured are not streamwise vortices but rather turbulence vortices with a streamwise vorticity component. In other words, the presented streamwise vortices here are the cross sections of three dimensional turbulence structures in spanwise/wall-normal plane.

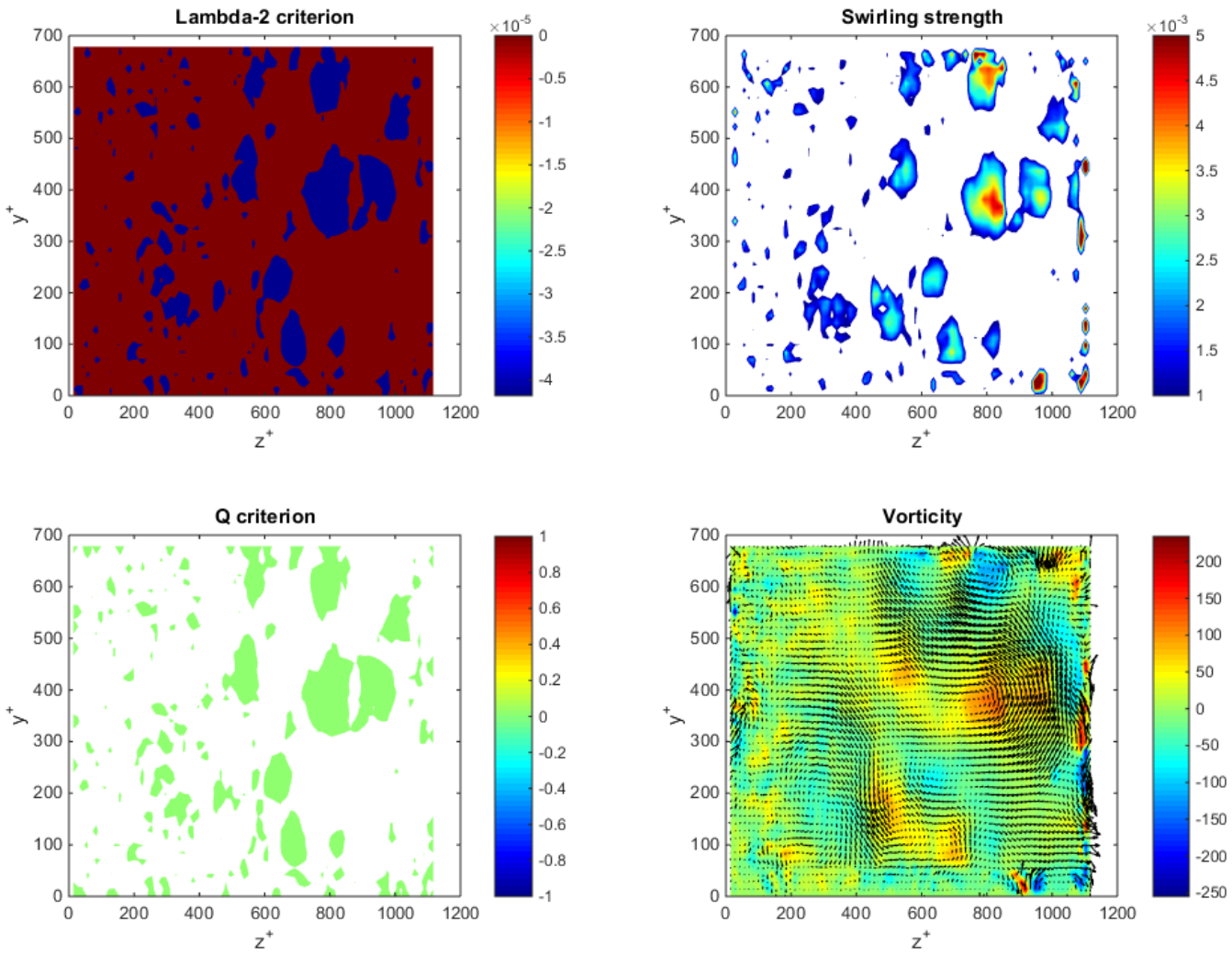


Figure 96: Example of vortex identification and extraction in an instantaneous, two dimensional PIV velocity field

4.3.4 Hairpin vortex packets in x-y plane

The technique used to detect the presence of hairpin packets in the present study can be summarized as follows:

First, all spanwise vortices are identified using the calculated swirling strength. The swirling strength criterion is defined as the imaginary part of the complex eigenvalues of the velocity gradient tensor to visualise vortices (Zhou et al., 1999). For planar calculation, the formula is simplified as velocity gradient in z-direction is set to zero as they are not available in our 2D experiment. The simplified formula (Adrian et al., 2000b) is given as follow:

$$\lambda_{ci} = \frac{1}{4}\left(\frac{\partial U}{\partial x}\right)^2 + \frac{1}{4}\left(\frac{\partial V}{\partial y}\right)^2 - \frac{1}{2}\frac{\partial U}{\partial x}\frac{\partial V}{\partial y} + \frac{\partial V}{\partial x}\frac{\partial U}{\partial y} \quad (19)$$

The vortices are found everywhere and some of them are hairpin heads. Then it must be determined which identified vortices are hairpin vortices.

A series of three or more spanwise vortices in close spatial proximity to each other are potential to be considered a hairpin packet. Although a series of two hairpins could probably form a hairpin packet, hairpin packets with three or more hairpins avoids random positioning and undesired parameter determination.

Finally, the selected vortices are analyzed to determine if they are part of a velocity signature typical of a hairpin. The simplest possible approach for the present *x-y* plane PIV data is to perform Reynolds decomposition of the instantaneous velocity vector fields. Reynolds decomposition is the traditional technique for decomposing turbulent velocity fields. In this method the decomposed vector patterns are obtained by subtracting the long-time averaged velocity field from the instantaneous velocity field.

The local maximum of swirling strength was used within a series of three or more vortices in close spatial proximity to each other in the streamwise direction to detect hairpin packets.

The velocity-vector map is shown in Figure 97. Four vortices are located in the range $175 < y^+ < 800$, with streamwise spacing of 325–467 viscous wall units. Three of those spanwise vortices possess the characteristics of a hairpin vortex signature. The fact that all of the vortex heads are nearly circular means that

they are being viewed in a frame that is moving with the convection velocity, U_c of the heads. Put another way, each of the heads circled in Figure 97 is moving at approximately identical U_c with U_{c2} = 3.6 m/s, U_{c3} = 3.2 m/s and U_{c4} = 2.9 m/s, i.e. the four hairpins are moving together as a packet. The velocity for each hairpin head was obtained from the fluctuating velocity map by dividing the distance covered by the hairpin head within a period of time ($\Delta x/\Delta t$) from several images containing the heads of hairpin. The inclined shear layers associated with the vortices are identified visually as the locus of points across which the vector direction changes abruptly. They are indicated by solid lines.

Examination of several instantaneous velocity-vector fields reveals that it is common to see multiple hairpin vortices in close spatial proximity to each other in the streamwise direction and convecting with nearly the same velocity. In fact, we found at least one hairpin vortex packet in 88% of all examined PIV data. Figure 97 illustrates examples of hairpin packets. As mentioned before, a minimum of three hairpin vortices in close spatial proximity to each other is necessary for us to define it as a packet.

It is worth mentioning that the streamwise spacing between vortex structures in our data are larger than those given by Adrian et al. (2000),where vortices are located in the range $80 < y^+ < 140$, with streamwise spacing of 120–160 viscous wall units.

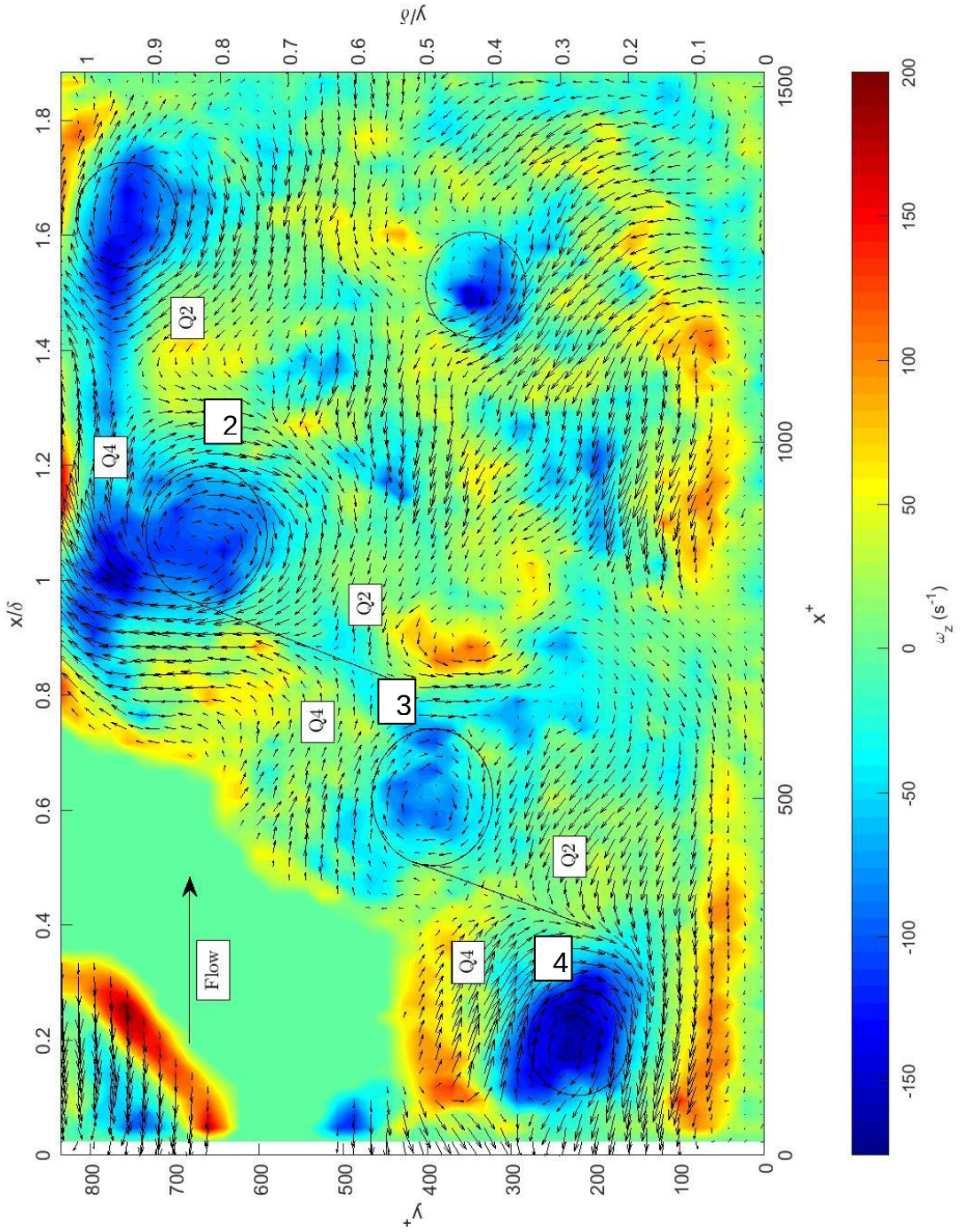


Figure 97: Packet of hairpin vortex with signature in the streamwise-wall-normal plane from fluctuating velocities

4.3.5 Large-scale structures using PIV

A 3D (3 dimensions) view was obtained from the 2D (y-z plane) fluctuating velocity maps by applying Taylor's hypothesis with a convection velocity of 13u* (2D data are projected in time as x). Afterwards, the swirling strength was calculated and the results were presented in 3D by applying iso-surface.

The flow direction in Figure 99 is from x^+ = 2500 to 0 (from top to bottom). It is hard to identify hairpin like structures. There are few streamwise vortices which might be the legs or necks of hairpins but using only 2D PIV it is difficult to see them clearly. Also considering the size of large scale structures we are interested in with length from 2δ to 20δ. Longer data are needed to analyse the reproducibility and the consistence. Furthermore it is difficult to associate the legs and necks with their counterparts as the spanwise vortices representing the head of the hairpins to link/relate them and they are missing because we only have 2D information. This being said, Figure 99 to Figure 102 gives us a good preliminary results as hairpin like structures.

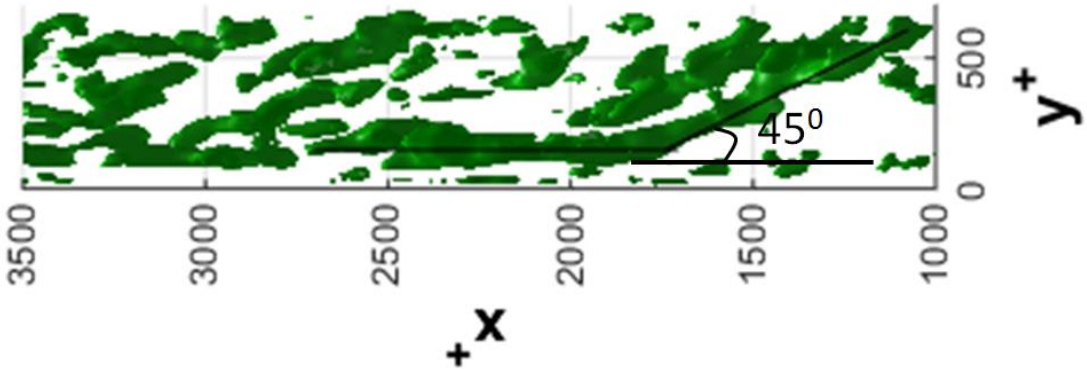


Figure 98: Hairpin structure identification in x-y plane from iso-contour

Figure 98 exhibits a pattern that elongates from the wall and expands at an angle of 45 degree from the wall with a total length of approximately 1500 wall unit. The same patterns are seen in Figure 100, Figure 101 and Figure 102, the size of the hairpins is found to be 1500 in the streamwise direction from the x-y plane images. The x-z plane illustrates the width of the hairpins of size approximately up to 125 wall unit in the spanwise direction, this is similar for all our experimental illustrations. A 3D view is also documented to confirm the findings (Table 23). The similarities between our results and the hairpin signatures of Zhou and co-workers also provide a strong basis for associating

the two-dimensional velocity patterns with three-dimensional hairpin vortex signature.

Table 13: Near-wall structures frequency of streamwise and spanwise length at Reт = 568

Re_τ	568	
	wall unit	%
x	1500	58
z	125	77

Although more complicated, these arrangements are broadly consistent with the instantaneous velocity realisations for channel flows observed by Adrian et al. (2000), Christensen & Adrian (2001) and other researchers. Figure 99 to Figure 102 show long vortex structure in 3D view as well as x-y and x-z planes. From all of our data, the longest vortex structure that have been observed is about x^+ = 1500 and about 1.2δ to 2.5 δ at Re_τ = 568.

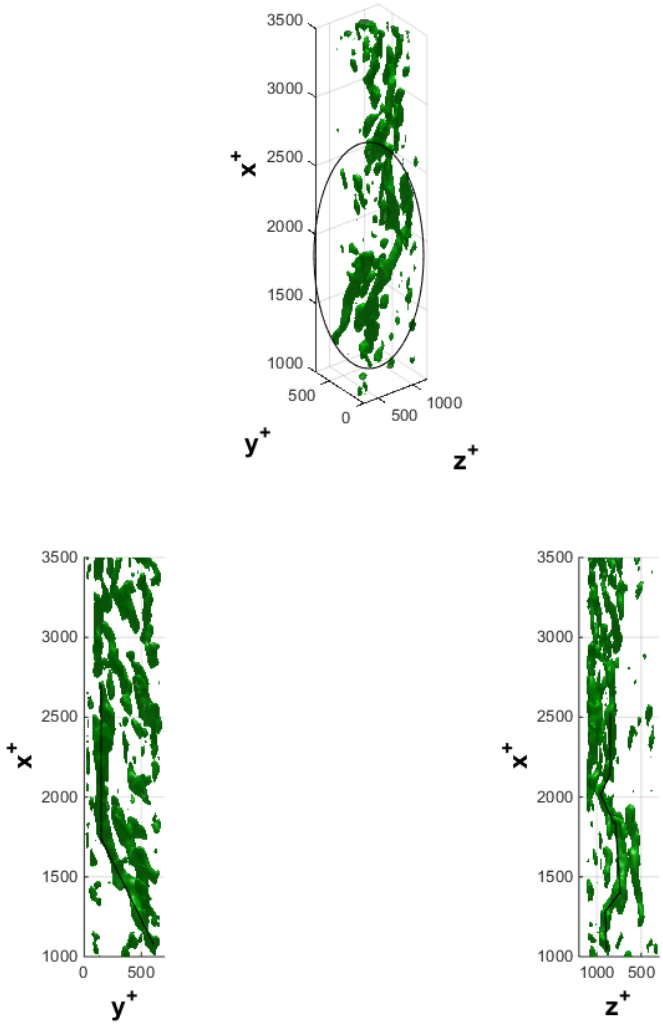


Figure 99: Visualisation of vortices. Green iso-surface: $|\lambda_{ci}|_{iso} = 0.18|\lambda_{ci}|_{max}$ at $x^+ = 1000$ to 3500.

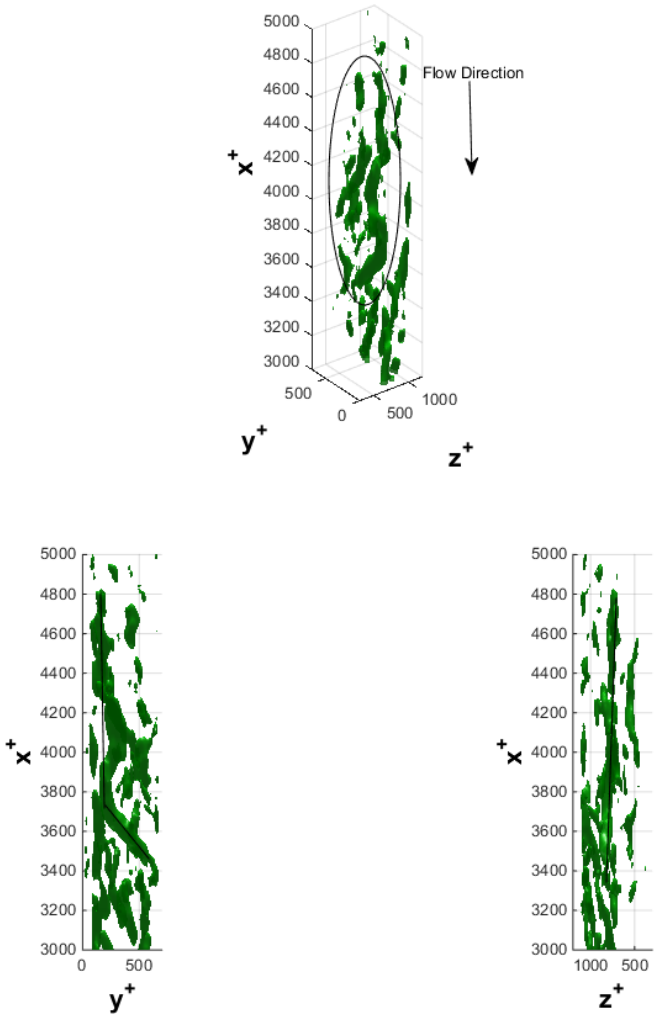


Figure 100: Visualisation of vortices. Green iso-surface: $|\lambda_{ci}|_{iso} = 0.18|\lambda_{ci}|_{max}$ at $x^+ = 3000$ to 5000.

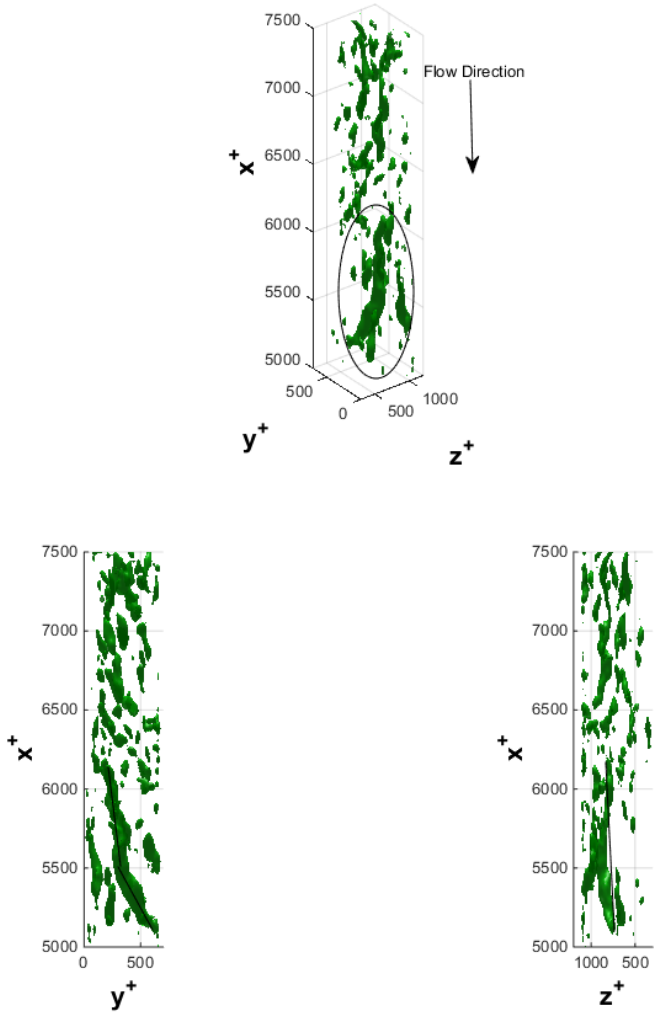


Figure 101: Visualisation of vortices. Green iso-surface: $|\lambda_{ci}|_{iso} = 0.18|\lambda_{ci}|_{max}$ at $x^+ = 5000$ to 7500.

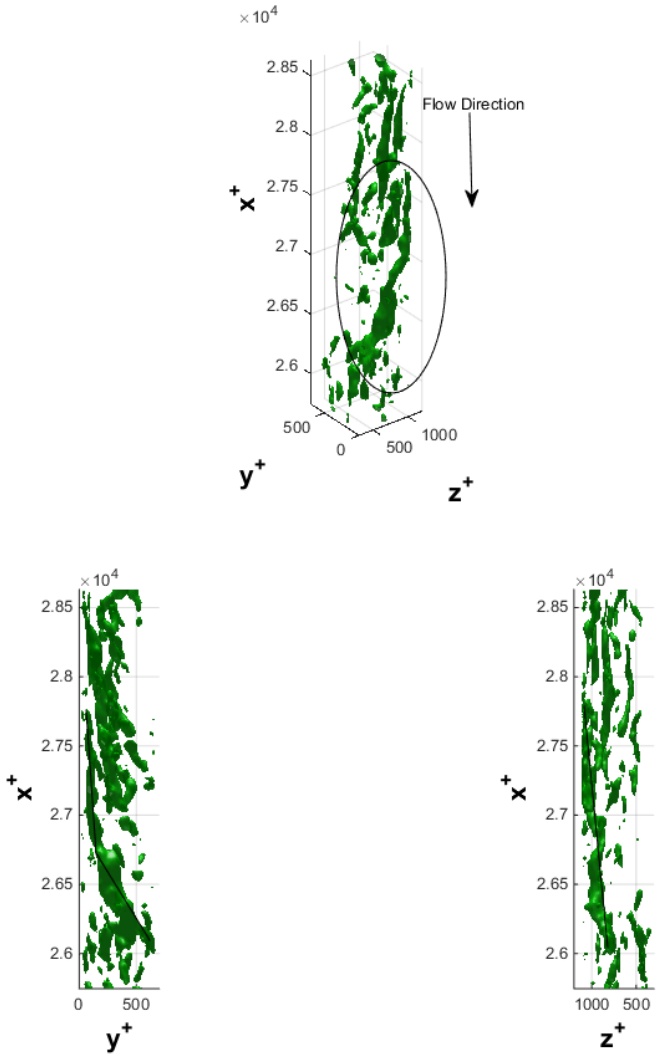


Figure 102: Visualisation of vortices. Green iso-surface: $|\lambda_{ci}|_{iso} = 0.18|\lambda_{ci}|_{max}$ at $x^+ = 2.5$ to $2.85*10^4$.

4.4 S-PIV accuracy and validation

In this section, interest is given to the sources of inaccuracy that might affect the flow statistics. Three sources were investigated:

4 The brightness of the images: intensity of laser (light emitted from laser)

5 The seeding density: particles number

6 Averaging the values in *z*-direction

4.4.1 Brightness of images

The laser energy level is set at 75%, this is in percent of the maximum and controls the energy of the laser light. Depending on the system configuration, the resulting images may lack the proper contrast, either through lack of sufficient laser power or weak signal from particles with low refractive index ratios.

The interrogation size used for this section is illustrated in Table 14.

Table 14: Quantities for the measurements in this section

Initial Interrogation area (IA) size	32 pixel x 32 pixel
Final IA size	16 pixel x 16 pixel
IA overlap	50%

The average was taken over 5000 instantaneous flow velocities and 2968 vectors (53 in the spanwise direction and 56 in the wall-normal direction) were obtained in each region with 50% overlap of the interrogation area. The distance between each vector ranges from 0.5 to 1 mm in spanwise and 0.8 and 1.6 mm in spanwise direction with a standard deviation of 0.1 mm (1 wall unit).

Laser pulse energy is to be constant, meaning that they are to be the same for the measurement images. The brightness of the images was verified by plotting the mean and statistics velocity with the different number of images to estimate the average values of the mean and statistics velocity. First, the data were plotted by using the 5000 images, and then only 4000 images were selected, followed by 3000 images, 2000 and 1000 images.

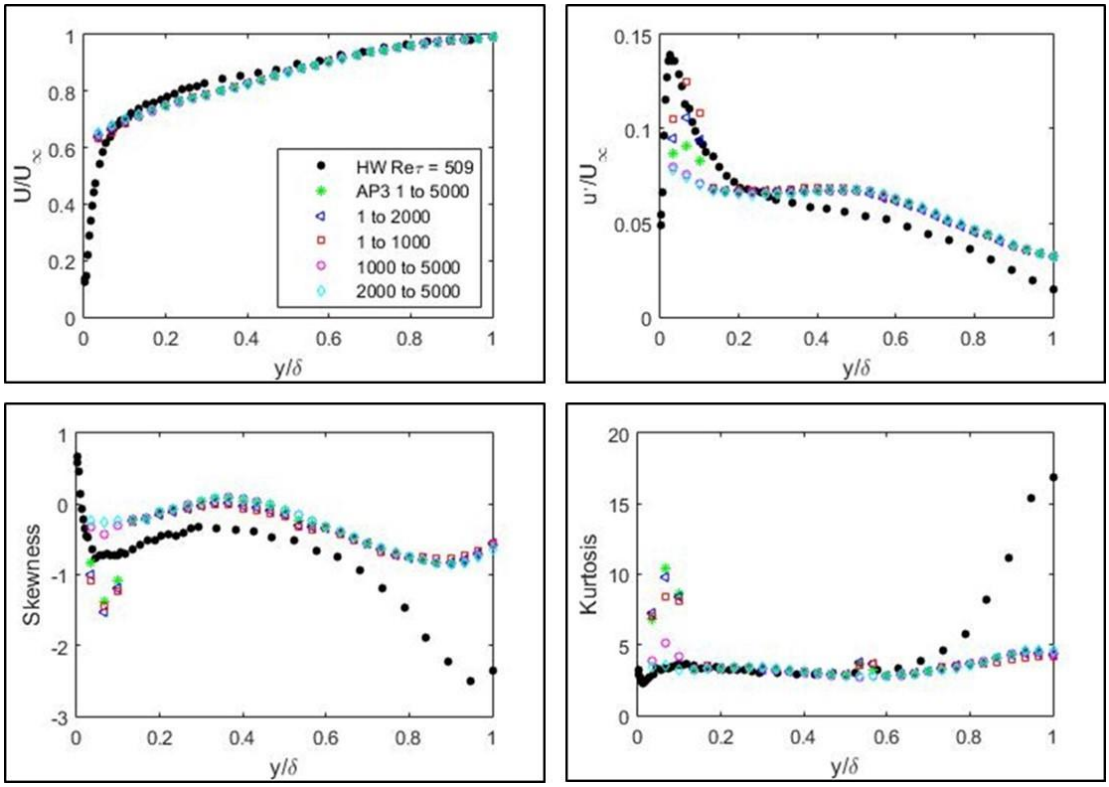


Figure 103: Statistics Profiles in linear abscissa.

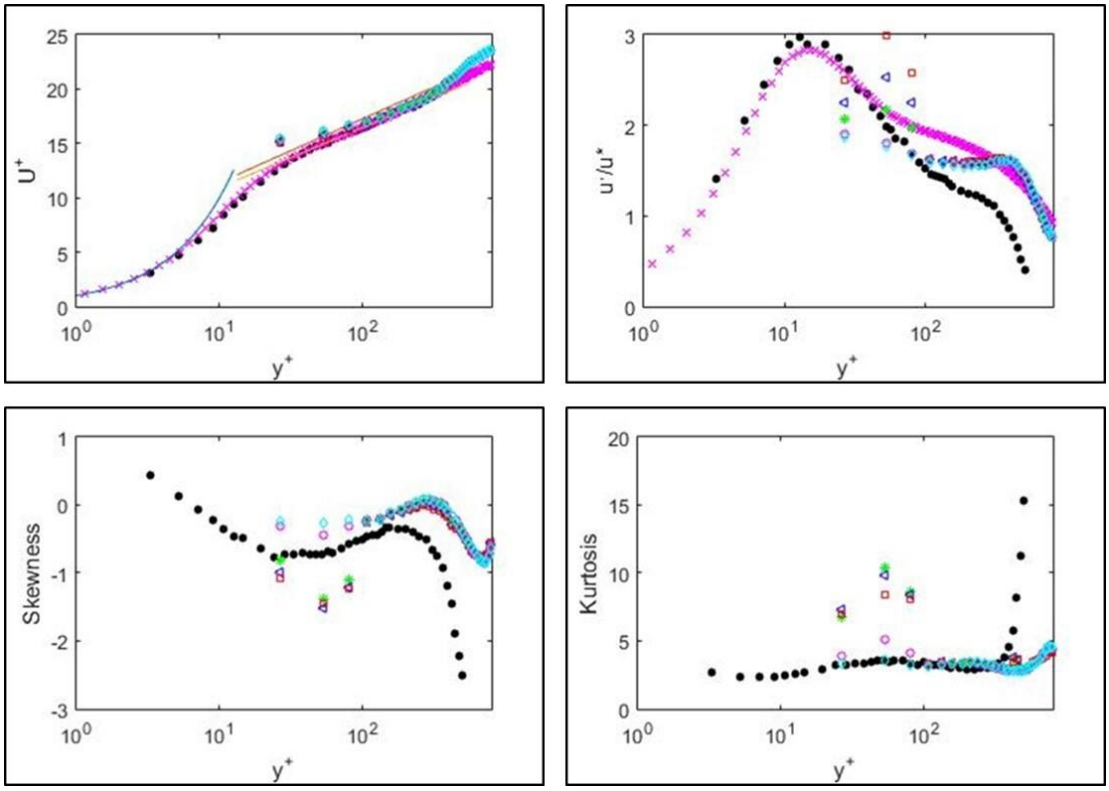


Figure 104: Statistics Profiles in logarithmic abscissa.

From Figure 103 and Figure 104, the values of *u'/u** for the cases of 1000 to 5000 and 2000 to 5000 are in good agreement with HW profile for $y^+ \geq 80$ with an error of 2%. A higher error is seen at $y^+ = 53$ ($y/\delta = 0.067$), 9 and 11% for

the first and second case, respectively. For the last 3 cases; 1 to 1000, 1 to 2000 and 1 to 5000, it appears that the errors reach values up to 52% at $y^+ \geq 80$; 52, 33 and 16%, respectively.

In summary, it seems that the brightness of images from 1000 to 5000 is identical or at least does not affect the statistical values. Indeed, the profiles are in good agreement for the cases of 1000 to 5000 and 2000 to 5000. On the other hand, for the cases; 1 to 1000, 1 to 2000 and 1 to 5000, the profiles deviate from HW profile. This might be explained by the brightness of the images becoming less intense after around 1500 images. Finally, the differences only appear below $y^+ = 106$ and $y/\delta = 0.13$ as all the cases are in good agreement at and above $y^+ = 106$ and $y/\delta = 0.13$.

For y+ ≥ 106, the mean and statistics velocity do not appear to depend anymore on either the brightness effect or the number of images.

It is important to note that the values below $y^+ = 53$ wall unit should not be considered due to the holes obstructing the near wall region (y < 4mm) and the reflection of the laser light on the Perspex.

The validity of the averaging along x for the s-PIV dataset should be checked by comparing mean velocity profiles obtained by averaging over the different samples and over an increasing number of points in x (from 500 to 5000 by steps of 1000). Convergence of the mean and standard deviations of the velocity components requires a large number of samples (N>1,000). A statistical analysis of the PIV results requires an ensemble consisting of a large number, N" of vector maps. The need for large sample sizes, particularly for higher order statistics. Although it would have been practical to acquire a statistically significant sample size of 3000 vector maps (from 1 to 3000 then from 2000 to 5000 and 1000 to 4000) so that accurate turbulence statistics could be calculated and a conclusion could be made about the brightness effect on the statistics.

4.4.2 Particle density/distribution (Particles per interrogation volume)

The influence of the seeding density was investigated in this section. The seeding particle analysis was carried out on the entire boundary layer and covering the entire span of the flow domain. The particle density was analysed by showing samples of all 5000 images every 500 images. It is useful to show a pair of images as although they are nearly identical in terms of seeding particle distribution, the number of particles varies.

The particle density was checked through several pairs of images. The number of particles in the region where the turbulence intensity values were low were assessed from, 95 to 70 mm (95 mm corresponding to the wall position), which corresponded to the upper half of the boundary layer thickness. By looking at the images, it seemed that the particles were denser in the upper half of the boundary layer thickness than the lower half where it could be seen that particle numbers were lower.

As an example, one of the images showing the seeding particle distributions can be seen in Figure 105. Images at different time spaced at an equal interval of 0.5 second (every 500 images out of 5000 images) were investigated but only one of them is shown in the thesis. The aim is to demonstrate the adequacy and uniformity of seeding distributions. The number of seeding particles is counted by Dynamic Studio Software with a probe area size of 64 x 64 pixel which was the minimum size available. In that way, to estimate the number of particles for each IA sizes of 32x32, 16x16 and 8x8, the value of particles number found for 64x64 were divided by 4, 16 and 64, respectively (Table 15).

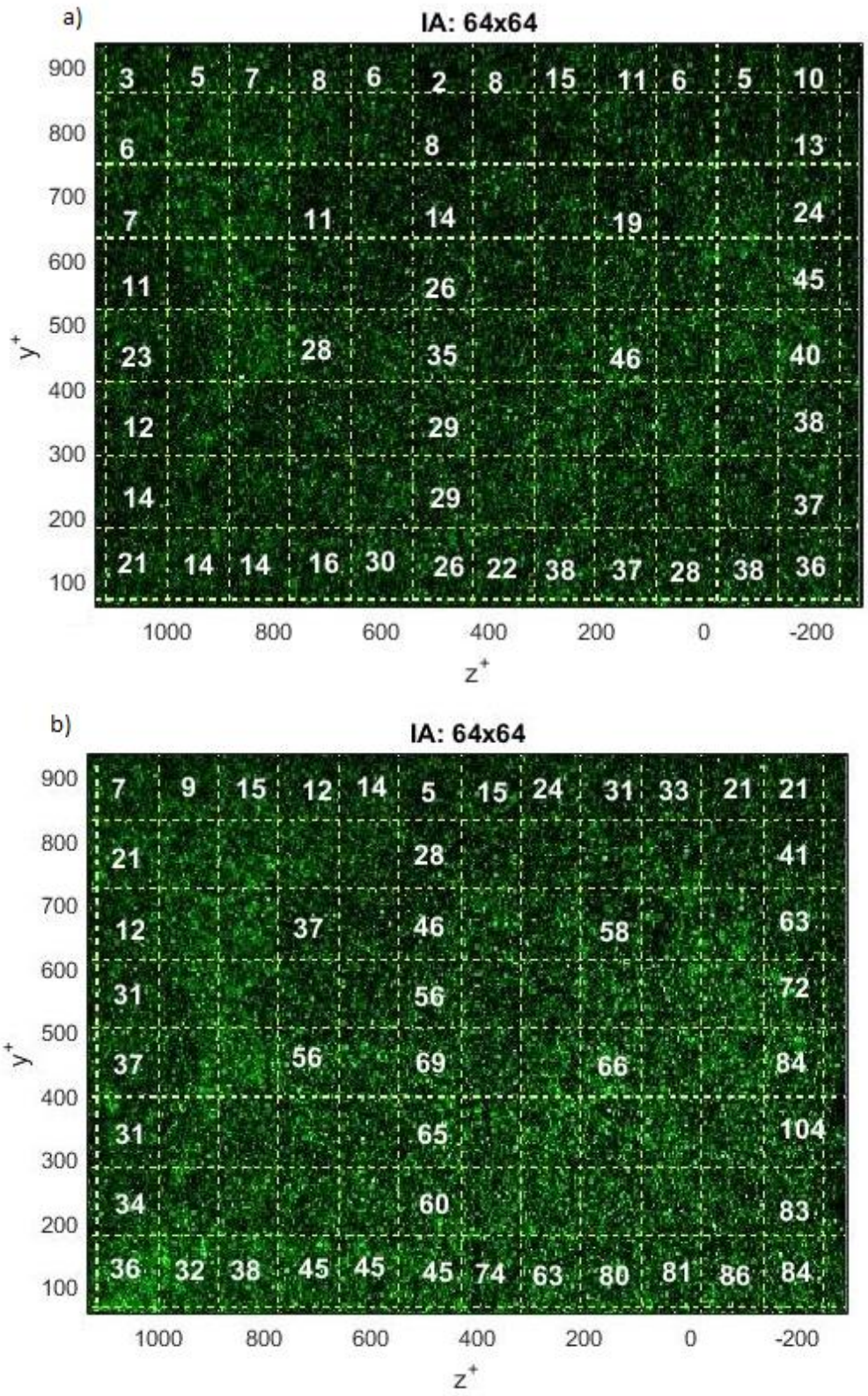


Figure 105: Particle density distribution, IA size 64x64pixels, image 1000 a) frame 1 and b) frame 2

Table 15: Number of particles for several images out of 5000 images (I) for IA of 64x64 pixel.

	Frame 1				Frame 2		
	0–311 wall unit	311-621 wall unit	621-932 wall unit		0-311 wall unit	311-621 wall unit	621-932 wall unit
I1	16 to 44	7 to 48	2 to 23				
I500	17 to 44	7 to 46	4 to 22	I500	18 to 91	23 to 81	5 to 56
I1000	14 to 38	12 to 46	3 to 24	I1000	32 to 86	31 to 104	5 to 63
I1500	16 to 45	10 to 42	1 to 24				
I2000	17 to 34	5 to 35	2 to 25	I2000	26 to 65	14 to 84	1 to 58
I2500	15 to 26	8 to 40	3 to 19				
I3000	8 to 37	8 to 42	4 to 18	I3000	21 to 78	15 to 74	3 to 42
I3500	11 to 35	2 to 37	4 to 19				
I4000	10 to 30	2 to 30	1 to 13				
I4500	12 to 28	4 to 32	1 to 17				
I5000	12 to 40	8 to 44	2 to 28				

It can be concluded that the particles were denser in the lower half of the boundary layer closer to the wall than the upper half where it can be seen from Table 15 that the average number of particles in the IA decreases. Moreover, it seems that the IA size which meets the requirements stated earlier is 64 x 64 and 32 x 32 as for the 16 x 16 and 8 x 8, not enough particles are present in the IA. Furthermore, for frame 2 the number of particles is higher than for frame 1, this can be explained by the power of laser 1 being lower than the power of laser 2. This led the software to recognise less particles on frame 1 than frame 2. Finally, the velocity vectors computed with s-PIV resulted in less than 6% erroneous vectors prior to validation from image 1000 to 5000 and up to 17% from image 1 to 1000 for IA size of 32x32 and 64x64 pixels.

4.4.3 Averaging values in z-direction

Assuming the flow is homogeneous within the field-of-view, an estimate can be obtained by averaging over all rows in the spanwise direction.

The values have been averaged first in *x*-direction (5000 data points) and then in *z*-direction (53 data points) to get the averaged value out of the instantaneous values. The data were plot with an averaged value out of 53 *z*-data points, in addition a profile for each *z*-position was also plotted. Finally, the profile at the *z*-position which best fits the HW and DNS data was highlighted.

In Figure 106, it can be seen that in *z*-direction the values of the streamwise velocity are not uniform. If the *y* position is kept constant, all the values along the z should be identical. As an example, along y^+ = 350 (black line in Figure 106), it seems that the values of *U* roughly vary from 4 to 3.8 m/s from z^+ = -200 to z^+ = 1000 (from orange to green in the colorbar).

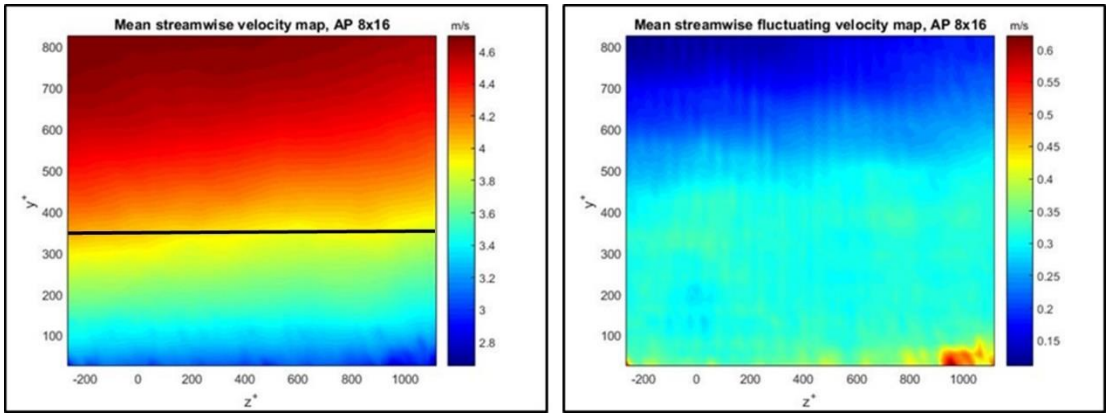


Figure 106: Mean Streamwise (left) and fluctuating (right) velocity maps

The lack of uniformity in the *z*-direction is explained by the laser sheet being angled with the 3D calibration target. A post-processing is done by rotating the set of data with an angle of 3° (Figure 107).

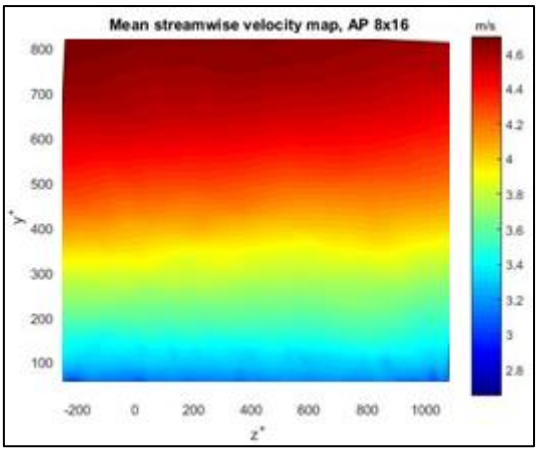


Figure 107: Mean Streamwise velocity map after post-processing, rotation of 3°.

After applying the post-processing to the data, the statistical values in the *z*-direction were averaged and compared with HW and DNS data. A profile was plotted at each *z*-position (shown in green in Figure 108 and Figure 109). The profile that fits best HW and DNS data are the one at *z* = 78mm (z^+ = 1035).

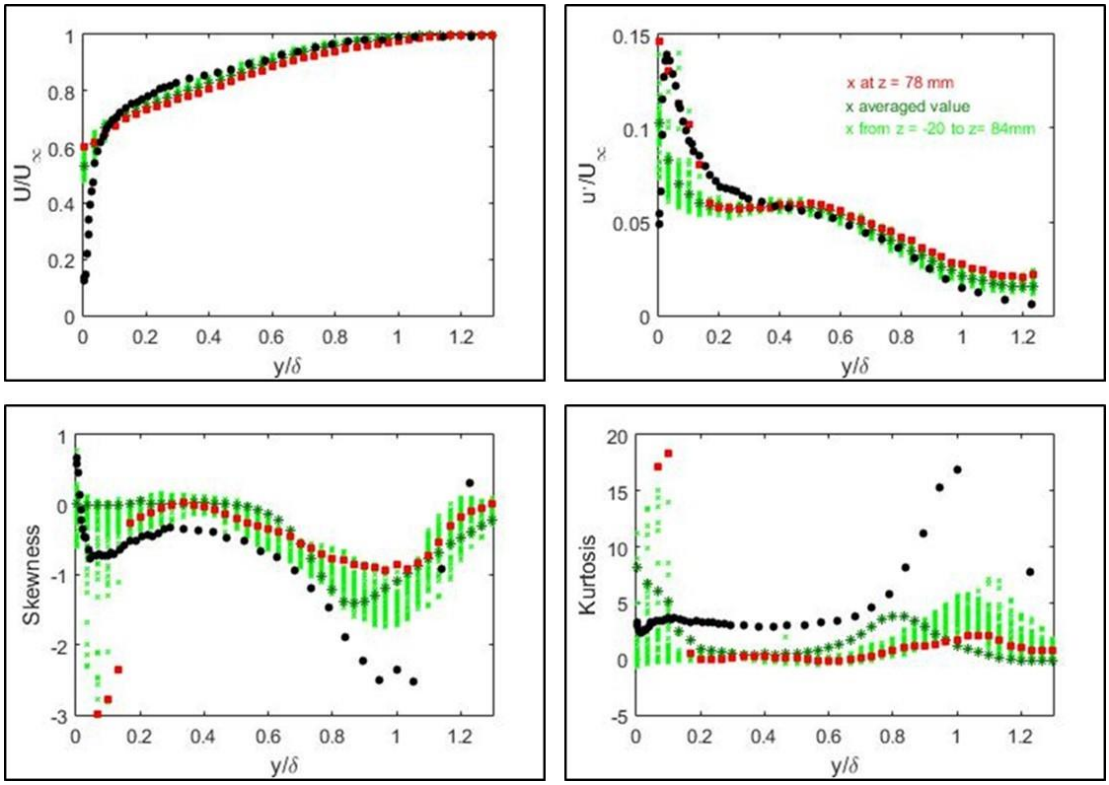


Figure 108: Statistics Profiles in linear abscissa.

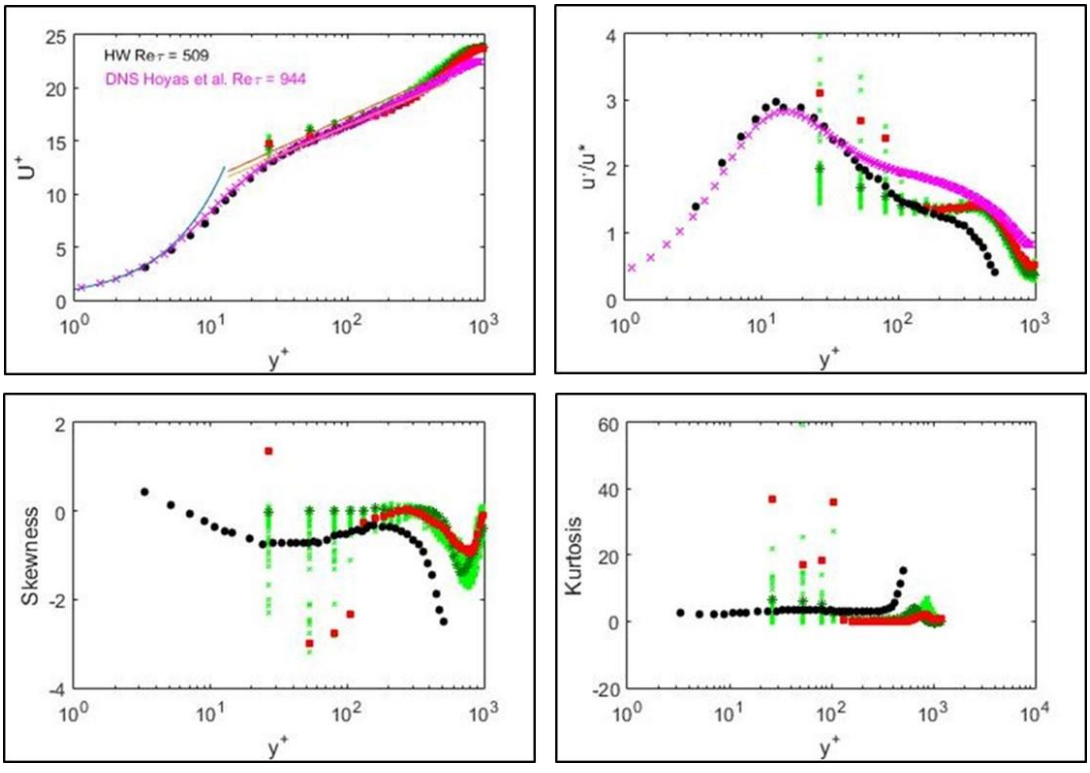


Figure 109: Statistics Profiles in logarithmic abscissa.

4.5 Comparison of stereoscopic PIV and Hot-Wire statistics of turbulent boundary layer

This section shows a cross checking of turbulent boundary layer measurements using large field of view s-PIV and hot-wire anemometry techniques.

4.5.1 Introduction

In this section, the aptitude of s-PIV to investigate coherent structures was evaluated. The mean and some turbulence statistics of the velocity fields were computed and the results obtained from the s-PIV approach were compared to HW anemometry technique. For s-PIV, the results are sensitive to vector estimation method and the interrogation area. The purpose is to show that the s-PIV technique can adequately captured the turbulent boundary despite this sensitivity.

4.5.2 S-PIV in comparison with HW

4.5.2.1 s-PIV and HW statistics comparison

An experimental investigation was performed to validate the accuracy of s-PIV by a comparison against hot-wire data.

The Reynolds number based on the friction velocity, Re_τ in this experimental test is 788 with a sampling frequency of 1 kHz and a time between pulses of 200 µs.

The values compared were:

- The mean velocity vector
- The standard deviation of the mean
- Skewness
- Kurtosis

The interrogation size used for this section is illustrated in Table 16.

- **Table 16: Quantities for the measurements in this section**

Initial Interrogation area (IA) size	64 pixel x 64 pixel
Final IA size	32 pixel x 32 pixel
IA overlap	50%

In this experiment, 5000 instantaneous realisations (vector maps) were used for the statistical calculations. Each vector map contains 56 x 53 vectors (2968) in an area of 110 x 105 mm in *y* and *z* direction, respectively. The values were averaged, in *x*-direction (5000 vectors, 5s) and z-direction (53 vectors), out of the instantaneous values. The average is performed by spatial averaging over the interrogation area. The standard deviation was calculated by substracting mean velocity vectors map from the instantaneous velocity vectors map.

Table 17: Formulae

Mean velocity	$\bar{u} = \frac{1}{N}\sum u_n$
Variance	$\sigma_u^2 = \frac{1}{N}\sum (u_n - \bar{u})^2$
Standard deviation	$\sigma_u = \sqrt{\sigma_u^2}$
Skewness	$s_u = \frac{\frac{1}{N}\sum (u_n - \bar{u})^3}{\left(\sqrt{\frac{1}{N}\sum (u_n - \bar{u})^2}\right)^3}$
Kurtosis	$k_u = \frac{\frac{1}{N}\sum (u_n - \bar{u})^4}{\left(\frac{1}{N}\sum (u_n - \bar{u})^2\right)^2}$

N represents data samples (number of vector maps) and is equal to 5000, so all sums are from n = 1 to n = 5000, u_n is the instantaneous streamwise velocity, $\bar{u}$ is the streamwise mean velocity.

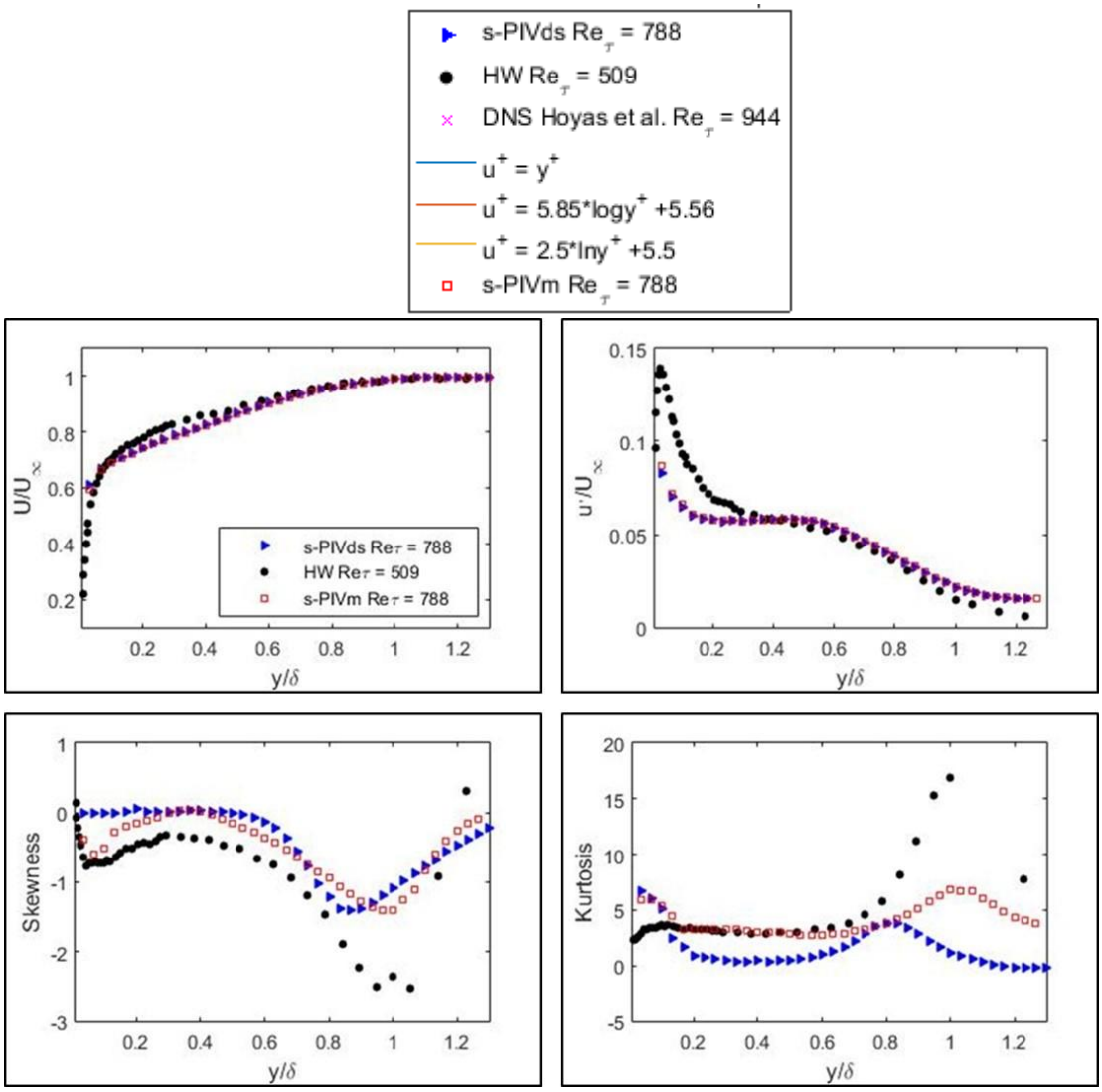


Figure 110: Mean velocity profile and turbulence statistics linear abscissa.

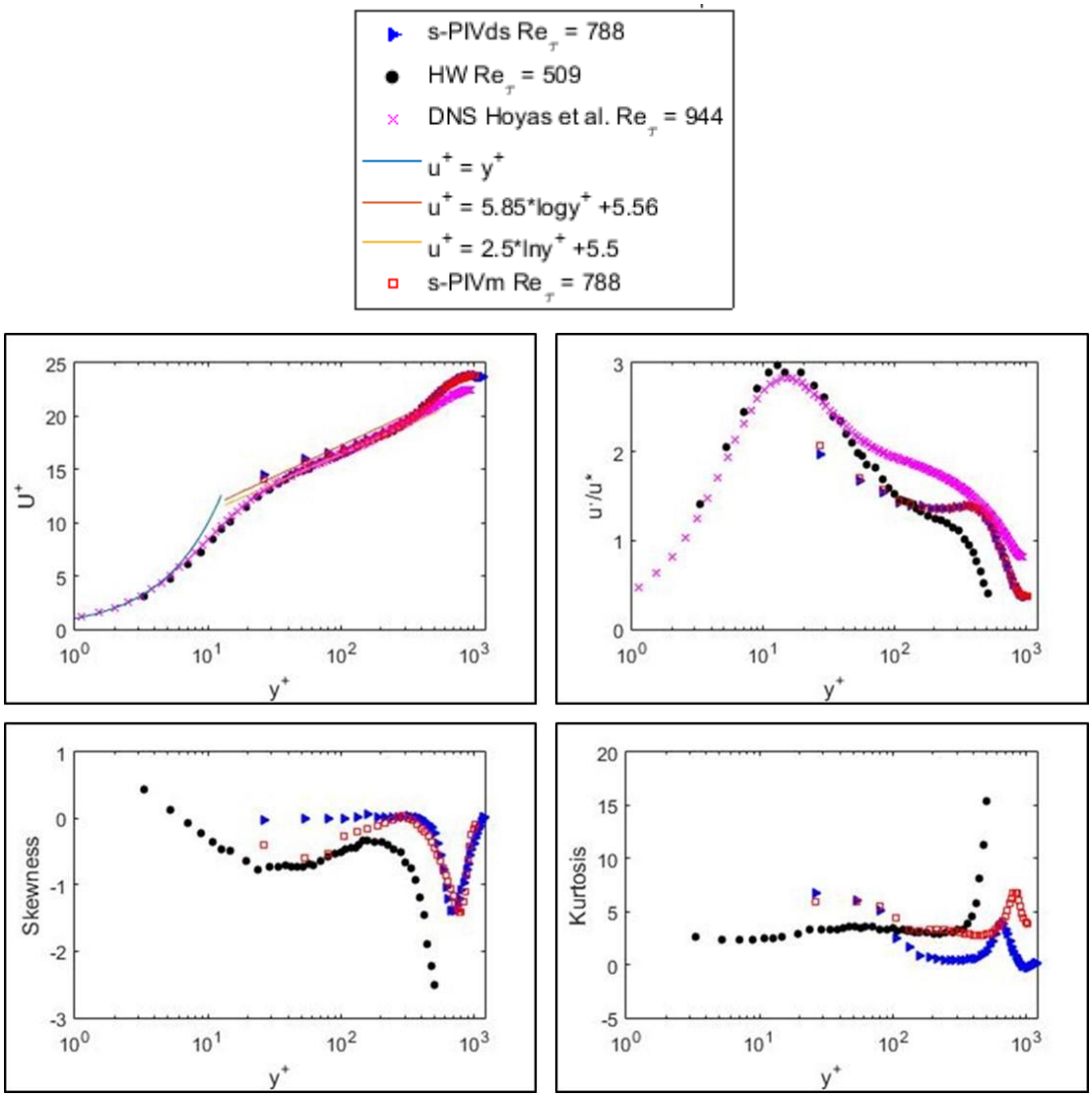


Figure 111: Mean velocity profile and turbulence statistics logarithmic abscissa.

The profiles are plotted in the log-law form as well as against y/δ. The normalised values were determined by estimating the friction velocity (u^*) using the Clauser chart method (Clauser, 1956).

The data for the mean streamwise velocity profile agree reasonably well with the HW data for $y^+ \geq 53$ with error ranging from 0.6 to 2.2%. This error is within the range of HW errors (5%). At $y^+ = 27$, the error was found to be 7.8% (Figure 111). The streamwise r.m.s. velocity is seen to be a reasonable match for $y^+ > 80$ with results converging. At $y^+ = 27$, 53 and 80, the errors were 20, 14 and 7.3%, respectively (Figure 111). The variation, below $y^+ = 80$, is because of the moderate spatial

resolution used in this experiment. Hence the aim to investigate the spatial resolution and vector estimation methods in section 5.2.2.

4.5.2.2 Comparisons of statistics for different s-PIV vector estimation methods

The turbulent statistics can be attenuated by spatial averaging, especially in the near-wall region as shown on section 5.2.1. The spatial resolutions of HW and s-PIV methods have substantial differences. This is mainly due to the large field of view of the s-PIV camera. The HW method gives a better resolution for closer position to the wall in comparison with s-PIV. The measuring point in the x and y direction is much smaller for the HW (5 μm), while for the s-PIV is given by the interrogation area size in Table 18. The velocity value using the s-PIV method is evaluated over the interrogation area. The flow images are divided into IA, and each IA produces a velocity vector. Since the PIV velocity vector is a local average over the interrogation area, when calculating turbulence statistics it is necessary to ensure the turbulent structures of interest are resolved. The side of the interrogation area corresponds to the diameter of the smallest turbulence structures that can be identified.

The effects of s-PIV IA size on turbulent quantities were studied in this section. Few interrogation area sizes (from 8 pixels to 64 pixels) were investigated and compared. Table 19 summarised the IA sizes used to process s-PIV data in mm and wall unit. It is important to mention that with a 50% overlap the spacing between vectors reduced from 32 to 8 pixels. It corresponds to 0.5 and 1.9 mm and 6.4 and 25 wall units, respectively in a wall-normal direction.

Table 18: IA sizes in pixels, mm and wall unit

	IA in pixels	IA in mm	IA in wall units
y	64	3.8	51
	32	1.9	25
	16	1.0	13
	8	0.5	6.4
z	64	6.4	85
	32	3.2	43
	16	1.6	21
	8	0.8	11

The s-PIV data were evaluated by 7 alternative methods (see Table 19).

Table 19: Summary of interrogation areas sizes.

	method	IA (pixel)	IA (mm)	Initial IA in pixels	Overlap	dy (pix)	dy (mm)	dy (w.u.)
AP1	Adaptive PIV	32 x 32	1.9 x 3.2	64 x 64	16 x 16	16	1.0	13
AP2	Adaptive PIV	16 x 16	1.0 x 1.6	32 x 32	8 x 8	8	0.5	6.4
AP3	Adaptive PIV	8 x 8	0.5 x 0.8	16 x 16	8 x 8	8	0.5	6.4
AP4	Adaptive PIV	16 x 32	1.0 x 3.2	/	32 x 32	16	1.0	13
AC1	Adaptive correlation	16 x 16	1.0 x 1.6	64 x 64	50%	8	0.5	6.4
AC2	Adaptive correlation	32 x 32	1.9 x 3.2	32 x 32	50%	16	1.0	13
AC3	Adaptive correlation	16 x 32	1.0 x 3.2	64 x 128	50%	8	0.5	6.4

Two different methods (Adaptive PIV and Adaptive correlation) of s-PIV were used for calculating velocity vectors based on particle images. The Adaptive PIV method iteratively determines an appropriate interrogation area size to use for each individual IA in order to adapt to local seeding densities, but specified minimum and maximum IA sizes limits the range. It starts with the largest IA size allowed, and then reduces the IA sizes where particle density is high enough. The Adaptive correlation method starts with an initial interrogation area and uses the intermediary results as information for the next IA of smaller size, until the final IA size is reached (Dynamic Studio Manual). Defined initial and final interrogation area size delimits their ranges.

Two parameters are important for the choice of the IA size to perform s-PIV:

- An IA should contain a minimum of 8 - 10 particles.
- The maximum particle displacement is less than one quarter of the IA size.

The measured statistics were compared with DNS data at close Reynolds number.

In the first case, using interrogation areas of 32 by 32 pixels (1.9 x 3.2 mm) and 50% IA overlap with a distance, *dy,* of 1.0 mm between each vector in *y* direction.

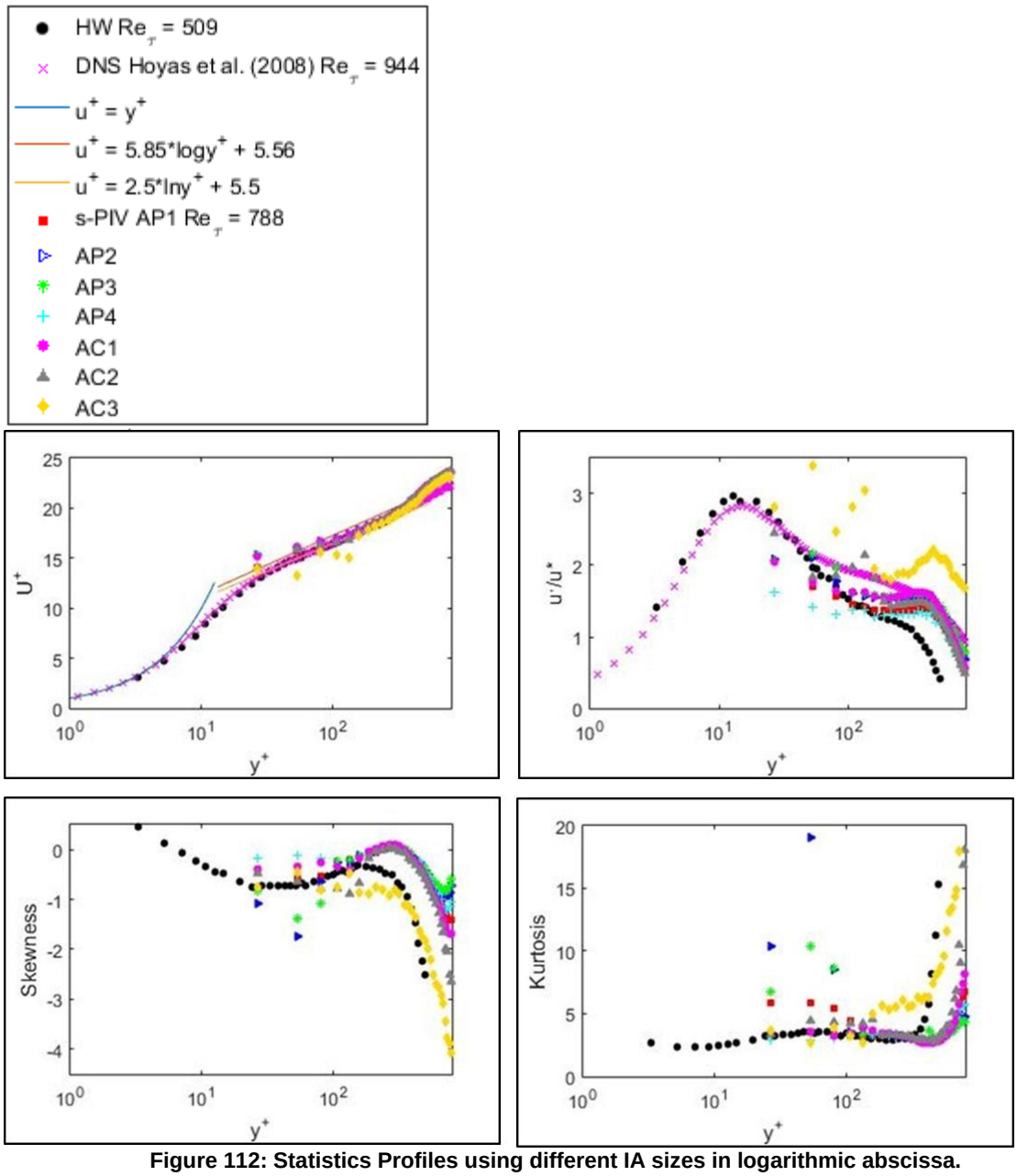


Figure 112: Statistics Profiles using different IA sizes in logarithmic abscissa.

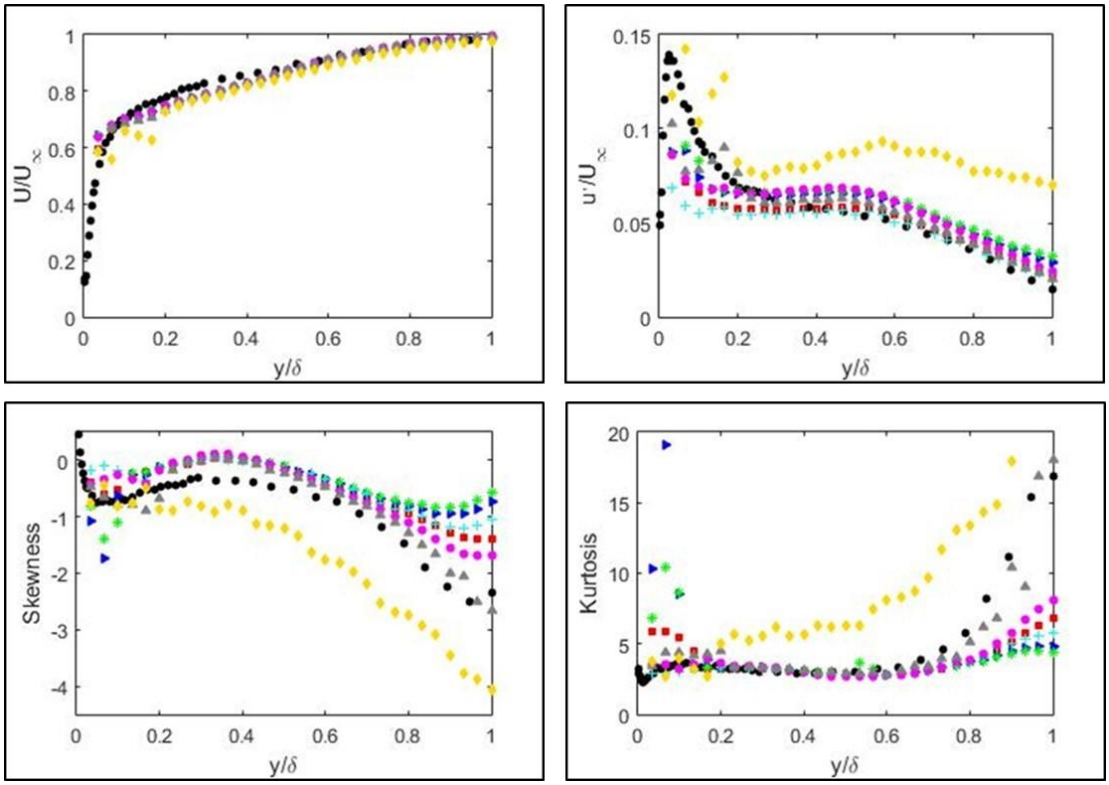


Figure 113: Statistics Profiles using different IA sizes in linear abscissa.

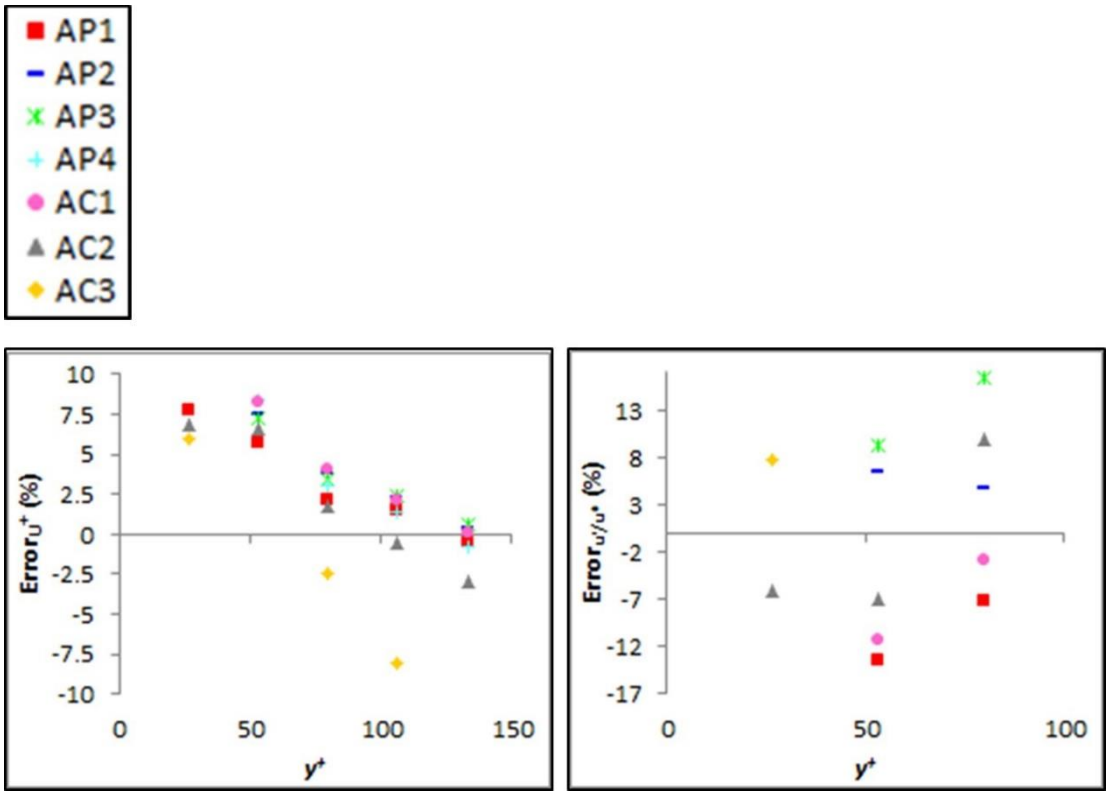


Figure 114: Errors estimated between values from different IA sizes and HW

No significant effects of IA on the streamwise velocity were found between the different IA sizes apart from AC3 (16x32) for values above y^+ = 27. For y^+ > 80, the errors estimated between s-PIV and HW were up to 2.4% apart from AC3 .

However, significant differences were reported for u'/u^*. AC2 seems to be a good compromise as it has low errors up to 10% in comparison with HW. It is then followed by AP2 with errors up to 6% if y^+ = 27 is disregarded. As for AP3, AP4 and AC3, the errors reach high value leading to 21, 38 and 71% respectively at position up to y^+ = 80. Finally, AC1 and AP1 shows errors of 3 and 7%, respectively at y^+ = 80. Above y+ = 80, the u'/u^* profiles from the various IA collapsed onto one curve. But profiles of skewness and kurtosis showed more sensitivity to IA (Figure 107, 108 and 109).

The values of U^+ from s-PIV in comparison with HW were identical from y^+ = 106 apart for AC3 while values of u'/u^* were different. It was found that the values of u increased with decreasing IA values. It is observed that special averaging effects are more severe in the viscous, and buffer regions and least in the outer region.

4.6 Chapter Summary

It was found that for Re_τ = 423 and 568, the mean velocity profiles in the near-wall region was not in good agreement with the profile of Kang (2008). This is mainly due to the calibration curve fit ranging from 0.7 to 8 m/s. It means that for velocity values below 0.7 m/s, they are extrapolated from the curve fit leading to an error higher than the 5% found for value ranging in 0.7 – 1 m/s. But at Re_τ = 1310, the profile was in very good agreement with Kang (2008) with velocity values in the near wall region from y^+ = 3 – 4 following the linear region. It is interesting to say that the wall effect seems to be reduced in comparison to Re_τ = 423 and 568. Also, for Re_τ = 1310, at y_n = 0.95 mm the velocity value is 0.75 m/s, it is reasonable for the calibration ranging from 0.67 - 8 m/s, there is a measure of confidence as the error was found to be of 5% for 0.68 < U < 1 m/s. It is interesting to mention that Johansson and Alfredsson (1983) showed that the maximum u'/u^* which is found around y^+ = 12, should be 2.9. All three sets of measurements reported here seem to have lower maximum u'/u^* than 2.9. One may think that this must likely be due to the calibration curve issues at low speed. This might be valid for Re_τ = 423 and 568 as it was seen in the mean velocity profile. But at

Re_τ = 1310, the mean velocity profile has shown a good fit even at low velocity near the wall, from y^+ = 3. The turbulence intensity profile that follows best the one of Alfredsson et al. (1988) is at Re_τ = 423 and getting worse with an increase in Reynolds number. This is explained by the hole effect, the effect of the holes increases with an increase in velocity. The skewness (*S*) and kurtosis (*K*) factors reached low values in the viscous sublayer in comparison with the oil channel data of Alfredsson et al. (1988). Their results indicate that S and K factors should approach 1.1 and 4.9 near the wall, respectively. The results obtained for 7.4 m/s are in reasonable good agreement with those of Alfredsson et al. (1988) for the oil channel. Although at Re_τ = 423 and 568, the skewness and kurtosis factors show clear differences in the viscous sublayer for $y^+ < 10$. It is related to the errors due to the calibration at low velocities. From those results one can conclude that most of the heat transferred to the fluid is going directly from the hot-wire sensor to the fluid for Re_τ = 1310. This indicates that the amount of heat transferred via the substrate to the fluid, wall effect, is negligible at Re_τ = 1310.

The hairpin properties which were found experimentally in the present work are qualitatively comparable with those found in the works of Hutchins' and Adrian's group.

In the region where the fluctuations are rather small, the PIV result varies from the HW and DNS. This is obvious for regions below y^+ = 107, where the fluctuation is smaller. A seeding density of 8-10 particles per interrogation area is generally desired to aid the cross-correlation function. These are dependent on the size of IA (spatial resolution). Indeed, it is difficult to have a small IA size to have enough resolution and enough particle numbers in each interrogation area. PIV performs spatial averaging over the interrogation area, while the HW operates in a small element (size of µm). The small-scale resolution affects the measurement of the fluctuation component of the velocity and then turbulent intensities. The discrepancy is particularly noticeable near the wall, where the problem of the small scales is most pertinent. In the region where the fluctuations are rather small, the PIV result varies from the HW and DNS. This is obvious for regions below $y+$ = 107 where the fluctuation is smaller. A few interrogation area (IA) sizes were compared and it seems that the profiles that are in good agreement with HW are AP3 (min. IA: 8x8 and max IA: 16x16) as well as AP2 (min. IA: 16x16 and max IA: 32x32). But AC2 (32x32) profile seems to be in better

agreement with DNS data. Our finding is consistent with the work of Shah et al. (2008) although in their studies, PIV system was used in comparison with s-PIV for our experiments. Their results demonstrate that the mean velocity is nearly independent of interrogation (IA) sizes. Note that the resolution of our study is smaller than that of the experiments of Dennis and Nickels (2011) as well as Elsinga et al. (1967). The former used a spatial resolution of 82 wall unit and the latter $l^+ = 58$. Despite this source of inaccuracy, the discrepancies are particularly noticeable near the wall but as the interest of this project is on the large-scale structures, this is not viewed as a major problem.

Chapter 5 Near-wall investigations at different wall-normal positions and Reynolds Number Dependence

5.1 Introduction

To our knowledge, an analysis of the near-wall structure scales based on streamwise, and spanwise two-point correlations and instantaneous skin-friction mapping in low Reynolds numbers dependence has not been yet attempted. In the present study, investigation of Reynolds numbers lower than available prior experimental data, and span the DNS ranges in the literature are presented.

In order to study the distribution of the instantaneous streamwise skin-friction in the turbulent boundary layer, it is necessary to sample them at many spanwise positions simultaneously. The entire spanwise instantaneous skin-friction must be known at a single instant. Each measurement position requires a separate hot-wire anemometer probe and a support which hold each probe in place. The spanwise length of the sensor array corresponds to 588, 1310 and 1818 respectively for Re_τ = 423, 568 and 1310.

In this chapter, the calibrations of the twenty hot-wire sensors were not carried out and the results are given in voltage instead of velocity. It is considered that the instantaneous velocity and skin-friction are functions of voltage and are very close to it. In the vicinity of the wall, the relationship between voltage and velocity is linear as detailed in Chapter 3 (Figure 29, page 40). Therefore, we will refer to velocity or skin-friction when talking about voltage data.

5.2 Near-wall structures in comparison with large-scale structures using hot-wire array and PIV

5.2.1 Instantaneous skin-friction mapping at different Reynolds Number Dependence

The aim is to investigate and compare the instantaneous fluctuating velocity map at different Reynolds numbers.

In this section, the intention is to compare the signal characteristic of the instantaneous skin-friction at different Re_{τ}.

Assuming frozen field, a streamwise-spanwise distributing of the velocity fluctuations is constructed by using Taylor's hypothesis (Taylor, 1938) given in Equation 22 (page 148). It is investigated that the convection velocity of near wall region is greater than local mean velocity up to $y^+ = 30$. The study of Henry and Choi (2006) found a convection velocity of 13u* at $Re_\tau = 786$, their value compares well with results of Kreplin and Eckelmann (1979) who reported a convection velocity at the wall of $12u^*$ at $Re_\tau = 7700$, which is equivalent to the local mean velocity at $y^+ = 17$. Several experimental results (Krogstad et al., 1998, Johansson et al., 1987) set convection velocity $12u^* \sim 16u^*$ up to $y^+ = 30$. The convection velocity used in our experiments has been set to $13u^* \approx 0.60U_\infty$.This convection velocity is estimated from the formula based on the log law and given by Hutchin et al. (2011) as

$$U_c^+ \equiv U^+ = \frac{1}{\kappa} ln\sqrt{15Re_\lambda} + A, \tag{20}$$

with κ = 0.41 and A = 5.

5.2.1.1 Without Filter

The fluctuating velocity data are normalised by their rms values. An interpolation using a third order polynomial was used to smooth the picture and have a better view as the spacing between each sensor (20 sensors in total) is equal to 0.5 mm in the spanwise direction.

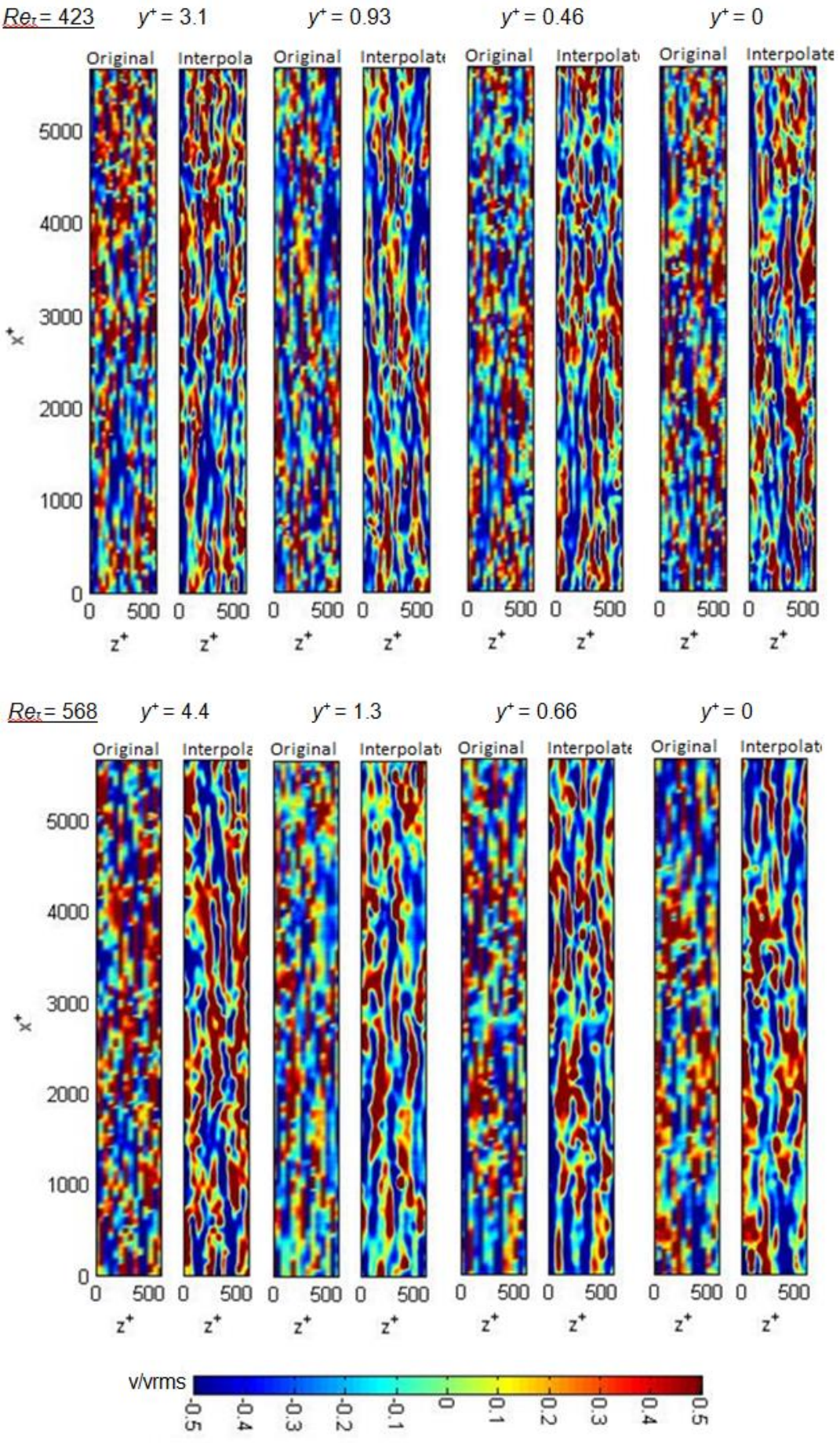
It can be seen that the data at low ($Re_\tau = 423$) and high ($Re_\tau = 1310$) Reynolds numbers show different patterns at the same y^+ positions such as $y^+ = 3.1$ at $Re_\tau = 423$ and $y^+ = 2.9$ at 1310. Indeed, at Re_τ =423, there are more streaks spread in the spanwise direction, 10-11 streaks (show number in figure) in comparison to 5 streaks at $Re_\tau = 1310$ for the same z^+ spacing. It means that given the resolution, the streaks at $Re_\tau = 1310$ are thicker than those at $Re_\tau = 423$, having a spanwise width of 100 and 50 wall unit, respectively. This can be explained by the fact that the spanwise spacing in wall unit between each sensor was not similar for each Reynolds number. The spacing between the centre of each sensor was $z_s = 5$ mm, giving the total rake dimension of $z_r = 95$

mm from the centre of the first sensor to the centre of the last one. In dimensionless values, it means that at Re_τ = 423, z_s^+ = 31 and z_r^+ = 588 and at Re_τ = 1310, z_s^+ = 96 and z_r^+ = 1818. In other words, in the spanwise direction, the near-wall structures thinner than 31 wall unit and 96 wall unit for Re_τ = 423 and 1310, respectively cannot be seen by the sensors.

As it can be seen in Figure 115, the z^+ scale is from 0 to 588 (z_r^+ value) wall unit, which is the maximum scale at Re_τ = 423 but at Re_τ = 1310, only less than a third of the full scale is shown to be compared with the lower Reynolds number (full scale at Re_τ = 1310 is from 0 to 1818 wall unit in spanwise direction). It means that out of the 20 sensors measurements, the data from only 6 sensors are being shown.

At Re_τ = 423 and 568, at y^+ = 0.93 and 1.3, it can be seen that the patterns seem alike although there are some differences that can be explained by the fact that because the sensors have a higher spacing at 568 then near-wall structures smaller than 44 wall unit are not caught. The streaks width for both Reynolds number are similar, 8-9 streaks are seen in the spanwise direction with width of 65-74 wall unit.

Finally, it is important to bear in mind that in our studies, we are only interested in large-scale structures with width equal or larger than 100 wall unit. The z_s^+ at Re_τ = 423 and 568, is equal to 31 and 44 respectively, so by analogy with the Nyquist theorem, 100 wall unit is twice of 31 and 44 wall unit. In that case, the signals are taken at spacing between sensors small enough at 423 and 568 Reynolds numbers to catch the large-scale structures as for higher Reynolds numbers such as 1310. It is also important to mention that the minimum width of large-scale structure is 100 wall unit but they can reach much higher width.


Re_τ = 423
y+ = 3.1
y+ = 0.93
y+ = 0.46
y+ = 0
Original
Interpola
Interpolate
x+
z+
Re_τ = 568
y+ = 4.4
y+ = 1.3
y+ = 0.66
y+ = 0
v/vrms
-0.5
-0.4
-0.3
-0.2
-0.1
0
0.1
0.2
0.3
0.4
0.5

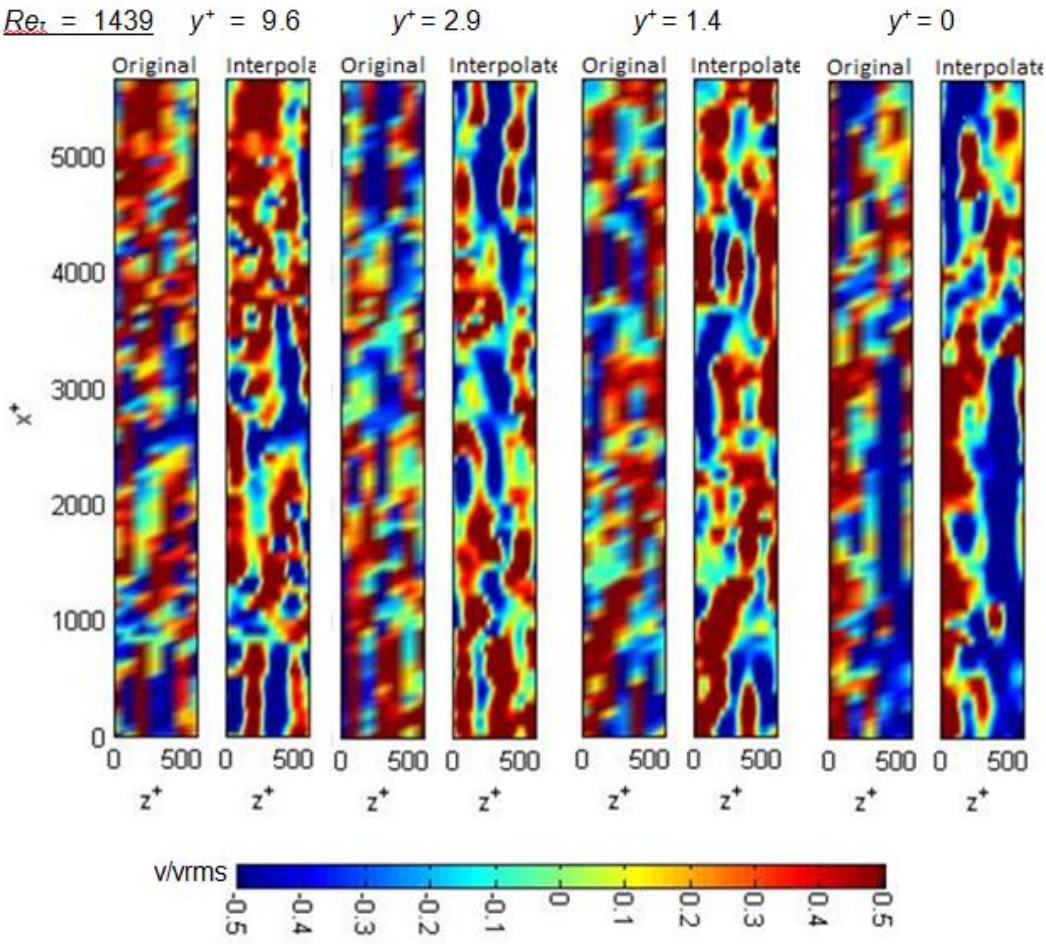


Figure 115: Streamwise- Spanwise instantaneous velocity fluctuation maps at 4 *y*+ positions and 3 Reynolds numbers without filter.

In conclusion, the near-wall structures are different between the graphs at different Reynolds number. It is believed that this is mainly due to the spanwise spacing in wall unit between each sensor that differs for each Reynolds number. Indeed, an increase in Reynolds number is followed by a decrease in the spanwise resolution. In the next section, the same number of sensors is used to compare the near wall structures with the same resolution for the three Reynolds numbers.

Less sensors used at lower Reynolds number

To be able to compare the maps of low and high Reynolds numbers such as at Re_τ = 418, 587 and 1439, less sensors are used at lower Reynolds numbers. The spanwise resolution is then similar or close for each Reynolds number. In that way, z_s^+ will be around the same value for all three Reynolds numbers, 93, 88 and 96 at Re_τ = 418, 587 and 1439, respectively.

Table 20: Modification of spacing between sensors at different Reynolds numbers

Re_τ	418	588	1439
z_s^+ (wall unit)	93	88	96

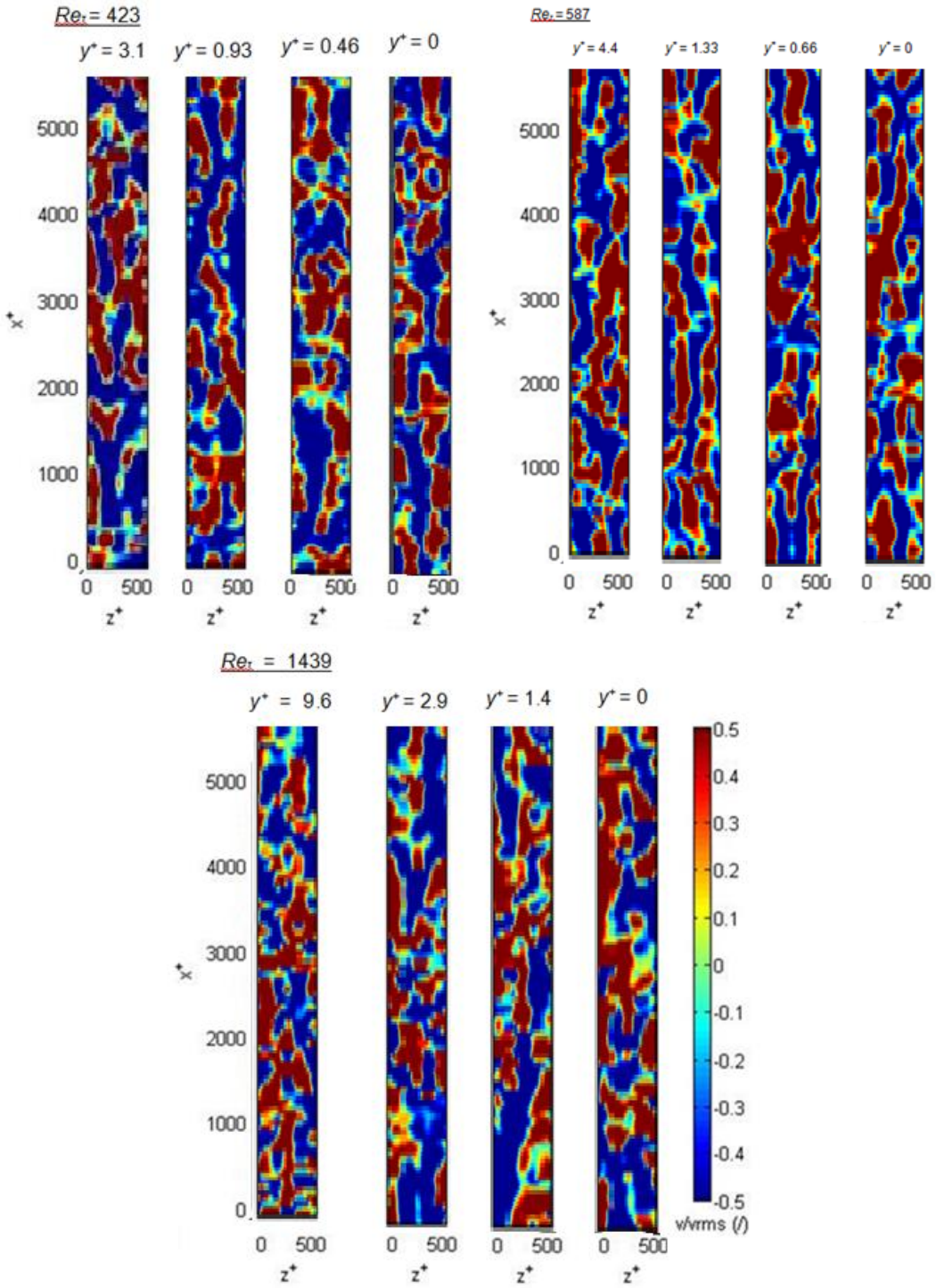


Figure 116: Streamwise- Spanwise instantaneous velocity fluctuation maps at 4 *y+* positions and 3 Reynolds numbers without filter with the spanwise resolution (same spacing between each sensor for all the Reynolds numbers).

It can be seen from Figure 116, that when the sensor spacing is almost equal for all the Reynolds numbers, the patterns seem identical. The streaks have the same length in streamwise direction and the same width in spanwise direction.

By comparing Figure 115 and Figure 116, at Re_τ = 418 and 587, it seems that the patterns are affected by the spanwise resolution due to the spanwise spacing between the sensors, the sensors number decrease with an increase in Reynolds number for the range $0 < x^+ < 500$.

5.2.1.2 Analysis and comparison of experimental filtered results

Several filter sizes were applied in the streamwise direction for median filtering operation in the aim to find patterns which could be large-scale footprint candidates. The use of filter enable us to distinguish and see more clearly the large patterns as without it, in Figure 127, 128 and 129, small and detached patterns make it difficult to visualise the large patterns. Also, it seems in good agreement with the filter size used by Hutchins et al (2011), 0.5δx0.16δ in streamwise and spanwise direction, respectively (corresponding to 209x67, 293x94 and 720x230 wall unit at Re_τ = 423, 568 and 1310 respectively) as they were also looking at large-scale structure. Although their Reynolds number was much higher, Re_τ = 14150 and they used another filter technique, 2D Gaussian filter.

y-position effect

At Re_τ = 423 and 1310, for the data filtered at 2δ in the streamwise direction, it seems that the patterns, low and high speed streaks (blue and red colour respectively) at different y^+ positions are the same. The y-position does not influence the structures of the instantaneous skin-friction within the viscous sublayer.

Although for higher filter size such as 20δ, the structures are longer near the wall than further from the wall. These structures are similar to the know streaks observed by Kline et al. (1967) but the visualised structures in the present work have longer length scale as their streaks are not that long.

Re_τ effect

Figures 127, 128 and 129 show the presence of meandering low- and high fluctuating voltage regions. In the case of Re_τ = 423, a few streaks of negative (blue colour) and positive fluctuations (red colour) are alternating. At higher velocity, it seems that these streaks of positive fluctuation are longer and clearly exhibit a large-scale pattern. At Re_τ = 1310, the streamwise size of the structure that appear are longer than at Re_τ = 423.

From Table 25, it can be said that the structures size in the spanwise and streamwise directions increase with an increase in Reynolds number. Indeed, at Re_τ = 1439 the structure width goes up to 400 w.u. for a length up to 5500 w.u. and decreases to 200 w.u and 3000 w.u., respectively for the width and length dimensions, for lower Reynolds number. It is important to note that this conclusion is given with spanwise spacing, z_s^+, for the three Reynolds number are different and affect the data as explained earlier due to the spanwise spacing between the sensors increasing with an increase in Reynolds number. The spanwise resolution at higher Reynolds number might not be sufficient even though we are interested in large structures (Table 24).

Table 21: Near-wall structures frequency of streamwise and spanwise length at different Reynolds numbers

Re_τ	428		568		1310	
	wall unit	%	wall unit	%	wall unit	%
x+	3000	33	3200	31	5500	29
z+	200	66	200	64	400	59

Table 22: Figure Legend

Reτ		423	568	1310
		z^+ - x	z^+ - x	z^+ - x
Filter size	(a)	none	none	none
	(b)	93w.u. - 2δ	88w.u. - 2δ	96w.u. - 2δ
	(c)	93w.u. - 20δ	88w.u. - 20δ	96w.u. - 20δ

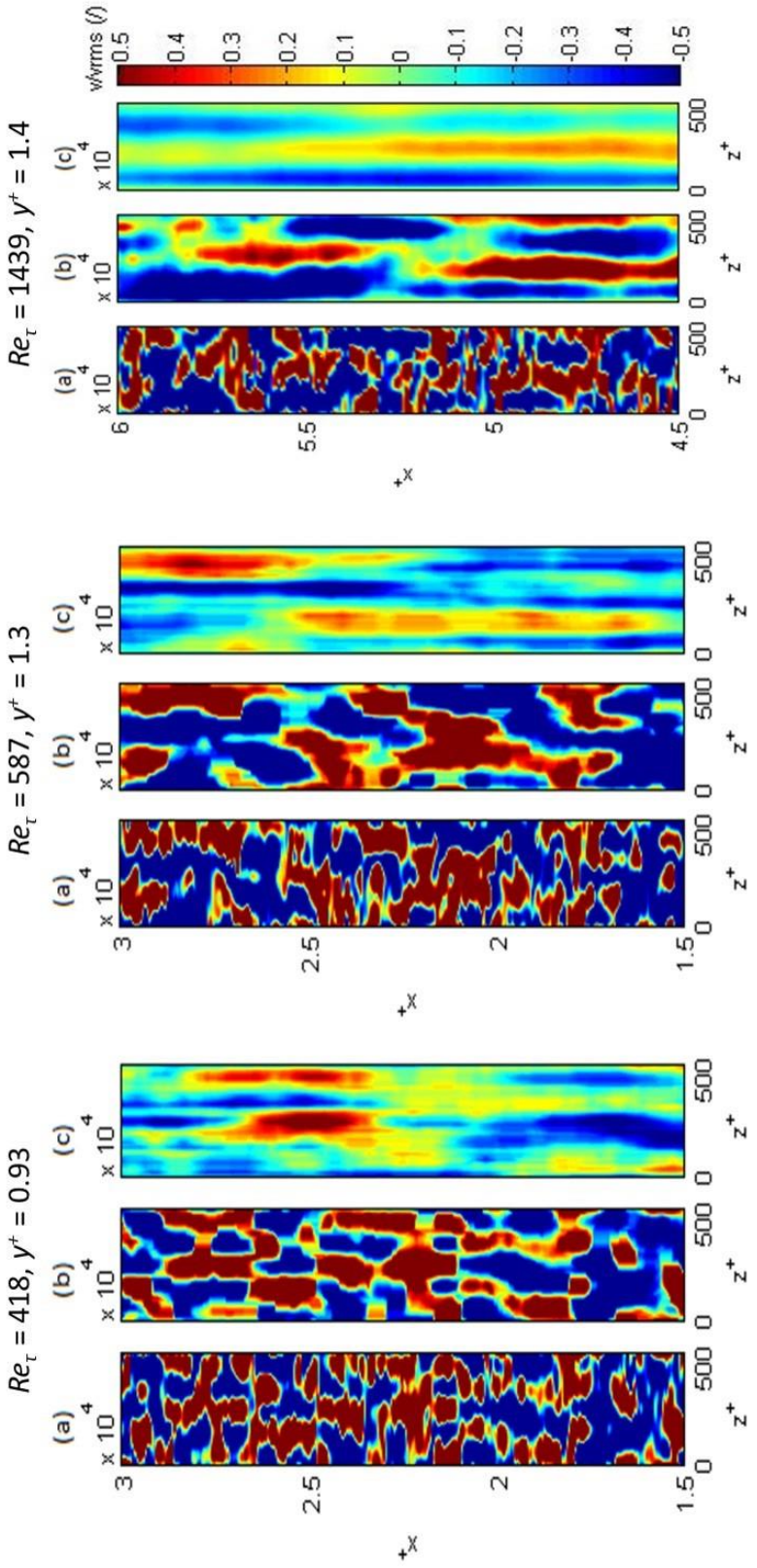


Figure 117: Streamwise- Spanwise instantaneous voltage fluctuation maps at different Reynolds Number and at *y*+ = 1. a) No filter. b) 93, 88 and 96 w.u. x 2δ filter size. c) 93, 88 and 96 w.u. x 20δ filter size

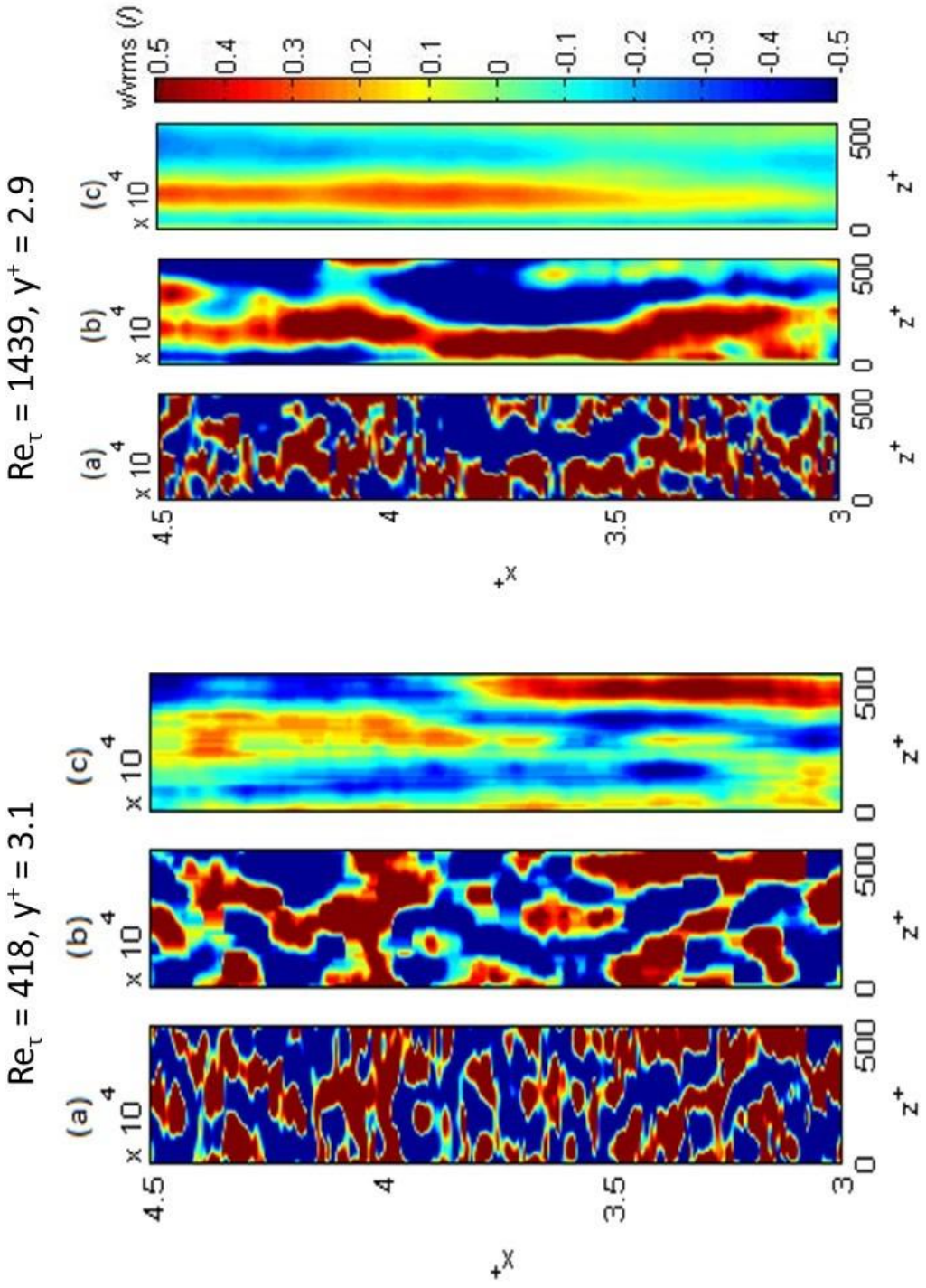


Figure 118: Streamwise- Spanwise instantaneous voltage fluctuation maps at different Reynolds Number and at y+ = 3.

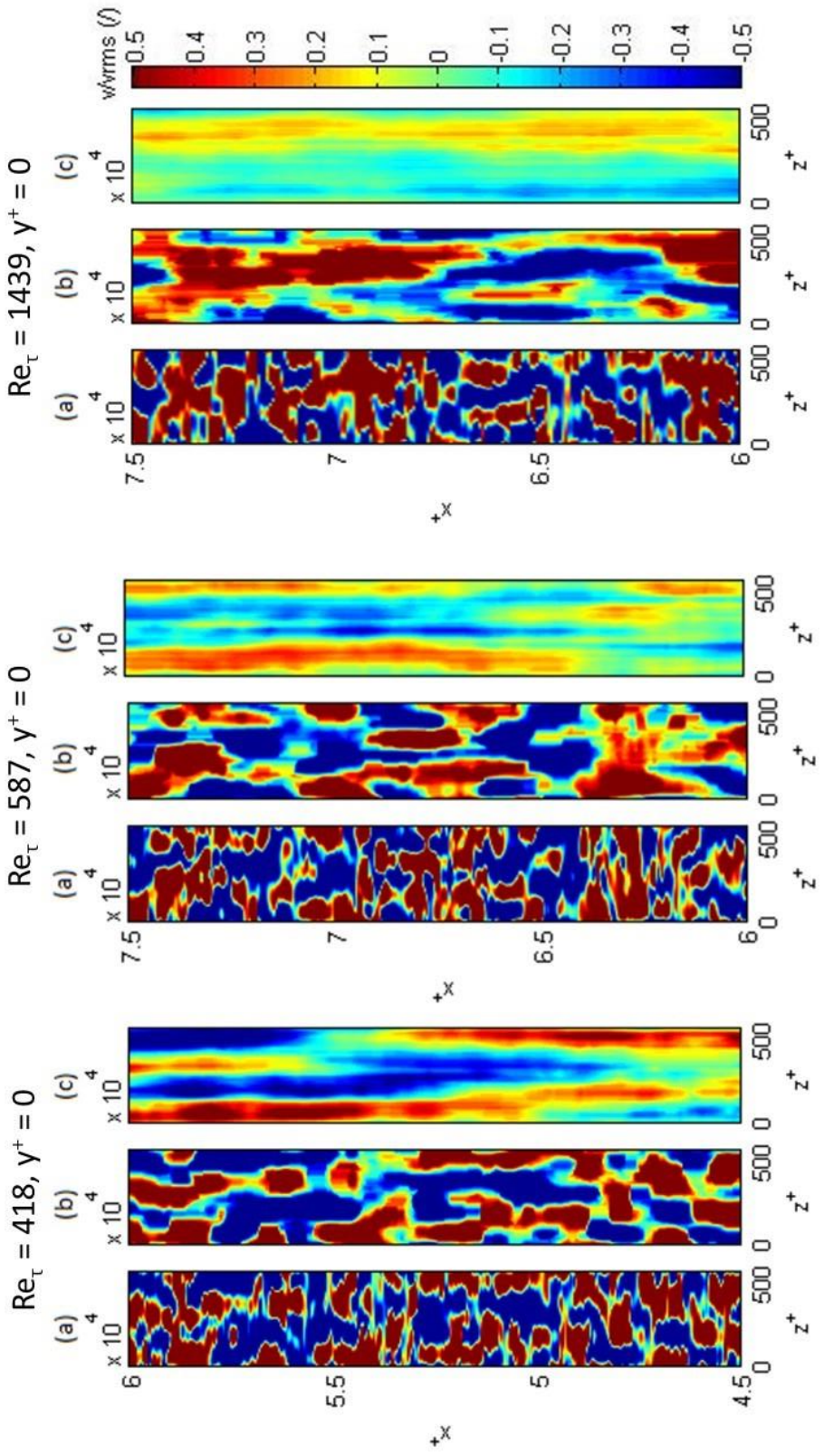


Figure 119: Streamwise- Spanwise instantaneous voltage fluctuation maps at different Reynolds Number and at y+ = 0.

Conclusion

To sum up, a streamwise–spanwise plane was reconstructed using a convection velocity equal to $13u^* \approx 0.60U_\infty$ from a sample segment from the rake of sensors placed in the viscous sublayer region.

The unfiltered signals show the appearance of small-scale “streaky” patterns. After the application of the filtering discussed earlier, the instantaneous streamwise–spanwise (*x-z* plane) skin-friction maps show long distinct alternating regions of positive and negative fluctuations. Those positive and negative fluctuations are respectively the high and low fluctuating velocity regions. They are revealed and appeared more clearly in the velocity fluctuations in the filtered plots. They seem to be recognised as large-scale structures patterns. At $Re_\tau = 1439$, a very long meandering feature appears to snake through the measurement domain for over 4000 w.u.

It can be suggested that the positive and negative dominant regions present in the instantaneous velocity fluctuations might correspond, respectively, to the high- and low-speed regions in the large and very large-scale motions in the outer layer as they appear to have the same streamwise and spanwise scale. Moreover, this can be supported by the results obtained by Abe, Kawamura and Choi (2004) in DNS of turbulent channels, indicating that the very large-scale structures existing in the instantaneous wall shear-stress fluctuations for $Re_\tau = 640$ are essentially phenomena associated with the very large-scale motions existing in the outer layer of the flow. Those very large-scale patterns according to them, have a spanwise spacing of about 1.3–1.6δ (about 1000 in wall units for $Re_\tau = 640$).

Large-scale structures have been observed with lengths as large as 20δ (δ is the boundary layer thickness) in the streamwise direction and significantly contribute to the total turbulent stress. Further, it is observed that such features in the flow leave a statistical footprint in the instantaneous skin-friction (Hutchins et al., 2011). In our study, the length of the large-scale pattern found at $Re_\tau = 1439$ was 5500 wall unit so 4δ.

These plots illustrate some of the recognised emergent features in the log region such as hairpin with length, found in our 2D investigation performed at the same Reynolds number $Re_\tau = 568$, of 1500 wall unit. A number of previous

studies have reported similar patterns of relatively low and high-speed velocity regions in the logarithmic region of wall-bounded turbulent flows over a wide range of Reynolds numbers (Ganapathisubramani et al., 2006, Monty et al., 2007, Hutchins and Marusic, 2007a). Those structures meander in the spanwise direction and cover a large streamwise domain (Hutchins and Marusic, 2007a). Recently, many authors found that large-scale motions modulate the small-scale components of the velocity fluctuations and the extent of modulation depends on Reynolds Number (Hutchins and Marusic, 2007b, Mathis et al., 2009a).

At the present study, it is found that near-wall structures in the viscous sublayer seem to share the characteristics with the hairpin structures present in the logarithmic region from our 2D investigation with PIV. The signature, of the large scale, takes a form resembling large streamwise structures. Elongated and meandering low and high skin-friction regions at the wall exist and share sufficient similarities such that they are almost certainly related to the large-scale structures in the logarithmic region.

5.3 Skewness and kurtosis measurements with respect to the Reynolds Number Dependence

The skewness and kurtosis factors of the instantaneous velocity, for twenty sensors were measured at four different y-positions.

Skewness and kurtosis factors are function of y^+ and decrease with an increase in y^+. The position of the sensors from the wall, at y = 0.5 mm, was found to have a standard deviation of 0.08 with position values ranging from 0.38 to 0.73 mm. At y = 0.15 mm, standard deviation was of 0.04 with position values varying from 0.06 to 0.21 mm. As for the ~ 0 mm position, it was an attempt to put the sensors as close as possible to the wall below y = 0.17 mm and the 0 mm position is the second attempt to reach the wall with another camera as explain in 3.1.1.1.

It can be seen from Table 23, that the skewness and kurtosis factors at 0 mm are significantly higher than those at 0.5 mm, indicating that the fluctuation is more intermittent at the wall. Indeed, as the wall is approached, the factors increase, indicating the highly intermittent character near the wall.

Moreover, the skewness is positive at all the wall-normal positions indicating that the distribution has a longer positive tail as compared with the negative tail. This indicates that large negative fluctuations are not as frequent as large positive fluctuations. Skewness and kurtosis values measured by other investigators (Alfredsson et al., 1988, Moser et al., 1999, Schlatter et al., 2009, Keirsbulck et al., 2012) are shown in Table 24.

Table 23: Skewness and Kurtosis at various Reynolds number and y^+ positions for 20 sensors

	Re_τ	y^+	*rms*	*S*				*K*			
			(V)	min	max	mean	σ	min	max	mean	σ
0.5 mm											
2.2 m/s	423	3.1	0.036	0.19	0.62	0.48	0.10	2.5	3.1	2.8	0.15
3.2 m/s	568	4.4	0.047	0.06	0.47	0.22	0.09	2.4	2.8	2.5	0.11
7.4 m/s	1310	9.6	0.062	-0.02	-0.37	-0.19	0.09	2.4	2.6	2.4	0.05
0.12 mm											
2.2 m/s	423	0.93	0.018	0.85	1.3	1.0	0.12	3.8	5.7	4.7	0.56
3.2 m/s	568	1.33	0.029	0.55	1.1	0.84	0.14	3.1	4.7	3.9	0.47
7.4 m/s	1310	2.87	0.060	0.05	0.59	0.37	0.13	2.4	3.3	2.9	0.23
~0 mm (trial 1)											
2.2 m/s	423	~0	0.015	0.91	1.3	1.1	0.12	4.1	7.0	5.2	0.79
3.2 m/s	568	~0	0.026	0.77	1.2	0.96	0.11	3.6	5.3	4.4	0.46
7.4 m/s	1310	~0	0.056	0.06	0.83	0.52	0.15	2.8	4.2	3.2	0.33
0 mm (trial 2)											
2.2 m/s	423	0	0.012	0.93	1.3	1.1	0.11	4.4	6.1	5.2	0.54
3.2 m/s	568	0	0.020	0.87	1.3	1.1	0.10	3.9	7.0	5.2	0.65
7.4 m/s	1310	0	0.049	0.54	1.2	0.77	0.15	3.2	5.7	3.9	0.55

The standard deviation, σ, is around 0.10 for the skewness factors for the 4 *y*-positions as for the kurtosis factors, it seems that it ranges from 0.05 to 0.8 depending on the *y*-position. The standard deviation for the kurtosis factors being large indicates that the data points tend to be spread out over a wide range of values. For the skewness factors, a small standard deviation indicates that they are clustered closely around the mean.

The skewness and kurtosis factors at 0.5 mm have a much smaller standard deviation than the other three; 0.15 mm, ~ 0 mm and 0 mm, meaning that its values are all close to their mean value. This can be explained by the fact that

the precision in placing all the 20 sensors at the same *y*-position decreases when approaching the wall.

The skewness and kurtosis factors are compared with measurements from Alfredsson et al. (1988), Moser et al. (1999), Schlatter et al. (2009) and Keirsbulck et al. (2012) with Reynolds number given in Table 20 and shown in Figure 120. Agreements among the values are satisfactory for y^+ near 0 at Re_τ = 423 and 568 but as the Reynolds number increases to 1310, the value decreases for the skewness. For the kurtosis, the factors also decrease with an increase in Re_τ but this time, there exists a significant discrepancy.

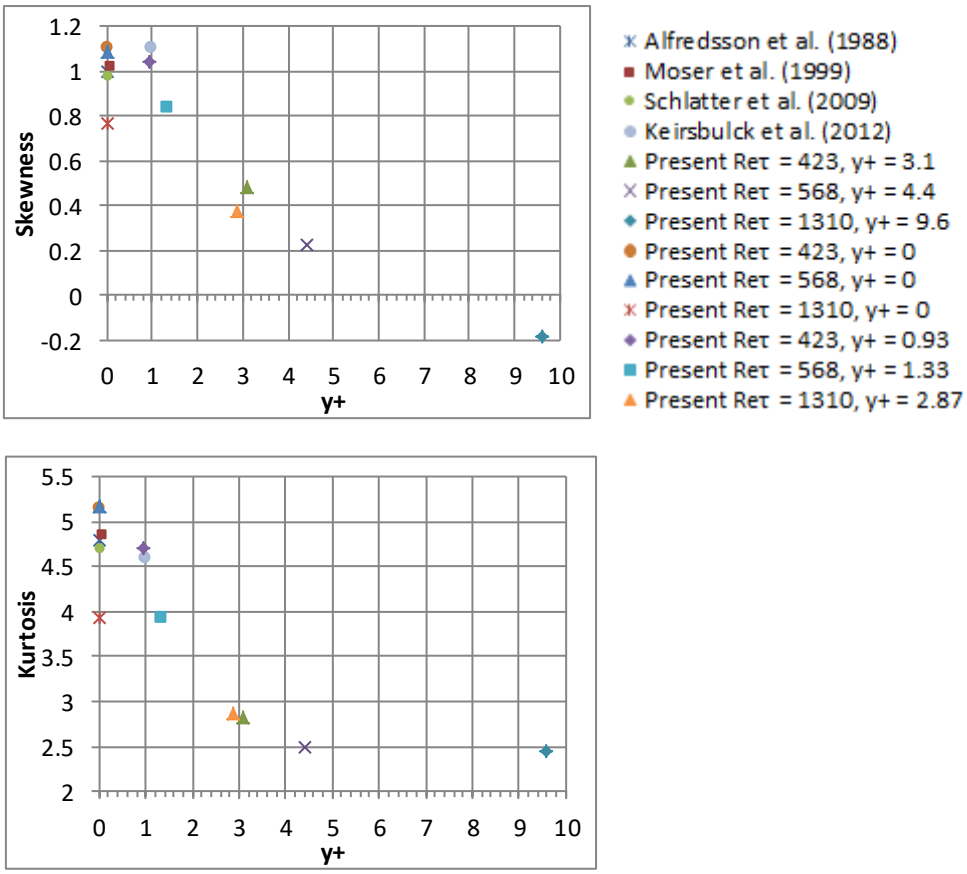


Figure 120: Skewness and Kurtosis with authors listed in Table 6 (right: $y^+ < 1.4$).

These results led to the conclusion that the sensors are not at the wall but close to the wall with value of $y^+ < 0.93$, 1.33 and 2.87 for Re_τ=423, 568 and 1310, respectively. Although the closer the sensors are to the wall, the smaller is the variation in the factors. An increase of the free-stream velocity, U_∞ was observed from 60% at 0.5 mm to 9% at 0 mm for the skewness factor and from 39% to 24% from 0.15 mm to 0 mm. It can also be concluded that our values

approach those of Alfredsson et al. (1988), Moser et al. (1999) and Schlatter et al. (2009) when approaching the wall.

Results for skewness and kurtosis of the velocity fluctuations measured with the 55P16 probes at three different Re_τ for $y^+ = 0$, are compiled in Table 24. The skewness and kurtosis factors measured at 7.2 m/s, $Re_\tau = 1310$ are quite far to the values obtained from other investigators. The difference can be explained by the fact that the *y*-positon for $Re_\tau = 1310$, was different for the actual data and those of the authors.

Table 24: Measured moments of the streamwise velocity fluctuations.

Authors	S	K	y^+	Flow	Technique	Re_δ	Re_τ
Alfredsson et al.(1988)	1.00	4.80	0.2	TBL flow	HWA	28000	
Moser et al. (1999)	1.02	4.87	0.044	TCH flow	DNS		587
Schlatter et al. (2009)	0.98	4.71	-	TBL flow	DNS		492
Keirsbulck et al. 2012	1.00	4.80	1	TBL flow	HWA		490
	1.1	4.6	1	TBL flow	HWA		1170
Present	1.1	5.1	< 0.93	TBL flow	HWA		423
	1.1	5.2	< 1.33	TBL flow	HWA		568
	0.77	3.9	< 2.87	TBL flow	HWA		1310

Finally, the kurtosis and skewness factors for the 20 sensors at different *y* positions and Reynolds number were chosen to be compared with papers mentioned in Table 24 and shown in Figure 121.

It seems that the values of the skewness and kurtosis factors for $Re_\tau = 423$ and 1310 are similar when they are at the same y^+ position. Indeed, at $y^+ = 2.87$ ($Re_\tau = 423$) and 3.1 ($Re_\tau = 1310$), the values range around 0.5 for the skewness and 3 for the kurtosis.

For the skewness factors, a mean value of 1.0 at $y^+ = 0$ and $Re_\tau = 423$ was obtained. As for the kurtosis, the value obtained was of 4.7. Those values are in really good agreement with those of Alfredsson et al. (1988), 1.00 and 4.80 and Schlatter et al. (2009), 0.98 and 4.71 for skewness and kurtosis respectively, 2% and 0% of difference which is a good agreement.

At almost 0 mm ($y^+ \sim 0$), values of 1.05 and 4.51 for skewness and kurtosis factors were acquired. A difference of approximately 30% between $Re_\tau = 423$ and 1310 was estimated. Note that this is mainly due to the difference in y+ position, $y^+ < 0.93$ and $y^+ < 2.87$ for $Re_\tau = 423$ and 1310, respectively. A difference of 6.5% and 8.5% for the value of skewness and kurtosis factors can be seen in comparison with data from Moser et al. (1999) and Schlatter et al. (2009). The difference can be explained by the fact that the y-positon is different for the actual data, $y^+ \sim 0$ and those of the authors, $y^+ = 0.044$ and 0.2.

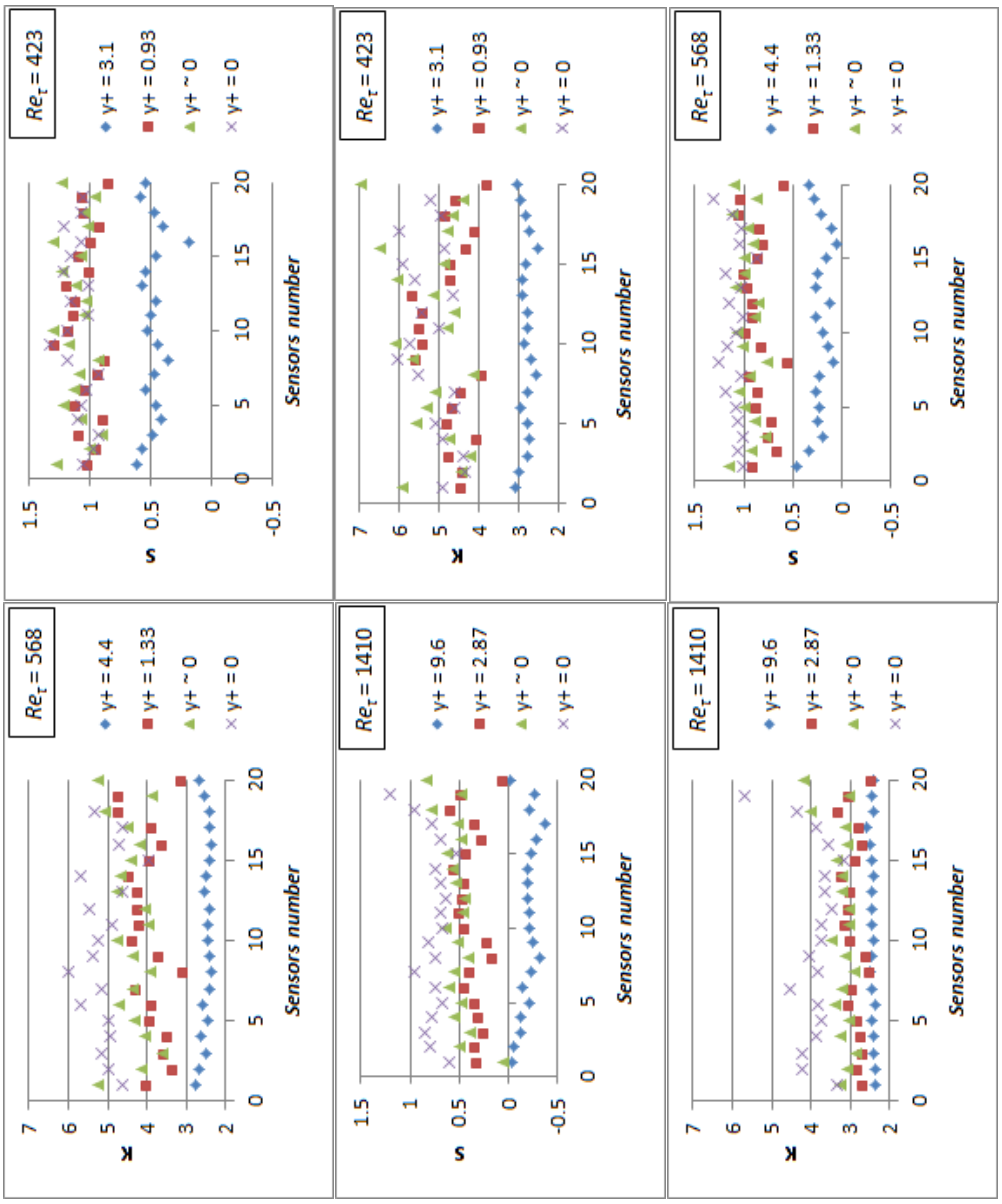


Figure 121: Skewness and Kurtosis at different y+ and Reτ for 20 sensors.

5.4 Cross-correlation measurements with respect to the Reynolds Number Dependence

5.4.1 Cross-correlation measurements with respect to the Reynolds Number Dependence in the spanwise direction

The spanwise two-point correlations of the velocity fluctuations were obtained at the same *x* but different *z* co-ordinates in the viscous sublayer. The two-point correlation coefficient, between the first sensor and all successive one, is defined as

$$\boldsymbol{R_{uu}} = \frac{\overline{\boldsymbol{u_1(t)} \times \boldsymbol{u_2(t)}}}{\sqrt{\overline{\boldsymbol{u_1}^2}}\sqrt{\overline{\boldsymbol{u_2}^2}}} \quad \textbf{(21)}$$

Figure 122 and Figure 124 show the variation of the correlation coefficient in the spanwise, z-direction. The probes location, y^+, is ranging from 0.93 to 9.6.

y^+ effect with Re_τ constant

Two-point correlation functions are plotted at four wall-normal (y^+) locations and shown in Figure 122. It can be seen that the minimum peak magnitude increases slightly with an increase in y^+ positon. This increase trend seems to be higher with an increase in Reynolds numbers as seen in Table 25.

Table 25: Minimum correlations coefficient peak at different Reynolds numbers

	Re_τ = 423		Re_τ = 568		Re_τ = 1310	
	y^+	Ruu_{min}	y^+	Ruu_{min}	y^+	Ruu_{min}
	3.1	0.097	4.4	0.074	9.6	0.056
	0.93	0.084	1.3	0.046	2.9	0.040
	< 0.93	0.068	< 1.3	0.038	< 2.9	0.034
	0	0.065	0	0.020	0	0.022
st.dev.		0.013		0.019		0.012

It is important to note that there is a lack available measurement points. The measurement points reduce with an increase in Reynolds number; at Re_τ = 568, only one point per z^+ = 44 and at Re_τ = 1310, only one point per z^+ = 96 (Table 26). In the range $0 < z^+ < 200$, at Re_τ = 423, 568 and 1310, the measurement points are respectively 7, 5 and 3 which means that the curve

accuracy decreases with an increase in Reynolds numbers. The curves at Re_τ = 1310 and 568 are respectively 2.3 and 1.4 times less accurate than the curve at Re_τ = 423 as less measurement points are available.

Table 26: Spanwise spacing between sensors at different Reynolds numbers

Re_τ	423	568	1310
z_s^+ (wall unit)	31	44	96

For Re_τ = 423, there is a decrease of 13, 30 and 33% between the minimum peak magnitude at y^+ =3.1 and 0.93, < 0.93, and 0, respectively.

In conclusion, the plots of the two-point correlation functions from Figure 122 seem to suggest that, in general, for small separation y^+ distance within the viscous sublayer, the correlation for the velocity in the direction of the displacement in the y-direction is approximately equal. A difference of 4% between the magnitude peak at y^+ < 0.93 and 0 is found at Re_τ = 423. The same cannot be said for Re_τ = 568 and 1310 with difference reaching value of 17 and 15%, respectively but for those Reynolds number, the curves are questionable due to a limited number of data available.

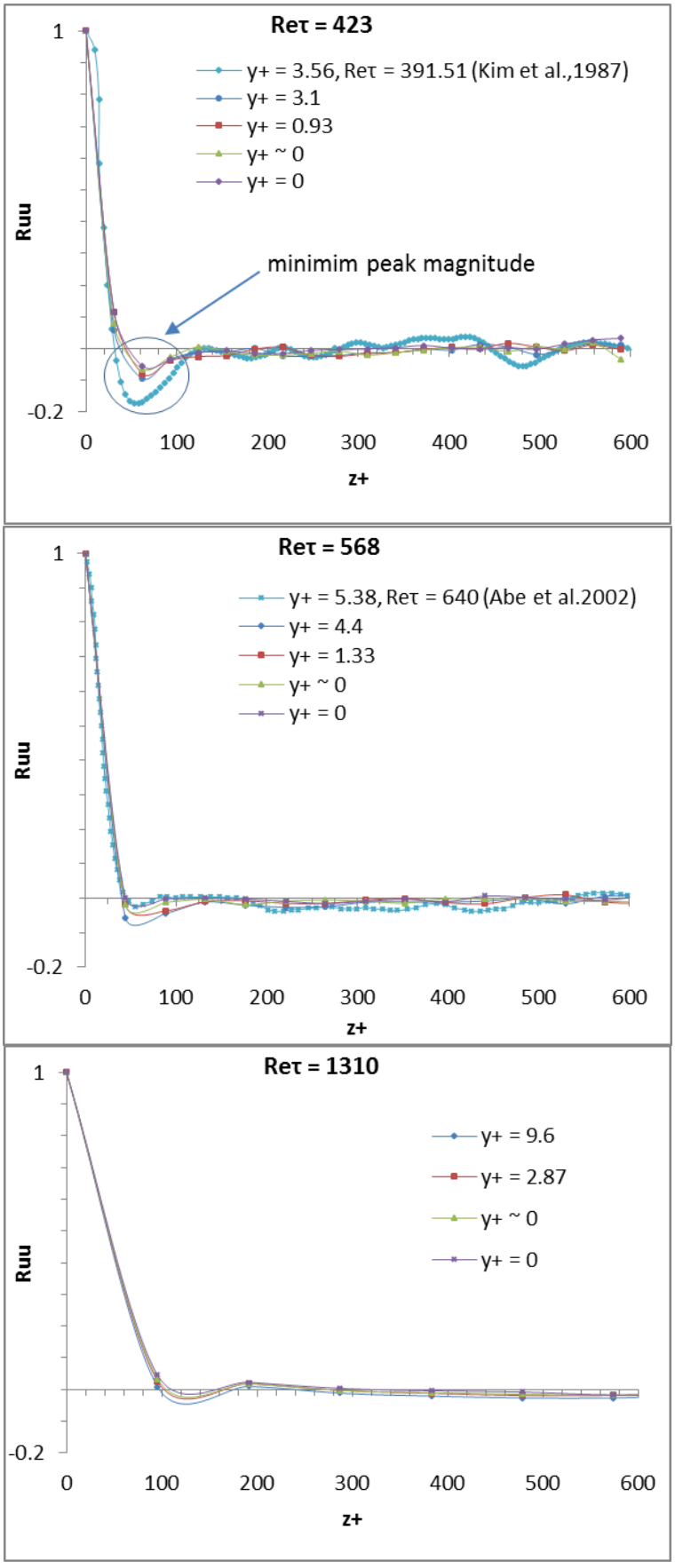


Figure 122: Two-point spanwise correlation coefficients of velocity fluctuations at different Reynolds Numbers and y-locations.

Re_τ effect with y^+ constant

The spanwise spatial correlation function R_{uu} (z^+) changes with the Reynolds numbers are shown in Figure 124.

At y^+ = 0, 3 and 11, it is interesting to note that the near-wall negative peak of the spanwise R_{uu} becomes less prominent with the increase of Re_τ. At y^+ = 11, the spanwise correlation R_{uu} was compared with Kim et al. (1987), Moser et al. (1999) and Abe et al. (2001) as seen in Figure 123 and Figure 122. Note that the comparisons are made at the locations where the y-coordinates and the Reynolds number of the present work with others were closest to each other. A trend is clearly visible at Re_τ = 423 but with an increase in Reynolds number, at Re_τ = 1310, the minimum is less pronounced. The negative lobe of R_{uu} is weaker at higher Reynolds numbers suggesting that coherence at at Re_τ = 1310 is narrower than at Re_τ = 423.

Moreover, the R_{uu} correlation in the spanwise direction drops from 1 to a negative value at z^+ = 17, 42, 45 and 100 for Re_τ being 180, 590, 640 and 1310, respectively. These profiles show that the R_{uu} correlation is narrower in the spanwise direction at low Re_τ than at high Re_τ. In conclusion, the spanwise extent of near-wall structures for low Re_τ is much smaller than for those at higher Re_τ. This seems to be in agreement with findings of Abe et al.(2001) as illustrated in Figure 123. Although it is important to mention that at Re_τ = 1310, the curve is questionable due to a limited number of data at this Reynolds numbers.

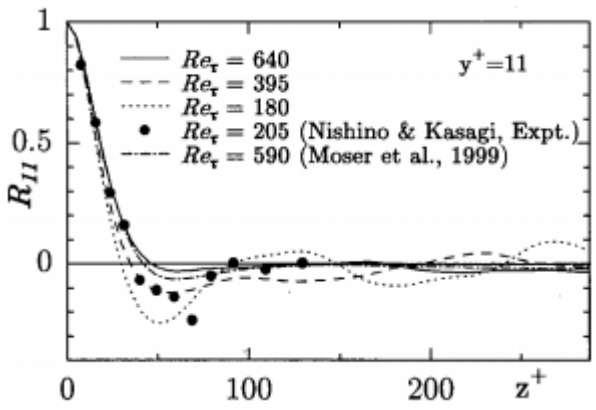


Figure 123: Spanwise two-point correlation coefficient at y+ = 11 from Abe et al. (1972)

At y^+ = 5, the spanwise two-point correlation R_{uu} *was* compared with the experiment by Abe et al. (2001). The results agree well with those of the present investigation, the correlations fall off to zero at around $z^+ = 40$ wall units for both data, except for a deviation at a certain z^+ range $40 < z^+ < 120$ where the minimum peak amplitude is 3 times bigger at $Re_\tau = 587$ than at $Re_\tau = 640$. Also, the correlation coefficient is nearly zero at distance $z^+ > 80$ for $Re_\tau = 640$ compared to 140 for $Re_\tau = 587$.

From the spanwise two-point correlations, it might be concluded that the structures observed near the wall are as narrow as $z^+ = 50$. This is one half of the distance of the low speed separation reported by Kline et al. (1967) and Gupta et al. (1971). The streak spacing was not consistent with our experimental results. The wall layer streaks observed experimentally have a mean spacing of z^+ = 100. This correlation becomes negative and reaches a minimum at z^+ = 50. To confirm this conclusion, more evidences are needed and it might be useful to visualise the streaks in the near wall region because the spanwise correlation might not give the right value of the spanwise size of the near-wall structures.

The plots in Figure 122 seem to show that there are undulations at low Re_τ. Those undulations could be related with large-scale structure. If there are no large-scale structures, we expect the trend to be flat (i.e. with no correlation). Small-scale structure means that the correlation is within that small-scale and it should not correlate with something far away. It might mean that there is a large-scale structure which could involve this. As for higher Re_τ, there are no undulations, the trend is quasi flat. But this can also be related to the limited number of data points at higher Reynolds number compared to low Reynolds number where more data points are available.

In conclusion, the cross-correlation coefficient illustrates a local minimum (peak negative value) followed by a weak positive maximum, the magnitude of the negative peak decreasing as Re_τ increases. The peak values shift away at high Re_τ, while at low Re_τ the peaks are located closer to $x^+ = 0$. One might conclude that the reason for this negative correlation is likely to be associated with the vortical motions, which occur one after the other with opposite signs of rotation. Indeed, this is probably due to the quasi-streamwise vortices and their effect

on the flow field. This reveals the spanwise width of the streamwise vortical structure of the near wall region.

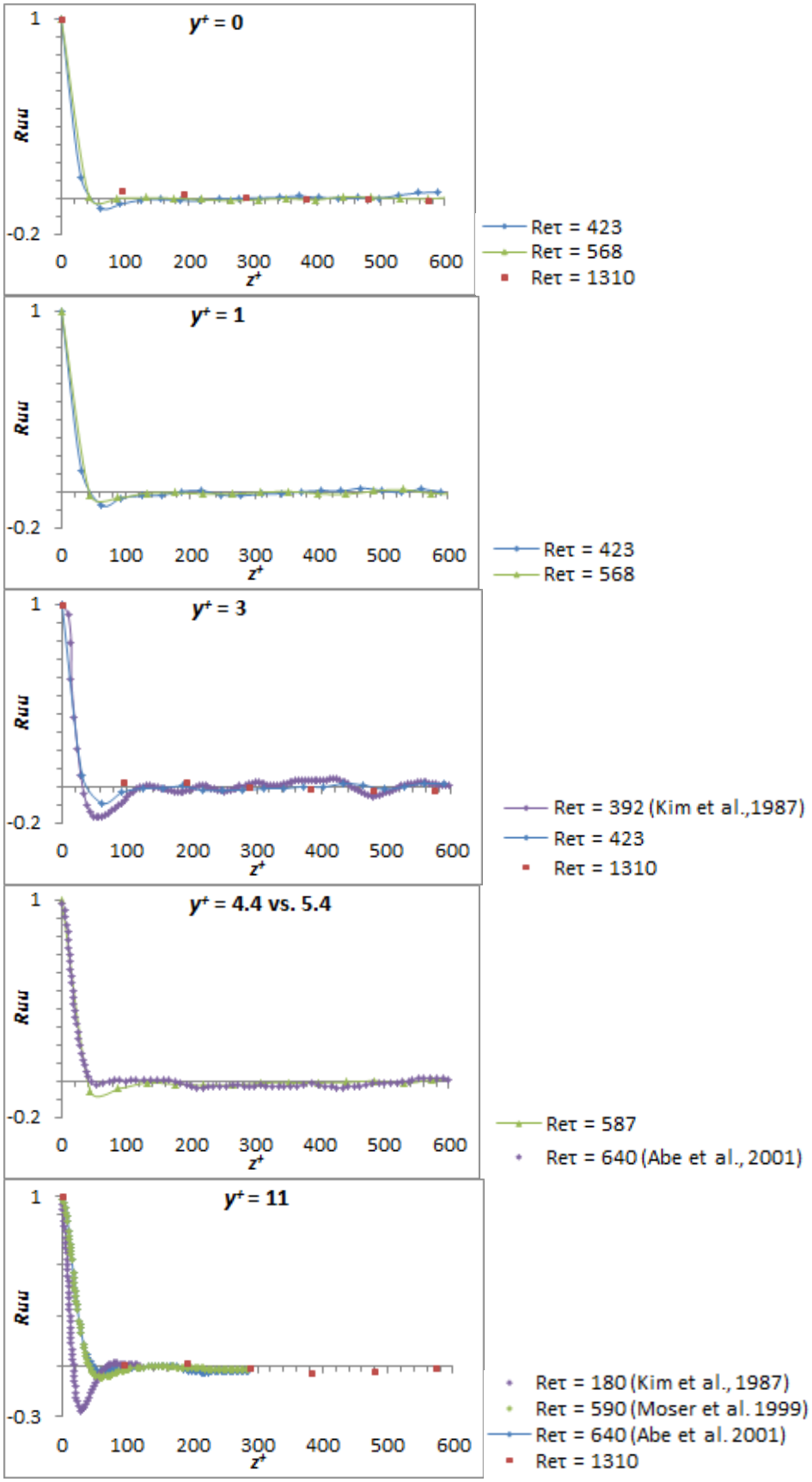


Figure 124: Two-point correlations in the spanwise direction at different y^+ locations from the wall.

5.4.2 Cross-correlation measurements with respect to the Reynolds Number Dependence in the streamwise direction

The normalised auto-correlation function of velocity fluctuation is defined as:

$$R_{uu} = \frac{\overline{u(t) \times u(t+\tau)}}{\overline{u}^2} \quad (22)$$

For a single-point measurement, where τ is the time lag, $\overline{u}$ is the time averaged velocity component.

The correlation coefficient quantifies the amount/degree of common variation between a variable sampled at time t and that same variable sampled at a later time, $t+\tau$. It is a correlation of variable with itself. At time t, the series is perfectly correlated with itself (i.e. has the same value) at exactly time t. In other words, the autocorrelation measures the persistence of a signal within the whole duration of time or space series. The capability to determine persistent signal or within a series is particularly valuable because the regular variation might be associated with a physical phenomenon such as an eddy.

$R_{uu}(\tau)$ was converted to $R_{uu}(x^+)$ by using Taylor's hypothesis (Taylor, 1938),

$$x = -U_c \cdot t \quad (23)$$

where U_c is the convective velocity, t the time and x the streamwise direction.

Figure 125 and Figure 126 show a typical curve of the distribution of the normalised autocorrelation of the streamwise instantaneous voltage for a single point analysis in a developing boundary layer above a flat plate. The correlations curves are measured in the x- direction at 4 y-locations- one at the wall and the others further away from the wall and at different free-stream velocities. The curve has the correlation coefficient as the vertical axis and x^+ as the horizontal axis.

Re_τ effect with y^+ constant

The slow decay of $R_{uu}(x^+)$ for increasing x^+ indicates that near the wall, the structures are highly elongated in the streamwise direction. It is evident from these figures that R_{uu} correlations are shorter in the streamwise direction at low Re_τ than at high Re_τ, indicating a reduced streamwise spatial coherence. The R_{uu} correlations extend up to $x^+ = 825$, 1090 and 2556 for $Re_\tau = 418$, 587 and

1439 (taken from 20 sensors), indicating the presence of long streamwise region, with the maximum length over which correlation exists, increasing with the Re_τ. This is a typical feature of an auto-correlation function in one direction. The length obtained from $R_{uu}(x+)$ is a minimum extent of those streaks as they meander which considerably reduces the length scales of the correlation. From the results presented it can be concluded that streamwise (x^+) elongated structures exist.

All values of R_{uu} are reduced when x^+ increases, the reduction increasing as Reynolds number increases. While the reduction of R_{uu} for Re_τ=418 occurs over a portion of $x^+ \leq 825$, the reduction of R_{uu} for Re_τ = 1439 occurs only for $x^+ \leq 2550$. It is interesting to observe that, for Re_τ = 418, R_{uu} becomes zero at about x^+ = 825, whilst for higher Re_τ, R_{uu} become zero at x^+ = 2556, suggesting possibly that the structure has a longer streamwise length scale than the other two Re_τ. The reduction observed in the autocorrelation coefficients suggests a change in the size of the long near-wall structures with Reynolds number.

y^+ effect with Re_τ constant

Comparison of the plots reveals that the streamwise length of the correlations does not seem to change much with the y^+ position in the near-wall region. This might be due to the fact that the probes are within the viscous sublayer.

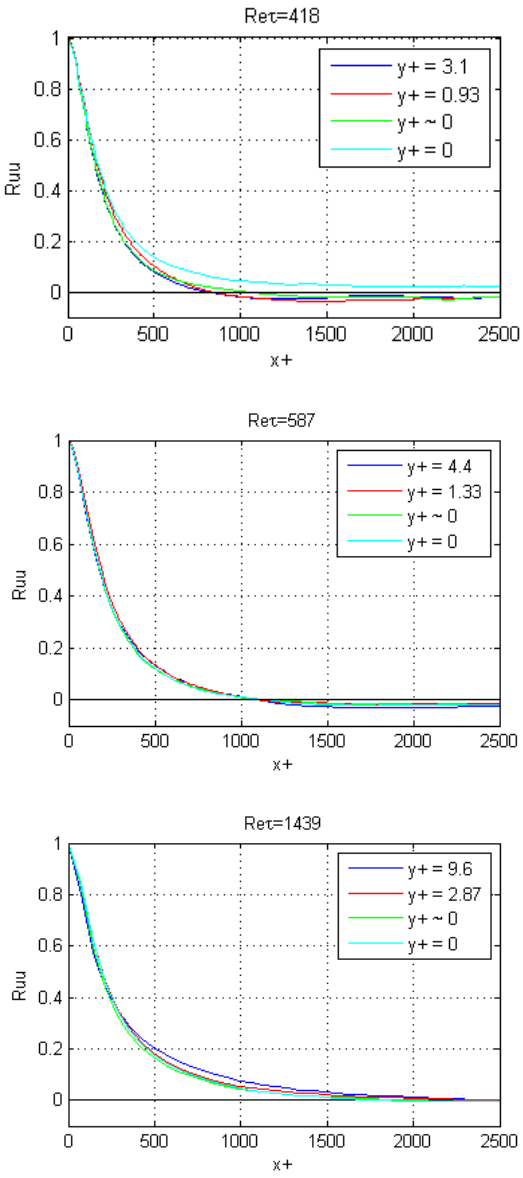


Figure 125: Two-point streamwise correlation coefficients at different Reynolds Number

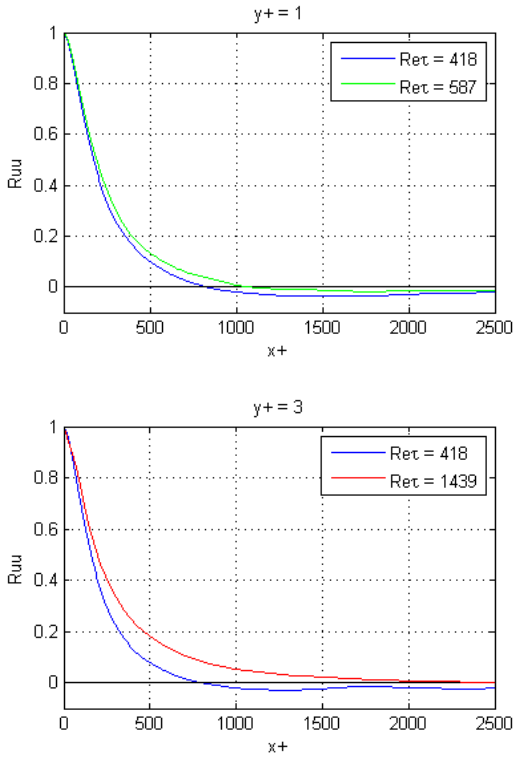


Figure 126: Two-point correlations in the streamwise direction at different locations from the wall.

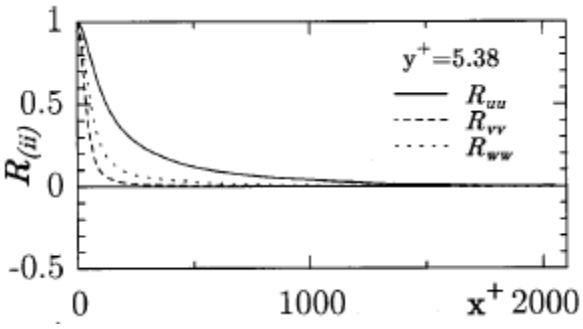


Figure 127: Two-point streamwise correlation coefficients of velocity fluctuations at Re_τ = 640 from Abe et al (2001)

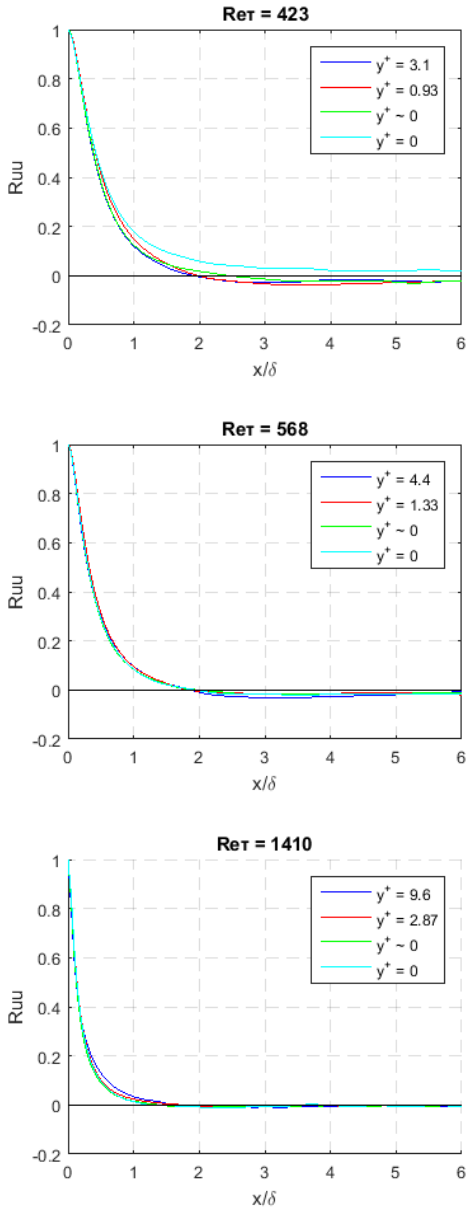


Figure 128: Two-point streamwise correlation coefficients at different Reynolds Number

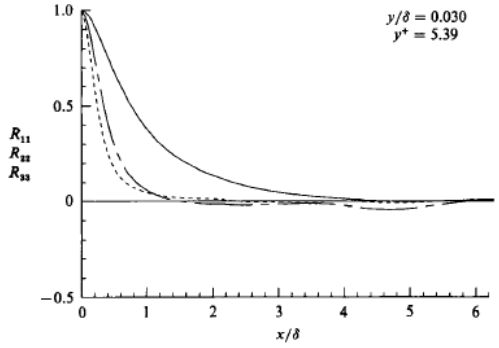


Figure 129: Two-point streamwise correlations Re_τ = 180 from Kim et al. (1987)

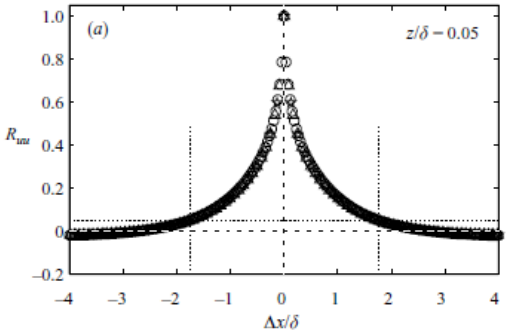


Figure 130: Streamwise correlations of the streamwise velocity fluctuation Ruu at (●) Re_τ = 1120 (Note their z-direction is our y-direction) from Hucthins et al. (2007a)

Those findings are in agreement with the findings of many authors (Kim et al., 1987, Willmarth, 1972, Hutchins and Marusic, 2007a) and shown in Figure 129, Figure 127 and Figure 130.

Length scale over boundary layer thickness at several Re_τ

A graph of length scale over boundary thickness at Re_T = 423, 568 and 1410 is presented, and compared to prior DNS results.

At Re_T = 423 and 568, the length scale over boundary layer thickness decreases from the wall up to the log region as seen in Figure 131. In the other hand, at Re_T = 1410, an increase is seen from the wall up to the log region. The late results are in line with the experimental work of Hutchins et al. (2007a) done at Re_T = 1120.

Considering Table 27, we note that the streamwise length scale over boundary layer seems to decrease with an increase in Reynolds numbers. From Re_T = 423 to 1410, a drop of 9% is observed in the length scale over boundary later thickness and 8% from Re_T = 423 to 568 at the same y+ position, respectively 3 and 1. It seems that the decrease effect is more important at lower Reynolds number, a reduction of 59% is noted for the length scale over boundary layer from Re_T = 180 (DNS data) to 568.

A universally applicable outcome from the length scale of turbulent structures observed in this section is demonstrated and compared to those discovered by DNS and by experimentation of prior investigations.

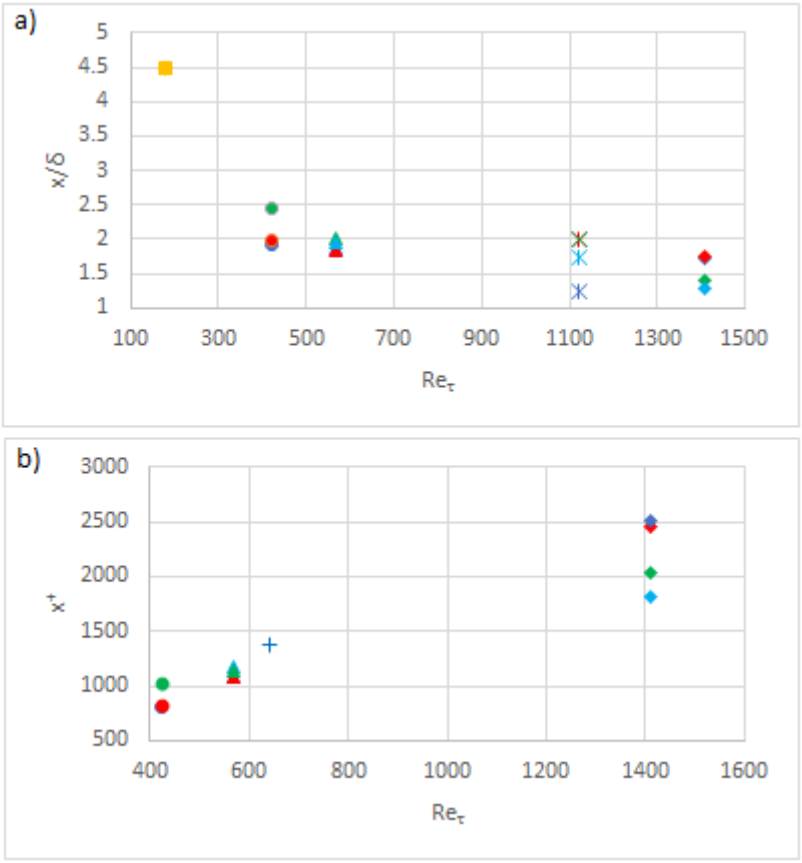


Figure 131: Length scale over boundary layer thickness at Reτ = 423, 568 and 1410.

Table 27: Length scale over boundary layer thickness at Reτ = 423, 568 and 1410.

Present - Experimental				Hutchins et al. (2007a) - Exp.			
Re_τ	y^+	x/δ	x^+	Re_τ	y^+	x/δ	x^+
423	3.1	1.92	803	1120	2.67	1.25	/
423	0.93	1.99	830	1120	0.8	2	/
423	~ 0	2.46	1026	1120	0.53	2	/
568	4.4	1.86	1092	1120	0.27	1.75	/
568	1.33	1.84	1081	Kim et al. (1987) - DNS			
568	~0	2.00	1174	Re_τ	y^+	x/δ	x^+
568	0	1.95	1143	180	5.39	4.5	/
1410	9.6	1.71	2453	Abe et al. (2001) - DNS			
1410	2.87	1.75	2519	Re_τ	y^+	x/δ	x^+
1410	~0	1.41	2031	640	5.38	/	1375
1410	0	1.27	1819				

5.5 Chapter Summary

Detailed information about the flow in the immediate vicinity of the wall is given in this chapter.

A spanwise array of hot-wire probes is used to examine the skin-friction fluctuations at different Reynolds number. The time-series fluctuating skin-friction data from the probes indicate the presence of structures that extend to large streamwise distance (5000 wall unit). As we move to higher Reynolds numbers, the patterns are longer and larger. Such skin-friction patterns seem to share similarities with those observed in the logarithmic region investigated in our 2D PIV results. Those data seem to support the assumptions proposed by many authors (Ganapathisubramani et al., 2012, Agostini and Leschziner, 2014a). Assumptions that small-scale structures are influenced by the passage of outer layer large-scale events (Hutchins and Marusic, 2007b, Mathis et al., 2009a).

Two-point correlations were obtained in the streamwise and spanwise directions using Taylor's hypothesis. The streamwise fluctuations are correlated for larger distances compared to the spanwise fluctuations suggesting the presence of long narrow structures. The signals are highly correlated in the streamwise direction, suggesting that it affects a large region and that the streamwise structures are quite long, $x^+ \leq 2500$. However, the spanwise correlation was much less, suggesting that the events are relatively thin, $z^+ \leq 100$. The data also seem to indicate an increase in the streamwise length with a decrease in Reynolds number. The spanwise length should grow with increasing wall-normal distance (Hutchins et al., 2005) but in our case, it seems that there is no change or really minimal change. In general, the rate of growth is found to be approximately linear across the boundary layer (Hutchins et al., 2005). This being said, it is important to bear in mind that the data points at higher Reynolds number were not sufficient for the two-point spanwise correlation to make such a statement.

A universally applicable outcome from the length scale of turbulent structures observed in this chapter is demonstrated and compared to those discovered by DNS and by experimentation of prior investigations. First, it is interesting to

see that at low Reynolds number, $Re_\tau \leq 568$, the length scale over boundary layer thickness decreases from the wall up to the log region but, in the contrary, for $Re_\tau = 1410$, an increase is seen from the wall up to the log region. Finally, we note that the streamwise length scale over boundary layer seems to decrease with an increase in Reynolds numbers, this decrease effect seems to be more important at lower Reynolds number.

Chapter 6 On the relation of large-scale structures and skin-friction

6.1 Introduction

It seems that very large scale structures that exist in the outer layer, are visible in the instantaneous wall skin friction fluctuations as suggested and analysed by Abe et al. (2004) in their instantaneous DNS data at $Re_\tau = 640$.

Their DNS work is the motivation of the present experimental investigation to study the correlation between the instantaneous wall skin-friction fluctuation signal and the fluctuating velocity signal in the buffer and logarithmic region at $Re_\tau = 568$.

The skin-friction is measured using twenty hot-wire sensors placed within the viscous sublayer of the turbulent boundary layer and the large-scale structures are identified using stereoscopic PIV (s-PIV). The main point is to take the data from hot-wire sensors and s-PIV simultaneously and use Taylor's frozen turbulence hypothesis, to evaluate the spatial structure based on time-resolved single-point measurements (relating temporal to spatial fluctuations in turbulent flows).

6.2 Effect of large-scale structures on the wall skin-friction fluctuations

The data from hot-wire array and s-PIV were taken at two different streamwise positions;

- at the same x^+ position, s-PIV is located directly beneath the hot wire
- s-PIV placed 310 mm upstream of the hot-wire array in x-direction. For the results to be comparable, the distance in x (310 mm) was divided by the convection velocity.

Skin-friction signals and velocity distribution were compared side-by-side at different times t_0 (three times 4000 image pairs, 12000 in total, were investigated at $Re_\tau = 568$ and $Re_\tau = 1310$). For briefness, one interval of data is

shown in this thesis at Re_τ = 568 to be in line with DNS study of Abe et al. (2004).

6.2.1 PIV plane at same level as hot-wire rake

The interrogation area size chosen for the following set of data is also 16 x 32 in *y* and *z*-directions, respectively.

The measurement positions between the PIV plane and the hot-wire array are the same. As the thickness of the laser sheet was 5 mm and the holes where the hot-wire sensors were placed were of 4 mm, there is an incertitude of +/- 2.5 mm (27 wall unit). However this is negligible considering that we were interested in large-scale structures with lengths from 2δ (140 mm, 1858 wall unit) to 20δ (1400 mm, 18 580 wall unit).

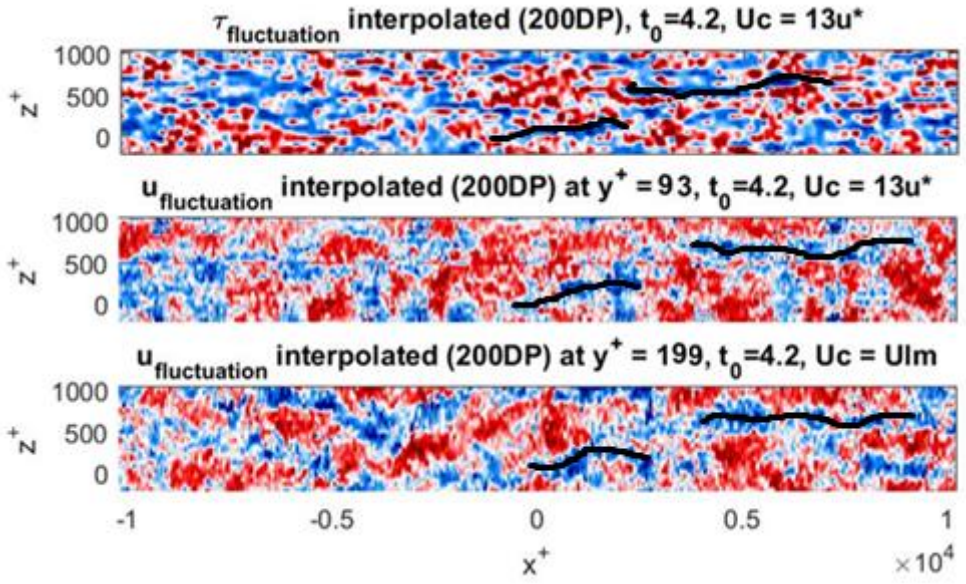


Figure 132: Fluctuating friction signals from the spanwise array and velocity signals from PIV at hole level. Interpolated data

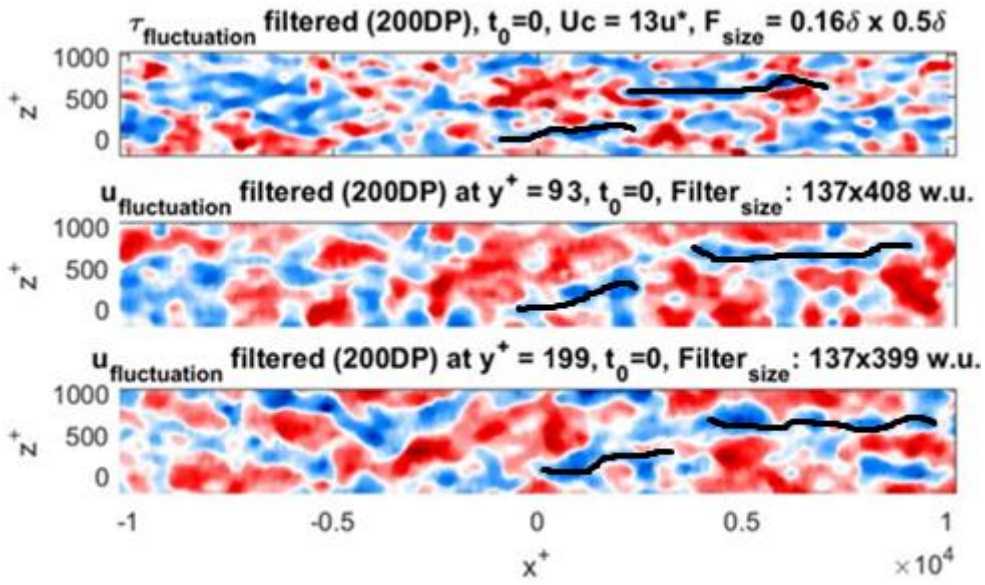


Figure 133: Fluctuating friction signals from the spanwise array and velocity signals from PIV, filter size: 137 x 408 wall unit in the spanwise and the streamwise directions, respectively at hole level. Filtered data

A two-dimensional representation of filtered skin-friction iso-contour is compared with velocity distribution at y^+ = 93 and 199 wall unit. After processing the data by applying a filter, a recognition for positive and negative (red and blue patterns, respectively) patterns between skin-friction and velocity maps is observed. Furthermore, this finding is highlighted by the detection of the long structures using the method of Lee et al. (2014).

6.2.2 S-PIV upstream of hot-wire rake

The interrogation area (IA) size chosen for the following set of data is 16 x 32 pixels in *y* and *z*-directions, respectively.

The hot-wire signals are normalised in such a way that the means of the velocity fluctuations are zero and the standard deviations are one. The data is shown in Table 28.

Table 28: Means and standard deviation of the normalised velocity fluctuations

Channel	τ_{mean}	τ_{rms}
1	0.0006	1
2	0.0041	1
3	0.0001	1
4	-0.0020	1
5	0.0025	1

6	-0.0016	1
7	0.0092	1
8	0.0031	1
9	-0.0005	1
10	-0.0039	1
11	0.0077	1
12	0.0114	1
13	-0.0038	1
14	-0.0069	1
15	-0.0009	1
16	0.0065	1
17	-0.0057	1
18	0.0134	1
19	0.0047	1
20	-0.0003	1

It seems that the mean values of voltage fluctuations (which should be zero) are quite low, of the order of 10^{-4} V for HW. For s-PIV, the mean value of fluctuating velocity at each z position is also in the order of 10^{-4} m/s.

First PIV and HW data were normalised by their root-mean-square (rms) value at each z position. Finally, interpolation of the velocity fluctuations is achieved. For the PIV data, there are 53 data points in comparison with 20 data points for HW in the z-direction. So, interpolation is implemented for both data in the spanwise direction using Piecewise Cubic Hermite Interpolating Polynomial (PCHIP). The number of spanwise interpolation for HW is the same as that of PIV velocity data in the spanwise direction, which is 200 data points.

Original and filtered instantaneous fluctuating skin-friction/velocity

The hot-wire signals and PIV data were time-series data and can be converted into spatial data by using Taylor's hypothesis as $x = -U_c \cdot t$. U_c is the convection velocity of the large-scale events taken to be $U_c = 13u^*$ at the wall and equal to the local mean velocity further away (Krogstad et al., 1998, Atkinson et al., 2015). The convection velocity in the turbulent boundary layer closer to the wall is constant, therefore the velocity signals close to the wall ($y^+ = 13$ and 27) is correlated with the skin-friction signals using the same convection velocity of $13u^*$ (Eq. 23). The signals are filtered using a median filter of different length to isolate only the large-scale signature of the flow.

Results and Discussion

Figure 134 show the original normalised unfiltered data. In those plots, the elongated regions have noisy smaller scale fluctuations within. These small scales are unreliable and can be removed using the median filters discussed in the previous chapter.

A detection method is used to quantify the visual inspections and findings. This detection method is based on the study of Lee et al. (2014). It is based on the fact that the long structures are extracted by using local extrema (shown in black in Figure 134).

A high skin-friction (red color) pattern is identified when the instantaneous skin-friction fluctuation is greater than zero and conversely, a low skin-friction (blue color) pattern is detected when the fluctuation goes below zero. A resemblance of patterns are seen in Figure 134 for s-PIV from y^+ = 27, buffer region to y^+ = 133, logarithmic region. This is in agreement with the DNS finding of Hutchins and Marusic (2007a) at Re_τ = 934, where they showed ((Figure 13, page 21) that the large-scale fluctuations of the logarithmic region (at y^+ = 150) are correlated with the near wall (at y^+ = 15).

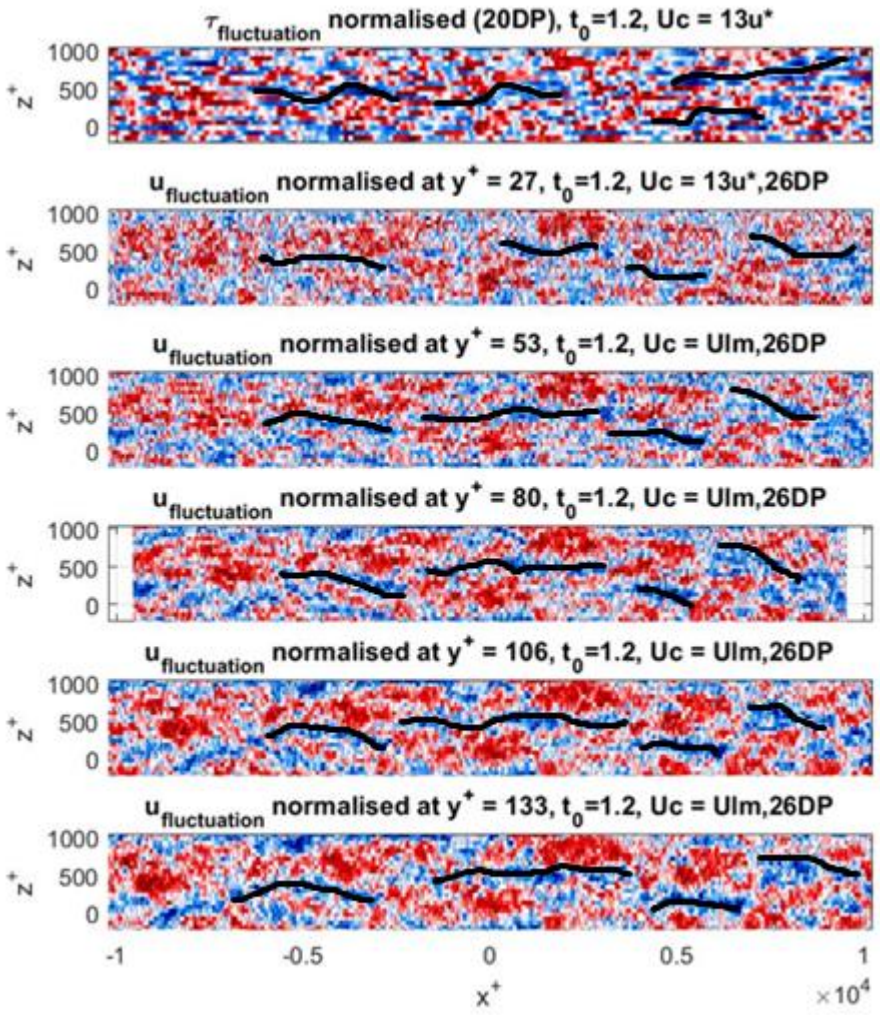


Figure 134: Skin-friction maps by hot-wires vs. velocity maps by PIV, Original data

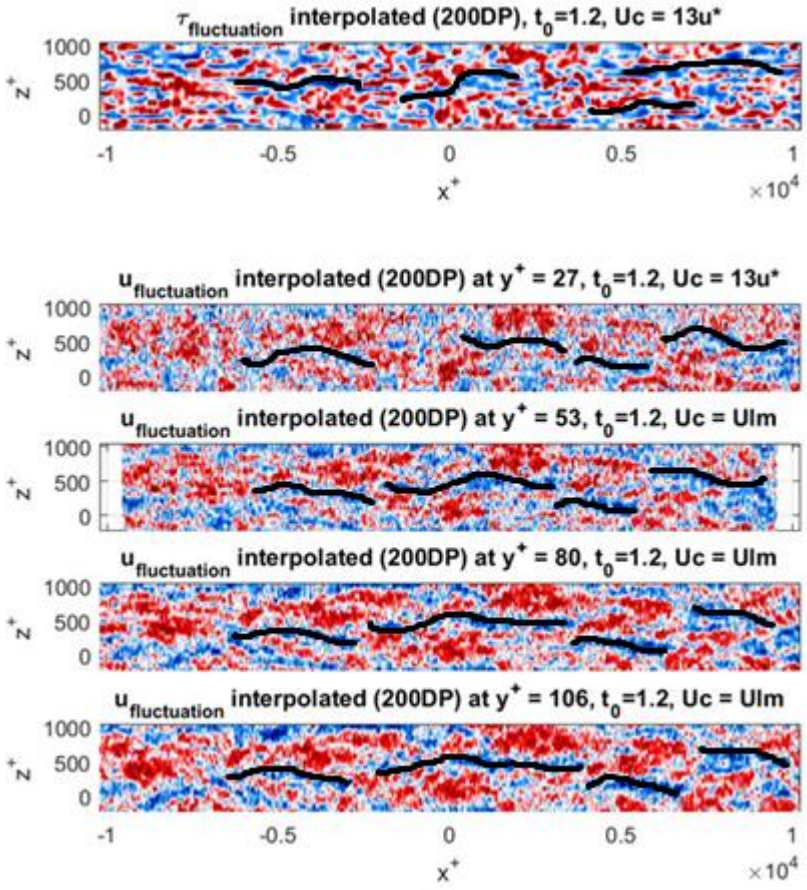


Figure 135: Skin-friction maps by hot-wires vs. velocity maps by PIV, interpolated data

Figure 136 displays the filtered skin-friction and velocity fluctuations, more clearly revealing the elongated, large scale, low skin-friction regions (blue) located between high skin-friction regions (red).

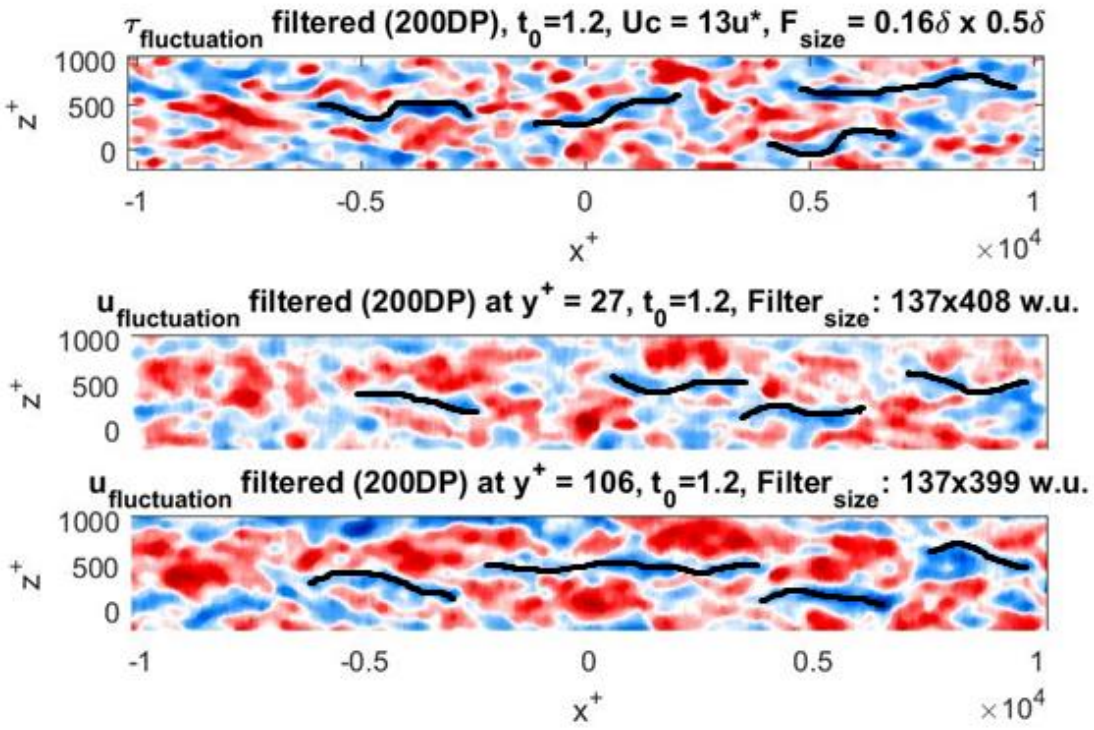


Figure 136: Fluctuating friction signals from the spanwise array and velocity signals from PIV, filter size: 137 x 408 wall unit in the spanwise (z) and the streamwise (x) directions, respectively.

It can be reported that patterns of low- and high-speed skin-friction and velocity regions exist in the viscous sublayer and logarithmic regions.

Data from HW and PIV at different *y*-positions are shown for comparison. A similar median filter has been applied; however the velocity fluctuation map is located in the buffer region and logarithmic regions and the skin-friction map in the viscous sublayer. We can infer that patterns of low and high skin-friction regions at the wall exist through similarities of patterns in the viscous sublayer and in the logarithmic region. It can be said that those patterns in the viscous sublayer are related to the large-scale structures in the buffer and logarithmic regions. This finding is highlighted by the detection of the long structures (traces) using the method of Lee et al. (2014). The traces show that there is a clear link between the wall stress with further from the wall structures. To examine this point more quantitatively, statistical analyses are made in the following sections.

Time series

A comparison between the velocity fluctuation at 4 y+ positions (27, 53, 80 and, 106) and the skin friction fluctuation obtained from the s-PIV and HW, respectively, is shown in Figure 137.

The time signals reveal similarity in the content of the two signals. This confirms the findings in the previous section.

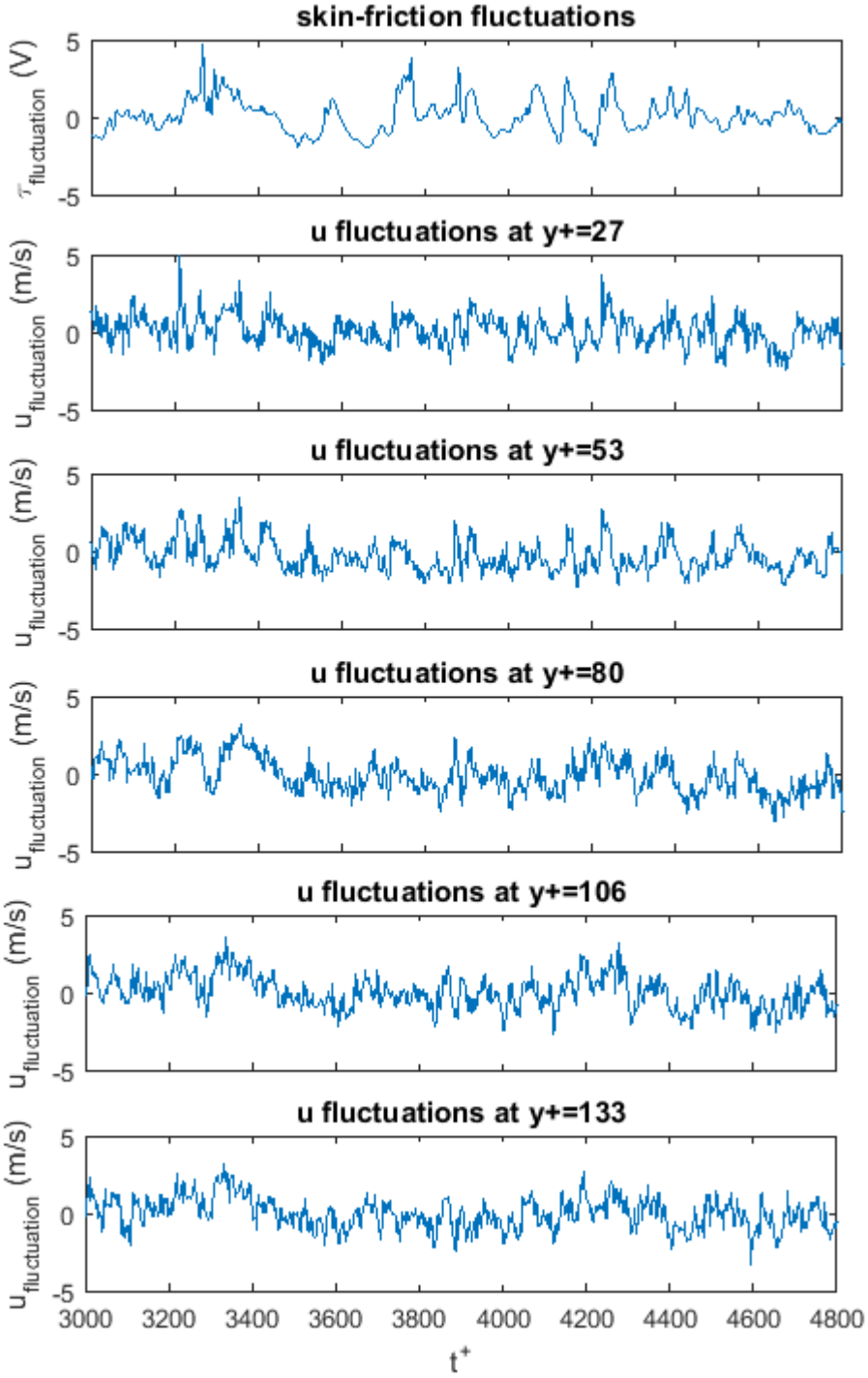


Figure 137: Time series of velocity fluctuations at y+ = 27, 53, 80 and 106 wall unit and skin-friction fluctuations (20 000 wall unit). The data was obtained simultaneously.

Cross-Correlation of skin-friction and velocity fluctuations at z+ = 400

Statistical analyses of the full data set are made to quantify the similarity between the wall shear and the turbulence response.

In Figure 138, R_{uu} is the normalised cross-correlation of two discrete-time sequences. It measures the similarity between the velocity fluctuation, u_1 and the skin-friction fluctuation, u_2 as a function of a shift (τ).

$$R_{uu} = \frac{\overline{u_1(t) \times u_2(t+\tau)}}{\sqrt{\overline{u_1^2}}\sqrt{\overline{u_2^2}}} \quad \textbf{(24)}$$

It also gives the position of peak value which indicates the time offset at which the two signals are the most similar. Regarding the correlation coefficient for Figure 138, there is a delay for the signal for each R_{uu}, but that delay was negligible, near zero. The formula becomes then as in Equation 25.

The cross-correlation of skin-friction fluctuation and velocity fluctuations at y+ = 27, 80, 106 and 133 have been plotted in Figure 138. It can be seen that the tendency of the cross-correlation between the velocity fluctuation at y+=27 and y+=133 in comparison with the one between the skin-friction fluctuation and the velocity fluctuation at y+ = 133 is similar in terms of the appearance of peaks and troughs at most instants in the trace.

In Table 29 and 30, R_{uu} represents the two-point correlation coefficient between the velocity (u_1) and skin-friction (u_2) fluctuations obtained at z+ = 400. It is defined as

$$R_{uu} = \frac{\overline{u_1(t) \times u_2(t)}}{\sqrt{\overline{u_1^2}}\sqrt{\overline{u_2^2}}} \quad \textbf{(25)}$$

Table 29 shows the correlation coefficient of skin-friction fluctuations and velocity fluctuations at y+ = 27, 106 and 133. It is then compared to the correlation coefficient of velocity fluctuations at y+ = 27 and 106, 133 as shown in Table 30.

By comparing the results from Table 30, it is seen that the velocity fluctuation at y+ = 27 vs. y+ = 56 has a higher correlation than y+=27 vs y+=133. In other words, the velocity map at y+=27 has a higher correlation with the map at y+ = 53 then with the map at y+ = 133 indicating that the velocity fluctuation correlation decreases with an increase in y-position.

In the other hand by comparing skin-friction fluctuation with velocity fluctuation at y+ = 27, 106 and 133, it is seen that the correlation increases with an increase in y-position. The tendency of the correlation with y-position is opposite for skin-friction fluctuation and velocity fluctuation. Indeed, there is a decrease of 65% between the correlation coefficient of y+=27 vs. y+=53 and y+=27 vs. y+=133, while an increase of 24% is shown between the correlation coefficient of skin-friction vs. y+=27 and skin-friction vs. y+ = 133.

The correlation coefficient between the skin-friction fluctuation and the velocity fluctuation at y+=133 equals 0.1172. As for the correlation coefficient between the velocity fluctuation at y+=27 and y+=133, it is equal to 0.1884. There is a difference of 38% between both correlations in comparison with 65%, being the difference between the correlation coefficient of y+=27 vs. y+=53 and y+=27 vs. y+=133.

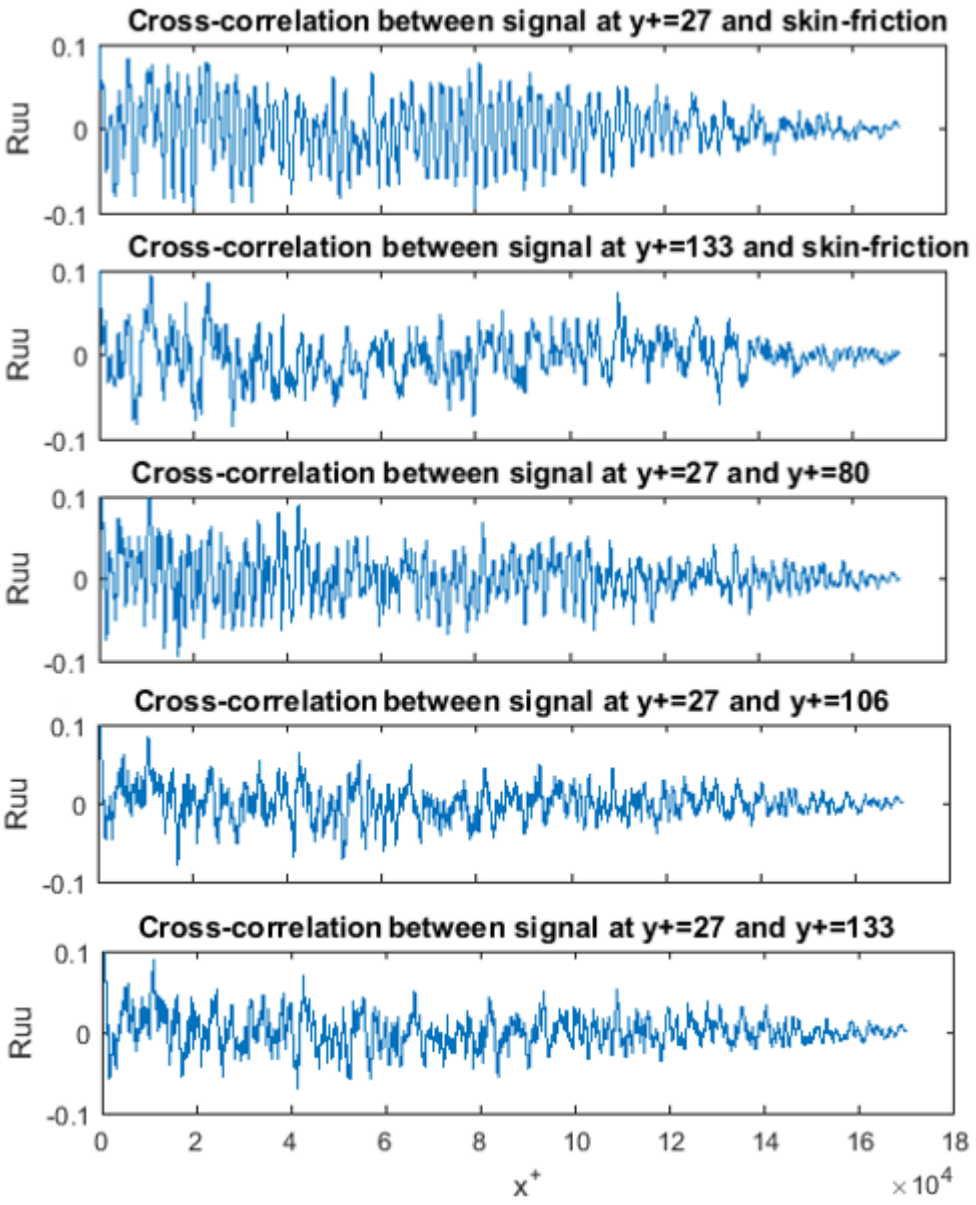


Figure 138: Cross-correlation of skin-friction fluctuation and velocity fluctuations at y+ = 27, 80, 106 and 133 in the streamwise direction at z+ = 400.

Table 29: Correlation coefficient between signal of skin-friction vs. y+=27,106, and 133

	y+=27 vs. skin-friction	y+=106 vs. skin-friction	y+=133 vs. skin-friction
Ruu	0.0944	0.1154	0.1172

Table 30: Correlation coefficient between signal at y+=27 vs. y+=106 and y+=133

	y+=27 vs. y+=53	y+=27 vs. y+=106	y+=27 vs. y+=133
Ruu	0.5357	0.2387	0.1884

Correlation coefficient between skin-friction and velocity fluctuations along z+

The correlation coefficient between the streamwise skin-friction and velocity fluctuations at y+=27, 56, 106, and 133 are represented along z+ in Figure 139.

The first 2 graphs show a representation of the correlation coefficient for the velocity. For comparison, the consecutive 3 graphs show comparable data from the skin-friction. These data are taken simultaneously from the rake and s-PIV; however, the rake is located at the wall and s-PIV in the log region.
Quantitatively, the correlations are slightly lower for the skin friction than exhibited by the log-region velocity signals as seen in Table 31. The correlation coefficient for the skin friction (R_{uu} mean = 0.14) is 52% lower than for the velocity (R_{uu} mean = 0.29) by comparing them both to the signal at y+=133. This is comparable with the drop of the correlation coefficient, equals to 47%, for velocity comparison at y+=27 versus (vs.) y+=56 (R_{uu} mean = 0.55) and vs. y+=133 (R_{uu} mean = 0.29). This gives an idea of the meaning behind the numbers for the correlation coefficient. It means that the similarities between the map at y+=27 vs. y+=56 and y+=27 vs. y+=133 (R_{uu} mean drop = 47%) are almost identical to the map of skin-friction vs. y+=133 and y+=27 vs. y+=133 (R_{uu} drop = 53%).

Furthermore, it is interesting to point out that the skin-friction fluctuations have a higher correlation with the velocity fluctuations further from the wall. Indeed, it is observed that the correlation of skin-friction with velocity fluctuation improves as y+ increases further from the wall. A higher correlation is seen for the map of skin-friction vs. y+=133 than skin-friction vs. y+=27. The skin-friction map has a higher similarity with the velocity map at y+=133 (R_{uu} mean = 0.14) than the map at y+=27 (R_{uu} mean = 0.08).

The skin-friction fluctuation is compared to velocity fluctuation at y+ = 27 (buffer region), y+ = 106 (logarithmic region) and y+ = 133 (log/wake region). From the mean velocity profile (Figure 88, page 99), it can be seen that the viscous sublayer extends from 0 < y+ < 5, the buffer region extends from 5 < y+ < 30, the logarithmic region extends from 30 < y+ < 125 and the wake region for y+

> 125. The inner layer represents the viscous sublayer and the buffer region as for the outer layer, it is composed of the logarithmic and wake region.

According to Adrian et al. (2000a), hairpin structures arranged together form large scale structures from y+ = 50, therefore, in the logarithmic region. Furthermore, Abe et al. (2004) showed from their DNS results, at Re_τ = 640, that the large-scale structures existing in the outer layer leave footprints in the instantaneous wall shear-stress fluctuations. This is in line with our findings that the skin-friction fluctuation has a higher correlation with structures in the logarithmic region (outer layer) than the buffer region (inner layer).

In summary, elongated and meandering low and high skin-friction regions at the wall exist and share sufficient similarities such that they are almost certainly related to the large-scale structures in the logarithmic region. These results further confirm the qualitative findings of the previous section. They clearly indicate that the large-scale structure observed with HW at the wall is essentially associated with the structures existing in the log/outer layer of the flow. For the first time, it is shown that there is a connection of the shear stress. Our experimental result indicates that the outer layer has a velocity fluctuation trace similar to the wall shear stress at the same stream-wise position. That relationship is reflected in Figure 13, p.21. Finally, the similarity of velocity fluctuation and wall stress is weaker for the layers between the outer layer and the wall. By looking at the relationship between the skin-friction and velocity fluctuations, it is shown from the cross-correlation coefficient, an increase of 43% from R_{uu} = 0.08 to R_{uu} = 0.14, respectively for y+=27 versus τ and y+=133 versus τ.

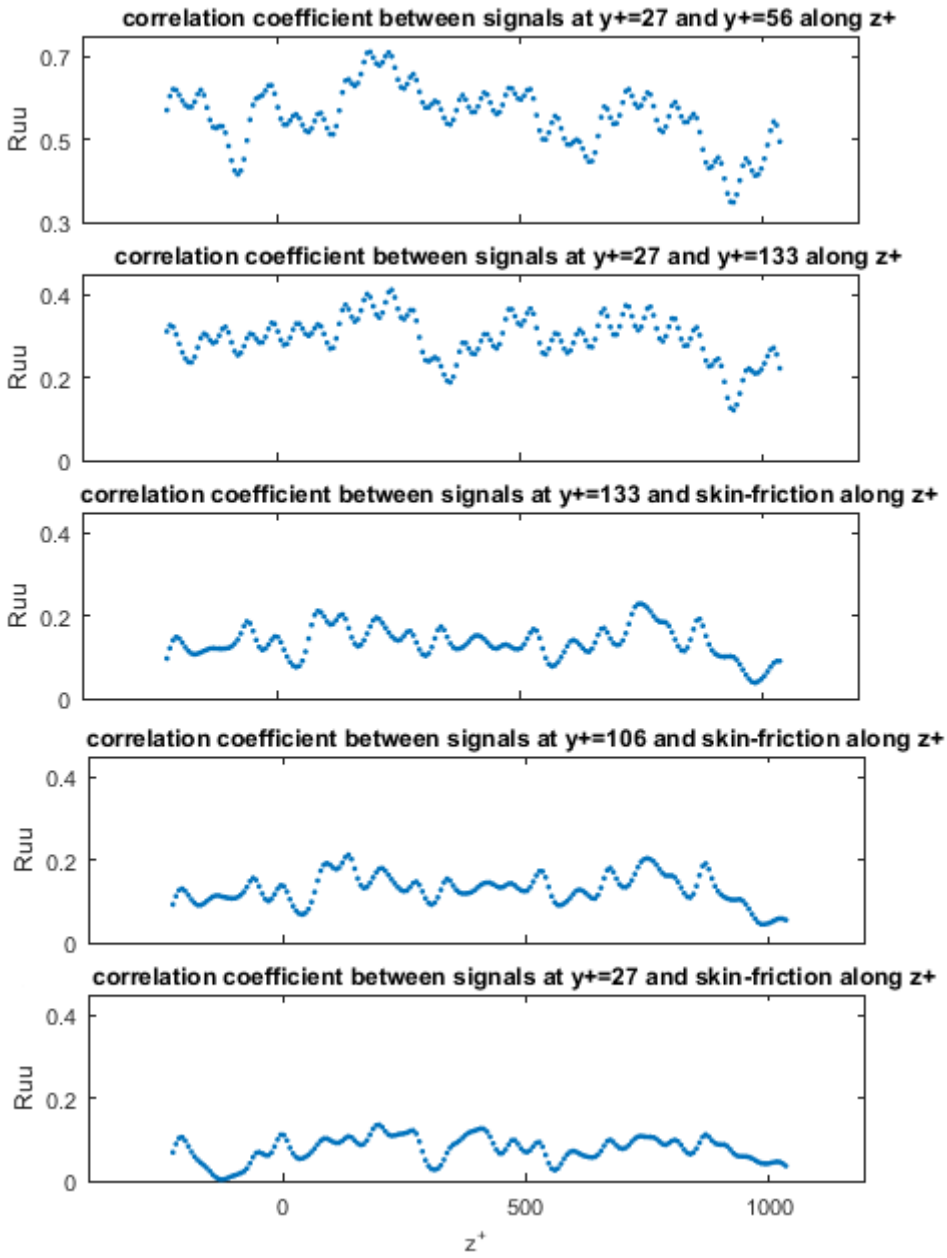


Figure 139: Correlation coefficient Ruu between skin-friction and 3 wall normal positions along z+

Table 31: Correlation coefficient Ruu between skin-friction and 3 wall normal positions along z+

		y+=27 vs. τ	y+=106 vs. τ	y+=133 vs. τ	y+=27 vs. y+=133	y+=27 vs. y+=56
Ruu	**min**	0.003	0.045	0.038	0.12	0.35
	max	0.13	0.21	0.23	0.41	0.71
	mean	0.08	0.13	0.14	0.29	0.55
	std	0.030	0.036	0.038	0.05	0.073

6.3 Chapter Summary

Many DNS studies have shown that there are footprints of large-scale structures in the near wall region. Studies have also correlated these structures to the ones present in the logarithmic region. The objective of this present investigation was to look at the skin-friction signals at the wall simultaneously with the velocity distributions at different y^+ positions in the buffer and logarithmic regions to compare those experimental data with the DNS results (Abe et al., 2004). Those DNS data, at Re_τ = 640, seem to suggest that there is a good correlation between the negative structures in the viscous sublayer and the buffer and logarithmic regions by mapping the velocity fluctuations. In our experimental studies, at Re_τ=568, the results showed that there were recognisable features from the near-wall region (viscous sublayer) measured with hot-wire sensors (skin-friction) and the buffer and logarithmic layers measured with s-PIV (velocity). Furthermore, large-scale structures were detected in the viscous sublayer and logarithmic regions to enhance the visual inspection. The present experimental results are in line with DNS data.

To sum up, first time measurement of 2D instantaneous skin-friction fluctuations at the wall with further from the wall structures is conducted. A reliable correlation between the two measurements is established qualitatively and quantitatively.

Chapter 7 Conclusions and Future Recommendations

Chapter 5: Near-wall investigations at different wall-normal positions and Reynolds Numbers Dependence

Instantaneous skin-friction measurement

This work was achieved to investigate and compare the instantaneous skin-friction maps at different Reynolds number within the viscous sublayer using a rake of 20 hot-wire sensors.

The signal characteristics of the instantaneous skin-friction were compared at different Re_τ. The intention was to investigate the near-wall large scale structures at different Re_τ. If Re_τ is changed, y+ is also changed so it led to compare instantaneous fluctuating velocity map at different y-locations and then comparing different structures. Nevertheless, if the sensors are positioned close enough to the wall within the viscous sublayer, it may not matter as y+ does not change much and instantaneous fluctuating velocity map can be compared. In other words, as our intention is to compare the instantaneous fluctuating velocity map at different Re_τ, it might be crucial to be as close to the wall as possible unless the structures does not change within a certain range of y+ in the viscous sublayer.

At low (Re_τ = 423) and high (Re_τ = 1310) Reynolds numbers the patterns length and width are different at the same y+ positions. But this is mainly due to a variation in the spanwise resolution with a variation of Reynolds number.

Finally, it is important to bear in mind that in our studies, we are only interested in large-scale structures with width equal or larger than 100 wall unit. At Re_τ = 423 and 568, the spanwise resolution is equal to 31 and 44, respectively by analogy with the Nyquist theorem, 100 wall unit is twice of 31 and 44 wall unit. In that case at 423 and 568 Reynolds numbers, the signals are taken at spacing between sensors small enough to catch the large-scale structures. This is not the case for higher Reynolds numbers such as 1310. When the sensor spacing (spanwise resolution) is identical for all the Reynolds number, the

instantaneous skin-friction maps show similar patterns with same order for the width and length of the streaks.

In conclusion, several filter sizes were applied in the streamwise direction for median filtering operation in the aim to find patterns which could be large-scale footprint candidates. The use of filter enables us to distinguish and see more clearly the large patterns as without it, small and detached patterns make it difficult to visualise the large patterns. The streamwise cross-correlation of the fluctuating skin-friction data from the probes indicate the presence of structures that extend to large streamwise distance (5000 wall unit). Such skin-friction patterns seem to share similarities with those observed in the logarithmic region investigated in our 2D PIV results in.

Cross-correlation coefficient measurement

The spanwise two-point correlations seem to suggest that, in general, for small separation distance (y+) within the viscous sublayer, the correlation for the velocity in the direction of the displacement in the y-direction is approximately equal. It also illustrates a local minimum (peak negative value) followed by a weak positive maximum. One might conclude that the reason for this negative correlation is likely to be associated with the vortical motions, which occur one after the other with opposite signs of rotation. Indeed, this is probably due to the quasi-streamwise vortices and their effect on the flow field. The magnitude of the negative peak is decreasing as Re_τ increases. The peak values shift away at high Re_τ, while at low Re_τ the peaks are located closer to x+ = 0. Although, considering the lack of data point for an increase in Reynolds number, this statement is not established. For, the streamwise cross-correlation measurements, the values of R_{uu} are reduced when x+ increases. The reduction increases as Reynolds number increases. It is suggested that the structure has a longer streamwise length for higher Reynolds number. This reduction observed in the streamwise cross-correlation measurements suggests a change in the size of the near-wall structures as a function of Reynolds number. In conclusion, it appears that, in accordance with the experimental observations, near the walls the flow consists of elongated streaky structures. Those structures have their length dimension increasing with an increase in Reynolds number. Finally, it can be concluded that both the

spanwise and streamwise fluctuations are highly correlated with the correlation decreasing as the Reynolds number increases. Although, the streamwise fluctuations are correlated for larger distances compared to the spanwise fluctuations meaning that the structures are longer in x-direction than z-direction. The signals are highly correlated in the streamwise direction, suggesting that it affects a large region and that the streamwise structures are quite long, $x+ \leq 2500$. However, the spanwise correlation was much less, suggesting that the events are relatively thin, $z+ \leq 100$. For the skewness and kurtosis factors, it seems that their values for $Re_\tau = 423$ and 1310 are similar when they are at the same wall-normal position. At $Re_\tau = 423$, the skewness and kurtosis obtained were similar to what is found in the literature. For Re_τ =568 and 1310, the results are not comparable to those of the literature with under-estimated values. This is mainly due to the positions of the sensors from the wall increasing with an increase in Reynolds number for dimensionless value. To sum up, it appears that, in accordance with the experimental observations, near the wall, the flow consists of elongated structures. Those structures have their length dimension increasing with an increase in Reynolds number. The spanwise and streamwise fluctuations are highly correlated, with the correlation decreasing as the Reynolds number increases. Although, the streamwise fluctuations are correlated for larger distances compared to the spanwise fluctuations meaning that the structures are longer in *x*-direction (streamwise) than *z*-direction (spanwise).

A universally applicable outcome from the length scale of turbulent structures observed in this chapter is demonstrated and compared to those discovered by DNS and by experimentation of prior investigations. First, it is interesting to see that at low Reynolds number, $Re_\tau \leq 568$, the length scale over boundary layer thickness decreases from the wall up to the log region but, in the contrary, for $Re_\tau = 1410$, an increase is seen from the wall up to the log region. Finally, we note that the streamwise length scale over boundary layer seems to decrease with an increase in Reynolds numbers, this decrease effect seems to be more important at lower Reynolds number.

Chapter 6: On the relation of large-scale structures and skin-friction

In order to investigate the effects of large-scale structures on the skin-friction fluctuations, stereoscopic PIV experiments were carried out in the outer layer along with a rake of 20 hot-wire sensors placed at the wall simultaneously. The aim of this experiment is to correlate the skin-friction map with the large-scale structures present in and beyond the logarithmic region of the turbulent boundary layer. This will enable to detect the large-scale structures from wall based sensors.

The iso-contours of $\tau+/u+$ were investigated. The original unfiltered maps, illustrate elongated regions with noisy smaller scale fluctuations within. These small scales are unreliable and can be removed using median filter. The resemblance of patterns are seen for s-PIV from $y+ = 27$, buffer region to $y+ = 133$, logarithmic region. The same observation can be found for the patterns from instantaneous skin-friction map in the viscous sublayer ($y+ < 5$) and the velocity map in the buffer and logarithmic regions. The filtered skin-friction and velocity fluctuations maps display more clearly the elongated, large scale, low skin-friction region (blue) located between high skin-friction regions (red). The patterns in the logarithmic regions show an elongated large high and low-speed feature, extending to a distance of 10δ (10 000 wall unit) in the streamwise direction. The relationship between wall shear-stress with further from wall structures was seen qualitatively through the contour plot and quantitatively through correlation coefficient for the full set of data measured. For the first time direct instantaneous comparisons of near-wall and large scale structures of turbulent boundary layers are given. Agreement in the similarity of the near-wall structures in comparison with large scale-structures is shown. The insight into the flow provided shows similarities such that the near-wall structures are almost certainly related to the large-scale structures in the logarithmic region. For future work, to obtain enough resolution, the measurement region should be divided into two regions and separate measurements should be performed.

References

ABE, H., KAWAMURA, H. & CHOI, H. 2004. Very Large-Scale Structures and Their Effects on the Wall Shear-Stress Fluctuations in a Turbulent Channel Flow up to Reτ=640. *Journal of Fluids Engineering,* 126(5)**,** 835-843.

ABE, H., KAWAMURA, H. & MATSUO, Y. 2001. Direct Numerical Simulation of a Fully Developed Turbulent Channel Flow With Respect to the Reynolds Number Dependence. *Journal of Fluids Engineering,* 123**,** 382-393.

ADRIAN, R. J. 2007. Hairpin vortex organization in wall turbulence. *Physics of Fluids,* 19**,** 1-16.

ADRIAN, R. J., CHRISTENSEN, K. T. & LIU, Z.-C. 2000b. Analysis and interpretation of instantaneous turbulent velocity fields. *Experiments in Fluids,* 29**,** 275-290.

ADRIAN, R. J., MEINHART, C. D. & TOMKINS, C. D. 2000a. Vortex organisation in the outer region of the turbulent boundary layer. *Journal of Fluid Mechanics,* 422**,** 1-54.

ADRIAN, R. J., MEINHART, C. D. & TOMKINS, C. D. 2000b. Vortex organization in the outer region of the turbulent boundary layer. *J. Fluid Mech.,* 422**,** 1-54.

AGOSTINI, L. & LESCHZINER, M. A. 2014a. On the influence of outer large-scale structures on near-wall turbulence in channel flow. *Physics of Fluids,* 26**,** 1-23

AGOSTINI, L. & LESCHZINER, M. A. 2014b. On the influence of outer large-scale structures on near wall-turbulence in channel flow. *Physics of fluids,* 26**,** 23.

ALFREDSSON, P. H., JOHANSSON, A. V., HARITONIDIS, J. H. & ECKELMANN, H. 1988. The fluctuating wallshear stress and the velocity field in the viscous sublayer. *Physics of fluids,* 31**,** 1026-1033.

ATKINSON, C., BUCHMANN, N. A. & SORIA, J. 2015. An experimental investigation of turbulent convection velocities in a turbulent boundary layer. *Flow Turbulence Combust,* 94**,** 79-95.

BALAKUMAR, B. J. & ADRIAN, R. J. 2007. Large- and very-large-scale motions in channel and boundary-layer flows. *Philosophical Transactions of the Royal Society A,* 365**,** 665-681.

BECHERT, D. W., BARTENWERFER, M., HOPPE, G. & REIF, W.-E. Drag reduction mechanisms derived from shark skin. INTERNATIONAL COUNCIL OF THE AERONAUTICAL SCIENCES (ICAS), September 7-12 1986 London, England. 1044-1068.

BECHERT, D. W., HOPPE, G. & REIF, W. E. 1985. On the drag reduction of the shark skin. *American Institute of Aeronautics and Astronautics*.

BENJAMIN, T. B. Fluid flow with flexible boundaries. In Proceedings of the Eleventh International Congress of Applied Mechanics 1964 Munich (Germany). 109-128.

BLACKWELDER, R. F. & ECKELMANN, H. 1979. Streamwise vortices associated with the bursting phenomenon. *Journal of Fluid Mechanics,* 94**,** 577-594.

BLACKWELDER, R. F. & HARITONIDIS, J. H. 1983. Scaling of the bursting frequency in turbulent boundary layers. *Journal of Fluid Mechanics,* 132**,** 87-103.

BLACKWELDER, R. F. & KAPLAN, R. E. 1976. On the structure of the turbulent boundary layer. *Journal of Fluid Mechanics,* 76**,** 89-112.

BROWN, G. L. & THOMAS, A. S. W. 1977. Large structure in a turbulent boundary layer. *Physics of fluids,* 20**,** S243-S252.

BRUUN 1995a. *Hot-wire anemometry*, Oxford science publications.

BRUUN, H. H. 1995b. *Hot-wire anemometry: principles and signal analysis,* United States, Oxford University Press Inc.

CANTWELL, B. J. 1981. Organized motion in turbulent flow. *Annual Reviews of Fluid Mechanics* 13**,** 457-515.

CHAUHAN, K. A., MARUSIC, I. & HUTCHINS, N. 2011. Organised motions in turbulent boundary layers over a wide range of Reynolds number. *6th AIAA Theoretical Fluid Mechanics Conference.* Honolulu, Hawaii: American Institute of Aeronautics and Astronautics.

CHOI, H., MOIN, P. & KIM 1994. Active turbulence control for drag reduction in wall bounded flows. *Journal of Fluid Mechanics,* 262**,** 75-110.

CHOI, K.-S. 1989. Near-wall Structure of Turbulent Boundary Layer with Riblets. *Journal of Fluid Mechanics,* 208**,** 417-458.

CHOI, K.-S. 2002. Near-wall structure of turbulent boundary layer with spanwise-wall oscillation. *Physics of Fluids,* 14**,** 2530-2542.

CHOI, K.-S., DEBISSCHOP, J.-R. & CLAYTON, B. R. 1998. Turbulent boundary-layer control by means of spanwise-wall oscillation. *Journal of American Institute of Aeronautics and Astronautics,* 36**,** 1157-1163.

CHOI, K.-S., YANG, X., CLAYTON, B. R., GLOVER, E., ATLAR, M., SEMENOV, B. N. & KULIK, V. 1997. Turbulent drag reduction using compliant surfaces. *Proceedings of the Royal Society A,* 453**,** 2229-2240.

COLES, D. 1969. Turbulent Boundray layers in pressure gradients: A survey lecture. Prepared for the 1968 AFOSR-IFP-Stanford Conference on computation of Turbulent Boundary Layers. *Computation of Turbulent Boundary Layers.* Stanford.

CORINO, E. R., AND BRODKEY, R. S., 1969. A visual investigation of the wall region in turbulent flow. *Journal of Fluid Mechanics,* 37**,** 1-30.

CORINO, E. R. & BRODKEY, R. S. 1969. A visual investigation of the wall region in turbulent flow. *Journal of Fluid Mechanics,* 37**,** 1-30.

CORKE, T. C., GUEZENNEC, Y. & NAGIB, H. M. 1979. Modification in drag of turbulent boundary layers resulting from manipulation of large-scale structures. *Viscous Flow Drag Reduction Progress in Astronautics and Aeronautics*.

DEL ALAMO, J. C. & JIMENEZ, J. 2003. Spectra of the very large anisotropic scales in turbulent channels. *Physics of Fluids,* 15**,** 41-44.

DEL ALAMO, J. C. & JIMENEZ, J. 2006. Linear energy amplification in turbulent channels. *Journal of Fluid Mechanics,* 559**,** 205-213.

DEL ALAMO, J. C., JIMENEZ, J., ZANDONADE, P. & MOSER, R. D. 2004. Scaling of the energy spectra of turbulent channels. *Journal of Fluid Mechanics,* 500**,** 135-144.

DIXIT, S. A. & RAMESH, O. N. 2010. Large-scale structures in turbulent and reverse-transitional sink flow boundary layers. *Journal of Fluid Mechanics,* 649**,** 233-273.

EUROPEAN COMMISSIONS, G. O. P. 2001. European Aeronautics: A vision for 2020.

FERNHOLZ, H. H., JANKE, G., SCHOBER, M., WAGNER, P. M. & WARNACK, D. 1996. New developments and applications of skin-friction measuring techniques. *Measurement Science and Technology,* 7**,** 1396-1409.

FREYMUTH, P. 1968. Noise in hot-wire anemometers. *Review of Scientific Instruments,* 39**,** 550-557.

FREYMUTH, P. 1977a. Frequency response and electronic testing for constant-temperature hot-wire anemometers. *Journal of Physics,* 10**,** 705-710.

FREYMUTH, P. 1977b. Further investigation of the non-linear theory for constant-temperature hot-wire anemometers. *Journal of Physics,* 10**,** 710-713.

GAD-EL-HAK, M. & BANDYOPADHYAY, P. R. 1994. Reynolds Number Effects in Wall-Bounded Flows. *Applied Mechanics Reviews,* 47**,** 307-365.

GANAPATHISUBRAMANI, B., CLEMENS, N. T. & DOLLING, D. S. 2006. Large-scale motions in a supersonic turbulent boundary layer. *Journal of Fluid Mechanics,* 556**,** 271-282.

GANAPATHISUBRAMANI, B., HUTCHINS, N., HAMBLETON, W. T., LONGMIRE, E. K. & MARUSIC, I. 2005. Investigations of large-scale coherence in a turbulent boundary layer using two-point correlations. *Journal of Fluid Mechanics,* 524**,** 57-80.

GANAPATHISUBRAMANI, B., HUTCHINS, N., MONTY, J. P., CHUNG, D. & MARUSIC, I. 2012. Amplitude and frequency modulation in wall turbulence. *Journal of Fluid Mechanics,* 712**,** 61-91.

GANAPATHISUBRAMANI, B., LONGMIRE, E. K. & MARUSIC, I. 2003. Characteristics of vortex packets in turbulent boundary layers. *Journal of Fluid Mechanics,* 478**,** 35-46.

GUALA, M., HOMMEMA, S. E. & ADRIAN, R. J. 2006. Large-scale and very-large-scale motions in turbulent pipe flow. *Journal of Fluid Mechanics,* 554**,** 521-542.

GUPTA, A. K., LAUFER, J. & KAPLAN, R. E. 1971. Spatial structure in the viscous sublayer *Journal of Fluid Mechanics,* 50**,** 493-512.

HAMBLETON, W. T., HUTCHINS, N. & MARUSIC, I. 2006. Simultaneous orthogonal-plane particle image velocimetry measurements in a turbulent boundary layer. *Journal of Fluid Mechanics,* 560**,** 53-64.

HEAD, M. R. & BANDYOPADHYAY, P. 1981. New aspects of turbulent boundar-layer structure. *Journal of Fluid Mechanics,* 107**,** 297-338.

HEFNER, J. N., WEINSTEIN, L. M. & BUSHNELL, D. M. 1979. Large Eddy Breakup scheme for viscous drag reduction. . *Viscous Flow Drag Reduction Progress in Astronautics and Aeronautics***,** 128-143.

HENRY, A. R. 2002. *Modification of the near wall structure of a turbulent boundary layer by opposition control.* Degree of Doctor of Philosophy, University of Nottingham.

HOYAS, S. & JIMENEZ, J. 2006. Scaling of the velocity fluctuations in turbulent channels up to Reτ=2003. *Physics of Fluids,* 18**,** 1-4.

HUANG, T. S., YANG, G. J. & TANG, G. Y. 1979. A fast two-diemsional median filtering algorithm. *Institute of Electrical and Electronics Engineers on acoustics, speech and signal processing,* ASSP-27**,** 13-18.

HUTCHINS, N. 2003. *An Investigation of Larger-Scale Coherent Structures in Fully Developed Turbulent Boundary Layers.* PhD, Nottingham.

HUTCHINS, N. & CHOI, K.-S. 2002. Accurate measurements of local skin-friction coefficient using hot-wire anemometry. *Progress in Aerospace Sciences,* 38**,** 421-446.

HUTCHINS, N. & CHOI, K.-S. Towards a greater understanding of turbulent skin-friction reduction. ASME Proceedings | Flow Instabilities and Control, 2002a. 1449-1454.

HUTCHINS, N. & CHOI, K.-S. 2002b. Accurate Measurements of Local Skin Friction Coefficient Using Hot-Wire Anemometry. *Progress in Aerospace Science***,** 421-446.

HUTCHINS, N. & CHOI, K.-S. 2003. Large-scale structure in the turbulent boundary layer. *Third International Symposium on Turbulence and Shear Flow Phenomena.* International Center, Sendai, Japan.

HUTCHINS, N., HAMBLETON, W. T. & MARUSIC, I. 2005. Inclined crossstream stereo particle image velocimetry measurements in turbulent boundary layers. *Journal of Fluid Mechanics,* 541**,** 21-54.

HUTCHINS, N. & MARUSIC, I. 2007a. Evidence of very long meandering features in the logarithmic region of turbulent boundary layers. *Journal of Fluid Mechanics,* 579**,** 1-28.

HUTCHINS, N. & MARUSIC, I. 2007b. Large-scale influences in near-wall turbulence. *Philosophical Transactions of the Royal Society A,* 365**,** 647-664.

HUTCHINS, N., MONTY, J. P., GANAPATHISUBRAMANI, B., NG, H. C. H. & MARUSIC, I. 2011. Three-dimensional conditional structure of a high-Reynolds-number turbulent boundary layer. *Journal of Fluid Mechanics,* 673**,** 255-285.

HUTCHINS, N., MONTY, J. P., GANAPATHISUBRAMANI, B., NG, H. C. H., AND MARUSIC, I., 2011. Three-dimensional conditional structure of a high-Reynolds-number turbulent boundary layer. *Journal of Fluid Mechanics,* 673**,** 255-285.

HUTCHINS, N., NICKELS, T. B., MARUSIC, I. & CHONG, M. S. 2009. Hot-wire spatial resolution issues in wall-bounded turbulence. *Journal of Fluid Mechanics,* 635**,** 103-136.

ICAO 2010. Aviation's contribution to climate change.

IEA, I. E. A. 2009. Transport, Energy and CO_2.

ITAKURA Manual of CTA KI-N1997.

IWAMOTO, K., KASAGI, N. & SUZUKI, Y. 2005. Direct Numerical Simulation of Turbulent Channel Flow at Reτ=2320. *Proceeding of 6th Symposium on Smart Control of Turbulence.* Tokyo, Japan.

IWAMOTO, K., SUZUKI, Y. & KASAGI, N. 2002. Reynolds Number Effect on Wall Turbulence: Toward Effective Feedback Control. *International Journal of Heat and Fluid Flow,* 23**,** 678-689.

JEONG, J. & HUSSAIN, F. 1995. On the identification of a vortex. *Journal of Fluid Mechanics,* 285**,** 69-94.

JOHANSSON, A. V. & ALFREDSSON, P. H. 1983. Effects of imperfect spatial resoltuion on measurements of wall-bounded turbulent shear flow. *Journal of Fluid Mechanics,* 137**,** 409-421.

JOHANSSON, A. V., ALFREDSSON, P. H. & KIM, J. Shear-layer structures in near-wall turbulence. Proceedings of the Summer Program, 1987 Centre for Turbulence Research. 237-251.

JOHNSON, R. W., SCHULTZ, R. R., ROACHE, P. J., CELIK, I. B., POINTER, W. D. & HASSAN, Y. A. 2006. Processes and Procedures for Application of CFD to Nuclear Reactor Safety Analysis. Idaho Falls, Idaho 83415: Idaho National Laboratory.

JUNG, W. J., MANGIAVACCHI, N. & AKHAVAN, R. 1992. Suppression of turbulence in wall-bounded flows by high-frequency spanwise oscillations. *Physics of Fluids,* 4**,** 1604-1607.

KANG, Y.-D. 2009. *Direct intervention of hairpin vortex in boundary layer to reduce friction drag.* PhD, Nottingham.

KANG, Y.-D. & CHOI, K.-S. 2005. Control of Outer Structures of the Turbulent Boundary Layer for Drag Reduction *2nd International Symposium on Seawater Drag Reduction* Busan, Korea.

KANG, Y. D., CHOI, K.-S. & CHUN, H. H. 2008. Direct intervention of hairpin structures for turbulent boundary-layer control. *Physics of Fluids,* 20**,** 1-13.

KARNIADAKIS, G. E., AND CHOI, K.-S., 2003. Mechanisms on transverse motions in turbulent wall flows. *Annual Review of Fluid Mecanichs,* 35**,** 45-62.

KARNIADAKIS, G. E. & CHOI, K.-S. 2003. Mechanisms on transverse motions in turbulent wall flows. *Annual Review of Fluid Mecanichs,* 35**,** 45-62.

KEIRSBULCK, L., FOURRIÉA, G., LABRAGAA, L. & GAD-EL-HAK, M. 2012. Scaling of statistics in wall-bounded turbulent flows. *Comptes Rendus Mecanique,* 340**,** 420-433.

KIM, H. T., KLINE, S. J. & REYNOLDS, W. C. 1971. The production of turbulence near a smooth wall in a turbulent boundary layer. *Journal of Fluid Mechanics,* 50**,** 133-160.

KIM, J., MOIN, P. & MOSER, R. 1987. Turbulence statistics in fully developed channel flow at low Reynolds number. *Journal of Fluid Mechanics,* 177**,** 133-166.

KIM, K. C. & ADRIAN, R. J. 1999. Very large-scale motion in the outer layer. *Physics of Fluids,* 11**,** 417-422.

KING, L. V. 1914. On the convection of heat from small cylinders in a stream of fluid. *Philosophical Transactions of the Royal Society A,* 214**,** 373-432.

KLEBANOFF, P. S. 1954. Characteristics of Turbulence in a Boundary Layer with Zero Pressure Gradient. *National Advisory Committee for Aaronautics TN 3178.*

KLINE, S. J., REYNOLDS, W. C., SCHRAUB, F. A. & RUNSTADLER, P. W. 1967. The structure of turbulent boundary layers. *Journal of Fluid Mechanics,* 30**,** 741-773.

KLINE, S. J., REYNOLDS, W. C., SCHRAUB, F. A., AND RUNSTADLER, P. W., 1967. The structure of turbulent boundary layers. *Journal of Fluid Mechanics,* 30**,** 741-773.

KRAMER, M. O. 1957. Boundary layer stabilisation by distributed damping. *Journal of Aeronautical Science,* 24**,** 459-460.

KRAMER, M. O. 1960. Boundary layer stabilisation by distributed damping. *Journal of the American Society of Naval Engineers,* 72**,** 25-33.

KREPLIN, H.-P. & ECKELMANN, H. 1979. Propagation of perturbations in the viscous sublayer and adjacent wall region. *Journal of Fluid Mechanics,* 95**,** 305-322.

KROGSTAD, P.-A., KASPERSEN, J. H. & RIMESTAD, S. 1998. Convection velocities in a turbulent boundary layer. *Physics of Fluids,* 10**,** 949-957.

LAUFER, J. 1954. The structure of turbulence in fully developed pipe flow. National Advisory Committee for Aeronautics.

LU, S. S. & WILLMARTH, W. W. 1973. Measurements of the structure of the Reynolds stress in a turbulent boundary layer. *Journal of Fluid Mechanics,* 60**,** 481-511.

MARUSIC, I., MATHIS, R. & HUTCHINS, N. 2010a. High Reynolds number effects in wall turbulence. *International Journal of Heat and Fluid Flow,* 31**,** 418-428.

MATHIS, R., HUTCHINS, N. & MARUSIC, I. 2009a. Large-scale amplitude modulation of the small-scale structures in turbulent boundary layers. *Journal of Fluid Mechanics,* 628**,** 311-337.

MATHIS, R., MONTY, J. P., HUTCHINS, N. & MARUSIC, I. 2009b. Comparison of large-scale amplitude modulation in turbulent boundary layers, pipes, and channel flows. *Physics of Fluids,* 21**,** 1-4.

MCKEON, B. J. & MORRISON, J. F. 2007. Asymptotic scaling in turbulent pipe flow. *Philosophical Transactions of the Royal Society A,* 365**,** 771-787.

METZGER, M. M. & KLEWICKI, J. C. 2001. A comparative study of nea-wall turbulence in high and low Reynolds number boundary layers. *Physics of Fluids,* 13**,** 692-701.

MOIN, P. & KIM, J. 1985. The structure of the vorticity field in turbulent channel flow. Part I: Analysis of instantaneous fields and statistical correlations. *Journal of Fluid Mechanics,* 155**,** 441-464.

MONTY, J. P., STEWART, J. A., WILLIAMS, R. C. & CHONG, M. S. 2007. Large-scale features in turbulent pipe and channel flows. *Journal of Fluid Mechanics,* 589**,** 147-156.

MORRISON, J. F. 2007. The interaction between inner and outer regions of turbulent wall-bounded flow. *Philosophical Transactions of the Royal Society A,* 365**,** 683-698.

MOSER, R. D., KIM, J. & MANSOUR, N. N. 1999. Direct numerical simulation of turbulent channel flow up to Reτ=590. *Physics of Fluids,* 11**,** 943-945.

NICOLAI, L. M. & CARICHMER, G. E. 2010. *Fundamentals of aircraft and airship design*, American Institute of Aeronautics and Astronautics.

PANTON, R. L. 2001. Overview of the self-sustaining mechanisms of wall turbulence. *Progress in Aerospace Sciences,* 37**,** 341-383.

PRASAD, A. K. 2000. Stereoscopic particle image velocimetry. *Experiments in Fluids,* 29**,** 103-116.

RAFFEL, M., WILLERT, C., WERELEY, S. & KOMPENHANS, J. 1998. *Particle image velocimetry: a practical guide,* Berlin, Springer.

RAHGOZAR, S. & MACIEL, Y. 2011. Low- and high-speed structures in the outer region of an adverse-pressure-gradient turbulent boundary layer. *Experimental Thermal and Fluid Science,* 35**,** 1575-1587.

REBBECK, H. & CHOI, K.-S. 2006. A wind-tunnel experiment on real-time opposition control of turbulence. *Physics of Fluids,* 18**,** 1-13.

RIGAS, G., JAMIESON, N. P., LI, L. K. B. & JUNIPER, M. P. 2016. Experimental sensitivity analysis and control of thermoacoustic systems. *Journal of Fluid Mechanics,* 787**,** null-null.

ROBINSON, S. K. 1991. Coherent motions in the turbulent boundary layer. *Annual Review of Fluid Mechanics,* 23**,** 601-639.

SCHLATTER, P., ÖRLÜ, R., LI, Q., BRETHOUWER, G., FRANSSON, J. H. M., JOHANSSON, A. V., ALFREDSSON, P. H. & HENNINGSON, D. S. 2009. Turbulent boundary layers up to Reθ=2500 studied through simulation and experiment. *Physics of Fluids,* 21**,** 1-4.

SCHLICHTING, H. 1979. *Boundary layer theory*.

SMITS, M. H. A. A. 2010. Temperature corrections for constant temperature and constant current hot-wire anemometers. *measurements science and technology,* 21.

TAKAGI., S. 1990. Burnout protection of a hot-wire anemometer. *Experiments in Fluids,* 9**,** 110-111.

TAYLOR, G. I. 1938. The spectrum of turbulence. *Proceedings of the Royal Society of London A,* 164**,** 476-490.

THEODORSEN, T. 1952. Mechanism of turbulence. *Proc. 2nd Midwestern Conference on Fluid Mechanics.* Ohio State University, Columbus, Ohio.

TOMKINS, C. D. & ADRIAN, R. J. 2003. Spanwise structure and scale growth in turbulent boundary layers. *Journal of Fluid Mechanics,* 490**,** 37-74.

TOWNSEND, A. A. 1961. Equilibrium Layers and Wall Turbulence. *Journal of Fluid Mechanics,* 11**,** 97-120.

WALLACE, J. M. 1985. The Vortical Structure of Bounded Turbulent Shear Flow. *Lecture Notes in Physics,* 235**,** 253-268.

WALLACE, J. M., ECKELMANN, H. & BRODKEY, R. S. 1972. The wall region in turbulent shear flow. *Journal of Fluid Mechanics,* 54**,** 39-48.

WALSH, M. J. 1980. Drag Characteristics of V-Groove and Transverse Curvature Riblets. *American Institute of Aeronautics and Astronautics***,** 168-184.

WALSH, M. J. 1982. Turbulent Boundary Layer Drag Reduction using Riblets. *In:* CENTER, N. L. R. (ed.) *AIAA 20th Aerospace Sciences Meeting.* Orlando, Florida.

WALSH, M. J. 1990. Riblets, in viscous drag reduction in boundary layers. *Progress in Astro and Aeronautics,* 123**,** 203-261.

WILLMARTH, W. W., AND LU, S. S., 1972. Structure of the Reynolds Stress Near the Wall. *Journal of Fluid Mechanics,* 55**,** 65-92.

WILLMARTH, W. W. & LU, S. S. 1972. Structure of the Reynolds Stress Near the Wall. *Journal of Fluid Mechanics,* 55**,** 65-92.

WILLS, J. A. B. 1962. The correction of hot-wire readings for proximity to a solid boundary. *Journal of Fluid Mechanics,* 12**,** 388-396.

WU, X. & MOIN, P. 2009. Direct numerical simulation of turbulence in a nominally zer-pressure-gradient flat-plate boundary layer. *Journal of Fluid Mechanics,* 630**,** 5-41.

ZHOU, J., ADRIAN, R. J. & KENDALL, T. M. 1999. Mechanisms for Generating Coherent Packets of Hairpin Vortices in Channel Flow. *Journal of Fluid Mechanics,* 387**,** 353-396.